

ISBN: 978-605-83575-0-1

2016 BOOK OF PROCEEDINGS

Chapter 1

ICENS

INTERNATIONAL CONFERENCE ON
ENGINEERING AND NATURAL SCIENCES

24-28 May 2016 / **Sarajevo**

Organized by



Supported by



Earthquake risk assessment in Central North Anatolian Fault Zone, Turkey

Eren Pamuk¹, Caglar Ozer²

Abstract

North Anatolian fault zone (NAFZ) which similar in many ways to the San Andreas Fault in California is one of the most active strike-slip faults in the world. It has been many devastating earthquakes occurring throughout NAFZ from past to present. Length and width of NAFZ reach up to 1500 km and 40 km; respectively. North Anatolian fault zone (NAFZ) is a unique example for continental plate-boundary transform fault zone which separate between Eurasian and Arabian plates and fault plane solutions indicate a typical right-lateral strike slip fault. In this study; we investigate distribution of big earthquakes and effect of Central North Anatolian Fault zone (CNAFZ) surrounding. Besides; we analysed a and b value for CNAFZ (especially Tokat, Samsun, Ordu). We observed a seismic gap in the study area and possible devastating earthquake may be affected some important settlement.

Keywords: North Anatolian fault zone, seismic risk, ZMAP

1. INTRODUCTION

Turkey has a lot of important fault zone and under active tectonic deformation. A lot of people have been died because of devastating earthquake past to present in Turkey. These earthquakes were produced by three tectonic systems (Aegean horst-graben system, North Anatolian fault zone, East Anatolian fault zone). North Anatolian fault zone (NAFZ); has been produced many earthquakes in the region and significant residential buildings constructed around this zone. In order to determinate this risk; we generate b-value map via ZMAP algorithm [1] for Tokat, Samsun, Ordu regions where is located CNAFZ (Fig. 1). We used Bogazici University Kandilli Observatory and Earthquake Research Institute (KOERI), Regional Earthquake-Tsunami monitoring center [2] homogenized seismicity catalogue which was recorded between 1900 and 2015. We researched important service buildings (airports, ports, hospitals, universities) and reviewed earthquake risks in the study area.

The main purpose of this study; determining b value map and obtained information about the seismicity of the region. Ormeni report that "Low b value shows that before the main shock; increase stress and should be used as an indicator of the earthquake by viewing the changes b-value with time in all parts of the study area. So; the mapping of b value can be used for future seismic hazard and interpreting more likely regions for future earthquakes" [3]. Bayrak show that b value close 1.0 in tectonic region. While high b values rise geological complexity, low b values are related to heterogeneity, stress and strain, deformation and great faults [4]. Study area has under big seismicity and a lot of devastating earthquake occurred especially CNAFZ (Fig. 1). North Anatolian fault zone is show typically right lateral strike slip transform fault zone and length of this zone approximately 1500 km and so similar many ways and characteristic for San Andreas fault zone.

¹Corresponding author: Dokuz Eylul University, Faculty of Engineering, Department of Geophysical Engineering, Izmir, Turkey. eren.pamuk@deu.edu.tr

²Dokuz Eylul University, Faculty of Engineering, Department of Geophysical Engineering, Izmir, caglar.ozel@deu.edu.tr

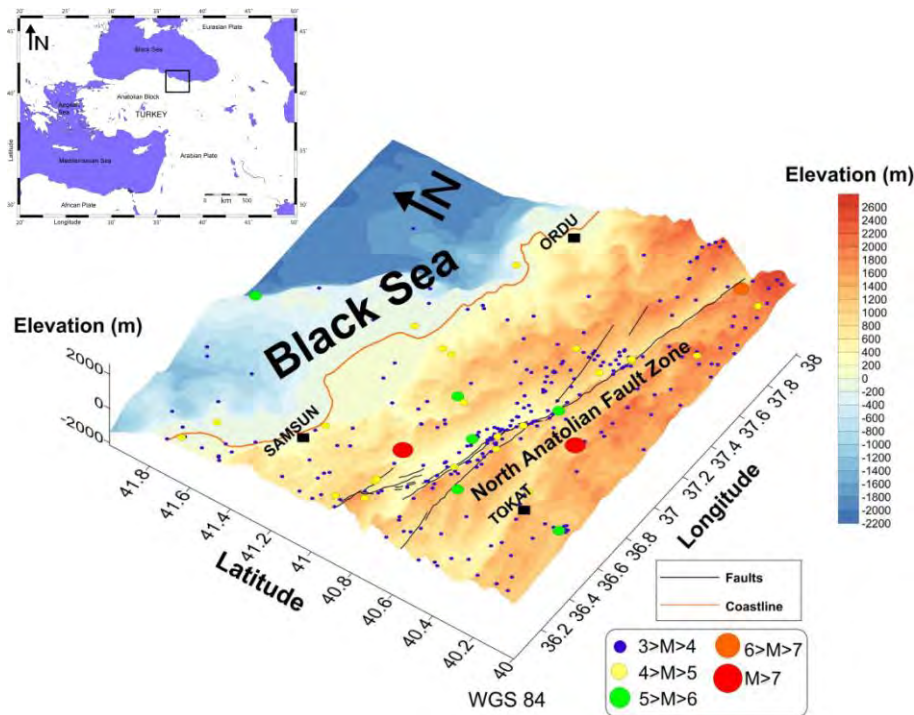


Figure 1. Study area (36° - 38° E / 40° - 42° N)

2. METHOD AND EXAMINATIONS

Scope of this study; we selected 302 earthquakes which magnitudes higher than three and occurred between 1900 and 2015. In order to data homogenisation; we used Bayrak et al. 2009 [6] equations which were produced for Turkey and used M_s magnitude formulate.

Gutenberg-Richter equation which is empirical relationship was used to calculate a and b value. This formula can be expressed as in the following formula [7]:

$$\log_{10}N = a - bM \quad (1)$$

where N is the cumulative number of earthquakes with magnitude greater or equal to M, a and b are constant parameters. These values shows important modifications from region to region as it based on the level of seismic activity, observation period and the length of the considered area as well as the size of earthquakes [5]. The parameter a display changes by areas and also seismic activity, observation period and size of region affected this parameter. The parameter b commensurate to tectonic activity and seismological characteristics [4].

The calculated b value which is gridding 0.05×0.05 is range from 0.6 to 1.4 (Fig. 2). While the lowest b value is observed in the Black Sea, the highest b value is shown along the Central North Anatolian fault zone especially Ordu region. This lowest value may be indicate high stress distribution.

It is evident that considering gravity values and topographic maps; NAFZ is clearly seen along blue colour (Fig. 3). Along the NAFZ; the gravity values divided by to trend as negative to positive. This sharp transition is clearly seen Bouguer gravity map.

Comparing Bouguer gravity map with the b value map exhibits good fit each other. Some studies compared gravity and b value in the scientific literature [8]. The positive gravity anomaly is suitable to low b values region especially in the Black Sea.

We observed good harmony between distribution of earthquake depth, magnitude, hour and earthquake number. Analyzing the histograms which were obtained ZMAP [1] (Figure 4); time distribution and earthquake number are not homogenized.

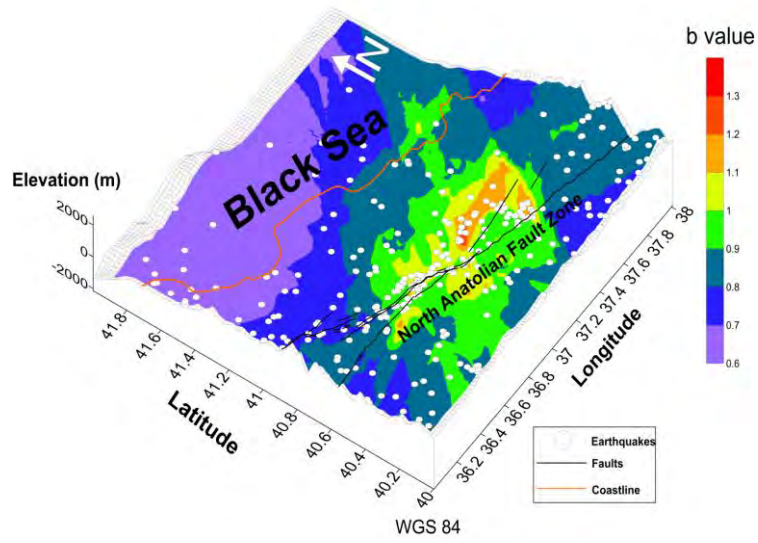


Figure 2. *b* value map in the study area

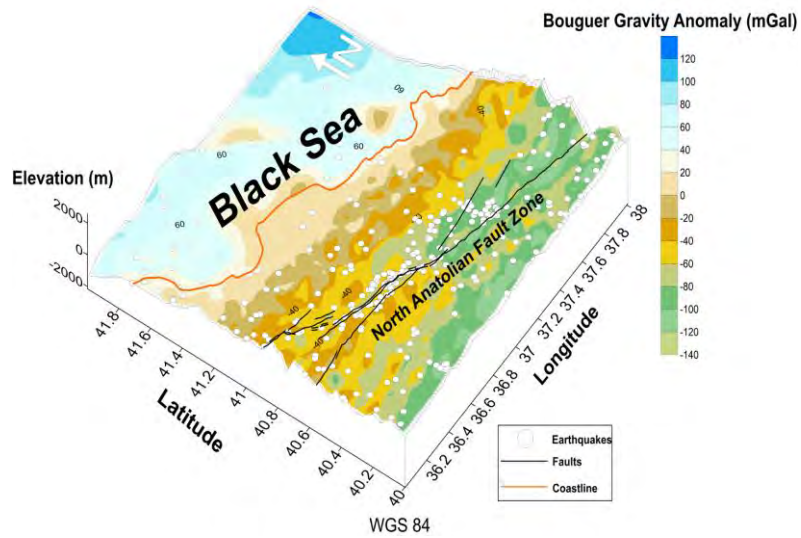


Figure 3. Bouguer gravity anomaly map in the study area

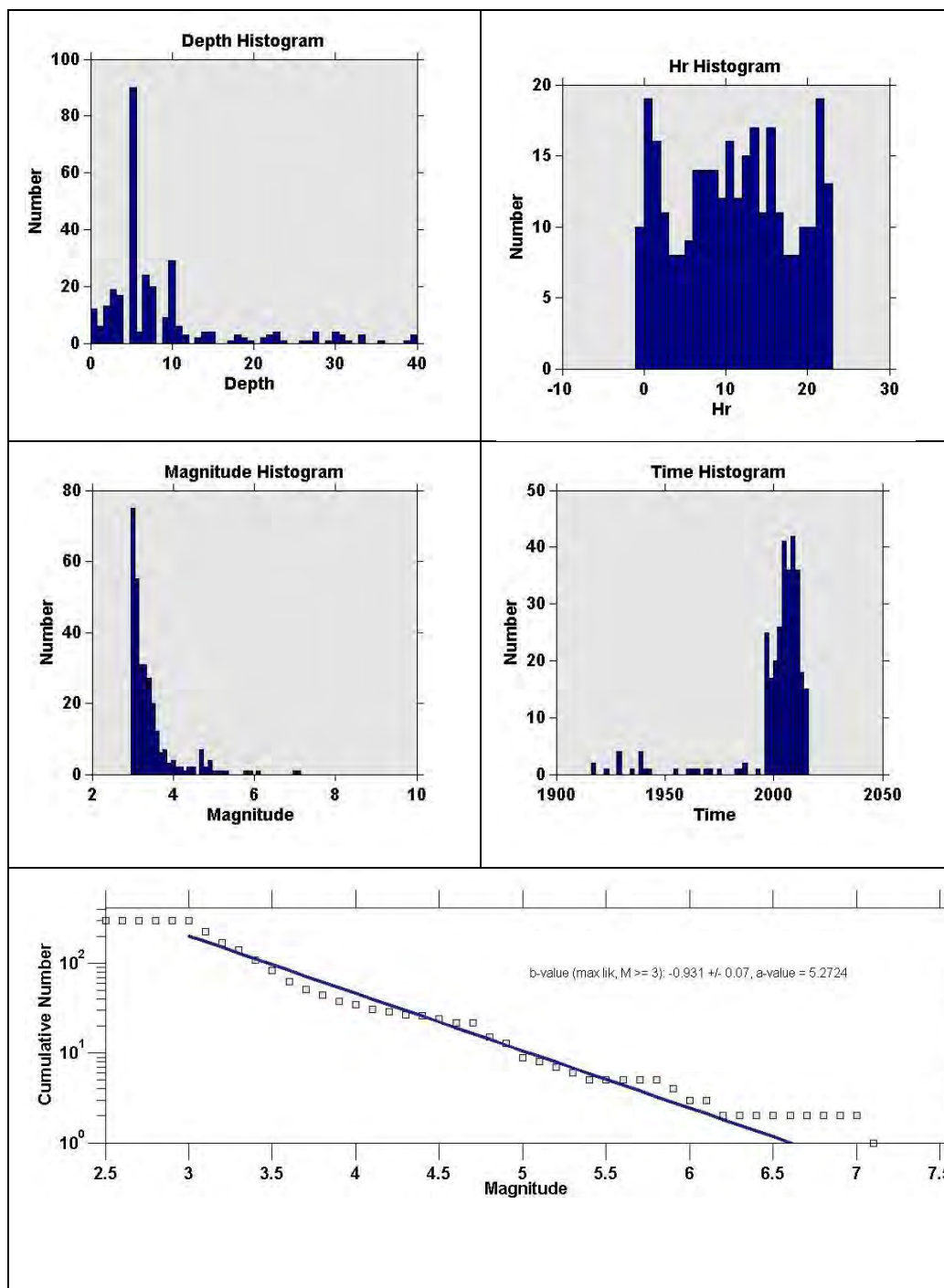


Figure 4. ZMAP [1] statistic in the study area

According to magnitude-number histogram; generally earthquake magnitude range from 4 to 5 which used in the catalogue. Time-number histogram; after 1975, there has been a further increase for station. Number-depth histogram is shown; the focal depth of the earthquake is not deeper than 30 km. The averaged a value and b value are calculated 5.27 and 0.93; respectively.

3. RESULTS

Scope of this study; we aim to investigate gravity and seismicity parameters of the CNAFZ. NAFZ produced big earthquakes periodically in history and it hasn't been come from devastating earthquakes in central Anatolian fault zone since long time. The a and b value were calculated 5.2 and 0.9; respectively. The low b value and positive gravity anomalies may be indicator of devastating earthquake. Because; low b values are associated with high stress accumulation. Bouguer gravity and b value map

were shown good correlation. The high b-values of the CNAFZ are associated with comparatively lower Bouguer gravity anomalies. Also the low b value and high Bouguer gravity value observed in Black Sea.

ACKNOWLEDGMENT

ZMAP [1] software packages were used to generate a parameter and b value map. In this study; Bogazici University Kandilli Observatory and Earthquake Research Institute (KOERI), Regional Earthquake-Tsunami monitoring center [2]'s earthquake seismicity catalogue data were used. Some part of figure 1 was generated by GMT software package [9]. Gravity data was obtained EGM 2008 [10,11]. Topography data was obtained TOPEX [12].

REFERENCES

- [1]. Wiemer, S., A software package to analyze seismicity: ZMAP. *Seismological Research Letters*, vol. 72, 373–382, 2001.
- [2]. (2015) Bogazici University Kandilli Observatory and Earthquake Research Institute Regional Earthquake-Tsunami monitoring center (KOERI) website. [Online]. Available: <http://www.koeri.boun.edu.tr/sismo/2/en/>
- [3]. R. Ormeni, Mapping b-Value in the Seismogenic Zones of Albania Region, *8th Congress of the Balkan Geophysical Society*, Chania, Greece, 5-8 October 2015.
- [4]. E. Bayrak, Ş. Yılmaz, M. Softa, T. Türker, Y. Bayrak, Earthquake hazard analysis for East Anatolian fault zone, Turkey, *Nat. Hazards*, 76, 1063-1077, 2015.
- [5]. Y. Bayrak, E. Bayrak, Regional variations and correlations of Gutenberg–Richter parameters and fractal dimension for the different seismogenic zones in Western Anatolia, *J. Asian Earth Sci.* vol. 58, 98–107, 2012.
- [6]. Y. Bayrak, S. Öztürk, H. Çınar, D. Kalafat, T.M. Tsapanos, G.C. Koravos and G.A. Leventakis, Estimating earthquake hazard parameters from instrumental data for different regions in and around Turkey, *Eng. Geology*, 105, 200-210, 2009
- [7]. R. Gutenberg and C.F. Richter, Earthquake magnitude, intensity, energy and acceleration, *Bull. of Seismol. Soc. America*, 32, 163-191, 1944.
- [8]. P.K. Khan and P.K. Chakraborty, The seismic b-value and its correlation with Bouguer gravity anomaly over the Shillong Plateau area: Tectonic implications, *Journal of Asian Earth Sciences*, 29, 136-147, 2007.
- [9]. Wessel, P., Smith, W.H.F., New version of the generic mapping tools (GMT). *EOS Trans.*, vol. 76, 329, 1995.
- [10]. N. K. Pavlis, S. A. Holmes, S. C. Kenyon, J. K. Factor. An Earth Gravitational Model to Degree 2160: EGM2008. EGU General Assembly 2008, Vienna, Austria, April 13-18, 2008. <http://earth-info.nga.mil/GandG/wgs84/gravitymod/egm2008>
- [11]. Fulla, J., Fernandez, M., Zeyen, H., 2008. "FA2BOUG - A FORTRAN 90 code to compute Bouguer gravity anomalies from gridded free-air anomalies: Application to the Atlantic-Mediterranean transition zone". *Computers & Geosciences*, Volume 34, Issue 12 (December 2008) pp. 1665-1681, ISSN:0098-3004. DOI: 10.1016/j.cageo.2008.02.018
- [12]. Smith, W. H. F., and D. T. Sandwell, Global seafloor topography from satellite altimetry and ship depth soundings, *Science*, vol. 277, p. 1957-1962, 26 Sept., 1997.

PRODUCTION AND CHARACTERIZATION OF Ni-Si₃N₄ COMPOSITE MATERIALS

Ahmet YÖNETKEN¹, Arzu YAKAR¹, Ayhan EROL²

Abstract

Nickel matrix composites containing 3,6,9,12,15%Si₃N₄ has been fabricated by conventional furnace sintering at 1200°C temperature. Compounds formation between Ni and Si₃N₄ powders are observed after sintering under Ar shroud. XRD, SEM (Scanning Electron Microscope), mechanical testing and measurements were employed to characterize the properties of Ni+12% Si₃N₄ composite. Experimental results suggest that the best properties as hardness 65,51 HB were obtained for Ni+15% Si₃N₄ composite.

Keywords: metallurgy, Sintering, Ceramic-Metal Composites

4. INTRODUCTION

Metals are very useful in making different components and their properties can be improved by adding reinforcement like B₄C, Si₃N₄, and TiC e.t.c. Nickel matrix composites (NMCs) are the competent material in the industrial world. These composite materials also offer outstanding properties such as high strength to- weight ratio, good corrosion resistance and versatility to the designer. Two major processing techniques that have been found suitable for these composites are powder metallurgy and solidification processing [1]. Silicon nitride (Si₃N₄) based ceramics have been studied intensively for more than 40 years and used in numerous applications as structural and functional ceramic materials due to its superior properties. such as high-temperature strength, good oxidation resistance, and low thermal expansion coefficient [2–4]. The ability to reinforce fine particulate matter such as hard ceramic or soft lubricious particles within metal matrix by PM method has lead to the development of composite coatings. Silicon Nitride-Nickel (Si₃N₄-Ni) cermets have been widely used in tooling because of their high hardness and excellent wear and corrosion resistant properties. Cutting tools, dies, rock drills, wear-resistant nozzles and coatings are a few examples of their various applications [5-8].

In the present work, Composites work Ni-%3Si₃N₄, Ni-%6Si₃N₄, Ni-%9Si₃N₄, Ni-%12Si₃N₄ and Ni-%15Si₃N₄, were fabricated, microstructure were characterized and mechanical properties such as hardness and density were studied. It was observed that

5. MATERIAL-METHOD AND PREPARATION OF SAMPLE

Starting powders employed in this study were as follows: the purity of 99.8% for Ni powders with a particle size lower than 70 μm, the purity of 99.95% for Si₃N₄ ceramic powders a particle size lower than 75 μm The composition of Ni-%3Si₃N₄, Ni-%6Si₃N₄, Ni-%9Si₃N₄, Ni-%12Si₃N₄ and Ni-%15Si₃N₄, powders specimens were prepared in 10g square prism compressed pre-form. They were mixed homogenously for 24 hours in a mixer following the weighing. The mixture was shaped by single axis cold hydraulic pressing using high strength steel die. A pressure of 300 Bar was used for the compacting all the powder mixtures. The cold pressed samples underwent for a sintering at 1200°C for 2 hours in a traditional tube furnace using Argon gas atmosphere. The specimens were cooled in the furnace after sintering and their hardness and shear strengths measurements were carried out using METTEST-HT (Vickers) micro hardness tester machine, respectively. LEO 1430 VP model Scanning Electron Microscope fitted with Oxford EDX analyzer was used for

microstructural and EDX compositional analysis. The volumetric changes of Ni-%3Si₃N₄, Ni-%6Si₃N₄, Ni-%9Si₃N₄, Ni-%12Si₃N₄ and Ni-%15Si₃N₄, composites material after sintering were calculated by using ($d=m/V$) formula (Fig. 1). The volume of post-sintered samples was measured with Archimedes principle. All the percentages and ratios are given in weight percent unless stated otherwise.

6. EXPERIMENTAL RESULTS AND DISCUSSION

6.1. Characterization of specimens

In the study, the samples prepared and shape were sintered at 1200°C in conventional furnace and made ready for physical, mechanical and metallographic analyses. Density-composition change curve is shown in figure 1. The highest sintered density was achieved at 1200°C as %3 and also lowest density %15 composition.

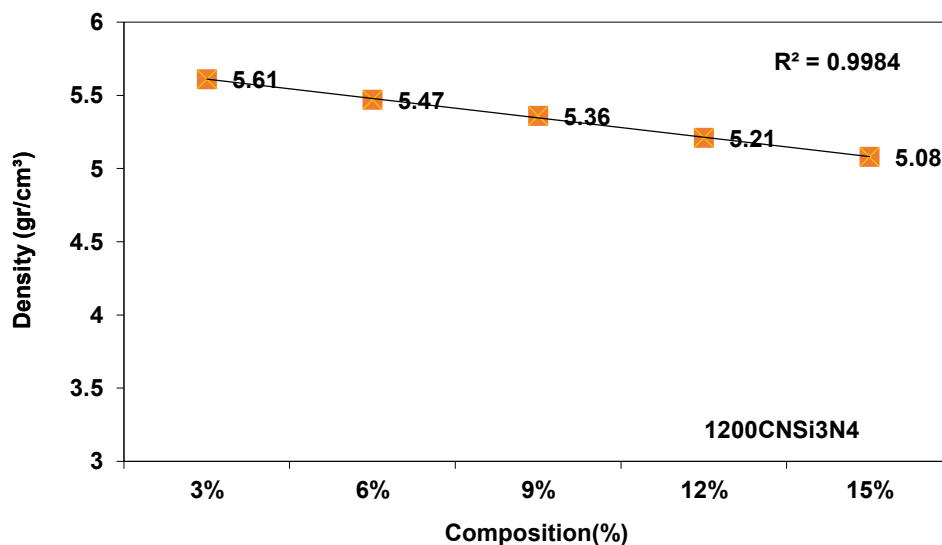


Figure 1. The density change with respect to sintering compositions

The hardness-compositions change diagram is shown in figure 2. The hardness values of the composite samples produced using conventional sintering technique within the temperature at 1200°C. According to this, the highest microhardness value in the composite samples fabricated using powder metallurgy method was observed to be 65.51HB at Ni-%15Si₃N₄ composites.

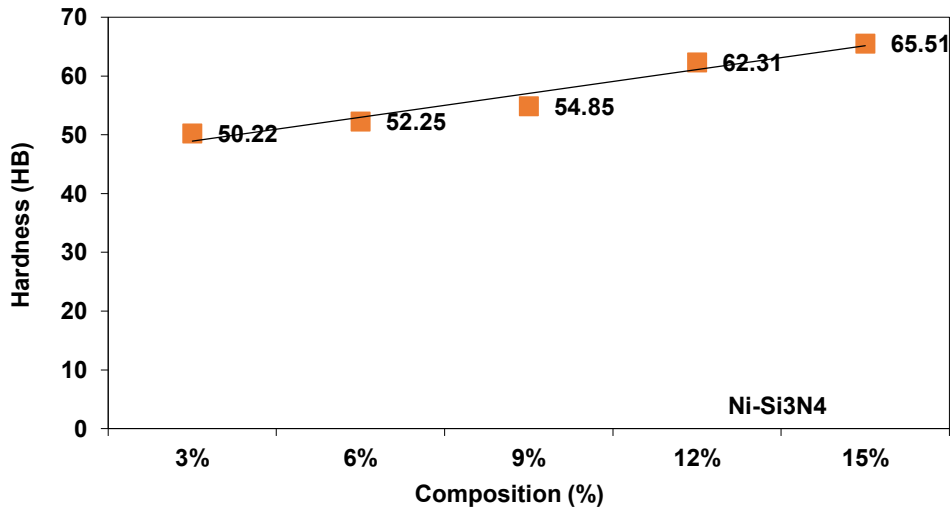


Figure 2. The hardness tests results from sintered specimens treated at different compositions

The compression-compositions change diagram is shown in figure 3. The compression values of the composite samples produced using conventional sintering technique within the temperature at 1200°C. According to this, the highest compression value in the composite samples fabricated using powder metallurgy method was observed to be 88MPa at Ni-15Si₃N₄ composites.

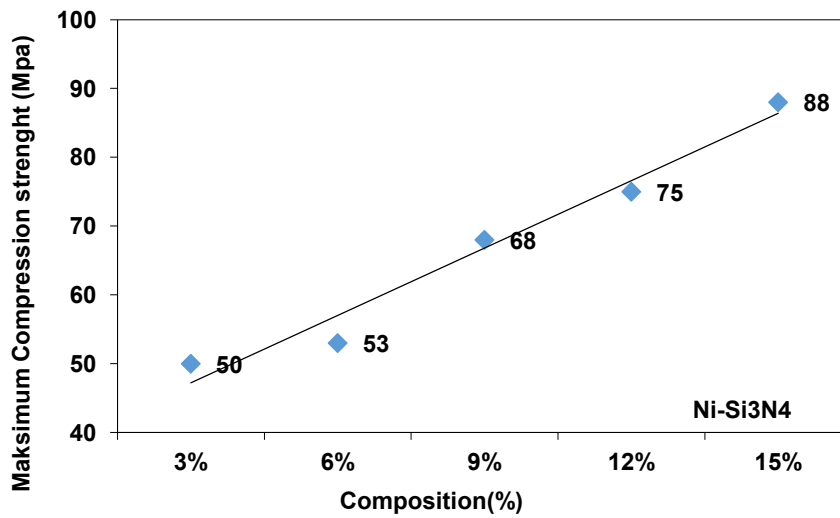


Figure 3. The compression tests results from sintered specimens treated at different compositions

3.2 Metallographic Analysis

The SEM analysis result of the metal matrix composite specimen obtained from Ni-3Si₃N₄ powders sintered at 1200 °C is shown in Figure 3. grain growth is observed and a homogeneous structure and grain boundaries can't be seen that the pores very smaller. This density, and hardness values are confirmed.

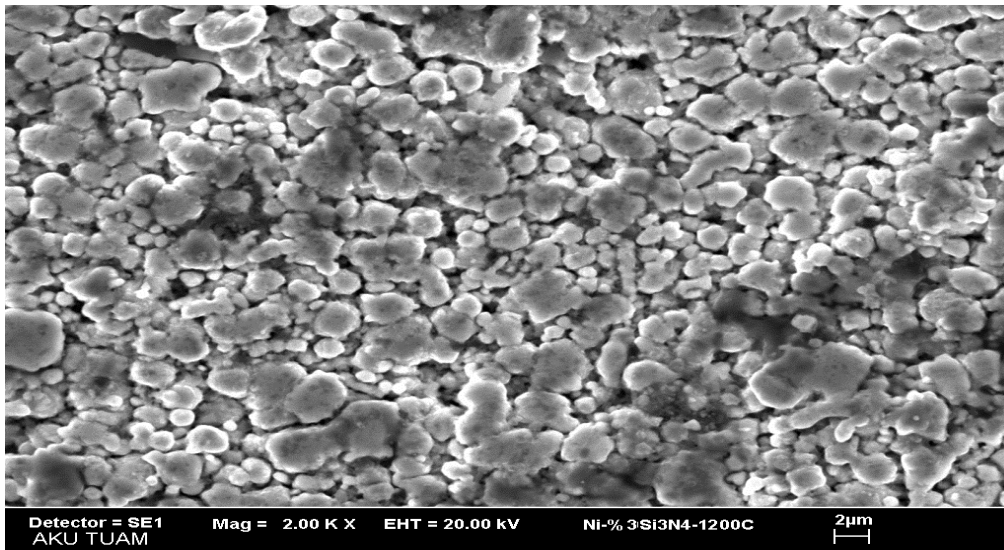


Figure 3. SEM view of Ni-3Si₃N₄ composite 1200°C

The SEM analysis result of the metal matrix composite specimen obtained from Ni-15Si₃N₄ powders sintered at 1200 °C is shown in Figure 4. grain growth is observed. It is a homogeneous structure and grain boundaries can be seen that the pores very smaller. This density, and hardness values are confirmed.

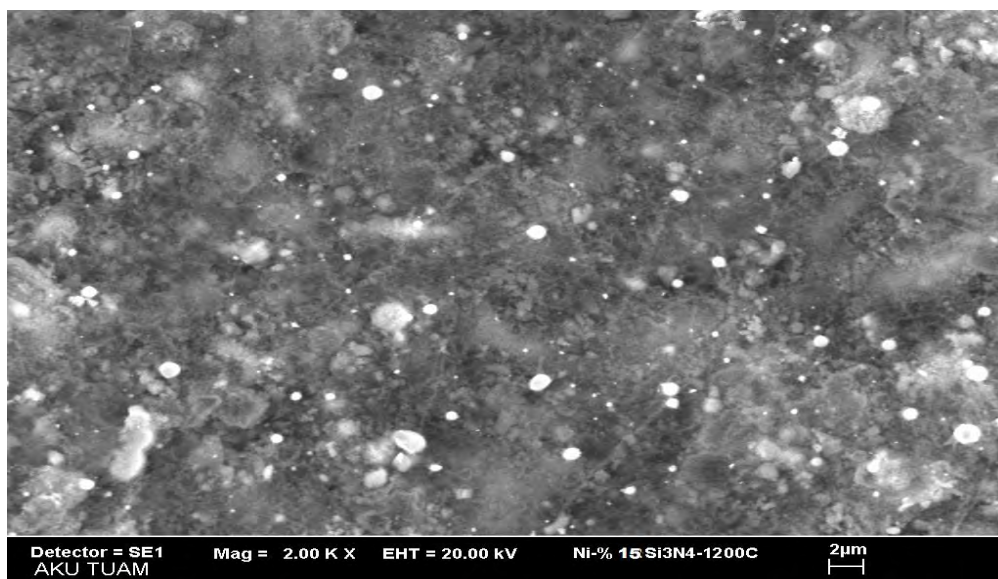


Figure 4. SEM view of Ni-%15Si₃N₄ composite 1200°C

In Figure 6, Ni and Si₃N₄ peaks can be seen in the XRD analysis from Ni-%3Si₃N₄ composite and Ni-%15Si₃N₄ composite sintered in tube furnace at 1200°C

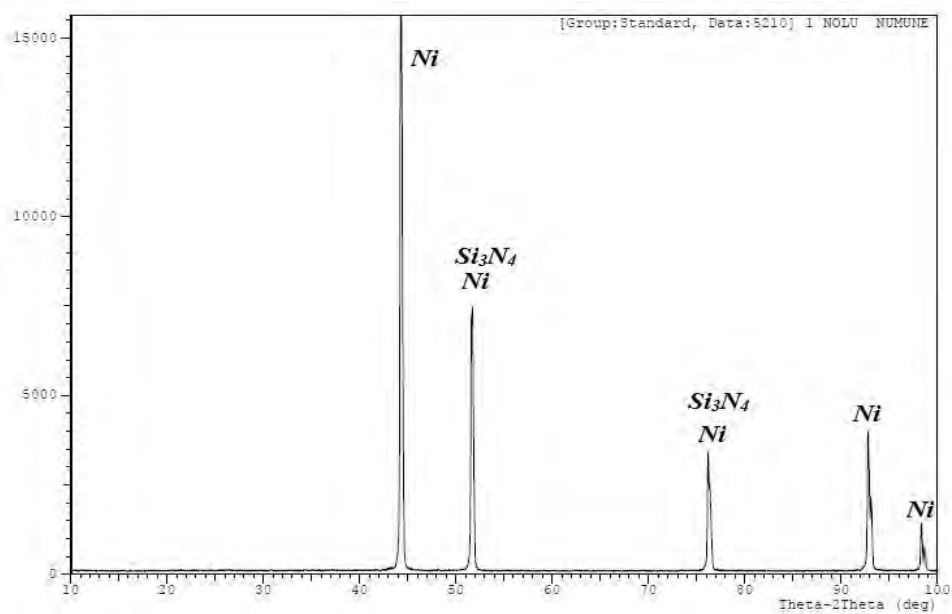


Figure 5. shows XRD analysis of Ni-%3Si₃N₄ composite 1200°C

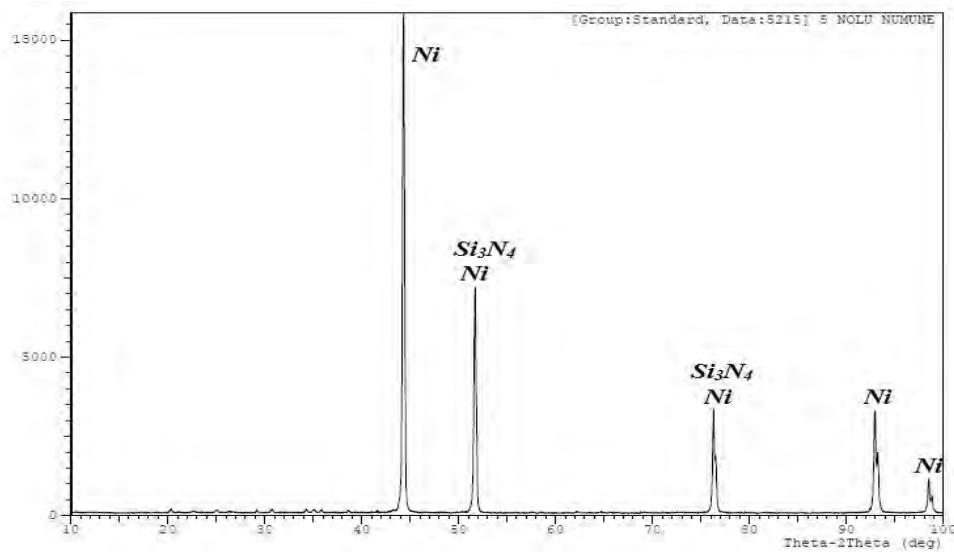


Figure 6. shows XRD analysis of Ni-15Si₃N₄ composite 1200°C

Ni-3Si₃N₄, Ni-6Si₃N₄, Ni-9Si₃N₄, Ni-12Si₃N₄ and Ni-15Si₃N₄ powders were mixed with 24 hours and then sintered in a conventional furnace within the temperature range 1200°C. After sintering, a considerable drop in the mechanical properties of specimens. It was concluded that Ni-15Si₃N₄ particles were occurred by Ni, and Si₃N₄ phases at 1200°C and Hardness test results suggest that Ni-15Si₃N₄ composite sintered at 1200°C shows Brinell hardness values respectively.

4. Conclusion

The following results were concluded from the experimental findings

The highest density in composite made from Ni-3Si₃N₄, Ni-6Si₃N₄, Ni-9Si₃N₄, Ni-12Si₃N₄, and Ni-15Si₃N₄ powders sintered at 1200°C temperatures was obtained as The highest density sample was found as 5, 61gr/cm³ at Ni-3Si₃N₄

The highest hardness in Ni-15Si₃N₄ composite samples fabricated using powder metallurgy method was found as 65,51HB at 1200°C.

The highest compression in Ni-15Si₃N₄ composite samples fabricated using powder metallurgy method was found as 88MPa at 1200°C.

ACKNOWLEDGMENT

This research was supported by the University of Afyon Kocatepe project no: 15.MUH.05 We would like to extend our gratitude to the Scientific Research Coordination Unit

REFERENCES

- [13]. S. M. Metev and V. P. Veiko, *Laser Assisted Microtechnology*, 2nd ed., R. M. Osgood, Jr., Ed. Berlin, Germany: Springer-Verlag, 1998.
- [14]. Poper P., Ruddlesden S.N., *Trans. br. ceram. soc.*, 60 (1961), 603.
- [15]. Ziegler G., Heinrich J., Wötting G., *J. Mater. Sci.*, 22 (1987), 3041.
- [16]. Guge E., Woetting G., *Ind. Cer.*, 19 (1999), 196.
- [17]. Yuhong Xiong, Ki Lau, Xiaoying Zhou, Julie M. Schoenung, A streamlined life cycle assessment on the fabrication of WC-Co cermets, *Journal of Cleaner Production*, Volume:16, 2008, 1118-1126.
- [18]. Ma X M, Ji G., Nanostructured WC-Co alloy prepared by mechanical Alloying, *Journal of Alloys and Compounds*, 245, 1996, 30-32.
- [19]. Mc Candlish L E, Kear B H, Kim B K., Processing and properties of nanostructured WC-Co. *Nanostructured Materials*, Volume: 1, 1992, 119-124.
- [20]. R. Koc, S. K. Kodambake, *J. Euro, Ceramic Materyals*, Volume: 20, 2000, 1859.

Comparison of EGM08 Bouguer Gravity with Ground Survey: A Case Study in Western Anatolian Region, Turkey

Fikret Doğru², Oya Pamukçu²

Abstract

In this study, using some predictions, the EGM08 Bouguer Gravity data were evaluated with the Bouguer gravity data which were ground survey of Western Anatolia. The study field includes graben, fault systems and various geological units. Topographic height is so changeable and terrain is so hilly over the field land. Firstly, the upward continuation method was applied on EGM08 Bouguer gravity data for different level. Thus it was determined that the EGM2008 Bouguer gravity data came close to ground Bouguer gravity data. After, it was obtained horizontal derivative (y-directional derivative) of applied upward analytical continuation EGM08 Bouguer gravity data. According to the derivatives, the grabens and faults were more visible. As the last step, the graben boundaries, faults and informations of different geological units were determined using tilt angle method. Consequently, all applications for EGM08 Bouguer gravity data and ground survey Bouguer gravity data were compared.

Keywords: EGM2008, upward continuation, Bouguer gravity data, fault.

7. INTRODUCTION

The Aegean region is one of the most active extensional regions in the world and is undergoing a N-S extension (e.g. [1]). The Western Anatolian grabens are some of the most important neotectonic structures in Anatolia (Turkey). The neotectonic evolution of these grabens has been discussed extensively and various geodynamic evolutionary models for the system proposed ([2]).

EGM08 Bouguer anomalies are the result of the project of WGM (World Gravity Map) with CGMW (Commission for the Geological Map of the World) and in collaboration with UNESCO. In this scope of this study, EGM08 Bouguer gravity variation was examined via evaluating ground survey Bouguer gravity data in the Western Anatolia. In previous, EGM08 Bouguer gravity data was used for crust modelling in Eastern Marmara region ([3]) and for determination of discontinuities over Van lake and surroundings ([4]).

In this study, the main purpose is to make useable the EGM2008 Bouguer gravity data for interpreting discontinuities in the small-scale fields. In the first step the upward analytical continuation and directional derivatives method applied on the EGM2008 and ground survey Bouguer gravity data. Then, the tilt angle which is the ratio of the total horizontal

derivatives to vertical derivative of potential field was applied for results of analytical continuations obtained from the EGM08 and ground survey Bouguer gravity data ([5], [6], [7]).

8. THE EARTH GRAVITATIONAL MODEL (EGM2008)

EGM2008 is a spherical harmonic model of the Earth's gravitational potential, developed by a least squares combination of the ITG-GRACE03S gravitational model and its associated error covariance

² Corresponding author: Dokuz Eylul University, Department of Geophysical Engineering, 35160, Buca/Izmir, Turkey. fikret.dogru@deu.edu.tr

² Dokuz Eylul University, Department of Geophysical Engineering, 35160, Buca/Izmir, Turkey. oya.pamukcu@deu.edu.tr

matrix, with the gravitational information obtained from a global set of area-mean free-air gravity anomalies defined on a 5 arc-minute equiangular grid. This grid was formed by merging terrestrial, altimetry-derived, and airborne gravity data. EGM2008 is complete to degree and order 2159, and contains additional coefficients up to degree 2190 and order 2159 ([8]).

The Earth's external gravitational potential, V , at a point P defined by its geocentric distance (r), geocentric colatitude (θ) (defined as 90° -latitude), and longitude (λ), is given by:

$$V(r, \theta, \lambda) = \frac{GM}{r} \left[1 + \sum_{n=2}^{\infty} \left(\frac{a}{r}\right)^n \sum_{m=-n}^n \bar{C}_{nm}^s \bar{Y}_{nm}(\theta, \lambda) \right], \quad (1)$$

$a=6378137.00$ m (semi-major axis of WGS 84 ellipsoid),
 $f=1/298.257223563$ (flattening of WGS 84 ellipsoid),
 $GM=3.986004418 \times 10^{14}$ m³s⁻² (Product of the Earth's mass and the Gravitational Constant),
 $\omega=7292115 \times 10^{-11}$ radians/sec (Earth's angular velocity).

where GM is the geocentric gravitational constant and a is a scaling factor associated with the fully normalized, unitless, spherical harmonic coefficients \bar{C}_{nm}^s . The superscript "s" identifies the coefficients as being spherical. a is usually numerically equal to the equatorial radius of an adopted reference ellipsoid. Eq. (1) refers to the permanent part of the gravity field, either ignoring or having corrected first for the variable part due to tides, changes in Earth rotation, etc.. The fully normalized surface spherical harmonic functions are defined as ([9]):

$$\bar{Y}_{nm}(\theta, \lambda) = \bar{P}_{n|m|}(\cos\theta) \cdot \begin{cases} \cos m\lambda & \text{if } m \geq 0 \\ \sin |m|\lambda & \text{if } m < 0 \end{cases} \quad (2)$$

Here $\bar{P}_{nm}(\theta, \lambda)$ is the fully normalized associated Legendre function of the first kind, of degree n and order $|m|$.

9. UPWARD CONTINUATION

Upward continuation is a method that transforms anomalies measured on one surface into those that would have been measured on some higher surface. The upward-continued anomalies do not provide direct information about the source, but they can be instructive nonetheless. In particular, the process of upward continuation tends to attenuate anomalies caused by local, near-surface sources relative to anomalies caused by deeper, more profound sources.

The potential data at two observation heights are related by the upward continuation operation ([10]),

$$T_h(x, y, \Delta h) = \frac{1}{2\pi} \int_{-\infty}^{\infty} \int_{-\infty}^{\infty} \frac{T_0(x', y') \Delta h}{[(x' - x)^2 + (y' - y)^2 + \Delta h^2]^{3/2}} dx' dy' \quad (3)$$

where $T_0(x, y)$ and $T_h(x, y, h)$ are respectively the potential data at two observation heights separated by a vertical distance Δh . Applying a two-dimensional Fourier transform to eq.(1) yields a simpler form in which the Fourier transforms of the two quantities are related to each other by a simple upward continuation operator,

$$\tilde{T}_h(\omega_x, \omega_y, \Delta h) = e^{-\Delta h \omega_r} \tilde{T}_0(\omega_x, \omega_y) \quad (4)$$

where $\tilde{T}_0(\omega_x, \omega_y)$ denotes the Fourier transform of $T_0(x, y)$, (ω_x, ω_y) are wavenumbers in x - and y -direction, and $\omega_r = \sqrt{\omega_x^2 + \omega_y^2}$ is the radial wavenumber. The upward continuation operator attenuates with height the high-frequency content of a potential anomaly.

10. TILT ANGLE

A number of methods have been proposed to make subtle anomalies more visible. The first filter developed for this purpose was the tilt angle ([5]), which is the ratio of the vertical derivative to the absolute value of the horizontal derivative of the potential field. The tilt angle is given by

$$Tilt = \tan^{-1} \left(\frac{\frac{\partial T}{\partial z}}{THDR} \right) \quad (5)$$

where

$$THDR = \sqrt{\left(\frac{\partial T}{\partial x}\right)^2 + \left(\frac{\partial T}{\partial y}\right)^2} \quad (6)$$

T is the potential anomaly and THDR is the total horizontal derivatives ([11]). The tilt angle produces a zero value over the source edges.

11. THE STUDY AREA

11.1. Geology of the Study Area

The study area is located western of Turkey that includes Gediz, Büyük and Küçük Menderes Grabens, and Usak-Gure basin (Figure 1). Bouguer gravity values were utilized Directorate of Mineral Research and Exploration (MTA), ([12]), from a region which covers the Gediz, Büyük and Küçük Menderes Grabens and located between 36°-39° N latitudes and 26°-30° E longitudes. The Gediz graben which is also known as the Alasehir graben form is 150-km-long, 3-40-km-wide, has an approximately E-W-trending structure and forms one of the most prominent arc shaped, structural elements of western Turkey ([13], [14]). The Büyük Menderes Graben is one of the most prominent structures of western Anatolia (Turkey). This graben is bounded to the north and to the south by the Menderes Massif metamorphic rocks and it is approximately 140 km long and 2.5-14 km wide, and forms an arc-shaped structural pattern. ([15]). The Küçük Menderes Graben is one of the least-known grabens in so far as its basin-fill sediments, age and geometry are concerned and the E-W-trending of Küçük Menderes Graben is 80-km long and 3-10 km wide ([16]).

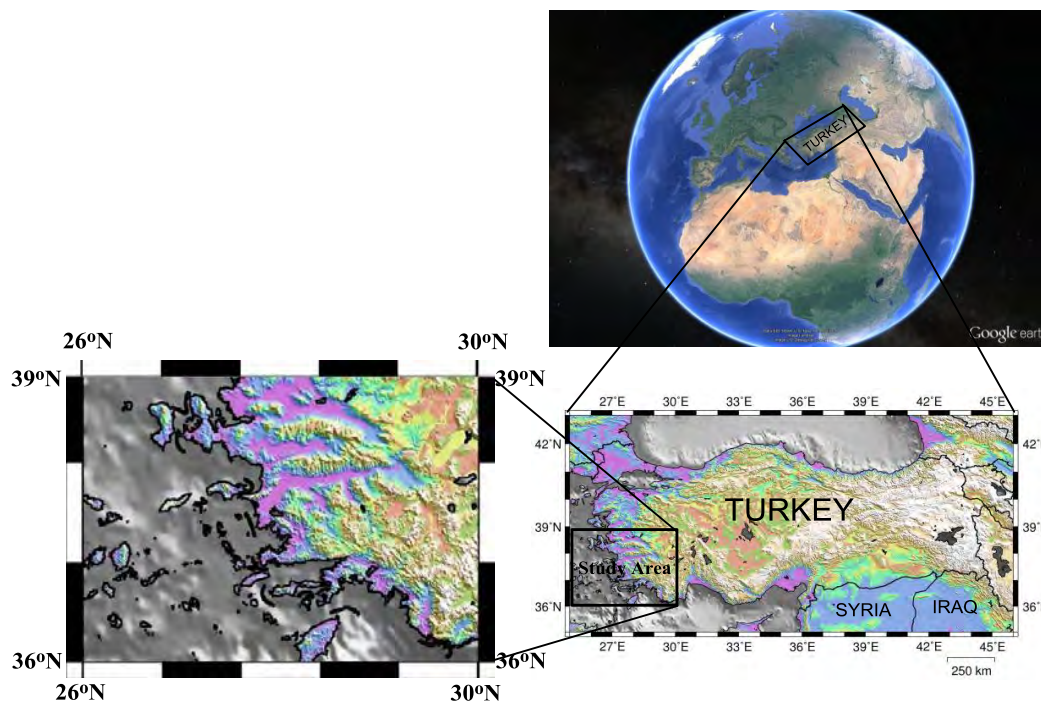


Figure 1. The location of the study area.

11.2. Geophysical Study

The ground survey was implemented by MTA and all of the corrections were done. The EGM08 Bouguer gravity data was obtained from International Gravimetric Bureau website ([17]). The same processes were applied both ground survey and EGM08 Bouguer gravity data. The results of the applications are shown in Figure 2. It was seen that the horst and graben systems were not clear in the ground survey Bouguer gravity data (Figure 2a). At first sight, the high noise rate was noticed in the EGM08 data (Figure 2d). This noise was tried to reduce via applying upward continuation method. The results show that also a shaded relief map is good tool for determining lineaments as shown in Figure 2b and 2e. Then the effects which cause deeper sources became more prominent. As thus, the faults and graben-horst systems were revealed via applying tilt angle for the results of continued upwards 5, 7, 9 km (Figure 2g, 2i and 2k). The results of tilt angle gave us minimum anomalies on the faults and maximum anomalies on the horsts. Tilt angle gave the results about both lineaments and geological units (Figure 2c, 2f, 2h, 2j and 2l). The faults were overlaid on the results to compare whether the results were satisfied or not. In addition, profiles were taken from south to north to see the differences between location of faults and grabens among the results of EGM08 data and ground survey data. The profile and the results are shown in Figure 3 and 4.

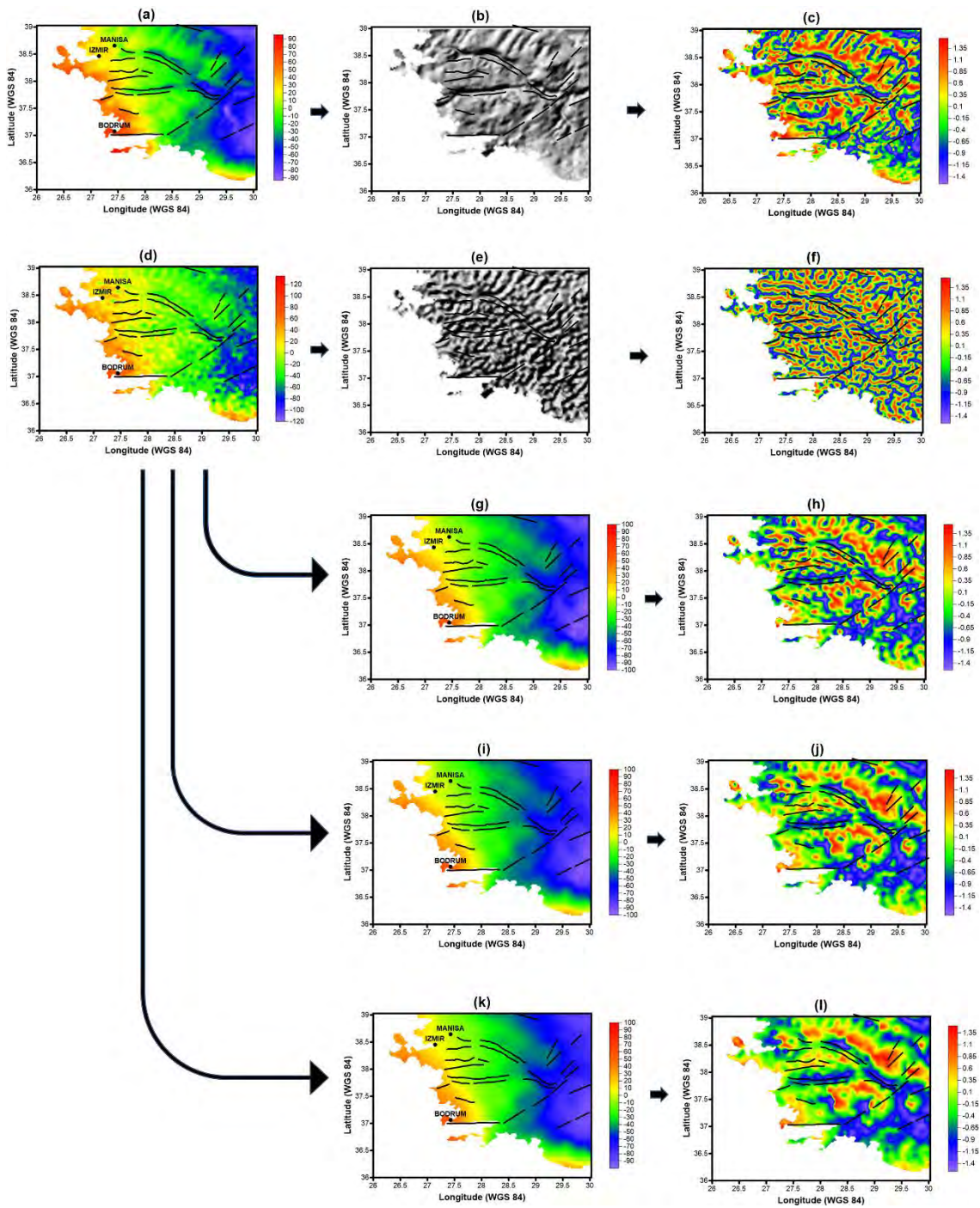


Figure 2. Ground survey and EGM2008 Bouguer gravity data and tilt angle, shaded relief map results: a) Ground survey Bouguer gravity data, b) The result of shaded relief map of a, c) The result of tilt angle of a, d)EGM08 Bouguer gravity data, e) The result of shaded relief map of d, f) The result of tilt angle of d, g) The result of 5km upward continuation of d, h) The result of tilt angle of g, i) The result of 7km upward continuation of d, h) The result of tilt angle of i, k) The result of 9km upward continuation of d, l) The result of tilt angle of k.

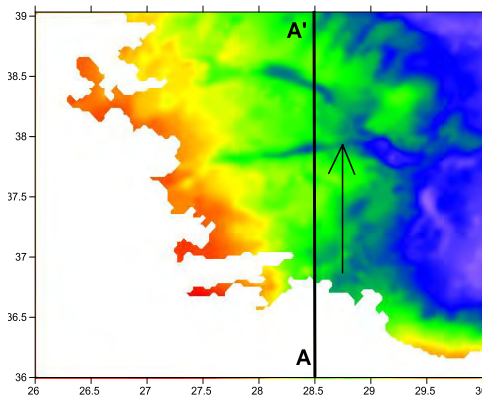


Figure 3. A-A' profile

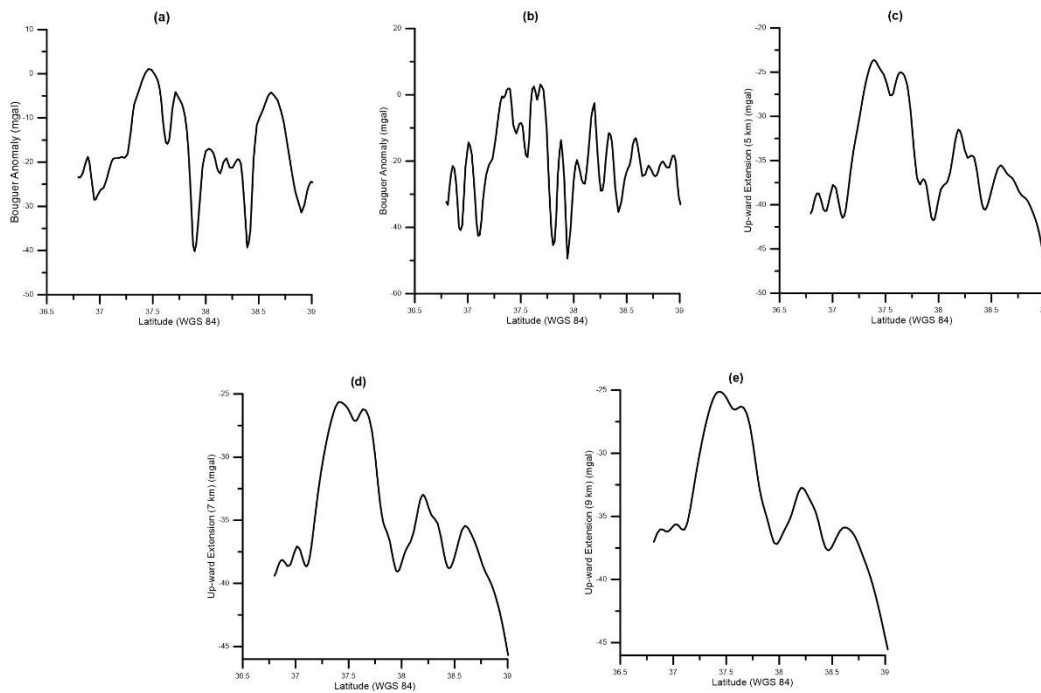


Figure 4. A-A' profiles: a) ground survey Bouguer data, b) EGM2008 Bouguer data, c) continued upward of EGM 2008 Bouguer data with 5km, d) continued upward of EGM 2008 Bouguer data with 7km, e) continued upward of EGM 2008 Bouguer data with 9km.

RESULTS

In this study, we aimed that defining some lineaments and regional features using both EGM08 and ground survey Bouguer gravity anomaly. The boundaries of grabens of West Anatolia were identified applying tilt angle method. Tilt angle gave minimum over the graben areas and maximum over the horsts as expected. EGM08 Bouguer gravity data include high noise so lineaments were not able to be realized. It is determined that amplitudes of EGM08 and ground survey Bouguer gravity data approach each other via upward analytical continuation method. The study also shows that the shaded relief map gives good result for detecting lineaments and different geological units. Determination of the location of graben-horst system has become easier when applying upward analytical continuation method to the EGM08 Bouguer gravity data. The analytical continuation clears the noise on EGM08, on the other hand, increasing continued upward level cause the amplitude to be smoother.

REFERENCES

- [1]. J. F. Dewey and A. M. C. Şengör, *Aegean and surrounding regions: Complex multiplate and continuum tectonics in a convergent zone*. Geological Society of America Bulletin 90, 84–92, 1979.
- [2]. E. Bozkurt, *Neotectonics of Turkey – a synthesis*, Geodinamica Acta, 14, 3-30, 2001.
- [3]. T. Sönmez, *Investigating the lithospheric dynamics of Eastern Marmara Region by EGM08 Gravity anomalies, isostatic and thermomechanical analysis*. MSc Thesis, Kocaeli University, The Graduate School of Natural and Applied Sciences, Kocaeli, Turkey, 2015 (in Turkish).
- [4]. B. Oruç, T. Sönmez, M.B. Doğan, *Investigation of Discontinuous of Van Lake and Surrounding Region from Horizontal Gradient Magnitude and Curvatures of Horizontal Gradient Tensor of EGM08 Bouguer Anomalies*, International Kocaeli Earthquake Symposium 2015.
- [5]. H.G. Miller and V. Singh, *Potential field tilt: a new concept for location of potential filed sources*, Journal of Applied Geophysics, 32, pp 213-217, 1994.
- [6]. B. Verduzco, J.D. Fairhead, C.M. Green and C. MacKenzie, *New insights into magnetic derivatives for structural mapping*, The Leading Edge, 23(2), pp 116-119, 2004.
- [7]. U. Akin, B. I. Şerifoğlu, M. Duru, *The Use of Tilt Angle in Gravity and Magnetic Methods*, Bulletin Of The Mineral Research and Exploration, 143, 1-12, 2011.
- [8]. N.K. Pavlis, S.A.Holmes, S.C. Kenyon and J.K. Factor, *An Earth Gravitational Model to Degree 2160: EGM2008*, Proceedings of European Geosciences Union, 13-14 April 2008, Vienna, Austria, 2008.
- [9]. N.K. Pavlis, S.A.Holmes, S.C. Kenyon and J.K. Factor, *The development and evaluation of the Earth Gravitational Model 2008 (EGM2008)*. Journal of Geophysical Research 117(B4), B04406, 2012.
- [10]. R.J. Blakely, *Potential theory in gravity and magnetic applications*, Cambridge University Press, 1995.
- [11]. L. Cordell and V.J.S. Grauch, *Mapping basement magnetization zones from aeromagnetic data in The San Juan Basin, New Mexico*. In: W.J., Hinze, Ed., *The utility of regional gravity and magnetic anomaly maps*: Society Exploration Geophysics, Tulsa, Oklahoma, 181-197, 1985.
- [12]. MTA (Directorate of Mineral Research and Exploration, Turkey) 1979. Bouguer Gravity Map of Western Turkey [unpublished].
- [13]. E. Bozkurt and H. Sözbilir, *Geology of the Gediz Graben: new field evidence and tectonic significance*, Geological Magazine 141, 63–79, 2004.
- [14]. E. Bozkurt and H. Sözbilir, *Evolution of the large-scale active Manisa fault, southwest Turkey: implications on fault development and regional tectonics*. Geodinamica Acta, 19, 427-453, 2006.
- [15]. Ö. F. Gürer, N. S.-Filoreau, M. Özburan, E. Sangu and B. Doğan, *Progressive development of the Büyük Menderes Graben based on new data, western Turkey*, Geological Magazine - Cambridge Journals Online, p 1-22, 2008.
- [16]. Ş. Özyalin, O. Pamukçu, T. Gönenc, A.Yurdakul and H. Sözbilir, *Application of boundary analysis and modeling methods on Bouguer gravity data of the Gediz Graben and surrounding area in Western Anatolia and its tectonic implications*, Journal of The Balkan Geophysical Society, Vol. 15, No. 2, p. 19-30 December, 2012.
- [17]. EGM2008 Bouguer gravity data : <http://bgi.omp.obs-mip.fr/data-products/Toolbox/EGM2008-anomaly-maps-visualization>.

Application of the ETHDR Method on Aeromagnetic Data: A Case Study Western of Bitlis, Turkey

Fikret Doğru³, Oya Pamukçu²

Abstract

Edge detection and edge enhancement techniques play a crucial role in interpreting potential field data. There has been various edge detection techniques applied to magnetic data in order to delineate the edges of subsurface structures in geophysics. The edge detection methods comprise analytic signal, total horizontal derivative (THDR), theta map, tilt angle, hyperbolic of tilt angle (HTA), normalized total horizontal gradient (TDX) and normalized horizontal derivative (NTHD). This paper applies an enhanced total horizontal derivative of the tilt angle (ETHDR) method for comparison results with the other edge detection filters. The sufficiency of the ETHDR method is indicated using theoretical models and field study. Compared with the formal methods, the ETHDR filter more detailed outcomes for buried models and is less sensitive to noise. Aeromagnetic anomaly of Bitlis Zagros suture zone (BZSZ) and its surroundings was used for field data. In first stage, the discontinuities were not found to be recognizable in the results of boundary analysis methods. Then, pole reduction and upward continuation (5 km) were applied to the aeromagnetic data for revealing the deeper effects on data. The same boundary analysis methods were applied after pole reduction and upward continuation. The results were compared to each other and the anomalies were associated with the geological units and faults.

Keywords: Edge detection, pole reduction, upward continuation, ETHDR, BZSZ.

12. INTRODUCTION

Gravity and magnetic anomalies are essential to geophysical approaches to geologic mapping ([1]). Accurate detection of source shape coordinates is becoming the main goal for interpretation and therefore enhanced methods are acquiring an increasing revival in data interpretation ([2]). There are various procedures that have been engaged to attain edge detection, for example, analytic signal (AS), tilt angle (TA), theta map (TM) and etc. ([3]).

An enhanced total horizontal derivative of the tilt angle (ETHDR) method was applied for the boundary analysis of aeromagnetic anomalies. This method was proposed by ([3]). Before interpreting the field measurements, three noise-corrupted theoretical models were utilized in order to determine spatial resolution of ETHDR method. Then same processes were applied on aeromagnetic data. When acceptable results could not be obtained from aeromagnetic data,

pole reduction and upward continuation were applied on aeromagnetic data and then analysis was implemented. The data was collected western of BSZS and its surroundings. The area is so complex in terms of geological units and tectonism. The tectonic regime along the fault changes from east to west; collision zone of Bitlis-Zagros produced by northward movement of Arabian Plate with respect to Eurasia ([4]).

³Corresponding author: Dokuz Eylul University, Department of Geophysical Engineering, 35160, Buca/Izmir, Turkey. fikret.dogru@deu.edu.tr

²Dokuz Eylul University, Department of Geophysical Engineering, 35160, Buca/Izmir, Turkey. oya.pamukcu@deu.edu.tr

13. METHODS

A number of methods have been proposed to make subtle anomalies more visible. The first filter developed for this purpose was the tilt angle ([5]), which is the ratio of the vertical derivative to the absolute value of the horizontal derivative of the potential field. The tilt angle is given by

$$Tilt = \tan^{-1} \left(\frac{\frac{\partial T}{\partial z}}{THDR} \right) \quad (1)$$

where

$$THDR = \sqrt{\left(\frac{\partial T}{\partial x}\right)^2 + \left(\frac{\partial T}{\partial y}\right)^2} \quad (2)$$

T is the potential anomaly and THDR is the total horizontal derivatives ([6]). The tilt angle amplitudes are restricted to values between $-\pi/2$ and $+\pi/2$; thus the method delimitates the amplitude variations into a certain range. Tilt angle therefore functions like an automatic-gain-control filter, and therefore responds equally well to shallow and deep sources. The tilt angle produces a zero value over the source edges ([3]).

([7]) introduced the theta map (θ), which is the normalization of the THDR by the AS, is given by

$$\cos\theta = \left(\frac{THDR}{AS} \right) \quad (3)$$

and

$$AS = \sqrt{\left(\frac{\partial T}{\partial x}\right)^2 + \left(\frac{\partial T}{\partial y}\right)^2 + \left(\frac{\partial T}{\partial z}\right)^2} \quad (4)$$

AS is the analytic signal for the 3D case ([8]). The theta map delineates model edges well, but the response of deeper bodies is diffused; consequently, it does not produce the expected sharp gradient over the edges.

Recently, ([9]) presented the horizontal tilt angle method (TDX) as an edge detector:

$$TDX = \tan^{-1} \left(\frac{THDR}{\left| \frac{\partial T}{\partial z} \right|} \right) \quad (5)$$

TDX responds equally well to shallow and deep bodies, and also delineates the edges of all the bodies well. TDX has a much sharper gradient over the edges of the magnetized bodies.

The proposed ETilt filter is the ratio of the vertical derivative to the total horizontal derivative of the AS:

$$Etilt = \tan^{-1} \left(k \frac{\frac{\partial T}{\partial z}}{\sqrt{\left(\frac{\partial A}{\partial x}\right)^2 + \left(\frac{\partial A}{\partial y}\right)^2}} \right) \quad (6)$$

where

$$k = \frac{1}{\sqrt{dx^2 + dy^2}} \quad (7)$$

k is the dimensional correction factor. dx and dy are sampling intervals in the x and y directions, respectively. The dimensional correction factor, k, does not have an effect on the Etilt response.

$$ETHDR = \sqrt{\left(\frac{\partial Etilt}{\partial x}\right)^2 + \left(\frac{\partial Etilt}{\partial y}\right)^2} \quad (8)$$

The ETHDR delineates the edges of the all bodies better than the filters discussed above, as it produces a very sharp gradient over the edges of the bodies. Thus, structural interpretation is very easy and powerful using the ETHDR method.

14. UPWARD CONTINUATION

Upward continuation is a method that transforms anomalies measured on one surface into those that would have been measured on some higher surface. The upward-continued anomalies do not provide direct information about the source, but they can be instructive nonetheless. In particular, the process of upward continuation tends to attenuate anomalies caused by local, near-surface sources relative to anomalies caused by deeper, more profound sources.

The potential data at two observation heights are related by the upward continuation operation ([10]),

$$T_h(x, y, \Delta h) = \frac{1}{2\pi} \int_{-\infty}^{\infty} \int_{-\infty}^{\infty} \frac{T_0(x', y') \Delta h}{[(x' - x)^2 + (y' - y)^2 + \Delta h^2]^{3/2}} dx' dy' \quad (9)$$

where $T_0(x, y)$ and $T_h(x, y, h)$ are respectively the potential data at two observation heights separated by a vertical distance Δh . Applying a two-dimensional Fourier transform to eq.(1) yields a simpler form in which the Fourier transforms of the two quantities are related to each other by a simple upward continuation operator,

$$\tilde{T}_h(\omega_x, \omega_y, \Delta h) = e^{-\Delta h \omega_r} \tilde{T}_0(\omega_x, \omega_y) \quad (10)$$

where $\tilde{T}_0(\omega_x, \omega_y)$ denotes the Fourier transform of $T_0(x, y)$, (ω_x, ω_y) are wavenumbers in x- and y- direction, and $\omega_r = \sqrt{\omega_x^2 + \omega_y^2}$ is the radial wavenumber. The upward continuation operator attenuates with height the high-frequency content of a potential anomaly.

15. POLE REDUCTION

Pole reduction is an operator which takes magnetic anomalies and changes their asymmetric form to the symmetric form which would have been observed had the causative magnetic bodies lain at the magnetic poles. The frequency domain operator is ([11]),

$$A'(u, v) = \frac{A(u, v)}{(\sin \theta + i \cos \theta \sin(\theta + \alpha))^2} \quad (11)$$

where $A(u, v)$ is the amplitude at frequencies (u, v) , θ and φ are the geomagnetic inclination and declination, respectively, and $\alpha = \tan^{-1}(v/u)$.

16. THEORETICAL STUDY

In this stage, synthetic magnetic anomaly of three prisms whose depths are 1, 3, 5 km were utilized for theoretical study (Figure 1a). %0.5 of the maximum magnetic data amplitude is added to magnetic anomaly for interpreting noise-corrupted conditions. Synthetic magnetic anomaly was obtained by using Potensoft program which is based on MATLAB ([12]). After edge detection, algorithms were carried out on noise-corrupted theoretical data. The results of THDR and AS gave similar anomalies, maximum values were over the prisms in both results but boundary of deeper body was not clear (Figure 1b and 1c). It seems that the ratio of the noise increased in the results of tilt angle, theta map, TDX, Etilt and ETHDR but ETHDR gave better results for determining the boundaries and were affected the least from noise (Figure 1d, 1e, 1f and 1g). For comparison, %5, %10 of the maximum magnetic data amplitude is added to synthetic magnetic anomaly (Figure 2a, 2c and 2e). The results are acceptable until the results of %10 noise-corrupted data, because the deeper bodies are not recognizable after %5 noise (Figure 2b, 2d and 2f).

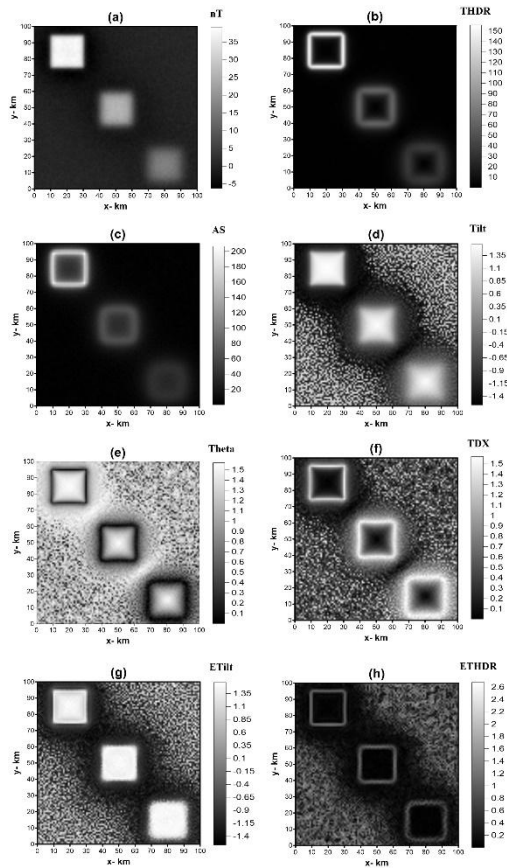


Figure 2. A comparison of boundary analysis filters: a) Theoretical magnetic data resulted from three prismatic bodies with depths of 1, 3 and 5 km. (Image covers 100x100 km area. Uniformly distributed random noise of amplitude equal to %0.5 of the maximum magnetic data amplitude is added to the magnetic data. b) Total horizontal derivative of magnetic data. c) Analytical signal of magnetic data. d) Tilt angle of magnetic data. e) Theta map of magnetic data. f) Horizontal tilt angle of magnetic data. g) Etilt of magnetic data. h) Enhanced total horizontal derivative of the tilt angle (ETHDR) of magnetic data.

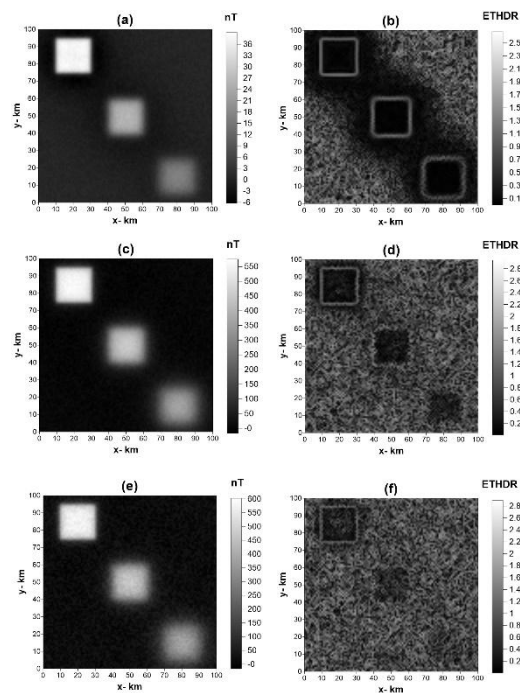


Figure 3. A comparison of different amounts of noise effects on the ETHDR responses. a) Magnetic data with uniformly distributed random noise of amplitude equal to %0.5 of the maximum magnetic data amplitude is added to the magnetic data. b) ETHDR image map of magnetic data in Figure 2a. c) Magnetic data with uniformly distributed random noise of amplitude equal %5 of the maximum magnetic data amplitude is added to the magnetic data. d) ETHDR image map of magnetic data in Figure 2c. e) Magnetic data with uniformly distributed random noise of amplitude equal %10 of the maximum magnetic data amplitude is added to the magnetic data. f) ETHDR image map of magnetic data in Figure 2e.

17. FIELD STUDY

The study area is located in the western of Bitlis that includes complex geological units and faults. Application stage of this study was provided by the contributions of the Directorate of Mineral Research and Exploration of Turkey (MTA) ([13]). Each point interval is 1 km. Figure 3 shows the location of the study area.

Firstly, the boundary analysis methods were applied to aeromagnetic data without using any filters. Maximum anomaly areas are over the northeast of the study area and minimum anomaly areas are over the southwest of the study area (Figure 4a). The faults boundaries could not be seen clearly in the results of THDR and AS because of the effects of deeper structure (Figure 4b and 4c). It seems that the noise caused to suppress effects of deeper structure because of the complex geological units in the area (Figure 4d, 4e and 4f). It needs pole reduction and other filters when examining the results of Etilt and ETHDR method (Figure 4g and 4h). The result of ETHDR could not be interpreted well because of complexity of area in terms of faults, variable topography and complex geology.

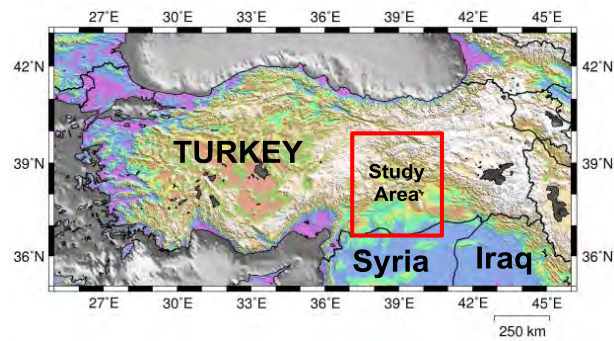


Figure 4. Location of the study area.

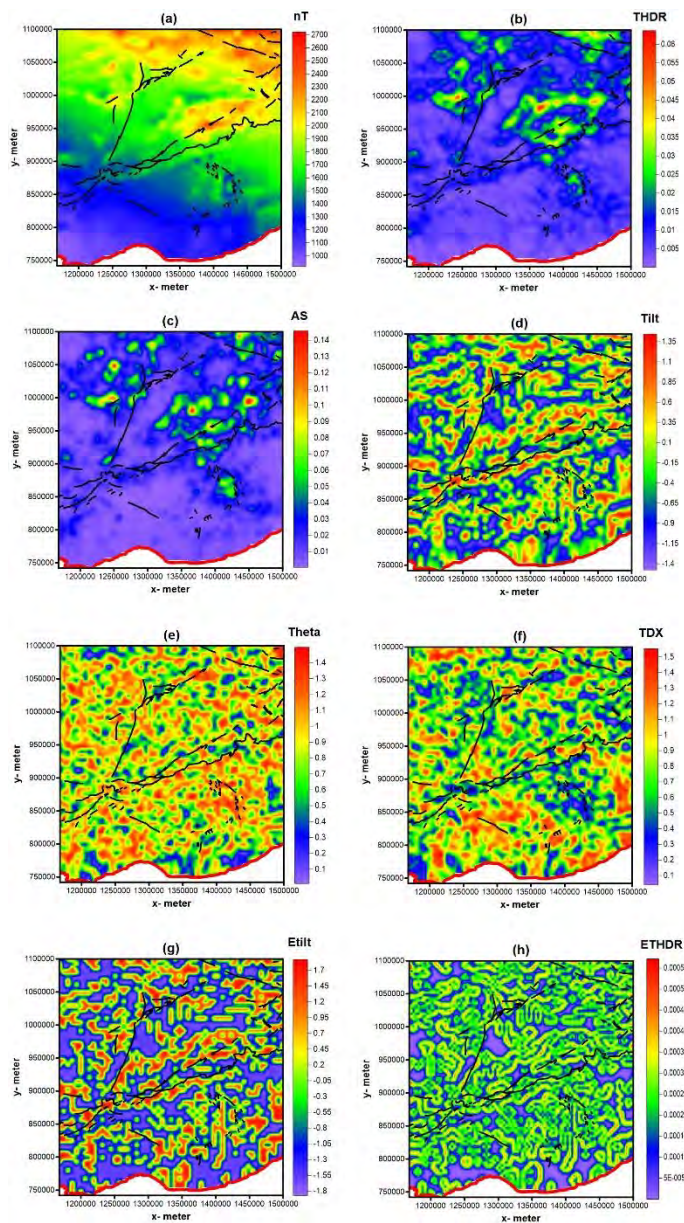


Figure 5. Magnetic anomaly and the results of boundary analysis: a) Magnetic anomaly of the western of Bitlis and its surroundings, b) The result of THDR, c) The result of AS, d) The result of tilt angle, e) The result of theta map, f) The result of TDX, g) The result of Etilt, h) The result of ETHDR method.

Afterwards, pole reduction and upward continuation (5 km) were applied to the aeromagnetic data, then same boundary analysis methods were implemented to the data. When applying to pole reduction and upward continuation, the maximum and minimum anomaly areas are

changed. The effects of deeper bodies were revealed after upward continuation (Figure 5a). The results of THDR and AS did not change more than the results of unfiltered data but anomalies were smoother (Figure 5b and 5c). The results of Etilt, TDX, tilt and theta map give information about the geological units of area (Figure 5d, 5e, 5f and 5g). The result of ETHDR gives apparent anomaly in the BSZS especially related to low amplitude anomaly areas (Figure 5h).

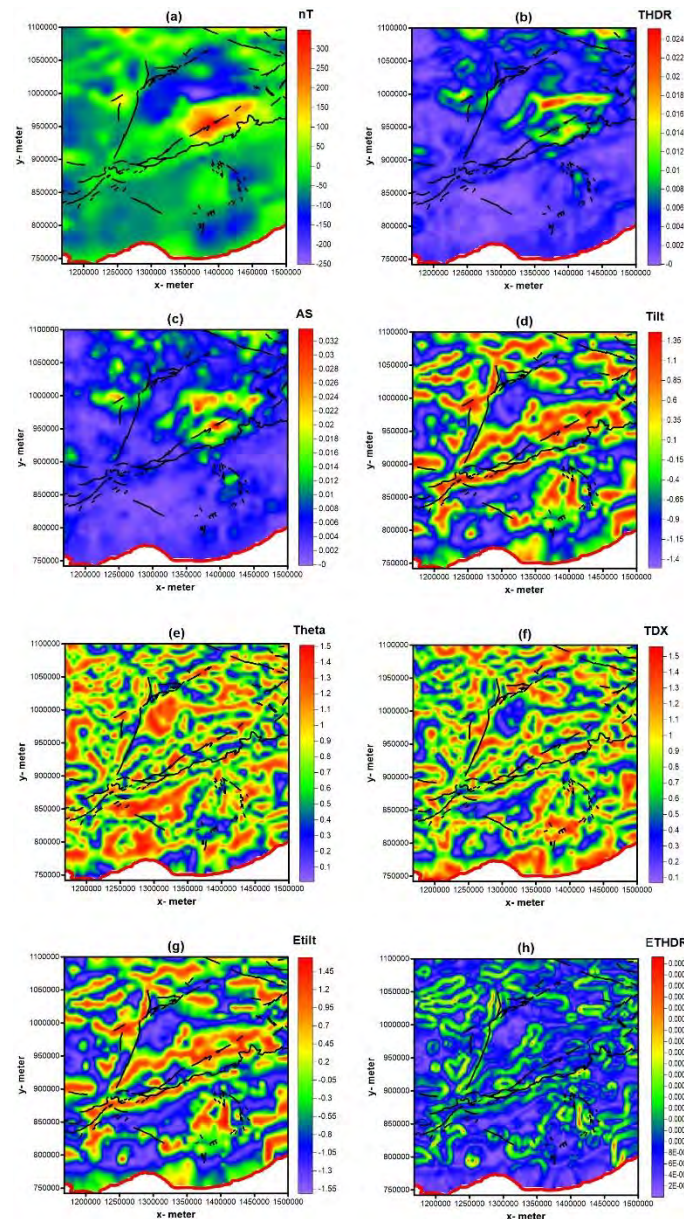


Figure 6. Upward continuation of magnetic anomaly (5km) and the results of boundary analysis: a) Upward continuation of magnetic anomaly of the western of Bitlis and its surroundings, b) The result of THDR, c) The result of AS, d) The result of tilt angle, e) The result of theta map, f) The result of TDX, g) The result of Etilt and h) The result of ETHDR method.

RESULTS

As a result of the study, THDR, AS, Tilt, Theta map, TDX, Etilt, ETHDR boundary analysis methods were implemented successfully to pole reduction and 5 km upward continuation of aeromagnetic data. The results of theta map and TDX were not able to explain the relationship between any tectonic or differences of geological units. The areas that offer close to zero amplitude are related to extension of BZSZ in the results of AS and THDR. The results of AS and THDR are related to geological unit differences and the result of ETHDR is related to tectonic elements.

ACKNOWLEDGEMENTS

In this study, the data of TUBITAK No:101Y124 project and DEU 02.KB.FEN.084 project were used. We would like to thank the Project workers.

REFERENCES

- [1]. M. Pilkington and P. Keating, *Geologic applications of magnetic data and using enhancements for contact mapping*, EGM international workshop Adding new value to electromagnetic, gravity and Magnetic methods for exploration, Capri, Italy, pp 11-14, 2010.
- [2]. N. Bournas and H.A. Baker, *Interpretation of magnetic anomalies using the horizontal gradient analytic signal*, Annali di Geofisica, 44 (3), pp 506-526, 2001.
- [3]. M.O. Arisoy and U. Dikmen, *Edge Detection of Magnetic Sources Using Enhanced Total Horizontal Derivative of the Tilt Angle*, Bulletin of the Earth Sciences Application and Research Centre of Hacettepe University, 34 (1), pp 73-82, 2013.
- [4] C.O. Faccenna, J. Bellier, , C.P. Martinod and V. Regard, *Slab Detachment Beneath Eastern Anatolia: A Possible Cause for the Formation of the North Anatolian Fault*, Earth and Planetary Science Letters, Vol. 242, pp. 85-97, 2006,.
- [5]. H.G. Miller and V. Singh, *Potential field tilt: a new concept for location of potential filed sources*, Journal of Applied Geophysics, 32, pp 213-217, 1994.

- [6]. L. Cordell and V.J.S. Grauch, *Mapping basement magnetization zones from aeromagnetic data in The San Juan Basin, New Mexico*. In: W.J., Hinze, Ed., *The utility of regional gravity and magnetic anomaly maps: Society Exploration Geophysics*, Tulsa, Oklahoma, 181-197, 1985.

- [7]. C. Wijns, C. Perez and P. Kowalczyk, *Theta map: edge detection in magnetic data*, Geophysics, 70(4), pp 39-43, 2005.

- [8]. W.R. Roest, J. Verhoef and M. Pilkington, *Magnetic interpretation using the 3-D analytic signal*, Geophysics, 57(1), pp. 116-125, 1992.

- [9]. G.R.J. Cooper and D.R. Cowan, *Enhancing potential field data using filters based on the local phase*, Computer and Geosciences, 32, pp 1585-1591, 2006.

- [10]. R.J. Blakely, *Potential theory in gravity and magnetic applications*, Cambridge University Press, 1995.
- [11]. V. Baranov, *A new method for interpretation of aeromagnetic maps: Pseudo-gravimetric anomalies*, Geophysics, 22, 359-383, 1957.
- [12]. M.O. Arisoy and U. Dikmen, *Potensoft: MATLAB-based software for potential field data processing, modeling and mapping*. Computer and Geosciences, 37, 935-942, 2011.
- [13]. MTA (Directorate of Mineral Research and Exploration, Turkey) 1979. Aeromagnetic Map of Eastern Turkey [unpublished].

Performance Characteristics of a Spark Ignition (SI) Engine Fueled with Liquid Fuels and Alcohols

Guven GONCA⁴, Aykut SAFA⁵, Fatih Mehmet KALE⁶, Eyup BAL⁷

Abstract

The effects of different liquid fuels and alcohols, such as gasoline, benzene, hexane, iso-octane, toluene, ethanol and methanol, on the engine performance and combustion characteristics of a spark ignition (SI) engine, running at stoichiometric combustion conditions, are investigated. A validated combustion model with experiments has been used to demonstrate the different fuel type influences on engine performance. The results obtained have been compared with the data of gasoline combustion case. In terms of engine performance, the results showed that the engine running on the liquid fuels, excluding gasoline, and alcohols has close results to the engine fueled with gasoline.

Keywords: *Liquid fuels; alcohols; equilibrium combustion products; combustion; spark ignition engine, engine performance.*

18. INTRODUCTION

The researchers have studied on different fuel types by considering economical and environmental factors. Contino et al. [1] experimentally and computationally analyzed the effect of initial NO concentrations on the ignition of iso-octane in a single cylinder HCCI engine. They used CFD simulation with a detailed mechanism involving over 1000 species and 4500 reactions to validate experimental data. Aleiferis et al. [2] investigated the combustion characteristics and flame development of ethanol, butanol, iso-octane, gasoline and methane in a direct-injection spark-ignition engine at stoichiometric and lean combustion conditions. Sileghem et al. [3] measured the laminar burning velocities of gasoline, iso-octane, n-heptane and toluene at different equivalence ratios and temperatures. Mansfield et al. [4] carried out various tests and modeling studies to examine the auto-ignition properties of iso-octane mixtures. Assanis et al. [5] experimentally investigated flame propagation and auto ignition interactions of iso-octane and air mixtures at different oxygen concentrations and equivalence ratios. Baloo et al. [6] added the methane into iso-octane at two volumetric fractions as 30% and 70% and examined laminar burning velocities and flame instabilities. Javed et al. [7] compared the oxidation characteristics of different gasoline fuels and n-heptane/iso-octane surrogate mixtures doing experiments and using detailed kinetic mechanisms. Liu et al. [8] examined the effects of pressure and temperature on laminar flame developments of n-butanol, iso-octane and their mixtures. Fu et al. [9] developed new correlations for

laminar burning velocities of n-butanol, iso-octane and their mixtures. Contino et al. [10] used CFD simulations with the Tabulation of Dynamic Adaptive Chemistry (TDAC) method to predict the effect of ozone seeding on the combustion of iso-octane in a HCCI engine. Jain et al. [11] developed a reduced mechanism containing 38 species and 74 reactions to examine the ignition behavior of iso-octane/H₂ and iso-octane/syngas blends. Di et al. [12] conducted theoretical and experimental investigations to understand the thermal and chemical effects of buffer gas composition on low temperature ignition of iso-octane and n-heptane. Also, they showed that the chemical effects of CO₂ are more important than the thermal effects at higher temperatures. Zhao et al. [13] simulated the working process of a porous medium (PM) engine fueled with isooctane using KIVA-3V. Li et al. [14] carried out simulation studies on laminar flame propagation and ignition properties of premixed isooctane-hydrogen mixtures at different equivalence ratios. Varea et al. [15] examined the pressure effects on laminar burning velocities of isooctane-ethanol blends. Rau et al. [16] measured laminar burning velocities of iso-octane-ethanol blends for different preheat temperatures using the Heat Flux method. They also carried out numerical simulations using different chemical

⁴ Yildiz Technical University, Naval Architecture and Marine Engineering Department, 34349, Besiktas/Istanbul, Turkey. ggonca@yildiz.edu.tr

⁵ Corresponding author: Yildiz Technical University, Naval Architecture and Marine Engineering Department, 34349, Besiktas/Istanbul, Turkey. safa.aykut@gmail.com

⁶ Corresponding author: Yildiz Technical University, Naval Architecture and Marine Engineering Department, 34349, Besiktas/Istanbul, Turkey. fatihmehmetkalevtu@gmail.com

⁷ Yildiz Technical University, Naval Architecture and Marine Engineering Department, 34349, Besiktas/Istanbul, Turkey. baleyupp@gmail.com

mechanisms for ethanol-air flames, iso-octane-air flames, fuel blends and preheating temperatures. Kim et al. [17] investigated syn-gas production capability of a new microwave plasma system and demonstrated the reforming characteristics of methane, iso-octane and gasoline using the developed plasma system. Sun et al. [18] performed numerical analysis based on non-equilibrium thermodynamics combined with detailed chemical kinetics to explore the exergy loss mechanism of gasoline engine using a fuel consisting iso-octane (57%), n-heptane (16%), toluene (23%), and 2-pentene (4%). They examined the influences of temperature, pressure, equivalence ratio, oxygen concentration on combustion exergy loss. Kukkadapu et al. [19] measured ignition delays of two surrogates for a research grade gasoline (RD387), including a three-component mixture of iso-octane, n-heptane, toluene and a four-component mixture with the addition of an olefin (2-pentene) using a rapid compression machine. Cai and Pitsch [20] developed a reduced combustion mechanism for mixtures of n-heptane and iso-octane and allowing the formulation of multi-component surrogate fuels including Polycyclic Aromatic Hydrocarbons in gasoline engines. Also, an ethanol model was also incorporated into the developed reduced mechanism. It was reported that the proposed model was verified against experimental measurements.

This work presents the influences of the different liquid fuels and alcohols such as benzene, hexane, iso-octane, toluene, ethanol, methanol and gasoline on the combustion characteristics such as in-cylinder pressure, in-cylinder temperature, cycle work and heat transfer for the SI engine at stoichiometric combustion conditions.

19. SIMULATION MODEL

In this study, an engine was used in ref. [21] since two-zone combustion model used was verified with the experimental data in [21]. Therefore, it is used to carry out the combustion simulation of spark ignition engine running with the different fuel types and brake power and brake thermal efficiency. The engine characteristics and the fuels used are given in Table 1 and Table 2, respectively.

Table 1. Engine Properties [21]

Cylinder number	1	
Engine speed	2000	rpm
Bore	10	cm
Stroke	8	cm
R	10	
RGF	0.1	
θ_b	60	CA
θ_s	35	BTDC
ϕ	1	
P_i	100	kPa
T_i	350	K
T_w	450	K

Table 2. The properties of the fuels.

Fuel Kind [22]	Chemical formula	Mole weight (g)	Lower heat value (MJ/kg)
Gasoline	C_7H_{17}	101	47.87
Propane	C_3H_8	44	50.40

Methane	CH ₄	16	52.42
Hydrogen	H ₂	2	120.70

In the theoretical model, the gas regions are divided as burned and unburned gas regions by region border. The energy conservation equation could be expressed as follows [22].

$$m \frac{du}{d\theta} + u \frac{dm}{d\theta} = - \frac{dQ_b}{d\theta} - \frac{dQ_u}{d\theta} - P \frac{dV}{d\theta} - \frac{dm_1}{d\theta} h_1 \quad (1)$$

where, h_1 is specific enthalpy loss during blowby (in J g⁻¹), m is mass (in g), P is pressure (in bar), Q_b is heat loss through cylinder walls from burned gas zone (in J), Q_u is heat loss through cylinder walls from unburned gas zone (in J), u is specific internal energy (in J g⁻¹), V is volume (in cm³), θ is crank angle (in degree),

20. RESULTS AND DISCUSSION

Figure 1 shows the variation of in-cylinder pressure with respect to crank angle. It is seen that in-cylinder pressure is increasing with raising crank angle during the compression and combustion processes. However, pressure increase rate of the combustion process is higher than that of the compression process. The in-cylinder pressure reduces with advancing crank angles during expansion process. It is clear that maximum pressure is obtained with toluene combustion but minimum pressure value is seen with methanol combustion. The maximum pressure of ethanol is higher than that of methanol, but it is lower than that of toluene. Also, there are no considerable differences between toluene, gasoline, benzene, hexane, iso-octane. If the Table 3 is investigated, it is understood that Fig. 1 and Table 3 are compatible. The order is toluene > benzene > iso-octane > hexane > gasoline > ethanol > methanol for the peak pressures. The main reason of this order is related to lower heat values and stoichiometric fuel-air ratios.

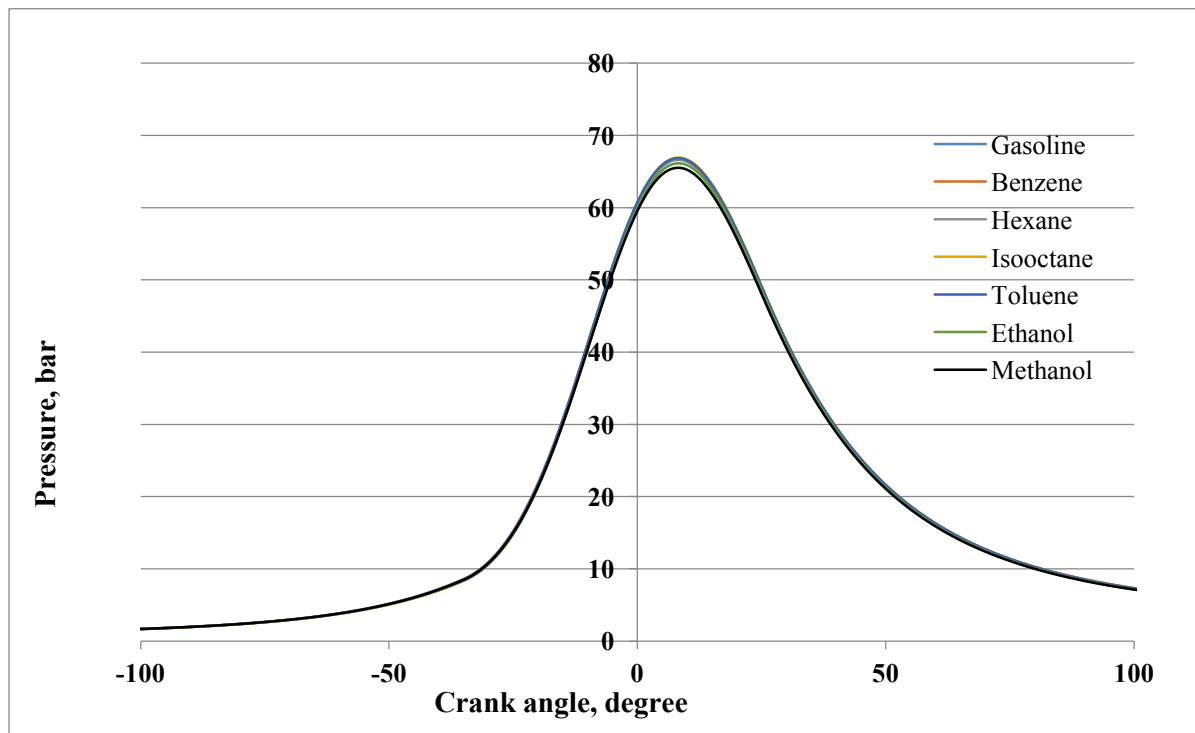


Fig. 1. Variation of in-cylinder pressure with respect to crank angle for different fuels.

Figure 2 demonstrates the variation of in-cylinder temperature with respect to crank angle. Similarly to curve trend of pressure in-cylinder temperature is increasing with raising crank angle during the compression and combustion processes. The temperature increase rate of the combustion process is higher than that of the compression process. The in-cylinder temperature decreases with enhancing crank angle during expansion process. It is obvious that benzene has the maximum temperature value while the methanol has the lowest temperature value. The order is benzene > toluene > hexane > iso-octane > gasoline > ethanol > methanol for in-cylinder combustion temperature.

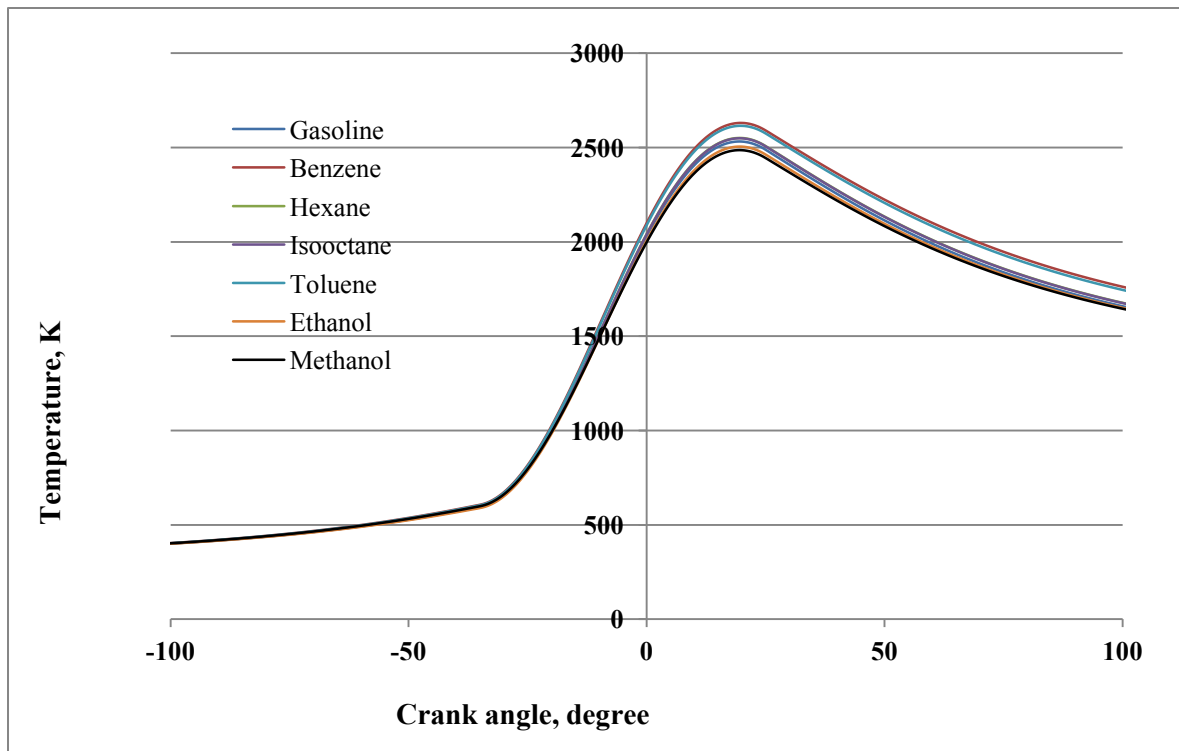


Fig. 2. Variation of in-cylinder temperature with respect to crank angle for different fuels

Figure 3. illustrates the variation of cycle work with respect to crank angle. We see that the cycle work decreases with increasing crank angle during the compression process. Negative work is seen during the process due to work input to the cylinder. During the combustion and expansion processes, cycle work raises and the positive work seems 30 crank angle after TDC. The highest cycle work is attained with toluene in accordance with the pressure figure and Table 3. The others have the same trends as similar to that of pressure.

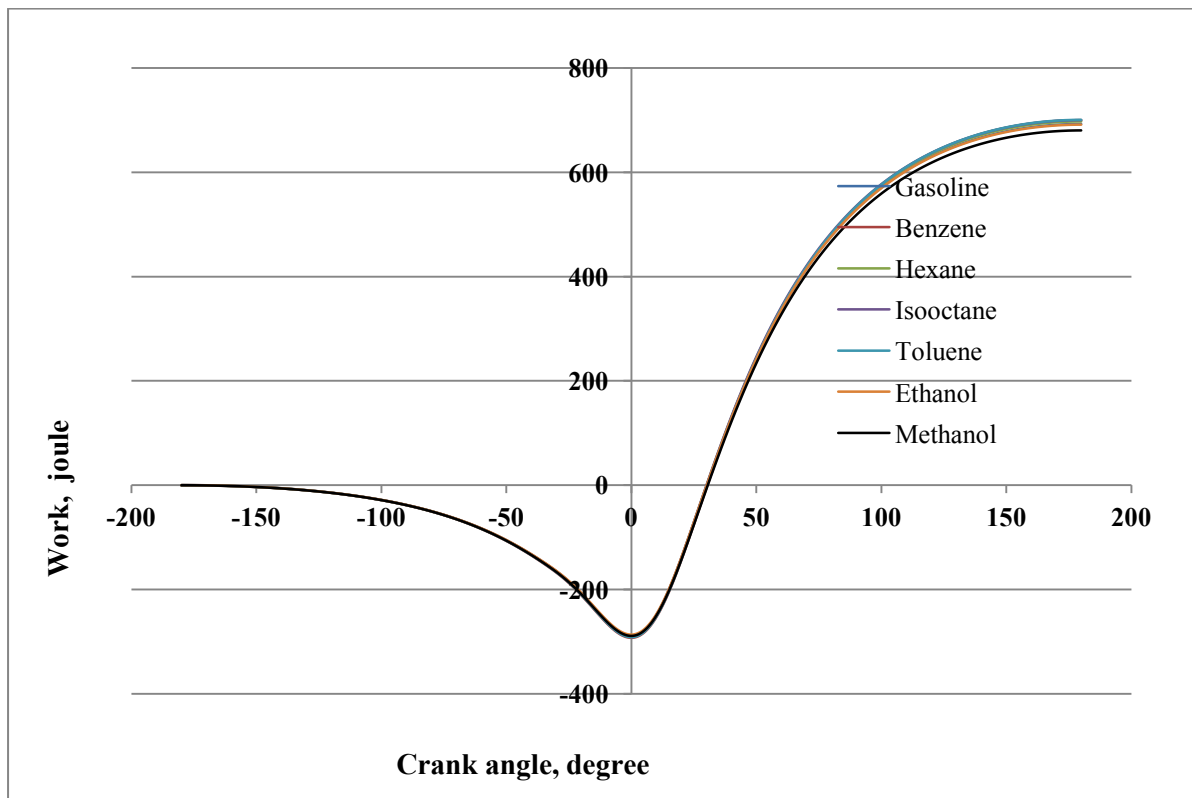


Fig. 3. Variation of cycle work with respect to crank angle for different fuels

Figure 4. indicates the variation of heat transfer with respect to crank angle. After start of combustion, heat transfer enhances with increasing of crank angle. Also, this figure has the same trend as that of the figure which gives the in-cylinder temperature since heat transfer changes with changing in-cylinder temperature.

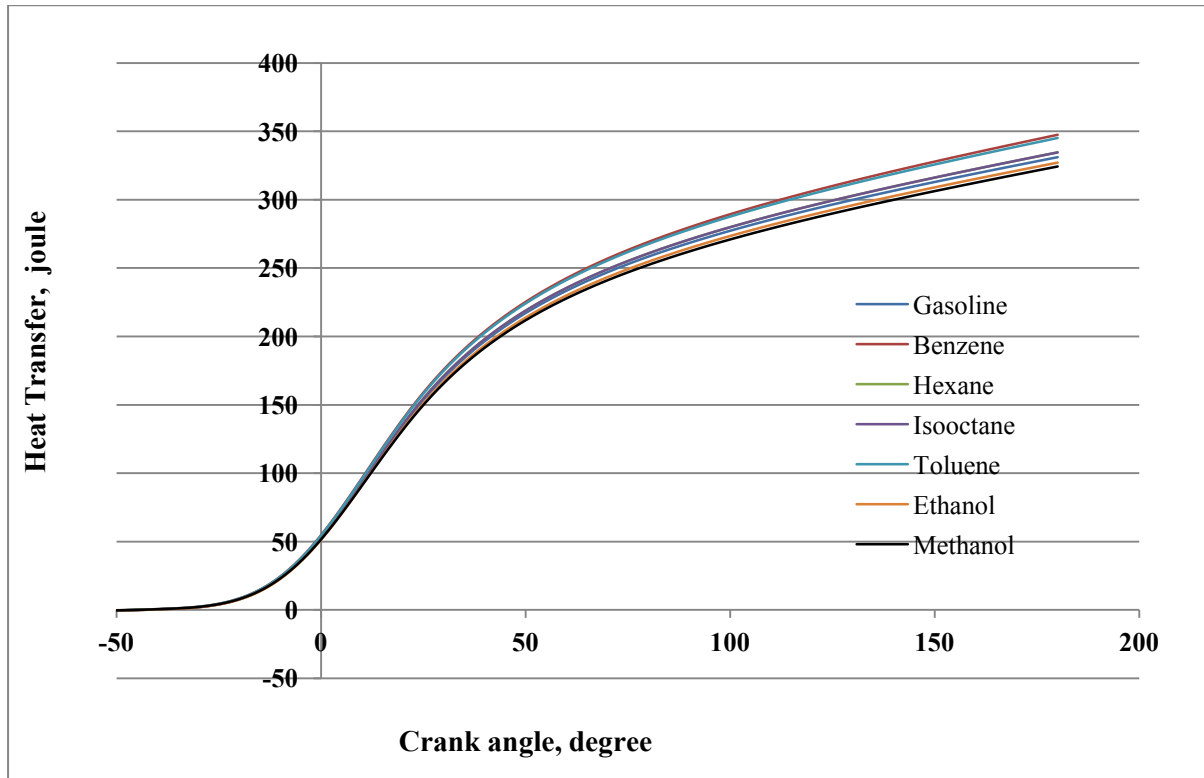


Fig. 4. Variation of heat transfer with respect to crank angle for different fuels

Table 3. The performance parameters of the liquid fuels and alcohols.

	Power	IMEP	η	Work
Gasoline	10.00	9.55	31.30	600.21
Benzene	10.13	9.67	31.23	607.89
Hexane	10.08	9.63	33.58	605.07
Isooctane	10.12	9.67	31.26	607.46
Toluene	10.14	9.68	31.42	608.50
Ethanol	9.98	9.53	30.88	598.88
Methanol	9.80	9.36	30.29	588.06

21. CONCLUSION

In this work, the effects of liquid fuels and alcohols, used in the internal combustion engines, such as, benzene, hexane, iso-octane, toluene, ethanol and methanol, on the combustion characteristics of a SI engine at stoichiometric combustion case have been obtained by a code validated with experiments. In the results, the maximum performance of iso-octane gets close to toluene and benzene, however, more studies are needed to determine emission characteristics of the fuels. It is clear that, generally, the performance characteristics of the fuels are close to each other. Therefore, the minimum emission values have to be obtained to determine the best environmentally friendly fuels. The results presented are valuable in terms of understanding the effects of different fuel types on the combustion characteristics for a SI engine.

REFERENCES

- [21]. F Contino, F Foucher, P Dagaut, T Lucchini, G D'Errico, C. Mounaïm-Rousselle, "Experimental and numerical analysis of nitric oxide effect on the ignition of iso-octane in a single cylinder HCCI engine", *Combustion and Flame*, vol. 160, pp. 1476–83, 2013.
- [22]. P. G. Aleiferis, J. Serras-Pereira, D. Richardson, "Characterisation of flame development with ethanol, butanol, iso-octane, gasoline and methane in a direct-injection spark-ignition engine", *Fuel*, vol. 109, pp. 256–78, 2013
- [23]. L. Sileghem, V. A. Alekseev, J. Vancoillie, K. M. Van Geem, E. J. K. Nilsson, S. Verhelst, A. A. Konnov, "Laminar burning velocity of gasoline and the gasoline surrogate components iso-octane, n-heptane and toluene", vol. 112, *Fuel*, pp. 355–365, 2013.
- [24]. A. B. Mansfield, M. S. Wooldridge, H. Di, X. He, "Low-temperature ignition behavior of iso-octane", vol. 139, *Fuel*, pp. 79–86, 2015.
- [25]. D. Assanis, S.W. Wagnon, MS Wooldridge, "An experimental study of flame and autoignition interactions of iso-octane and air mixtures", *Combustion and Flame*, vol. 162, pp.1214–1224, 2015.
- [26]. M. Baloo, B.M. Dariani, M. Akhlaghi, I. Chitsaz, "Effect of iso-octane/methane blend on laminar burning velocity and flame instability", *Fuel*, vol. 144, pp. 264–273, 2015.
- [27]. T. Javed, E.F. Nasir, E. Es-sebbar, A. Farooq, "A comparative study of the oxidation characteristics of two gasoline fuels and an n-heptane/iso-octane surrogate mixture", *Fuel*, vol. 140, pp. 201–8, 2015.
- [28]. K. Liu, J. Fu, B. Deng, J. Yang, Q. Tang, J. Liu, "The influences of pressure and temperature on laminar flame propagations of n-butanol, iso-octane and their blends", *Energy*, vol. 73, pp. 703–15, 2014.
- [29]. J. Fu, B. Deng, Y. Wang, J. Yang, D. Zhang, Z. Xu, J. Liu, "Numerical study and correlation development on laminar burning velocities of n-butanol, iso-octane and their blends: Focusing on diluent and blend ratio effects", *Fuel* 2014;124:102–12.
- [30]. F. Contino, J.B. Masurier, F. Foucher, T. Lucchini, G. D'Errico, P. Dagaut, "CFD simulations using the TDAC method to model iso-octane combustion for a large range of ozone seeding and temperature conditions in a single cylinder HCCI engine", *Fuel* 2014;137:179–84.
- [31]. S. Jain, D. Li, S.K. Aggarwal, "Effect of hydrogen and syngas addition on the ignition of iso-octane/air mixture", *International journal of hydrogen energy*, 2013;38:4163–76.
- [32]. H. Di, X. He, P. Zhang, Z. Wang, M. S. Wooldridge, CK Law, C Wang, S Shuai, J Wang, "Effects of buffer gas composition on low temperature ignition of iso-octane and n-heptane", *Combustion and Flame*, vol. 161, pp. 2531–2538, 2014.
- [33]. Z. Zhao, C. Wang, M. Xie, "Numerical study on the realization of compression ignition in a type of porous medium engine fueled with Isooctane", *Fuel*; 88: 2291–2296, 2009.
- [34]. Z. Li, W. Han, D. Liu, Z. Chen, "Laminar flame propagation and ignition properties of premixed iso-octane/air with hydrogen addition", *Fuel*, 2015; 158: 443–450.
- [35]. E. Varea, V. Modica, B. Renou, A. M. Boukhalfa, "Pressure effects on laminar burning velocities and Markstein lengths for Isooctane–Ethanol–Air mixtures", *Proceedings of the Combustion Institute*, vol. 34, pp. 735–744, 2013;.
- [36]. F. Rau, S. Hartl, S. Voss, M. Still, C. Hasse, D. Trimis, "Laminar burning velocity measurements using the Heat Flux method and numerical predictions of iso-octane/ethanol blends for different preheat temperatures", *Fuel*, vol. 140, pp. 10–16, 2015.
- [37]. T. S. Kim, S. Song, K. M. Chun, S. H. Lee, "An experimental study of syn-gas production via microwave plasma reforming of methane, iso-octane and gasoline", *Energy* 2010, vol. 35: 2734–43.
- [38]. H. Sun, F. Yan, H. Yu, W. H. Su, "Analysis of exergy loss of gasoline surrogate combustion process based on detailed chemical kinetics", *Applied Energy* 2015;152:11–9.
- [39]. G. Kukkadapu, K. Kumar, C. J. Sung, M. Mehl, W. J. Pitz, "Autoignition of gasoline surrogates at low temperature combustion conditions", *Combustion and Flame* 2015;162:2272–85.
- [40]. L. Cai, H. Pitsch, "Optimized chemical mechanism for combustion of gasoline surrogate fuels", *Combustion and Flame* 2015;162:1623–37.
- [41]. I. Cesur, A. Parlak, A. Ayhan, G. Gonca and B. Boru, "The effects of electronic controlled steam injection on spark ignition engine", *Appl Therm Eng*, vol. 55, pp. 61–68, 2013.
- [42]. C. R. Ferguson, *Internal Combustion Engines, Applied Thermodynamics*, New York, USA: John Wiley & Sons, 1986.
- [43]. G. F. Hohenberg. Advanced approaches for heat transfer calculation, SAE Tech;1979.
- [44]. G. Kokkulunk, G. Gonca, V. Ayhan, I. Cesur and A. Parlak, "Theoretical and experimental investigation of diesel engine with steam injection system on performance and emission parameters", *Appl Therm Eng*, vol. 54, pp. 161–170, 2013.
- [45]. G. Gonca, B. Sahin, Y. Ust and A. Parlak, "A study on late intake valve closing Miller cycled diesel engine", *Arab J Sci Eng*, vol. 38, 383–393, 2013.
- [46]. G. Gonca, Investigation of the effects of steam injection on performance and NO emissions of a diesel engine running with ethanol–diesel blend, *Energy Convers Manage*, vol. 77, pp.450–457, 2014.
- [47]. G. Kokkulunk, G. Gonca and A. Parlak, The effects of design parameters on performance and no emissions of steam-injected diesel engine with exhaust gas recirculation, *Arab J Sci Eng*, vol.39 (5), pp. 4119–4129, 2014.
- [48]. G. Kokkulunk, A. Parlak, V. Ayhan, I. Cesur, G. Gonca and B. Boru, Theoretical and experimental investigation of steam injected diesel engine with EGR, *Energy*, vol.74 (1), 2014, 331–339.
- [49]. G. Gonca, B. Sahin, A. Parlak, Y. Ust, V. Ayhan, I. Cesur and B. Boru, The effects of steam injection on the performance and emission parameters of a Miller cycle diesel engine, *Energy*, vol.78, pp. 266–275, 2014.
- [50]. G. Gonca, B. Sahin, Y. Ust, A. Parlak and A. Safa, "Comparison of steam injected diesel engine and miller cycled diesel engine by using two zone combustion model", *J Energy Inst*, vol. . 88 (1), pp. 43–52, 2015.
- [51]. G. Gonca, B. Sahin, A. Parlak, Y. Ust, V. Ayhan, I. Cesur and B. Boru, "Theoretical and experimental investigation of the Miller cycle diesel engine in terms of performance and emission parameters", *Appl. Energy*, vol. 138, pp. 11–20, 2015.
- [52]. G. Gonca, Investigation of the influences of steam injection on the equilibrium combustion products and thermodynamic properties of bio fuels (biodiesels and alcohols)", *Fuel*, vol. 144, pp. 244–258, 2015.

- [53]. G. Gonca, B. Sahin, A. Parlak, V. Ayhan, I. Cesur and S. Koksal, "Application of the Miller cycle and turbo charging into a diesel engine to improve performance and decrease NO emissions", *Energy*, vol. 93, 2015, 795–800.
- [54]. J.B. Heywood, *Internal Combustion Engine Fundamentals*, New York: USA: McGraw-Hill Inc., 1998.

Comparison of GPS-TEC Measurements with IRI-PLAS and IRI-2012 Models Over a Mid-Latitude Station, MADR, Spain

Salih Alcay⁸, Gurkan Oztan⁹

Abstract

The International Reference Ionosphere (IRI) is an empirical model for specifying ionospheric parameters such as electron density, total electron content (TEC), electron and ion temperature, etc. IRI model specifies the ionosphere only up to 2000 km. In order to extend the IRI for the plasmasphere, IRI PLAS model was proposed by the researchers. Besides such empirical models TEC values can be generated using GPS measurements. In this study TEC prediction performance of IRI model, IRI-PLAS model and GPS over a mid-latitude station (MADR) in Spain, was examined for the magnetically active (09.03.2012) and quiet (02.06.2015) ionospheric days. The results exhibit good agreement among GPS-TEC, IRI-PLAS and IRI-2012 models for the quiet day. However, they are not relatively high in most part of the active day, in some part of the day (e.g. 13 UT) differences reached 13 and 15 TECu levels for GPS-TEC / IRI-PLAS and GPS-TEC / IRI-2012 respectively.

Keywords: GPS, IRI-2012, IRI-PLAS, Total Electron Content

22. INTRODUCTION

Monitoring of the ionosphere is an important task for many study areas including communication, safety-critical, navigation and space based systems. In order to monitor the ionosphere, empirical models and Global Positioning System (GPS) are generally used in terms of Total Electron Content (TEC) estimation. Recently GPS is widely used for studying the ionosphere because of its temporal and spatial coverage. In addition, GPS allows the estimation of TEC owing to the dispersive nature of the ionosphere [1]. [2] gives an overview of GPS based ionosphere modeling studies.

The International Reference Ionosphere (IRI) provides ionospheric parameters such as; total electron content, electron density, electron and ion temperature. The comparison of GPS-TEC measurements with IRI-2007 and IRI-2012 modeled TEC is given by [3]. Results show that IRI-2012 model based TEC values are more compatible with the GPS-TEC measurements. [4] performed a statistical comparison of TEC values for the years 2012-2013 from the IRI-2012 model with corresponding TEC data from the GPS. According to the results, the IRI TEC values generally compared well with the GPS-TEC values, having correlation coefficients about 0.9.

However since the IRI model specifies the ionosphere only up to 2000 km, IRI extended to Plasmasphere (IRI-PLAS) was introduced by the researchers which provides model values up to 20200 km [5]. [6] investigated the performance of IRI-2012 and IRI-PLAS models based on GPS based TEC data and the possible reasons of data-model discrepancies were given in detailed way.

This study analysis the results coming from comparison of GPS based TEC data with the TEC values derived by IRI-2012 and IRI-PLAS models over a mid-latitude GPS station, MADR.

⁸ Necmettin Erbakan University, Geomatics Engineering Department, Konya, TURKEY, salcay@konya.edu.tr

⁹ Necmettin Erbakan University, Geomatics Engineering Department, Konya, TURKEY, oztangurkan@gmail.com

23. MATERIAL AND METHODS

23.1. *The IRI-2012 model*

The international reference ionosphere (IRI) is a joint project of Committee on Space Research (COSPAR) and the International Union of Radio Science (URSI). IRI is an empirical model based on ground and space observation data. The major data sources are ionosondes, the powerful incoherent scatter radars, the International Satellites for Ionospheric studies and Alouette topside sounders [7]. IRI describes several parameters, including TEC values, in the altitude range from 60 km to 2000 km. In this study, in order to compute TEC values, a web interface from the IRI homepage at <http://iri.gsfc.nasa.gov> was used.

23.2. *The IRI-PLAS model*

The IRI-PLAS is an empirical model approach extending beyond the ionosphere, up to 20200 km which is the orbit of GPS satellites [5]. IONOLAB group presented a new user interactive service which is available online at www.ionolab.org. In this study IRI-PLAS TEC values were estimated using this service.

23.3. *GPS-TEC data*

GPS receivers can provide code and phase observations. While the ionospheric range delay is positive for code measurements, negative for phase measurements. The geometry free linear combination (ionospheric observable) is classically used for ionospheric investigation which is obtained by subtracting simultaneous code or phase observations [8]. Using such observations slant TEC values are generated. STEC values are converted VTEC values by using single layer model and mapping function. For the details of the GPS based TEC determination, authors refer to [8]. In this study VTEC values were generated from the RINEX data using ionolabtec v1.0 program, downloaded from the website: www.ionolab.org.

24. RESULTS AND DISCUSSION

The TEC from the GPS data, IRI-2012 and IRI PLAS models for a quiet day (02.06.2015) and an active day (09.03.2012) were computed and compared. In order to indicate the geomagnetic activity level, kp [9] and Dst [10] index values are given in figure 1 and figure 2 respectively. As given in figure 1, while kp index values are 0.33 level for the quiet day, they are in the high level for the active day. Kp value reached 8 value for 6-9 UT, representing severe geomagnetic activity. In addition, similar to the kp values Dst index value reached highest level (-131) at 9 UT (Figure 2). For the quiet day Dst values are stable and relatively low.

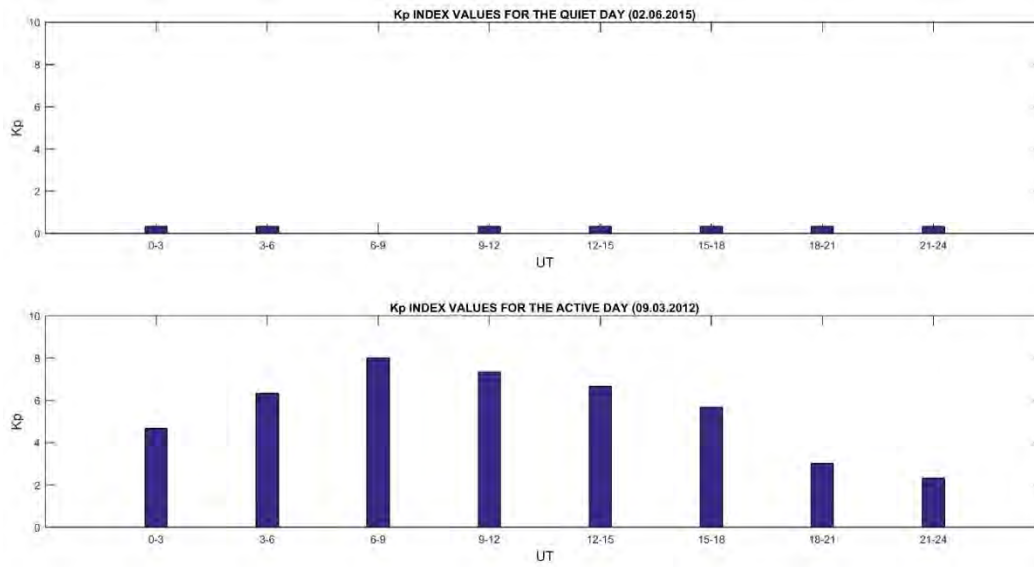


Figure 7. Kp index values for active and quiet days

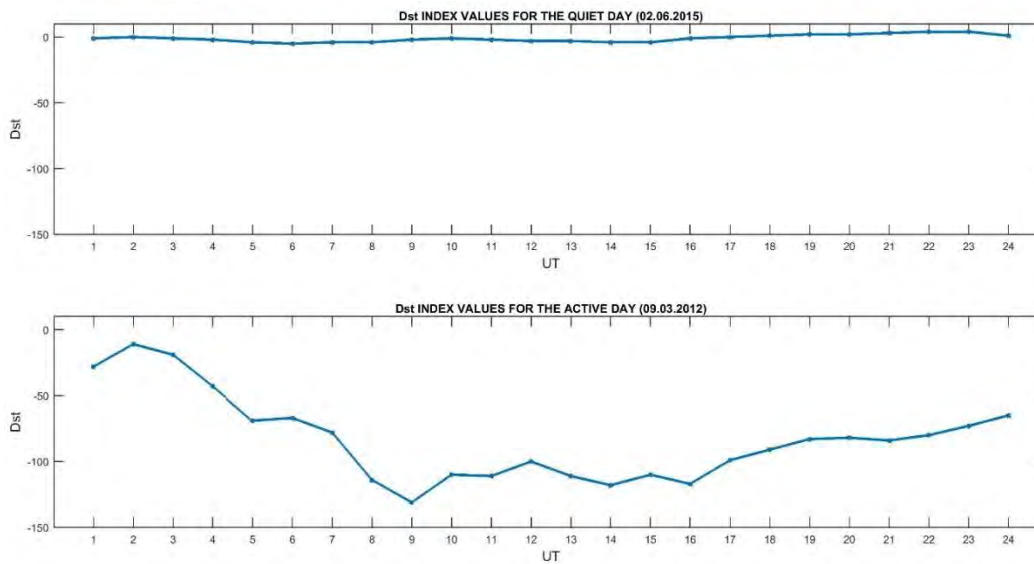


Figure 8. Dst index values for active and quiet days

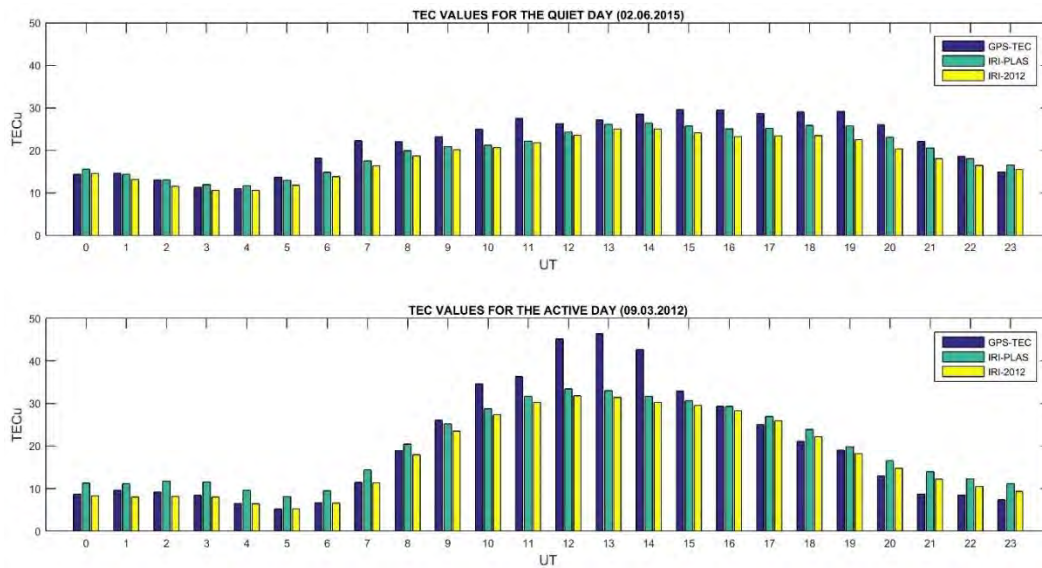


Figure 9. TEC values corresponding to GPS, IRI-PLAS and IRI-2012

Figure 3 provides the hourly TEC values corresponding to GPS, IRI-2012 and IRI-PLAS for the active and quiet days. For the quiet day, IRI-PLAS and IRI-2012 models show good agreement with the GPS results. As expected, IRI-PLAS based TEC values are a little larger than the IRI-2012 results and they are closer to the GPS-based TEC values for the each UT. Nevertheless, for the active day, while the IRI-PLAS and IRI-2012 values are consistent, GPS based TEC data overestimate the model based data during 10 UT to 14 UT which is directly related to the geomagnetic activity level (Figures 1, 2). Besides, in the rest of the day, TEC values based on all data are in good agreement (Figure 3).

In order to facilitate comparisons, statistical values derived from the differences between GPS-TEC and empirical models are given in table 1.

Table 1. Statistical values corresponding to differences between obtained TEC values

Statistical Values	Differences Between GPS-TEC and IRI-PLAS		Differences Between GPS-TEC and IRI-2012		Differences Between IRI-PLAS and IRI-2012	
	09.03.2012	02.06.2015	09.03.2012	02.06.2015	09.03.2012	02.06.2015
Maximum	13.3	5.4	15.0	6.7	3.6	3.3
Minimum	-5.2	-1.6	-3.4	-0.5	0.9	0.4
Range	18.5	6.9	18.4	7.3	2.6	2.9
Mean	0.2	2.0	2.3	3.4	2.1	1.4
Std	5.2	1.9	4.9	2.1	0.8	0.7

As depicted in table 1, differences between GPS and IRI-2012 are a little larger than the differences between GPS and IRI-PLAS in terms of mean, range and std for the quiet day. Maximum differences between GPS and IRI-2012, reaching nearly 15 TECu, which is larger than the maximum differences between GPS and IRI-PLAS (13.3 TECu), for the active day. In addition, TEC values corresponding to empirical models are closer to each other when compared to the GPS based TEC values (Table 1).

25. CONCLUSION

In this study, GPS-TEC values, estimated over MADR mid-latitude station in Spain, for a quiet day and an active day were compared with the IRI-2012 and IRI-PLAS models. According to the analysis results, the IRI-PLAS model mimicked the GPS-TEC values better than the IRI-2012 model for the quiet day. However overestimation of TEC with GPS was clear particularly around noon, in the active day. Such condition shows that while IRI-2012 and IRI-PLAS models based TEC remain smooth and can not response to the magnetic storm well, GPS based TEC can reflect this anomaly.

ACKNOWLEDGMENT

This study was funded by the Scientific Research Projects Grant of Necmettin Erbakan University (Project No:162518001-069). The authors wish to express their thanks to IONOLAB group for the IRI-PLAS model and GPS based TEC values.

REFERENCES

- [55]. S. J. Adebisi, O. O. Odeyemi, I. A. Adimula, O. A. Oladipo, S. O. Ikubanni, B. O. Adebisin, B. W. Joshua, *GPS derived TEC and foF2 variability at an equatorial station and the performance of IRI-model*, *Advances in Space Research*, **54** (4), 565–575, (2014).
- [56]. S. Alcay, C. O. Yigit, G. Seemala, A. Ceylan, *GPS-Based Ionosphere Modeling: A Brief Review*, *Fresenius Environmental Bulletin*, 23(3a), 815-824, (2014).
- [57]. S. Arunpold, N. K. Tripathi, V. R. Chowdhary, D. K. Raju, *Comparison of GPS-TEC measurements with IRI-2007 and IRI-2012 modeled TEC at an equatorial latitude station*, Bangkok, Thailand, *Journal of Atmospheric and Solar-Terrestrial Physics* 117, 88–94, (2014).
- [58]. V. S. Rathore, S. Kumar, A. K. Singh, *A statistical comparison of IRI TEC prediction with GPS TEC measurement over Varanasi, India*, *Journal of Atmospheric and Solar-Terrestrial Physics* 124, 1-9, (2015).
- [59]. F. Arikani, U. Sezen, T. L. Gulyaeva, O. Cilibas, *Online, automatic, ionospheric maps: IRI-PLAS-MAP*. *Advances in Space Research*, **55** (8), 2106–2113, (2015).
- [60]. I. E. Zakharenkova, I. V. Cherniak, A. Krankowski, I. I. Shagimuratov, *Vertical TEC representation by IRI 2012 and IRI Plas models for European midlatitudes*. *Advances in Space Research*, 55, 2070-2076, (2015).
- [61]. S. K. Leong, T. A. Musa, K. Omar, M. D. Subari, N. B. Pathy, M. F. Asillam, *Assessment of ionosphere models at Banting: Performance of IRI-2007, IRI-2012 and NeQuick 2 models during the ascending phase of Solar Cycle 24*, *Advances in Space Research*, **55**, 8, 1928–1940, (2015).
- [62]. M. Nohutcu, M. O. Karslioglu, M. Schmidt, *B-Spline modeling of VTEC over Turkey using GPS observations*, *Journal of Atmospheric and Solar-Terrestrial Physics*, 72, 7-8, 617-624, (2010).
- [63]. <http://www.gfz-potsdam.de/kp-index>
- [64]. <http://wdc.kugi.kyoto-u.ac.jp/dstdir/index.html>

Diagnosis of Coronary Artery Disease Using Deep Belief Networks

Novruz ALLAHVERDI¹⁰, Gokhan ALTAN¹¹, Yakup KUTLU¹²

Abstract

In this study, a decision-support system is presented to aid cardiologists during the diagnosis and to create a base for a new diagnosis system which separates two classes (CAD and no-CAD patients) using an electrocardiogram (ECG).

24 hour filtered ECG signals from PhysioNet were used. 15 second short-term ECG segments were extracted from 24 hour ECG signals to increase the number of samples and to provide a convenient transformation in a short period of time. The Hilbert-Huang Transform, which is effective on non-linear and non-stationary signals, was used to extract the features from short-term ECG signals. Instinct Mode Function (IMF) was extracted by applying Empirical Mode Decomposition to short-term ECG signals. The Hilbert Transform (HT) was applied to each IMF to obtain instantaneous frequency characteristics of the signal. Dataset was created by extracting statistical features from HT applied to IMF. Deep Belief Networks (DBN) which have a common use in Deep Learning algorithms were used as the classifier. DBN classification accuracy in the diagnosis of the CAD is discussed. The extracted dataset was tested using the 10-fold cross validation method.

The test characteristics (sensitivity, accuracy and specificity) that are the basic parameters of independent testing in the medical diagnostic systems were calculated using this validation method. Short-term ECG signals of CAD patients and no-CAD groups were classified by the DBN with the rates of 98.05%, 98.88% and 96.02%, for accuracy, specificity and sensitivity, respectively.

The DBN model achieved higher accuracy rates than the Neural Network classifier.

Keywords: Coronary Artery Disease, CAD, Deep Belief Networks, DBN, Deep Learning Algorithm, Hilbert-Huang Transform

26. INTRODUCTION

An electrocardiogram (ECG) is a uniform signal that records electrical changes at certain intervals of the heartbeat. It is also known as a map which shows the electrical activity of the heart. The ECG signals (ECGs), which are recorded with the aid of electrodes placed at different parts of the body, can have different electrical charges at any time. Electrical charges specify leads in the ECG. Bipolar and unipolar leads occur as a result of the position of the electrodes [1]. The ECG is a type of biomedical signal that is widely used for a variety of diagnosis and monitoring of cardiac diseases [2]. The electrical charges that are obtained directly as the result of discomfort of the heart and segments and intervals between waves on the ECG are of a paramount importance for the identification of the cardiac abnormalities in a subject [3].

Cardiac diseases have a high mortality rate worldwide. One of the most common cardiac diseases is Coronary Artery Disease (CAD). It is usually known as atherosclerosis in which there is a cardiac abnormality because of the narrowing of the arteries that feed the heart in time. In this cardiac disease, plaque caused by cholesterol collects in the coronary arteries and over time congestion results due to dilation of plaque. As a result of biological conditions, the arteries fail to feed the heart and it disrupts the rhythmic systole activity of the heart [4], [5]. CAD in adults results in heart attacks or a congestive heart. In the diagnosis of CAD, there are many clinical trials like physical examinations from which ST-deviation is measured, lab tests, Electrocardiogram (ECG), echocardiogram, stress tests and electron beam computed tomography, coronary angiography and cardiac catheterization [4]. In the literature, a diagnosis of the CAD has worked with various signal-processing methods using the clinical dataset (age, sex, history, physical exam, cardiac

risk factors, exercise stress test data, heart rate, etc.) on the rule-based fuzzy classification [6]. Other methods include using the clinical attributes on data mining techniques [7]–[14]; the chronic conditions, risk factors, and laboratory results of data mining techniques [15]; the clinical attributes on data discretization, data partitioning and reduced error pruning [16]; the history and physical examination data and the diastolic heart sounds [17]; both the heart rate variability (HRV) features and the non-linear features (Poincare Plot, entropy, etc.) [18]–[22]; the P wave features on the ECG [7]; the Wavelet Packet Transformation (10

¹⁰ Karatay University, Department of Computer Engineering, Konya, Turkey. novruz.allahverdi@karatay.edu.tr

¹¹ Corresponding author: Mustafa Kemal University, Department of Informatics, Hatay, Turkey, gokhan.altan@hotmail.com

¹² Iskenderun Technical University, Department of Computer Engineering, Hatay, Turkey, yakupkutlu@gmail.com

levels) [23]; the cardiac analysis of ST measures [24], [25]; the Empirical Mode Decomposition (EMD) and Teager Energy operator [26]; the Discrete Wavelet Transformation (DWT) [27], [28] and using the Principal Component Analysis (PCA) [28], [29]. In this study, the Hilbert-Huang Transform (HHT) is applied to filtered short-term ECGs from the PhysioNet database to extract features.

HHT is an adaptive method to analyze the nonlinear and non-stationary signals [30]. It has a common use in the biomedical signal analysis transformations due to these characteristics. The HHT is applied to the ECG for the diagnosis of Atrial Fibrillation [31] and Congestive Heart Failure [32]. In this study, the HHT would be applied to the filtered short-term ECGs for designing an effective statistical feature extraction model and classification of HHT-based statistical features using Deep Learning (DL) algorithms.

The DL is a comparatively new algorithm that is utilized to estimate the classification performances in many distributions such as speech recognition [33], [34], computer vision [35], [36], natural language processing [37]–[39], physiological data [40]–[42], biomedical datasets [43], [44] and non-linear signals [45], [46]. The DL aims to discover the multiple and deeper levels of distributions for a better classification performance. The basic concept of the DL is based on enhancing the classification performance using an artificial neural network model with multilayer hidden units. The most important difference of the DL is this: while both the multilayer neural network model and the DL has the same structure, it has at least two hidden layers and an unsupervised pre-training phase [47]. The depth of the DL is defined by the number of hidden layers on the model. The DL can also show a higher performance than neural networks with a small number of neurons. A fewer number of neurons on models can make it more convenient to calculate weights using supervised learning [48].

The aim of this study is to design a deep CAD diagnosis system that can be an alternative short-term ECG-based statistical feature based classification method to studies in the literature. 100 instances of 15 second ECG forms would be extracted from long-time ECGs in preprocessing. In this way, using short-term ECG forms would solve analysis problems and would enhance the number of samples up to 100x. The HHT would be applied to separated short-term ECGs and Instinct Mode Functions (IMFs) would be extracted. The system would extract statistical features from IMFs that are obtained applying the HHT. Each Instinct Mode Function (IMF) group obtained would be classified using the Deep Belief Networks (DBN) algorithm. Classification performances of the diagnosed subjects with or without the CAD would be examined.

27. MATERIALS AND METHODS

ECGs were used in the proposed diagnosis system. We preferred the moving window analysis technique and segmented long-time ECGs recorded into 15 second windows which were used in the preprocessing part. 15 second short-term ECGs were utilized in this study. IMFs were extracted applying HHT and statistical features were calculated for the obtained IMFs in feature extraction. Statistical features were classified using the DBN. A detailed description of the structure of the system is presented in the following sections.

27.1. Database

In the literature, different databases including different diagnosis systems were used for the diagnosis of the CAD. Clinical characteristics in particular [7]–[14] were used to separate subjects with or without CAD. Outside of the literature, the Long-Term ST Database [49] was used in the diagnosis of the CAD. The Long-Term ST Database contains 85 long-term ECGs from 80 subjects, chosen to exhibit a variety of events of ST segment changes. There are 25 subjects labeled as undiagnosed CAD patients and 60 subjects labeled as diagnosed CAD in this database. The individual recordings of the Long-Term ST Database are between 21 and 24 hours in duration.

27.2. Preprocessing

The information in a biomedical signal is unevenly distributed. We would like to call attention to the fact that all data records were from the PhysioNet databases as filtered long-term ECGs. Long-term ECGs may have too much noise while being recorded because of physical and recording conditions. The short-term ECGs usually have an ability to represent the Long-term ECG characteristics. The short-term ECG is a less affected form of represented Long-term ECG. That is why short-term ECGs were randomly segmented into 15 second short-term ECGs using the moving window analysis technique 100 times. In this way, the number of instances from each subject in the dataset could be increased by 100x.

27.3. Hilbert-Huang Transform

HHT is an effective analysis technique for non-linear signals. It has a common use in biomedical signals (ECG, EMG, EEG, etc.). It has a flexible mathematical formulation and is easily adaptable for various types of processes [32]. HHT is a two-stage transform. The first stage is EMD and the second stage is the Hilbert Spectrum Analysis (HSA). EMD extracts frequency-modulated signals that are named IMFs. After IMFs are extracted, HSA is applied to each IMF to calculate the instantaneous frequency and amplitude [50]. Considering all these characteristics, our work focuses on HHT analysis in short-term ECGs.

EMD is an algorithm that breaks down natural form non-linear signals without leaving the time domain. EMD assumes a random signal which consists of its own self-oscillation at different frequencies. Oscillations are symmetrical to the mean of the local minimum and the local maximum at a t time. EMD extracts Instinct Mode functions which are a complete and nearly orthogonal basis at different frequencies [31]. IMFs are all in the time-domain and of the same length as the original signal. EMD has a

detailed formula in the literature [30]. In the formula, X represents the original signal, c represents extracted IMF and r_n represents the residual signal [30], [31].

$$X(t) = \sum_{j=1}^n c_j + r_n \quad (1)$$

After sifting through IMFs by obtaining a monotonic residual signal, the Hilbert Transform (HT) can be applied to each IMF to compute the instantaneous frequencies spectral analysis. The instantaneous frequencies give most important information about the signal characteristics. After performing the HT to each IMF component, the amplitude and frequency of each component as functions of time is [30]:

$$x(t) = \Re\{\sum_{i=1}^n a_i(t) e^{j\omega(t)dt}\} \quad (2)$$

The frequency-time distribution of the amplitude is designated as the HSA, $H(\omega, t)$ and the marginal spectrum is $h(\omega)$ as follows [30] :

$$h(\omega) = \int_0^t H(\omega, t) dt \quad (3)$$

27.4. Deep Belief Networks

The DBN is a machine learning algorithm become more popular because of its semi-supervised learning methods. The DBN has a two stage learning process: unsupervised learning followed by supervised learning. In the first stage, it evaluates weights and biases between visible and hidden layers using an unsupervised pre-training of stacked Restricted Boltzmann Machines (RBM). RBMs are stacked between two adjacent layers which are visible-hidden layers or hidden-hidden layers. RBMs are energy-based functions and have only connections between adjacent nodes. Weights and biases between hidden and visible layers are evaluated with the aid of the probability of greedy layer-wise method. At the second stage, pre-training is followed by supervised fine-tuning with weighted neurons and biases to improve parameters.

The DBN can be defined as a specialized model with many hidden layers of DL. The upper layers of the DBN may hold more detailed and descriptive features to identify the solution of diagnosing systems, whereas lower layers may not. The DBN has more important advantages than the classical neural networks such as achieving high performance with a small number of training sets, and having the ability of utilizing the connections between the features in deeper processes. In the supervised learning phase, weights and biases are updated using fine-tuning in which the gradient descent or ascent algorithms are used for improving the accuracies and sensitivities of models [51], [52]. The DBN is a probabilistic joint distribution of input vector x and the ℓ hidden layers as follows:

$$P(x, h^1, \dots, h^\ell) = \left(\prod_{k=0}^{\ell-2} P(h^k | h^{k+1}) \right) P(h^{\ell-1}, h^\ell) \quad (4)$$

$P(h^{\ell-1}, h^\ell)$ is the probability of conditional distribution between the adjacent layers and h^0 is the input vector.

The energy function of the state (h^{k-1}, h^k) is defined as:

$$E(h^{k-1}, h^k; \theta) = - \sum_{s=1}^{D_{k-1}} \sum_{t=1}^{D_k} w_{st}^k h_s^{k-1} h_t^k - \sum_{s=1}^{D_{k-1}} b_s h_s^{k-1} - \sum_{t=1}^{D_k} c_t h_t^k \quad (5)$$

where $\theta = (w_{st}, b, c)$ which are the parameters of the DBN; w_{st}^k is the weight between s^{th} neuron in the layer h^{k-1} and t^{th} neuron in the layer h^k ; b_s is the s^{th} bias of layer h^{k-1} and c_t is the t^{th} bias of layer h^k . D_k is the number of neurons in the k^{th} layer. The probabilistic distribution of the energy function is:

$$P(h^{k-1}; \theta) = \frac{\sum_{h^k} \exp(-E(h^{k-1}, h^k; \theta))}{\sum_{h^{k-1}} \sum_{h^k} \exp(-E(h^{k-1}, h^k; \theta))} \quad (6)$$

After layer-wise unsupervised learning, calculated weights are refined using supervised learning based on gradient descent. This fine-tuning process updates w parameters for a better discriminative ability and for obtaining higher classification performances [53].

Accuracy (ACC), Specificity (SPE) and Sensitivity (SEN) are used to evaluate the performance of medical diagnosis systems. Calculation of these performance measurements are described in [22], [54].

28. RESULTS

Various biomedical signals and clinical characteristics are analyzed with lots of digital signal processing methods and data mining algorithms in medical diagnosis systems. Computer-based diagnosis systems may have support decision systems for improving clinicians' performance and classification performance. Computer-based diagnosis systems can also be enhanced using biomedical signal processing methods and can be utilized as an alternative or additional method to the clinical

characteristics of the subjects. In this study, the ECG is used to diagnose the subjects with or without CAD. The DBN structure of the proposed diagnosis system is seen in Fig.1.

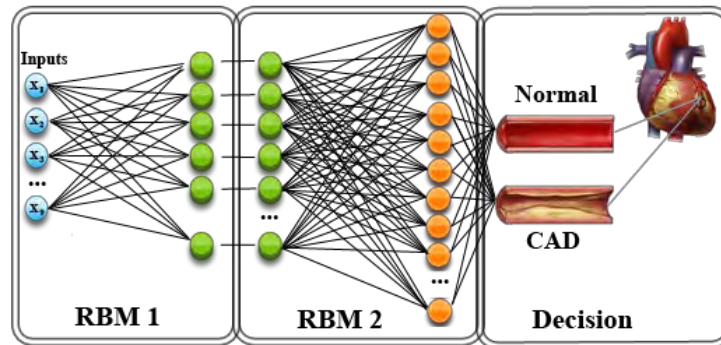


Figure 1. Structure of the DBN Classifier to diagnose CAD

Long-term ECGs may have much more noise than the short-term ECGs. Physical conditions such as coughing, changing the standing position, instantaneous movements and recording conditions such as dislocation of the probe, etc. can handle noise in the long-term ECGs. The short-term ECG is less affected by these kinds of conditions. The short-term ECGs usually have an ability to represent the long-term ECG characteristics in most cardiac diseases. 15 second short-term ECGs were segmented from 85 long-term ECGs using the moving window analysis technique 100 times. The number of instances was increased to 8500 ECGs.

EMD was applied to each short-term ECG and the IMFs ranging in number from 10 to 14 were extracted for 8500 ECGs. Obtained IMFs can be seen in Fig.2. HT was applied to each IMF and the instantaneous frequencies spectral features were computed. HT allows deriving the analytic representation of a signal and includes phase features.

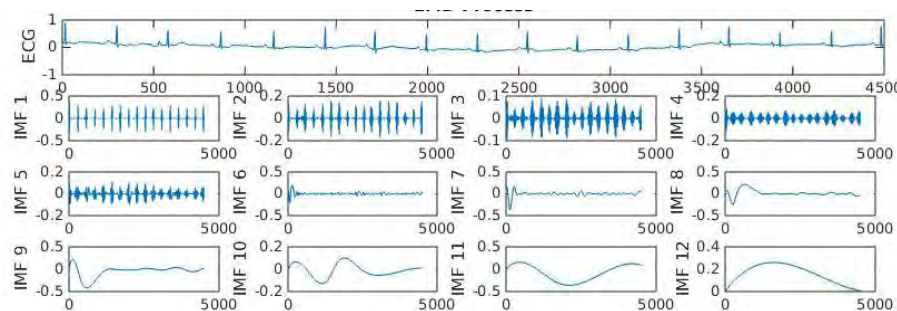


Figure 2. A randomly selected Short-term ECG and Extracted IMFs by applying EMD

HHT is used for feature extraction using the Hilbert Spectral Analysis in most of the studies. In this study, the IMFs that were extracted after the HHT process were used as the base of the features, but not directly used as the features. Statistical features (minimum (Min), maximum (Max), skewness (Skw), median, mean, Standard Deviation (SD), correlation (Corr), mode and energy) were calculated from each IMF for creating the diagnosis dataset. Each short-term ECG had a number of 9 statistical features multiplied by the number of the extracted IMF. The MATLAB statistical toolbox is used for calculation of statistical features. As seen in Table 1, the highest five responsible features in the diagnosis of the CAD are Max and Min of the 3rd IMF, Max and Corr of the 4th IMF and Min of the 5th IMF. The lowest responsible features are mode values of IMFs.

Table 2. Performance of each statistical feature for reduced the short-term ECG in diagnosis of the CAD

	Max	Min	Corr	Energy	Mean	SD	Skw	Median	Mode	All
SEN	85.05	80.98	78.72	60.67	52.70	57.10	43.50	39.77	21.05	96.02
SPE	92.56	81.40	62.52	78.52	73.20	30.24	22.52	5.36	28.00	98.88
ACC	87.26	81.11	73.95	65.92	58.73	49.20	37.33	29.65	23.09	98.05

The system was tested using a 10-fold cross validation. The dataset was randomly divided into 10 folds with the same number of subjects with and without the CAD. 9-folds of dataset were used for the training of the DBN classifier and one fold was used for testing the DBN. We subdivided the 9-folds of the dataset into 100 batches to speed-up and update weights step by step on the learning phase. The DBN that was utilized in the proposed diagnosis model has one input layer, 2 hidden layers and one output layer (Fig.1). The input layer has 9 input units for statistical features. Greedy layer-wise pre-training is used in this model at the unsupervised learning stage of the DBN with 5 epochs. The DBN has 2 hidden layers with 100 hidden units for each. All feature sets were normalized to 0-1. The output layer has two outputs (subjects with and without CAD). To unfold the DBN to a neural network for the supervised learning stage of DBN, model parameters were selected by iterations. The learning rate is 2 and the

activation function of the hidden layers on the supervised learning phase is the hyperbolic tangent function to avoid bias in the gradients and to have a stronger gradient. And a sigmoid output function was utilized. After training the DBN, test results were performed and the reliability and statistical performances of the model were calculated.

Table 2. Comparison of the models on diagnosis of the CAD

Authors	ACC	SPE	SEN	Method	Classification	Data
Lee et. al [21]	85.00-90.00	-	-	HRV measurements	SVM	HRV
Dua et. al. [20]	89.50	-	-	HRV measurements	ANN	HRV
Kim et. al. [22]	75.00	-	-	HRV measurements	MDA	HRV
Giri et. al. [28]	96.80	93.70	100.00	DWT, LDA, PCA	GMM	HRV
Patidar et. al. [29]	99.70	99.80	99.60	Co-entropy, PCA	SVM	HRV
Arafat et. al. [24]	86.00	-	-	ST measures	Fuzzy Clustering	ECG
Alizadensani et. al. [25]	94.08	-	-	Q wave and ST measures	SVM	ECG
This study	98.05	98.88	96.02	HHT, Statistical Features	DBN	ECG

*MDA: Multiple Discriminant Analysis, SVM: Support Vector Machines, ANN: Artificial Neural Network, LDA: Linear Discriminant Analysis, GMM: Gaussian Mixture Model, HRV: Heart Rate Variability

As it is seen in Table 2, when we compared the classification performances in literature, high accuracy rates were achieved using various classification methods on both ECG and HRV data. The highest classification performance on ECG data is achieved using the DBN on ECG based features. The achieved performance measurements that are achieved using the proposed method have a remarkable point in both HRV and ECG studies. Subjects with and without CAD were separated with a classification accuracy rate of 98.05%, a specificity of 98.88% and a sensitivity of 96.02% using statistical features from IMFs.

29. CONCLUSIONS

Linear and non-linear HRV features, various analysis techniques on ECG, heart sounds and clinical characteristics were used to evaluate the diagnosis of the CAD. Different classification methods were utilized on these features to achieve high classification performances. In this study, the HHT that is used widely on non-linear signals was used to extract features from filtered ECGs. The proposed system diagnoses the subjects with or without the CAD. In this integrated system, DBN was used to classify the statistical features of IMFs. Accuracy, specificity and sensitivity achievements were used to evaluate system performance.

HRV includes the Poincare plots, cross Corr, SD, arithmetic mean, Skw, kurtosis, and approximate entropy measurements between R waves which are extracted from 5 min short-term ECGs. Using HRV does not take into consideration the durations and intervals of the other waves except R waves on the ECGs. In this study, the ECG was used considering that all waves (whole ECG) may carry significant characteristics in the diagnosis of the CAD. As seen in Table 1, an accuracy rate of 98.05%, a specificity rate of 98.88% and a sensitivity rate of 96.02% were achieved in the diagnosis of the CAD. It is difficult to compare the classification accuracies with the literature, because of different databases. Achieved performances show that the proposed method has an ability to separate the subjects with and without the CAD. Thus, the highest accuracy is achieved in the studies using ECG signals and most of the studies using HRV. The biggest advantage of the proposed method compared to HRV is using 15 second short-term ECG segments.

References

- [1] M. Gabriel Khan, *Rapid ECG Interpretation(Contemporary Cardiology)*, 3rd edition. Humana Press, 2007.
- [2] U. F. Chan, W. W. Chan, S. H. Pun, M. I. Vai, and P. U. Mak, "Flexible implementation of front-end bioelectric signal amplifier using fpa for telemedicine system," in *Annual International Conference of the IEEE Engineering in Medicine and Biology - Proceedings*, 2007, pp. 3721–3724.
- [3] Y. Özbay and G. Tezel, "A new method for classification of ECG arrhythmias using neural network with adaptive activation function," *Digit. Signal Process.*, vol. 20, no. 4, pp. 1040–1049, 2010.
- [4] "CAD Information." [Online]. Available: <http://www.nhlbi.nih.gov/health/health->. [Accessed: 01-Jan-2016].
- [5] G. K. Hansson, "Inflammation, atherosclerosis, and coronary artery disease," *N. Engl. J. Med.*, vol. 352, no. 16, pp. 1685–1695, 2005.
- [6] K. Polat and S. Güneş, "A hybrid approach to medical decision support systems: Combining feature selection, fuzzy weighted pre-processing and AIRS," *Comput. Methods Programs Biomed.*, vol. 88, no. 2, pp. 164–174, 2007.
- [7] R. Yilmaz and R. Demirbag, "P-wave dispersion in patients with stable coronary artery disease and its relationship with severity of the

- disease,” *J. Electrocardiol.*, vol. 38, no. 3, pp. 279–284, 2005.
- [8] İ. Babaoglu, O. Findik, and E. Ülker, “A comparison of feature selection models utilizing binary particle swarm optimization and genetic algorithm in determining coronary artery disease using support vector machine,” *Expert Syst. Appl.*, vol. 37, no. 4, pp. 3177–3183, 2010.
 - [9] Y. N. Devi and S. Anto, “An Evolutionary-Fuzzy Expert System for the Diagnosis of Coronary Artery Disease,” *An Evol. Fuzzy Expert Syst. Diagnosis Coron. Artery Dis.*, vol. 3, no. 4, pp. 1478–1484, 2014.
 - [10] M. G. Tsipouras, T. P. Exarchos, D. I. Fotiadis, A. P. Kotsia, K. V. Vakalis, K. K. Naka, and L. K. Michalis, “Automated Diagnosis of Coronary Artery Disease Based on Data Mining and Fuzzy Modeling,” *IEEE Trans. Inf. Technol. Biomed.*, vol. 12, no. 4, pp. 447–458, 2008.
 - [11] Noor Akhmad Setiawan, P. A. Venkatachalam, and Ahmad Fadzil M. Hani, “Diagnosis of coronary artery disease using artificial intelligence based decision support system,” *Proc. Int. Conf. Man-Machine Syst.*, 2009.
 - [12] N. Ghadiri Hedeshi and M. Saniee Abadeh, “Coronary artery disease detection using a fuzzy-boosting PSO approach,” *Comput. Intell. Neurosci.*, vol. 2014, 2014.
 - [13] M. C. Colak, C. Colak, H. Kocatürk, S. Sağıroğlu, and I. Barutçu, “Predicting coronary artery disease using different artificial neural network models,” *Anadolu Kardiyol. Derg.*, vol. 8, no. 4, pp. 249–254, 2008.
 - [14] A. Rajkumar and M. G. S. Reena, “Diagnosis Of Heart Disease Using Datamining Algorithm,” *Glob. J. Comput. Sci. Technol.*, vol. 10, no. 10, pp. 38–43, 2010.
 - [15] N. Lavesson, A. Halling, and M. Freitag, “Classifying the Severity of an Acute Coronary Syndrome by Mining Patient Data,” *26th Annu. Work. Swedish Artif. Intell. Soc.*, vol. 35, pp. 55–63, 2009.
 - [16] M. Shouman, T. Turner, and R. Stocker, “Using data mining techniques in heart disease diagnosis and treatment,” *Japan-Egypt Conf. Electron. Commun. Comput.*, pp. 173–177, 2012.
 - [17] M. Akay, W. Welkowitz, J. L. Semmlow, and J. Kostis, “Application of the ARMA method to acoustic detection of coronary artery disease,” *Med. Biol. Eng. Comput.*, vol. 29, no. 4, pp. 365–372, 1991.
 - [18] U. R. Acharya, O. Faust, V. Sree, G. Swapna, R. J. Martis, N. A. Kadri, and J. S. Suri, “Linear and nonlinear analysis of normal and CAD-affected heart rate signals,” *Comput. Methods Programs Biomed.*, vol. 113, no. 1, pp. 55–68, 2014.
 - [19] H. G. Lee, K. Y. Noh, and K. H. Ryu, “Mining biosignal data: Coronary artery disease diagnosis using linear and nonlinear features of HRV,” in *Lecture Notes in Computer Science (including subseries Lecture Notes in Artificial Intelligence and Lecture Notes in Bioinformatics)*, 2007, vol. 4819 LNAI, pp. 218–228.
 - [20] S. Dua, X. Du, S. Vinitha Sree, and V. I. Thajudin Ahamed, “Novel classification of coronary artery disease using heart rate variability analysis,” *J. Mech. Med. Biol.*, vol. 12, no. 4, p. 1240017, 2012.
 - [21] H. G. L. H. G. Lee, K. Y. N. K. Y. Noh, and K. H. R. K. H. Ryu, “A Data Mining Approach for Coronary Heart Disease Prediction using HRV Features and Carotid Arterial Wall Thickness,” *2008 Int. Conf. Biomed. Eng. Informatics*, vol. 1, 2008.
 - [22] H. C. W. Kim, S. Jin, Y. Park, “A study on development of multi-parametric measure of heart rate variability diagnosing cardiovascular disease,” *IFMBE Proc. 14*, pp. 3480–3483, 2007.
 - [23] M. Karimi, R. Amirfattahi, S. Sadri, and S. A. Marvasti, “Noninvasive detection and classification of coronary artery occlusions using wavelet analysis of heart sounds with neural networks,” in *Medical Applications of Signal Processing, 2005. The 3rd IEE International Seminar on (Ref. No. 2005-1119)*, 2005, pp. 117–120.
 - [24] S. Arafat, M. Dohrmann, and M. Skubic, “Classification of Coronary Artery Disease Stress ECGs using Uncertainty Modeling,” in *2005 ICSC Congress on Computational Intelligence Methods and Applications*, 2005, pp. 1–4.
 - [25] R. Alizadehsani, J. Habibi, M. J. Hosseini, H. Mashayekhi, R. Boghrati, A. Ghandeharioun, B. Bahadorian, and Z. A. Sani, “A data mining approach for diagnosis of coronary artery disease,” *Comput. Methods Programs Biomed.*, vol. 111, no. 1, pp. 52–61, 2013.
 - [26] Z. Zhao and C. Ma, “An Intelligent System for Noninvasive Diagnosis of Coronary Artery Disease with EMD-TEO and BP Neural Network,” in *2008 International Workshop on Education Technology and Training & 2008 International Workshop on Geoscience and Remote Sensing*, 2008, pp. 631–635.
 - [27] U. R. Acharya, S. V. Sree, M. Muthu Rama Krishnan, N. Krishnananda, S. Ranjan, P. Umesh, and J. S. Suri, “Automated classification of patients with coronary artery disease using grayscale features from left ventricle echocardiographic images,” *Comput. Methods Programs Biomed.*, vol. 112, no. 3, pp. 624–632, 2013.
 - [28] D. Giri, U. Rajendra Acharya, R. J. Martis, S. Vinitha Sree, T. C. Lim, T. Ahamed, and J. S. Suri, “Automated diagnosis of Coronary Artery Disease affected patients using LDA, PCA, ICA and Discrete Wavelet Transform,” *Knowledge-Based Syst.*, vol. 37, pp. 274–282, 2013.
 - [29] S. Patidar, R. B. Pachori, and U. Rajendra Acharya, “Automated diagnosis of coronary artery disease using tunable-Q wavelet transform applied on heart rate signals,” *Knowledge-Based Syst.*, vol. 82, pp. 1–10, 2015.
 - [30] N. E. Huang, Z. Shen, S. R. Long, M. C. Wu, H. H. Shih, Q. Zheng, N.-C. Yen, C. C. Tung, and H. H. Liu, “The empirical mode decomposition and the Hilbert spectrum for nonlinear and non-stationary time series analysis,” *Proc. R. Soc. A Math. Phys. Eng. Sci.*, vol. 454, no. 1971, pp. 903–995, 1998.
 - [31] U. Maji, M. Mitra, and S. Pal, “Automatic Detection of Atrial Fibrillation Using Empirical Mode Decomposition and Statistical Approach,”

- Procedia Technol.*, vol. 10, pp. 45–52, 2013.
- [32] G. Altan, A. Yayik, Y. Kutlu, S. Yildirim, and E. Yildirim, “Analyse of Congestive Heart Failure Using Hilbert- Huang Transform,” *Dokuz Eylul Univ. Eng. Sci.*, vol. 16, pp. 94–103, 2014.
- [33] G. Hinton, L. Deng, D. Yu, G. Dahl, A. Mohamed, N. Jaitly, V. Vanhoucke, P. Nguyen, T. Sainath, and B. Kingsbury, “Deep Neural Networks for Acoustic Modeling in Speech Recognition,” *IEEE Signal Process. Mag.*, vol. 29, no. 6, pp. 82–97, 2012.
- [34] S. M. Siniscalchi, D. Yu, L. Deng, and C. H. Lee, “Exploiting deep neural networks for detection-based speech recognition,” *Neurocomputing*, vol. 106, pp. 148–157, 2013.
- [35] C. Farabet, C. Couprie, L. Najman, and Y. Lecun, “Learning hierarchical features for scene labeling,” *IEEE Trans. Pattern Anal. Mach. Intell.*, vol. 35, no. 8, pp. 1915–1929, 2013.
- [36] P. Sermanet, K. Kavukcuoglu, S. Chintala, and Y. Lecun, “Pedestrian detection with unsupervised multi-stage feature learning,” in *Proceedings of the IEEE Computer Society Conference on Computer Vision and Pattern Recognition*, 2013, pp. 3626–3633.
- [37] Q. Le and T. Mikolov, “Distributed Representations of Sentences and Documents,” *Int. Conf. Mach. Learn. - ICML 2014*, vol. 32, pp. 1188–1196, 2014.
- [38] I. Sutskever, O. Vinyals, and Q. Le, “Sequence to sequence learning with neural networks,” *Adv. Neural Inf. ...*, p. 9, 2014.
- [39] H. Lee, R. Grosse, R. Ranganath, and A. Y. Ng, “Convolutional deep belief networks for scalable unsupervised learning of hierarchical representations,” *Proc. 26th Annu. Int. Conf. Mach. Learn. ICML 09*, vol. 2008, pp. 1–8, 2009.
- [40] P. W. Mirowski, Y. LeCun, D. Madhavan, and R. Kuzniecky, “Comparing SVM and convolutional networks for epileptic seizure prediction from intracranial EEG,” in *Proceedings of the 2008 IEEE Workshop on Machine Learning for Signal Processing, MLSP 2008*, 2008, pp. 244–249.
- [41] P. W. Mirowski, D. Madhavan, and Y. Lecun, “Time-delay neural networks and independent component analysis for eeg-based prediction of epileptic seizures propagation,” in *Advancement of Artificial Intelligence Conference*, 2007, pp. 1892–1893.
- [42] D. Wang and Y. Shang, “Modeling Physiological Data with Deep Belief Networks,” *Int. J. Inf. Educ. Technol.*, vol. 3, no. 5, pp. 505–511, 2013.
- [43] P. Drotár, J. Gazda, and Z. Smékal, “An experimental comparison of feature selection methods on two-class biomedical datasets,” *Comput. Biol. Med.*, vol. 66, pp. 1–10, 2015.
- [44] P. Tamilselvan and P. Wang, “Failure diagnosis using deep belief learning based health state classification,” *Reliab. Eng. Syst. Saf.*, vol. 115, pp. 124–135, 2013.
- [45] E. de la Rosa and W. Yu, “Randomized algorithms for nonlinear system identification with deep learning modification,” *Inf. Sci. (Ny)*, p. -, 2015.
- [46] M. Långkvist, L. Karlsson, and A. Loutfi, “A review of unsupervised feature learning and deep learning for time-series modeling,” *Pattern Recognit. Lett.*, vol. 42, no. 1, pp. 11–24, 2014.
- [47] Y. Bengio and O. Delalleau, “Justifying and generalizing contrastive divergence,” *Neural Comput.*, vol. 21, no. 6, pp. 1601–1621, 2009.
- [48] G. Hinton, G. Hinton, T. Sejnowski, and T. Sejnowski, *Learning and relearning in Boltzmann machines*, vol. 1. 1986.
- [49] A. L. Goldberger, L. A. N. Amaral, L. Glass, J. M. Hausdorff, P. C. Ivanov, R. G. Mark, J. E. Mietus, G. B. Moody, C.-K. Peng, and H. Stanley, “PhysioBank, PhysioToolkit, and PhysioNet: Components of a New Research Resource for Complex Physiologic Signals,” *Circulation*, vol. 101, pp. 215–220, 2000.
- [50] N. E. Huang, Z. Shen, S. R. Long, M. C. Wu, H. H. Shih, Q. Zheng, N.-C. Yen, C. C. Tung, and H. H. Liu, “The empirical mode decomposition and the Hilbert spectrum for nonlinear and non-stationary time series analysis,” *Proceedings of the Royal Society A: Mathematical, Physical and Engineering Sciences*, vol. 454, no. 1971, pp. 903–995, 1998.
- [51] G. E. Hinton, S. Osindero, and Y.-W. Teh, “A fast learning algorithm for deep belief nets,” *Neural Comput.*, vol. 18, no. 7, pp. 1527–54, 2006.
- [52] Y. Bengio, P. Lamblin, D. Popovici, and H. Larochelle, “Greedy Layer-Wise Training of Deep Networks,” *Adv. Neural Inf. Process. Syst.*, vol. 19, no. 1, p. 153, 2007.
- [53] Y. Liu, S. Zhou, and Q. Chen, “Discriminative deep belief networks for visual data classification,” *Pattern Recognit.*, vol. 44, no. 10–11, pp. 2287–2296, 2011.
- [54] R. O. Duda, P. E. Hart, and D. G. Stork, *Pattern Classification*. 2000.

Design and Implementation of a Simple, AES-Based Secure Messaging Platform

Resul Daş¹³, Gurkan Tuna¹⁴

Abstract

Cryptography can be defined as a set of mathematical methods that works for providing information security, especially in terms of privacy and data integrity. Cryptographic methods aim to protect the information and also along with it - the sender and receiver of the information- from active or passive attacks during the transmission of information. In other words, cryptography consists of all of techniques used to convert the readable information into the condition that cannot be read by the unwanted parties. In this study, a multi-language messaging platform consisting of a web interface and a software application is proposed to enable secure communication between the sender and the receiver within an institution. Since the proposed platform is based on Advanced Encryption Standard (AES) in its web interface, it provides security required for messaging-based communication. For internal communication within an institution, the proposed platform is an alternative to popular e-mail services.

Keywords: Security threats, information security, cryptology, Advanced Encryption Standard (AES).

30. INTRODUCTION

Information systems can be defined as a set of interrelated elements that work together in order to gather information for planning, control, analysis and decision-making with the aim of preservation and spread. The function of the information system is to collect data and information for planning, control and decision support, and to record, convert and spread them.

Nowadays, the Internet is one of the key elements of the relationship between information systems and business processes. For most businesses, most of the communication occurs by e-mail. Although e-mail is necessary for business, it is associated with a number of severe threats including spam, viruses, data theft, and hacking. Since the Internet provides an insecure channel for exchanging sensitive information and leads to a high risk of intrusion and fraud [1-4], different approaches and methods to establish rules and measures against cyber security attacks over the Internet have been proposed to protect the transfer of information.

As it is known, common methods of e-mail delivery over public networks such as the Internet are vulnerable to a number of information security risks. In [5], a trusted mail gateway is proposed to provide reliable, trusted end-to-end e-mail delivery. The proposed mail gateway provides the basic security services such as confidentiality, integrity, non-repudiation, origin authentication and availability for e-mails delivered through the Internet. Zhang *et al.* in [6] propose a secure e-mail system which is based on elliptic curve cryptography combined public key algorithm. Compared to existing well-known secure e-mail protocols such as PGP and S/MIME, the proposed approach does not need the third on-line certificate agent and demands less key storage space and low processing and memory requirements. For users who prefer commonly-used methods and protocols for e-mail security, there exist a number of alternatives including OpenPGP, S/MIME, SSL and TLS [7].

¹³ Corresponding author: Department of Software Engineering, Technology Faculty, Firat University, Elazığ, Turkey, resuldas@gmail.com

¹⁴ Department of Computer Programming, Trakya University, Edirne, Turkey, gurkantuna@trakya.edu.tr

In this paper, a multi-language, secure messaging platform consisting of two complementary components is proposed to address common information security risks encountered during message transfers, and in this way ensure the privacy and integrity of sensitive messages. The remainder of this paper is organized as follows. The details of the proposed platform and its components are explained in Section 2. The paper is concluded in Section 3.

31. PROPOSED SECURE MESSAGING PLATFORM

The proposed platform consists of two components: a web interface, shown in Fig. 1, and a software application, shown in Fig. 2 (a). The platform is web-based, relies on a dynamic and content-rich database system, and both of its components are based on the use of Advanced Encryption Standard (AES) [8, 9]. Cryptanalysis studies in the literature proved that AES is very strong against different kinds of attacks [10, 11].

Since the proposed platform is web-based and has a simple and easy-to-use graphical user interface (GUI). The proposed platform can be accessed through its web-interface, its computational requirements are minimal; hence, it can easily be accessed from smart phones, tablets, tablets, notebooks, as well as personal computers.

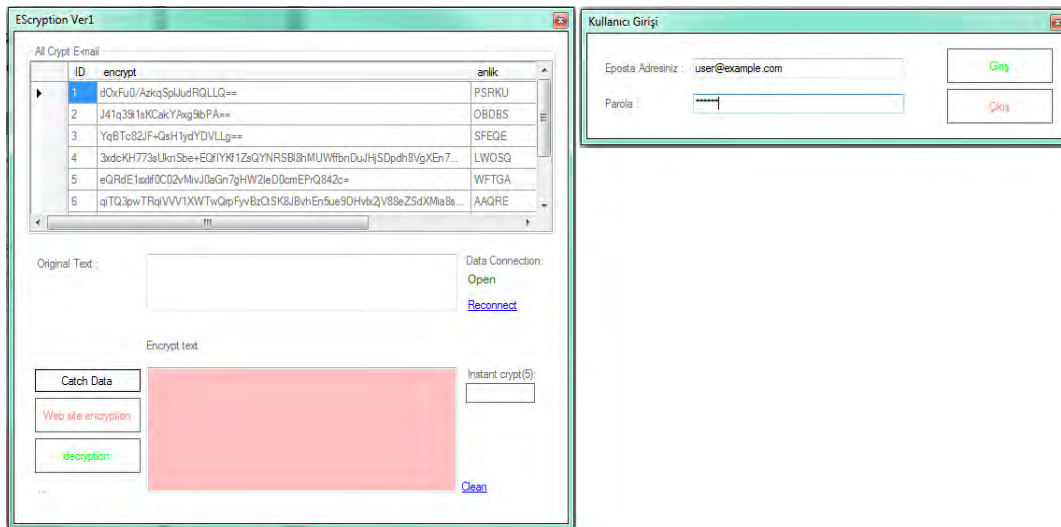
As the proposed platform provides login forms, as shown in Fig. 1 and Fig. 2 (b), to both the web interface and the software application, the security of the proposed platform mainly relies on user authentication as well as the 128-bit encryption provided by the AES. In addition, the proposed platform provides logging ability for analysis. All messages sent/received by the proposed platform and the proposed platform's settings are managed by a relational MySQL database [12] as shown in Fig. 3.

All the messages in the platform are stored in the database in encrypted form. The database is managed by a free administration tool called phpMyAdmin [13]. In the database, Sp_setting table contains site settings such as site e-mail address, theme folder name and admin user name. Sp_mail table contains information about e-mails including topic, e-mail, date of sending, and recipient e-mail. Sp_user table contains the user information such as user name, last name, email address, password, sex and picture. Online, trans and update tables record the log activities and changes made by the user in the system.



Figure 1: Homepage of the proposed application.

Since user authentication is one of principles that the proposed platform relies on, users must first fill user registration form found on the homepage of the web interface. After a user's application is approved by the system administrator, he/she can use the web interface after logging into the platform. When the user is logged in the platform, as shown in Fig. 4, he/she can read his/her messages, send messages to the platform users, and, thanks to the logging ability of the proposed platform, can check his/her activities in the platform. The interface also allows the user to change his/her password. In case the user forgets his/her password, the system administrator can reset the password.



(a) Homepage of the software application

(b) Login form of the software application

Figure 2: Screens of the software application.

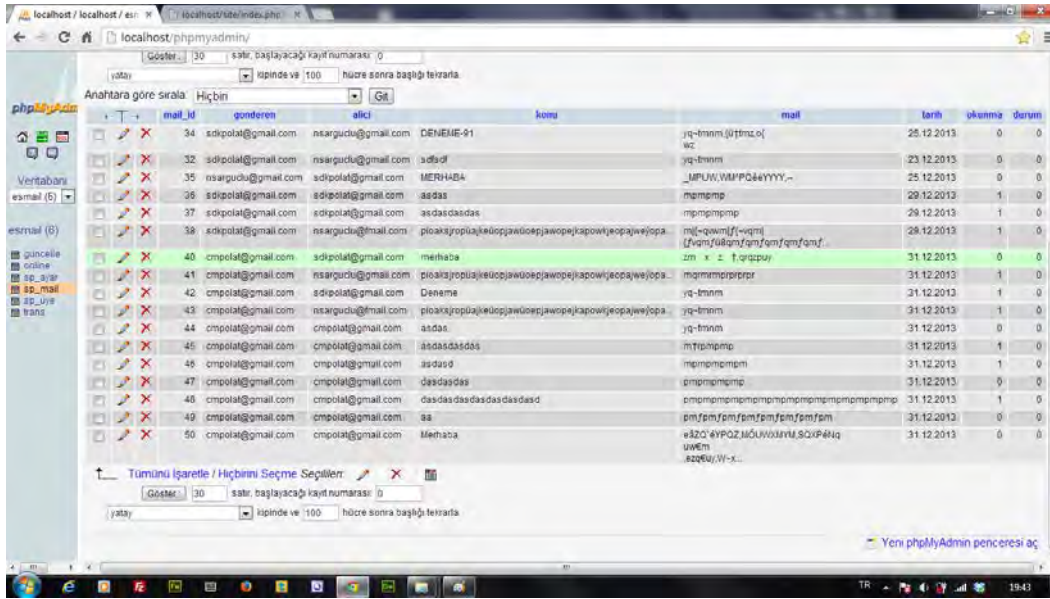


Figure 3: The database that involves e-mails processed by the proposed platform.



Figure 4: Reading an e-mail.

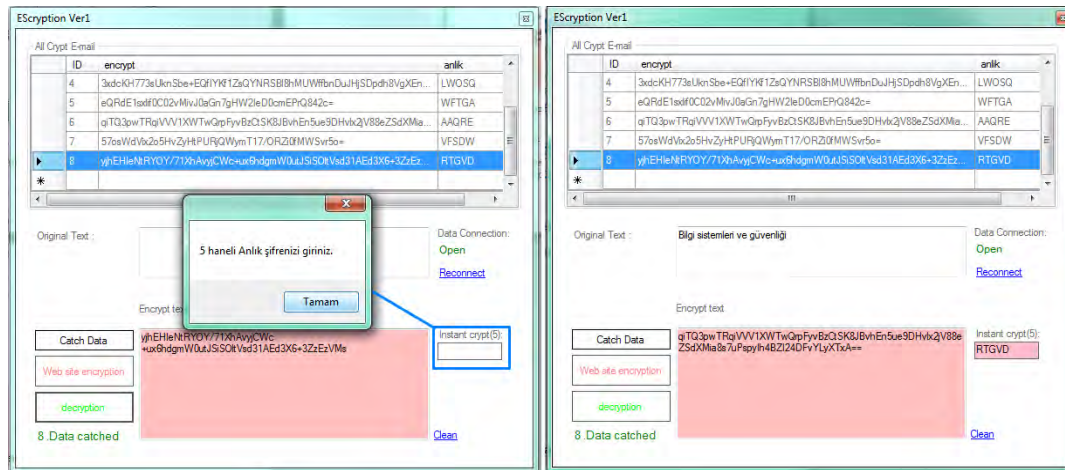
Similar to its web interface, the proposed platform's the other component, its software application, has also an easy-to-use GUI and was designed to be run on personal computers with limited processing capabilities. Using this application, users can decrypt the encrypted messages they receive and then read them. However, different from the web interface, this application does not allow creating users, changing passwords, or sending messages. The abilities of this application are rather limited compared to the web interface.

When the software application is run, its login form appears on the screen. Then the user can enter his/her username and password registered using the web interface and starts using the software application. When the software application's main page appears on the screen, the user can read the messages he/she received after decrypting them. However, before receiving the messages, the user must first start a data connection to the database of the proposed platform.

As shown in Fig. 5 (a), when the user clicks the button called "Catch Data", he/she can receive one of the encrypted messages found in the grid on the screen. To read the message he/she received in original form, after clicking the button called "Decryption", the user must enter a 5-digit code sent by the sender to the Instant crypt (5) textbox as shown in Fig. 5 (b). When the 5-digit code is entered into the textbox,

the user can see the original unencrypted message. If the user clicks the button “Web site encryption”, the web interface of the platform appears on the screen.

To sum up how the proposed platform runs, the sender runs the web interface of the proposed platform and after preparing the original message for the receiver, the original message is encrypted by using AES algorithm and then transmitted to the receiver. The receiver runs the desktop application of the proposed platform and then by logging in, he/she can reach his/her messages in their original unencrypted form decrypted by the AES decryption algorithm.



(a) Warning for the instant 5-digit code

(b) Entering the code and reading the original text.

Figure 5: Homepage of the software application.

32. CONCLUSION

Even though the Internet is an insecure channel for exchanging information and is associated with a variety of information security threats, it is one of the major elements of business processes. As proven in the literature and practice, common methods of e-mail delivery over the Internet are highly vulnerable to a number of significant information security risks. Hence, mechanisms are needed to protect the transfer of sensitive information in terms of integrity, confidentiality, and availability. Although some protocols such as OpenPGP, S/MIME, SSL and TLS provide the security needed for e-mail transfers, they cannot be used alone and therefore need to be integrated into applications.

In this paper, to address potential information security risks encountered during message transfers, a platform consisting of a web interface and its complementary software application is proposed. Supported by well-known Advanced Encryption Standard, the proposed platform provides required information security; hence, it is an alternative platform for e-mail-based secure communication.

REFERENCES

- [65]. M. Bloch, J. Barros, M. R. D. Rodrigues, and S. W. McLaughlin, “Wireless Information-Theoretic Security,” IEEE Transactions on Information Theory, vol. 54, no. 6, pp. 2515-2534, 2008.
- [66]. C. K. Wong, M. Gouda, and S. S. Lam, “Secure group communications using key graphs,” IEEE/ACM Trans. Network, vol. 8, no. 1, pp. 16-30, 2000.
- [67]. H. Yang, H. Luo, F. Ye, S. Lu, and L. Zhang, “Security in mobile ad hoc networks: challenges and solutions,” IEEE Wireless Communications, vol. 11, no. 1, pp. 38-47, 2004.

- [68]. D. Dzung, M. Naedele, T. P. Von Hoff, and M. Crevatin, "Security for industrial communication systems," Proceedings of the IEEE, pp. 1152-1177, 2005.
- [69]. E.S. Ayla, A. Özgit, "An Architecture For End-To-End and Inter-Domain Trusted Mail Delivery Service", "Proceedings of ISCN'06 7th International Symposium on Computer Networks", (2006), p.220-225.
- [70]. Y. Zhang, T. Cui, H. Tang, "A New Secure E-mail Scheme Based on Elliptic Curve Cryptography Combined Public Key", IFIP International Conference on Network and Parallel Computing, 2008 (NPC 2008), 18-21 Oct. 2008, Shanghai, 336 - 340
- [71]. M. Baykara, R. Daş, "A Steganography Application for Secure Data Communication", 10th International Conference on Electronics, Computer and Computation (ICECCO 2013), Turgut Özal University, pp.309-313, 7-9 November 2013, Ankara.
- [72]. J. Daemen, V.R. Vincent, "AES Proposal: Rijndael," <http://csrc.nist.gov/archive/aes/rijndael/Rijndael-ammended.pdf> [Accessed 11 May 2015]
- [73]. S. Murphy, "The Advanced Encryption Standard (AES)," Information Security Technical Report, vol. 4, no. 4, pp. 12-17, 1999.
- [74]. A. Biryukov and D. Khovratovich, "Related-Key Cryptanalysis of the Full AES-192 and AES-256," Lecture Notes in Computer Science, vol. 5912, pp. 1-8, 2009.
- [75]. A. Bogdanov, D. Khovratovich, and C. Rechberger, "Biclique Cryptanalysis of the Full AES," Lecture Notes in Computer Science, vol. 7073, pp. 344-371, 2011.
- [76]. *Internet*: <https://www.mysql.com> , [Accessed March 2016].
- [77]. *Internet*: <https://www.phpmyadmin.net> , [Accessed March 2016].

Stress Changes in Gediz Graben (Western Anatolia)

Ayça Çirmik¹⁵, Oya Pamukçu¹

Abstract

Western Anatolia is one of the most seismically active and rapidly extending regions in the world and is currently experiencing an approximately N–S continental extension since at least Miocene time. In this study the stress changes on best known graben of Western Anatolia, namely Gediz graben, was investigated. Therefore, northern normal fault of Gediz Graben was examined for calculating static displacements (at GNSS stations), strains, and stresses at any depth caused by fault slip by using Coulomb 3.3 graphic-rich stress change software. As the first step, the GNSS data were processed relative to the stations which were located on opposite sides of the fault by GAMIT/GLOBK (GG) software. Secondly, by taking into account the GNSS velocities which were obtained by GG and by using the fault and elastic parameters of the graben, the faults were modeled by Coulomb 3.3 software. Then the coulomb stress changes were calculated for different depths by using the best fitting fault parameters. At the last step, the coulomb stress changes were compared with the occurred earthquakes between the years 1970 and 2014. Consequently, the occurred earthquakes were found as coherent with the coulomb stress change regions.

Keywords: Gediz Graben, GNSS, stress changes, Western Anatolia.

33. INTRODUCTION

Gediz graben is one of the principal active structures of Western Anatolia, which is one of the most seismically active and rapidly extending regions of the world ([1], [2]). In this study, Coulomb stress change method was used to resolve stress changes on Gediz Graben. In this scope, for calculating static displacements, strains, and stresses at any depth caused by fault slip, Coulomb 3.3 software ([3], [4]) was used. In this software, the calculations are performed in an elastic half space with uniform isotropic elastic properties ([5]). The Coulomb stress change which is on a specified fault depends on the fault geometry and sense of slip, and the coefficient of friction but it is independent of regional stress ([6]).

In this study, GNSS Stations of “Multi-Disciplinary Earthquake Researches in High Risk Regions of Turkey Representing Different Tectonic Regimes” (TURDEP) Project, namely; AKHT (Akhisar, Manisa), BORT (Borlu, Manisa), CALT (Çal, Denizli), ESMT (Eşme, Uşak), TRGT (Turgutlu, Manisa) and “Continuously Operating Reference Stations-Turkey” (CORS-TR) Project namely, SALH (Salihli, Manisa) were used processed together by using GAMIT/GLOBK ([7], [8]) software for the days between 180th – 195th (as Julian days) of 2009-2010-2011 years. According to locations of the GNSS stations, Northern normal fault of Gediz Graben was modeled. In GNSS

¹⁵ Dokuz Eylul University, Engineering Faculty, Department of Geophysical Engineering, 35160, Buca/Izmir, Turkey.

Corresponding author: ayca.yurdakul@deu.edu.tr.

processing, the solutions were done relative to the stations which were located on opposite sides of the fault. It means that when calculating the velocity of the stations which were located at one side, the opposite side stations were assumed like as stabile (not moving). Therefore, the effect of the fault on the GNSS stations can be interpreted.

In the second step, Coulomb 3.3 software modeled GNSS velocity vectors for Gediz Graben by using the fault parameters ([9]) and elastic parameters. By taking into account the GNSS velocities which were obtained by GAMIT/ GLOBK software, two types of GNSS velocities (modeled and obtained) were compared and tried to do best fitting between them. In the third step; the coulomb stress changes were calculated by using the best fitting fault parameters, which were determined from the observed and modeled GNSS vectors. Finally as the last step, the coulomb stress changes were compared with the occurred earthquakes between the years 1970 and 2014.

34. COULOMB FAILURE CRITERION

In the Coulomb criterion, when the Coulomb stress σ_f exceeds a specific value, failure consists on a plane is given as;

$$\sigma_f = \tau_\beta - \mu (\sigma_\beta - p) \quad (1)$$

where τ_β is the shear stress on the failure plane, σ_β is the normal stress, p is the pore fluid pressure and μ is the coefficient of friction. The value of τ_β must be positive in this statement. The stress on fault plane get negative or positive value depends on whether the slip of fault is right or left lateral. Therefore, the sign of τ_β must be chosen properly ([6]).

If the failure plane is directed at β to the σ_1 axis, the stress components can be described in the terms of principal stresses,

$$\sigma_\beta = \frac{1}{2}(\sigma_1 + \sigma_3) - \frac{1}{2}(\sigma_1 - \sigma_3) \cos 2\beta \quad (2)$$

$$\tau_\beta = \frac{1}{2}(\sigma_1 - \sigma_3) \sin 2\beta \quad (3)$$

where σ_1 is the biggest, σ_3 is the smallest principal stress. In this way, Equation (1) becomes;

$$\sigma_f = \frac{1}{2}(\sigma_1 - \sigma_3)(\sin 2\beta - \mu \cos 2\beta) - \frac{1}{2}\mu(\sigma_1 + \sigma_3) + \mu p \quad (4)$$

Pore fluid pressure affects the normal stress across the fault plan, as given in equation (1). If the rock stress is changed faster than fluid pressure, p can be related to stress in the rock by a coefficient which calls Skempton's pore pressure parameter, B . The value of B varies between 0 and 1. Therefore, Equation (1) can be simplified by taking account assumptions for pore fluid pressure and Equation (1) becomes;

$$\sigma_f = \tau_\beta - \mu' \sigma_\beta \quad (5)$$

where the coefficient of friction is described by $\mu' = \mu(1-B)$.

If the x and y axes and fault displacements are at horizontal direction, and fault planes are at vertical direction (along z direction), stress on a plane at an angle ψ from the x -axis is given as ([6]),

$$\begin{aligned} \sigma_{11} &= \sigma_{xx} \cos^2 \psi + 2\sigma_{xy} \sin \psi \cos \psi + \sigma_{yy} \sin^2 \psi \\ \sigma_{33} &= \sigma_{xx} \sin^2 \psi + 2\sigma_{xy} \sin \psi \cos \psi + \sigma_{yy} \cos^2 \psi \\ \tau_{13} &= \frac{1}{2} (\sigma_{yy} - \sigma_{xx}) \sin 2\psi + \tau_{xy} \cos 2\psi \end{aligned} \quad (6)$$

35. APPLICATIONS

3.1 Northern Normal Fault of Gediz Graben

For GAMIT/GLOBK processing, the stations; AKHT (Akhisar, Manisa), BORT (Borlu, Manisa), ESMT (Eşme, Usak) and CALT (Çal, Denizli) which were located at north side and TRGT (Turgutlu, Manisa) and SALH (Salihli, Manisa) were located at south side of Northern Normal fault of Gediz Graben were chosen. The GNSS velocities of northern side stations (AKHT, BORT, ESMT, CALT) were calculated relative to Southern stations and GNSS velocities of southern side stations (TRGT and SALH) were calculated relative to Northern stations for the days between 180th and 195th, the years of 2009, 2010 and 2011.

As the second step, in Coulomb 3.3 software Gediz graben was modeled by using elastic parameters and fault parameters given the best fitting between the observed by GAMIT/GLOBK and modeled by Coulomb 3.3 GNSS velocities (Figure 1).

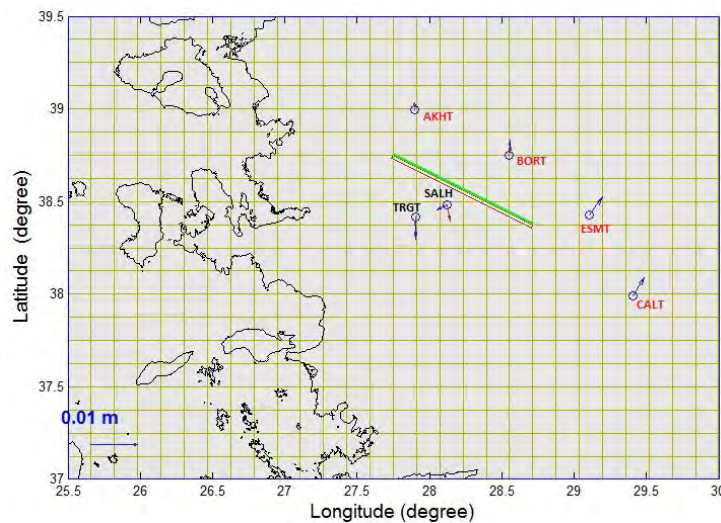


Figure 1. Blue vectors represent the obtained GNSS velocities by GAMIT/GLOBK and red vectors represent modeled GNSS velocities by Coluomb 3.3. Green line defines Northern Normal fault of Gediz Graben.

In the next step, by using the best fitting parameters which obtained from the observed and modeled GNSS vectors, the coulomb stress changes were calculated and plotted for the depth range between 0-4 km and for the depths of 4 km and (Figure 2a, 2c).

As the last step, the coulomb stress change values were compared with the earthquake focus distributions which were obtained from USGS (United States Geological Survey) between the years 1970-2014 occurred up to 7km depth (Figure 2b, 2d).

RESULTS

In Figure 1, it was seen that, the modeled and observed GNSS velocities were fitted at AKHT, BORT and TRGT. But there was not compliance between the velocities for SALH. Additionally, Coulomb software can not model velocities for ESMT and CALT stations due to their far away locations from the fault. According to observed and modeled GNSS velocities it can be said that BORT and TRGT stations were coherent with the N-S directional extension system. However, SALH was not moving properly with this system. It was thought that this case was occurred since its location was near to Northern normal fault as well as Southern normal fault of Gediz Graben. Therefore, it can be said that SALH was affected by both faults (Figure 1).

It was noticed that at depth figures (Figure 2a and 2c) the coulomb stress change values were similar on the stations points. Additionally, the SALH was located on the main stress region caused by the fault because its location was very near to the fault. Besides, this case can be the reason of the inability of the previous step for SALH. As the result of the seismic activity, the non-stabile duration of subsurface structures which were in the stress region can contain air, water, etc. Therefore, it can be seen some problems on modeling of the non-stabile region like as SALH.

For investigating the stress source depth, the coulomb stress changes were calculated for the depths of 4 km ([10]) and for the depth range between 0-4 km (Figure 2 a, 2c). Consequently, it can be said that the stress area has regional effects for the depth range between 0-4 km.

It was noticed that the earthquakes which occurred near the modeled fault are seen on high stress region (red colored areas) and at the NW side of the modeled fault (Figure 2 b, 2d). The earthquakes were coherent with the high stress region at the west and east boundaries of the fault ([11]).

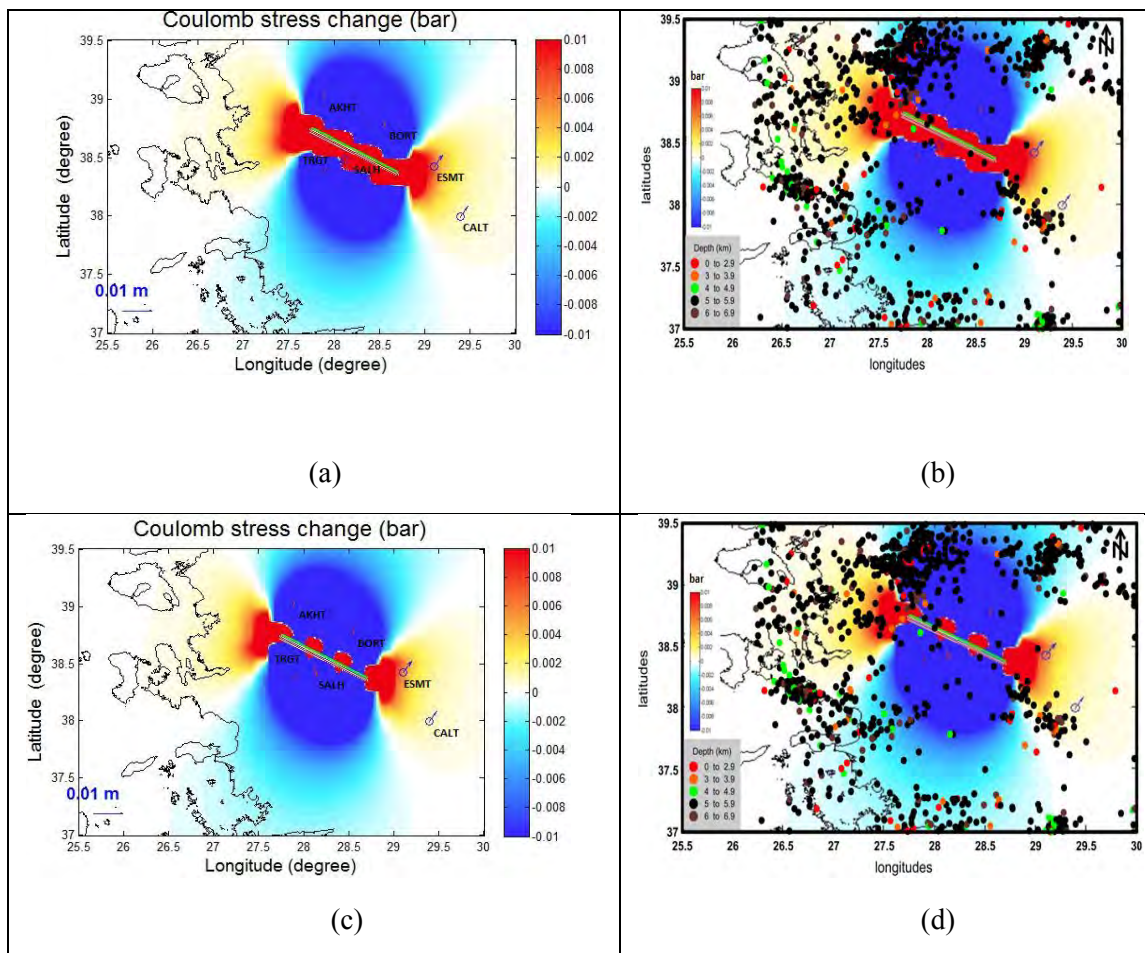


Figure 2 (a) Coulomb stress changes between the depths of 0-4 km. (b) Earthquake focus distributions on the study area. USGS earthquake archive was used between the years 1970-2014. (c) Coulomb stress changes at depth 4 km. (d) Earthquake focus distributions on the study area. USGS earthquake archive was used between the years 1970-2014.

REFERENCES

- [78]. A.M.C. Şengör, N. Görür, and F. Şaroğlu, "Strike-slip faulting and related basin formation in zones of tectonic escape: Turkey as a case study. In: Biddle, K.T., Christie- Blick, N. (eds), Strike-slip Faulting and Basin Formation and Sedimentation," *Society of Economic Paleontologists and Mineralogists Special Publication*, vol. 37, pp. 227–264, 1985.
- [79]. J.A. Jackson and D.P. McKenzie, "Rates of active deformation in the Aegean Sea and surrounding regions," *Basin Research*, vol. 1, pp. 121–128, 1988.
- [80]. S. Toda, R. S. Stein, K. Richards-Dinger and S. Bozkurt, "Forecasting the evolution of seismicity in southern California: Animations built on earthquake stress transfer," *Journal of Geophysical Research*, vol. 110, B05S16, 2005.
- [81]. J. Lin and R.S. Stein, "Stress triggering in thrust and subduction earthquakes and stress interaction between the southern San Andreas and nearby thrust and strike-slip faults," *Journal of Geophysical Research*, vol. 109, B02303, 2004.

- [82]. Y. Okada, "Internal deformation due to shear and tensile faults in a half-space," *Bulletin of the Seismological Society of America*, vol. 82, pp. 1018-1040, 1992.
- [83]. G.C.P. King, R. S. Stein and J. Lin, "Static stress changes and the triggering of earthquakes," *Bulletin of Seismological Society of America*, vol. 84, pp. 935-953, 1994.
- [84]. T. A. Herring, R.W. King and S.C. McClusky, *GAMIT reference manual: GPS analysis at MIT*, Release 10.4: MIT, Cambridge, USA. (2010a).
- [85]. T. A. Herring, R.W. King and S.C. McClusky, *GLOBK global Kalman filter VLBI and GPS analysis program*, Release 10.4: MIT, Cambridge, USA. (2010b).
- [86]. E. Bozkurt and H. Sözbilir, "Tectonic evolution of the Gediz Graben: Field evidence for an episodic, two extension in western Turkey," *Geological Magazine*, vol. 141, pp. 63-79, 2004.
- [87]. O. Pamukçu and A. Yurdakul, "Isostatic compensation in Western Anatolia with estimate of the effective elastic thickness," *Turkish Journal of Earth Science*, vol. 17, pp. 545-557, 2008.
- [88]. A. Çırmık, "Determining the deformations in Western Anatolia with GPS and gravity measurements," Ph.D. Thesis, Dokuz Eylül University, The Graduate School of Natural and Applied Sciences, Izmir, Turkey, 2014.

Latent Heat Thermal Energy Storage Characteristics of Kaolin/Capric Acid Composite as a Building Mass with Phase Change-Energy Storage/Release Ability

Ahmet Sari

Abstract

In recent years, latent heat thermal energy storage (LHTES) by using phase change materials (PCMs) has become an extremely essential subject in energy management applications. One of the LHTES applications is the inserting suitable PCM into a porous building material to decrease the temperature fluctuation inside the building envelopes. In this regard, this paper deals with the preparation, characterization and determination of LHTES properties of kaolin/capric acid (CA) composite as a building mass with energy storage/release ability. The morphology, physical/chemical compatibility, LHTES properties, thermal endurance, thermal conductivity and its effect on the melting times of prepared kaolin/CA composite were investigated by using SEM, FT-IR, DSC, TG and thermal conductivity meter. The leakage test indicated that CA was impregnated maximally into kaolin as 17.5 wt%. The prepared kaolin/CA composite composite PCM had a phase change temperature of 30.71 °C and a latent heat of 27.23 J/g, respectively. The composite PCM had good thermal reliability after repeated 1000 heating-cooling cycling. The heat storage time of the composite PCM was reduced noticeably by introducing expanded graphite (EG; 5 wt%). All the fabricated kaolin/CA had good LHTES function for heating, ventilating and air conditioning (HVAC) in building envelopes.

Keywords: Capric acid, kaolin, thermal energy storage, thermal reliability, thermal durability, thermal conductivity.

Karadeniz Technical University, Department of Metallurgical and Material Engineering, 61080, Trabzon, Turkey; ahmet.sari@ktu.edu.tr

1. INTRODUCTION

Latent heat storage (LHS) using phase change material (PCM) has drawn substantial interest since it makes possible to storage and release high energy at narrow servicing temperature range [1]. This method has been extensively used for heating, ventilating, and air conditioning (HVAC) purposes in buildings to

achieve thermal comfort and acceptable indoor air quality by flattening the fluctuations at indoor temperature [2].

The organic solid-liquid PCMs have high latent heat of fusion and suitable phase change temperature and they are generally non-corrosive, non-toxic, chemically stable and do not show no or a little supercooling (except PCMs in PEG group) behavior [3,4]. However, low thermal conductivity (0.15-0.20 W/mK) has an considerably effect on the rate of energy storage and release.

On the other hand, to get rid of the leakage problem encountered during the phase change of organic PCMs, many researchers have strived about the encapsulation of PCMs using the different methods such as confining into a polymeric network, grafting with polymeric materials and impregnating with porous building materials. Among these methods, the combination of porous materials with PCM is simple, cost-effective and thus relatively proficient way to fabricate form-stable lightweight constructive materials with high LHTES capacity

[5]. In addition to natural clays as porous building materials, such as perlite [6], attapulgite [7], vermiculite [8], bentonite [9], silica-fume [10] and diatomite [11] have been evaluated in the incorporation of several organic PCMs.

As well as the above-mentioned clay materials, kaolin with chemical composition of $\text{Al}_2\text{Si}_2\text{O}_5(\text{OH})_4$ is one of the most common industrial clays. It is generally used in ceramics, toothpaste, light bulbs, cosmetics, water and wastewater treatment. Additionally, low cost (e.g.: its wholesale price is about 0.25 \$/kg in Turkish markets), large surface area, porous structure, abundantly availability, easy handling, direct usability without extra encapsulation and good compatibility with mortar and concrete make it a potential matrix for the fabrication of building PCM composites. Therefore, successful integration of kaolin with organic PCMs for the TES purposes in buildings can expand its industrial usage areas. In this regard, the kaolin/CA composite PCM was prepared, characterized chemically-morphologically and measured its LHTES properties in this work. The chemical and morphological characterization of the fabricated kaolin/CA composite PCM was carried out by using FTIR and SEM techniques. Its LHTES properties before and after thermal cycling test were measured by using DSC technique. Thermal degradation temperatures of the composite PCM were measured by using TG analysis. The thermal degradation temperatures of the composite PCM were also determined by using TG analysis. In addition, the thermal conductivity was increased by addition of expanded graphite (EG) and the reduction occurred in its melting times was confirmed.

2. MATERIALS AND METHODS

2.1. Materials

Kaolin clay used in this work is originated with of Balikesir city of Turkey. The dried sample is mainly consisted of SiO_2 (48 wt%), Al_2O_3 (36.6 wt%), K_2O (2 wt%) and other metal oxides [12]. The selected organic PCM, capric acid (CA), was supplied from Sigma-Aldrich Company. Before the experiments, the kaolin was dried at 105°C in an oven to remove its humidity and then sieved form 200 mesh.

2.2. Methods

Kaolin/CA composites in mass fractions varied from 10 to 30% were prepared using vacuum impregnation method. The highest mass portion of the CA combined with kaolin was determined by performing the leakage test. For this test, the composite was placed on the heater plate and its temperature was settled above the melting point of CA. The heating treatment was continued for 60 min to check the leakage behavior of the PCM melted into pores of the composite. The composite sample that did not any seepage was described as form-stable composite PCM (F-SCPCM). The mass fraction of eutectic PCM in the form-stable composite was 34 wt%. As long as the PCM ratio was below this value, the kaolin matrix could show resistance against the exudation of the melted CA due to the capillary forces among the components.

The morphologies of kaolin and the prepared kaolin/CA composite PCM were investigated by using a SEM instrument (LEO 440 model). The compatibility among the components of the composites was characterized chemically using a FT-IR spectrophotometer (JASCO 430 model, USA). The LHTES properties of the kaolin/CA composite were measured under nitrogen atmosphere and at a heating rate of 5°C/min using by a DSC instrument (Perkin Elmer JADE model, USA).

The measurements during heating and cooling periods were carried out at heating rate of 5°C/min under nitrogen atmosphere. The phase change temperature was taken as on-set temperature which was obtained by drawing a tangent line at the point of peak with maximum slope and interpolating to the baseline. The latent heat storage capacity was calculated by dividing the integrated area between the base line and the DSC curve. Both of LHTES properties were determined automatically by means of the software of DSC instrument. By considering the averages of three measurements, the maximum deviation in phase change temperature and latent heat values was calculated as $\pm 0.11^\circ\text{C}$ for and ± 0.45 J/g, respectively. The thermal reliability of the kaolin/CA composite was evaluated after repeated for 1000 heating-cooling cycles, which were carried out by using BIOER TC-25/H model thermal cyler.

Thermal durability of the CA and kaolin/CA composite determined by TGA analyzer (Perkin–Elmer TGA7 model, USA) were compared. Furthermore, the thermal conductivities of the prepared composite PCM was improved by addition of 5wt% EG with high thermal conductivity (4.26 W/m K). The measurements were carried out at room temperature by using a thermal property analyzer (Decagon KD2 model, China). The enhancement in its thermal conductivity was confirmed by comparing the melting times of the composites with and without EG additive.

3. RESULTS AND DISCUSSION

3.1. Morphological Characterization of the Prepared Kaolin/CA Composite PCM

Figure 1(a-b) shows the SEM photographs of the kaolin and the prepared kaolin/CA composite. As evidently observed from Figure 1(a), the surface of the kaolin clay is consisted of the particles with indiscriminate shape and different sizes and the layers formed by these particles are dispersed randomly through the surface.

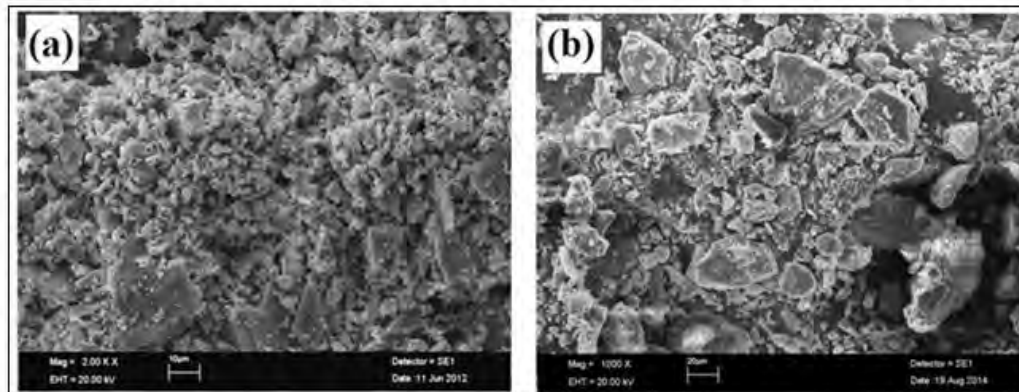


Figure 1. SEM images of (a)kaolin (b)kaolin/CA composite PCM

The holes and hiatuses among the layers facilitate the sorption of the CA molecules. As also clearly seen from Figure 1(b), the micro holes or channels between the particles wholly were occupied with CA. Moreover, the surface tension and capillary forces caused good physically compatibility between the clay matrix and the organic PCMs [13], which was resulted in forming excellent resistant-composite with against the leakage problem of its PCM content.

3.2. Chemical Characterization of the Prepared Kaolin/CA Composite PCM

The FT-IR spectrum of kaolin/CA composite was taken and compared with that of CA. As seen from Figure 2, the $-CH_2$ characteristic bands were observed in the range of $2921-3000\text{ cm}^{-1}$ for pure CA.

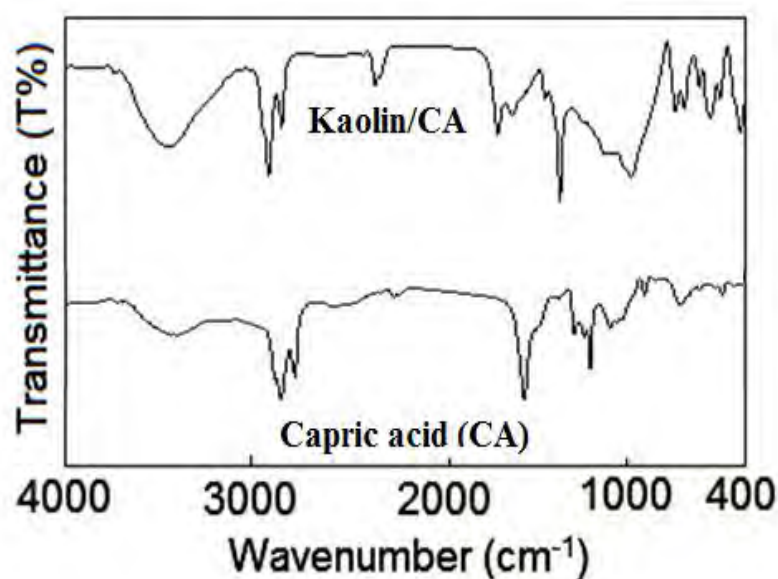


Figure 2. FT-IR spectra of the kaolin/CA composite PCM

The absorption wavenumber values regarding C=O and C-O groups of pure CA were reported as 1735 cm^{-1} and 1100 cm^{-1} , respectively. Moreover, the O-H characteristic band was determined in the range of $3400\text{--}3700\text{ cm}^{-1}$ for CA. The FT-IR analysis of the kaolin indicated that the absorption band in the range of $3478\text{--}3552\text{ cm}^{-1}$ was attributed to the O-H stretching vibration of its silanol (Si-OH) groups and the bands at 1070 cm^{-1} and 584 cm^{-1} represent the asymmetric stretching and bending vibrations of its Si-O-Si groups, respectively. On the other hand, compared these results, it is possible to observe all characteristic bands of the pure components in the spectrums of the kaolin/CA composite. The symmetrical stretching bands of $-\text{CH}_2$ groups was observed below 3000 cm^{-1} in the spectrum of all composites. The absorption bands of C=O and C-O groups were detected at 1710 cm^{-1} and 1108 cm^{-1} for the K/CA composite, respectively. The O-H band was monitored in the range of $3162\text{--}3702\text{ cm}^{-1}$ and the asymmetric stretching and bending vibrations of Si-O-Si groups were detected at 1139 cm^{-1} and 536 cm^{-1} , respectively. Moreover, after incorporation of CA with the kaolin, the absence of any new peak in the spectrum means that any chemical reaction was not occurred between the components of the kaolin. However, the small shifts occurred in the wavenumber values of the characteristic bands of the composite could be due to capillary forces or surface tension forces between the confined CA molecules and the surface functional groups of the kaolin. All of the FT-IR results proved the presence of good compatibility between the ingredients of the composite PCM.

3.3. LHTES properties of the Prepared Kaolin/CA Composite PCM

The LHTES properties of a building composite PCM such as melting temperature and latent heat capacity are decisive key parameters in terms of its usage in building envelopes to reach the comfort temperature level. The solid-liquid phase change temperature and enthalpy of the CA were measured as 31.04°C and 190.21 J/g for pure CA. The properties of the CA is rather convenient material for the fabrication of the building composite PCM, which will be used for low temperature-thermal applications in buildings.

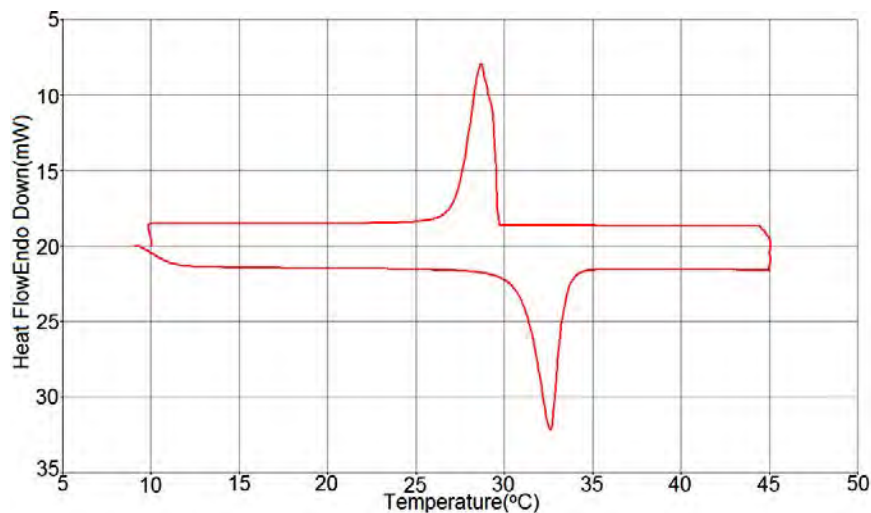


Figure 3. DSC curves of the kaolin/CA composite PCM

On the other hand, as can be clearly seen from the DSC thermogram in Figure 3, the fabricated the composite PCM including maximum amount of CA melts at 30.71°C and stores a latent heat as 27.23 J/g while it freezes at 28.21°C and releases a latent heat as -25.51 J/g. These LHTES properties make it hopeful composite PCM with energy storing function for solar passive heating and cooling intentions in buildings with respect to the different climate conditions. Moreover, the change occurred in the melting and freezing temperatures of the composite PCM compared to that of CA could be because of strong physical attractions between the characteristics silanol groups of the kaolin and the functional groups of the PCMs, which are proved by the FT-IR analysis. Additionally, the theoretical CA fraction (17wt%) in the composite calculated by dividing the latent heat value to that of CA are very close to its experimental incorporation fractions (17.5 wt%) determined after the leakage test. By comparing the latent heat capacity of the fabricated composite PCM with other type building composite PCMs in literature [14-17], it is deduced that the prepared kaolin/CA composite PCM can be drawn a conclusion that it has adequately high LHTES capacity.

3.4. Thermal Reliability and Chemical Stability of the Prepared Kaolin/CA Composite PCM

Prior knowledge of the thermal reliability property of newly developed composite PCM is important in term of its handling in real long-term TES applications. For that purpose, the LHTES properties of prepared composite PCM were measured again by DSC analysis after the thermal cycling test. The changes in the phase change temperatures of the composite were calculated as -0.27°C for melting period and -0.5°C for freezing period. Moreover, the decrease occurred in its latent heat values were determined as 9.8 and 2.4% for melting and freezing period, respectively. These results showed that the fabricated composite PCM had good thermal reliability for practical TES applications.

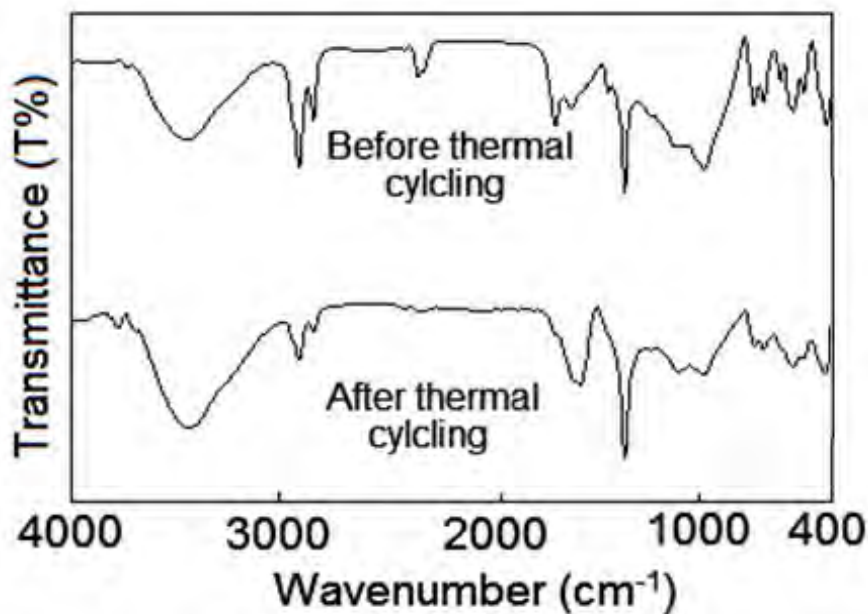


Figure 4. FT-IR spectra of the kaolin/CA composite PCM after thermal cycling

On the other hand, to evaluate chemical stability of the composite PCM, its FT-IR spectrums taken after and before thermal cycling were compared. As evidently seen from Fig. 4, the spectrums of the composite PCM had no new band and all of the characteristic bands were observed again without no occurring any change in their shapes and wavenumbers after the cycling test. These results are apparent pointer of its good chemical stability.

3.6. Thermal Durability of the Prepared Kaolin/CA Composite PCM

A newly fabricated composite PCM should be durable thermally when heated over its operating temperature. From this view, this property of the fabricated composite PCM was determined by evaluating the thermal degradation temperatures limits. As seen from TG curves in Figure 5, the pure CA degraded thermally at one-step in the range of 90-170°C while the fabricated composite PCM have two degradation stages, corresponding to the first one, 145°C and the second one, 200°C. The sublimit values of the degradation temperatures of the composite PCM are fairly over its working temperatures and thus it has good thermal stability.

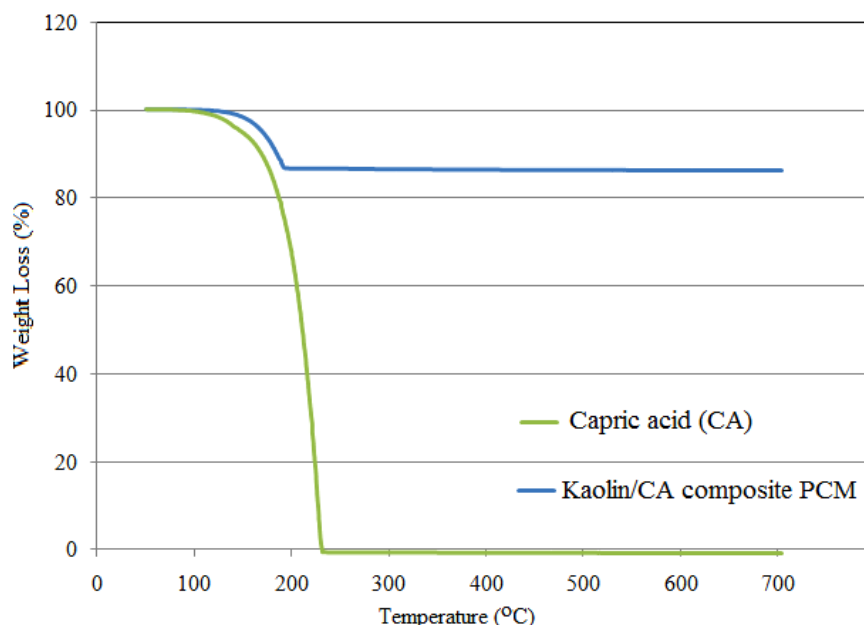


Figure 5. TG curves of the kaolin/CA composite PCM

3.7. Thermal Conductivity Improvement of the Prepared Kaolin/CA Composite PCM by Addition of EG

Thermal conductivity of a PCM is one of the parameters which noticeably influence the heat transfer rates during heat charging/discharging periods of the LHS systems. Based on this the fact, in this study, the

thermal conductivity of the composite PCM was improved with EG additive in mass fraction of 5%wt. The thermal conductivity of composite PCM was increased from 0.17 W/m.K to 0.23 W/m.K after EG addition, which corresponds to an increase amount of 35%.

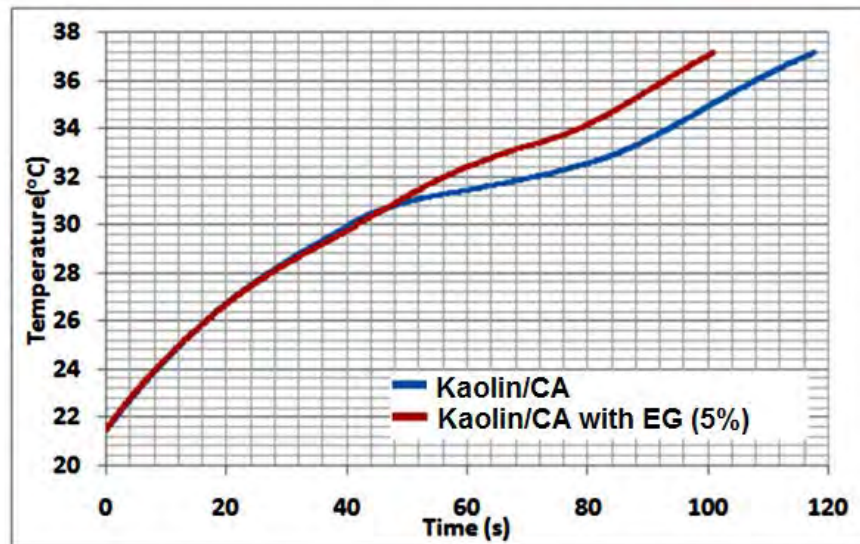


Figure 6. Time-temperature data recorded during the heating period of the kaolin/CA composite PCM

Additionally, Figure 6 shows the effect of EG additive on the melting times of the fabricated composite PCM. From the temperature-time curves, the melting time was established as 78 s for Kaolin/CA/EG composite as it was determined to be 98 s for the composite without EG additive. These results mean that the melting time of composite PCM was reduced as about 20% due to the accelerating effect of the improved thermal conductivity on the heat transfer during its heating period.

4. CONCLUSION

In this work, the kaolin/CA composite PCM was fabricated as new energy storing/releasing building materials through vacuum incorporation method. According to the leakage test, the maximum weight fraction of CA into the kaolin was established as 17.5 wt%. The chemical and morphological results obtained by the SEM and FT-IR analyses proved the existence of good compatibility among the components of the prepared composite. The measured LHTES properties of the composite PCM make them promising energy storing/releasing materials for passive solar HVAC applications in building envelopes. The thermal cycling test demonstrated that the composite PCM have good thermal reliability and chemical stability. The TG analysis confirmed that the fabricated composite PCM had good thermal durability. The EG addition caused an increase in the thermal conductivities of the composite PCM as much as 35% and this improvement was proved with the reduction taken place in its melting time. Based on all results it can be also concluded that the fabricated kaolin/CA composite can be evaluated as potential building PCM to diminish the energy requirement for HVAC intention in buildings by adjusting indoor temperature to the human thermal comfort temperature range.

REFERENCES

- [1] M. Kenisarin, K. Mahkamov, Solar energy storage using phase change materials, *Renewable and Sustainable Energy Review* 11 (2007) 1913-1965.
- [2] A. Sharma V.V. Tyagi, C. Chen, D. Buddhi, Review on thermal energy storage with phase change materials and applications, *Renewable and Sustainable Energy Reviews* 13 (2009) 318-345.
- [3] H. Mehling, L.F. Cabeza, Heat and cold storage with PCM. An up to date introduction into basics and applications. Springer; 2008.
- [4] D. Rozanna, A. Salmiah, T.G. Chuah, R. Medyan, S.Y. Thomas choong, M. Sa'ari, A study on thermal characteristics of phase change material (PCM) in gypsum board for building application, *J. Oil Palm Research* 17 (2005) 41–46.
- [5] T.C. Ling, C.S. Poon, Use of phase change materials for thermal energy storage in concrete: An overview, *Construction and Building Materials* 46 (2013) 55-62.
- [6] T. Nomura, N. Okinaka, T. Akiyama, Impregnation of porous material with phase change material for thermal energy storage, *Material Chemistry and Physics* 115 (2009) 846-850.
- [7] M. Li, Z. Wu, H. Kao, Study on preparation, structure and thermal energy storage property of capric-palmitic acid/attapulgitic composite phase change materials, *Applied Energy* 88 (2011) 3125–3132.
- [8] A. Biçer, A. Sari, New kinds of energy-storing building composite PCMs for thermal energy storage, *Energy Conversion and Management* 69 (2013) 148–156.
- [9] M. Li, Z. Wu, H. Kao, J. Tan, Experimental investigation of preparation and thermal performances of paraffin/bentonite composite phase change material, *Energy Conversion and Management* 52 (2011) 3275-3281.
- [10] Y. Wang, T.D. Xia, H. Zheng, H.X. Feng, Stearic acid/silica fume composite as form-stable phase change material for thermal energy storage, *Energy and Buildings* 43 (2011) 2365-2370.
- [11] M. Li, H. Kao, Z. Wu, J. Tan, Study on preparation and thermal property of binary fatty acid and the binary fatty acids/diatomite composite phase change materials, *Applied Energy* 88 (2011) 1606-1612.
- [12] A. Sari, M. Tuzen, D. Citak, M. Soylak, Equilibrium, kinetic and thermodynamic studies of adsorption of Pb(II) from aqueous solution onto Turkish kaolinite clay, *J. Hazardous Materials* 149 (2007) 283-291.
- [13] S. Song, L. Dong, Y. Zhang, S. Chen, Q.Y. Guo, S. Si, C. Xiong, Lauric acid/intercalated kaolinite as form-stable phase change material for thermal energy storage, *Energy* 76 (2014) 385-389.
- [14] P.W. Griffiths, P.C. Eames, Performance of chilled ceiling panels using phase change materials slurries as the heat transport medium, *Applied Thermal Engineering* 27 (2007) 1756-1760.
- [15] K. Nagano, S. Takeda, T. Mochida, K. Shimakura, T. Nakamura, Study of a floor supply air conditioning system using granular phase change material to augment building mass thermal storage-heat response in small scale experiments, *Energy and Buildings* 38 (2006) 436-446.
- [16] X. Xu, Y.P. Zhang, K.P. Lin, H.F. Di, R. Yang, Modeling and simulation on the thermal performance of shape-stabilized phase change material floor used in passive solar buildings, *Energy and Buildings* 37 (2005) 1084-1109.
- [17] P. Principi, R. Fioretti, Thermal analysis of the application of PCM and low emissivity coating in hollow bricks, *Energy and Buildings*, 51 (2012) 131-142.

Thermal energy storage characteristics of bentonite-based composite PCM with enhanced thermal conductivity

Ahmet Sari

Abstract

Phase change materials (PCMs) have been widely used in many thermal energy storage (TES) applications. PCMs can be integrated with different building materials such as in gypsum board, plaster, concrete, porous clay minerals or other wall-covering materials. However, they also have some inherent limitations, such as low thermal conductivity, and the needing for a container to prevent leaking. To solve these problems, some investigators have studied the possibility of a container that can prevent the leaking of liquid PCMs by using form-stable composite PCM (F-SCPCM). In this regard, this paper deals with preparation, characterization and investigations of TES properties of bentonite/heptadecane(HD) composite for energy saving. The microstructure and chemical structure and TES properties of the prepared bentonite/HD composite was made by using SEM, FT-IR, DSC and TGA analyses. The FT-IR and SEM results showed that the bentonite show good physicochemical compatibility against HD which was well-infiltrated into the porous structure. The DSC findings revealed that the fabricated bentonite/HD including 20%HD has a melting temperature of 22.07 °C and latent heat of melting of 28.42 J/g, which are suitable for heating and cooling applications of buildings envelopes. The TG analysis showed that the produced F-SCPCM has greater thermal durability compared with pure HD. The heat storage rates of the prepared F-SCPCM were increased noticeably due to enhanced thermal conductivity after EG(5w%) addition.

Keywords: Composite PCM, bentonite, heptadecane, thermal energy storage, thermal conductivity.

*Karadeniz Technical University, Department of Metallurgical and Material Engineering, 61080;
ahmet.sari@ktu.edu.tr*

1. INTRODUCTION

In thermal energy storage (TES) system, phase change material (PCM) can store or release large amounts of latent heat via phase change in a constant or narrow temperature range [1]. This method is becoming attractive in recent years because energy consumption in building and industrial sectors has about one third share in total energy consumption in the world [2]. In order to accomplish thermal comfort and decreasing the fluctuations at indoor temperature, several studies focused on TES performance of form-stable PCM/construction composites such as concrete blocks, hollow bricks and wallboard plasters have been carried out in recent years [3,4].

Paraffins as organic PCMs have been generally preferred for heating and cooling applications because of some advantageous TES properties [5]. However, their low thermal conductivity (generally in the range of 0.15 and 0.20 W/mK) could be eliminated by introducing high thermal conductive-materials [6]. The other problem is that they need storage container to dispose the outflow problem occurred in phase change stage. Therefore, the holding of PCMs by them into a porous building materials can take away the necessity of extra container usage. The integration of PCM with porous and lightweight materials is simple, cost-effective, environment friendly

and does not need any solvent [7]. The incorporation of different organic PCMs with porous building clays such as perlite [8], diatomite [9] and vermiculite [10].

Bentonite is consisted basically with clay minerals of the smectite (montmorillonite) group and one of the most common industrial clays. It has some advantageous properties such as low cost, excellent absorption capacity, and direct usability with cement, mortar and concrete. In addition to all beneficial properties above-mentioned, the incorporation feasibility of bentonite with PCMs make it strong candidate for the fabrication of form-stable composite PCMs (F-SCPCMs) for the TES purposes in buildings. However, the studies about the investigation functionality of bentonite as host matrix to incorporate organic PCMs is limited by a few studies [11-13]. From this point, a comprehensive study on the development and improvement thermal properties of bentonite/heptadecane composite as F-SCPCM. The thermal conductivity of the obtained F-SCPCM was enhanced with EG addition and the effect of this additive on its energy storage times was also evaluated.

2. EXPERIMENTAL

2.1. Materials

Bentonite used as supporting matrix is Turkish origin (in Reşadiye region of Tokat, Turkey). The dried bentonite is mainly composed of 61.82wt% SiO₂, 17.3 wt%Al₂O₃, 4.5wt%CaO, 3wt%Fe₂O₃, 2.7wt%Na₂O, 2.1wt%MgO and other metal oxides [13]. Before use, it was dried at 105°C for 24 h to remove the humidity and then sieved from 100 mesh. The HD and EG were obtained from Sigma-Aldrich company (Germany).

2.2. Method

The bentonite/HD composites were produced using vacuum impregnation method. Bentonite sample at a specified amount was put inside a flask connected to vacuum pump. The vacuum operation was maintained for 90 min under 65 kPa pressure. In the second state, the liquid HD placed into funnel was flowed gradually to the surface of bentonite. Subsequently, the vacuum was broken and air was allowed for 30 min to enter inside of flask in order to make easy the infiltration of HD. The prepared composite PCM was then cooled for 24 h to guarantee the solidification of the impregnated PCM. All of these treatments were applied for the preparation of the composites including different impregnation percentages of the eutectic mixture varied from 10 and 30% . The optimum impregnation percentage of the eutectic PCM was established by adopting leakage test. For this test, the composite was placed on the heater plate and its temperature was settled above the melting point of eutectic PCM. The heating treatment was continued for 45 min to check the leakage behavior of the PCM melted into pores of bentonite. Based on the leakage tests applied for each combination, the maximum mass fraction of HD into the bentonite was 18wt%, which was characterized as F-SCPCM.

As long as the PCM ratio was below this value, the bentonite matrix could show resistance against the exudation of the melted PCM due to the capillary forces among the components.

2.2. Instrumentation

The morphological investigations were carried out by using a SEM instrument with LEO 440 model. The chemical characterization was made by using a FT-IR spectrophotometer with JASCO 430 model (Japan).

The TES properties, *i.e.*, the phase change temperatures and latent heat storage capacity per unit mass of HD and the fabricated F-SCPCM were determined by a DSC instrument (Perkin Elmer-JADE model, USA). The measurements during heating and cooling periods were carried out at heating rate of 5°C/min under nitrogen atmosphere. Both of LHTES properties were determined automatically by means of the software of DSC instrument. By considering the averages of three measurements, the maximum deviation in phase change temperature and latent heat values was calculated as $\pm 0.12^\circ\text{C}$ for and ± 0.52 J/g, respectively.

Thermal resistance temperatures of the HD and fabricated F-SCPCM were obtained through TG analysis (Perkin–Elmer TGA7 model instrument, USA). The analyses were carried out at heating rate of 10 °C/min between 50 and 500°C. During the analysis period, nitrogen gas was passed into the system to obtain inert atmosphere at a flow rate of 20 mL/min.

Thermal conductivity measurements were carried out by using a thermal property analyzer with Decagon KD2 model. The TES reliability of the prepared F-SCPCM was determined by using a thermal cycler with BIOER TC-25/H model. Additionally, the effect of this addition on the reduction of heating times of the prepared F-SCPCM was investigated experimentally. The temperature of the prepared F-SCPCM were recorded against time by using a data logger NOVA5000 model.

3. RESULTS AND DISCUSSION

3.1. Microstructure Characterization

Figure 1 shows the morphological images of bentonite before and after impregnation of PCM obtained from SEM analysis. As can be seen from micrograph of bentonite before impregnation process, it is consisted with haphazard shaped-coarse particles dispersed arbitrarily through the surface. The most of them are unconnected each other and thus the spaces among the particle layers enable the holding HD molecules and thus preventing their exudation from the surface of matrix.

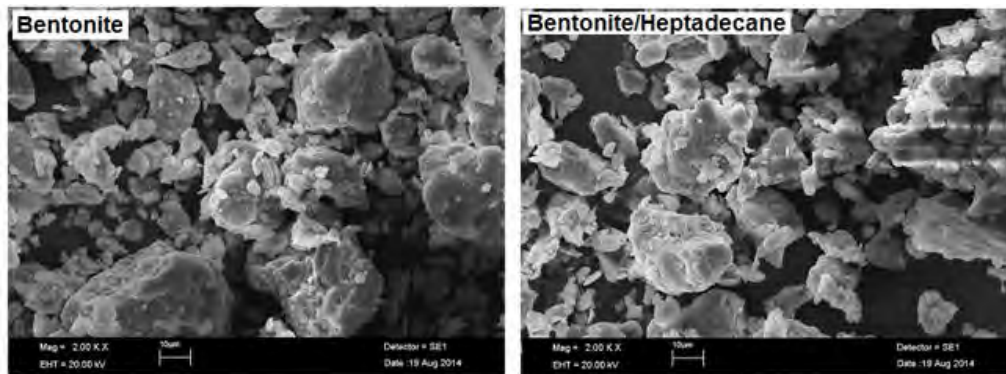


Figure 1. SEM images of bentonite and bentonite /HD composite as F-SCPCM

After impregnation process, the spaces between the micro particles of bentonite completely were occupied separately with HD used as PCM. Moreover, the surface tension and capillary forces between the PCM molecules and inter layers of bentonite make whole matrix structurally durable against the exudation problem of PCMs above their melting temperatures.

3.2. Chemical Characterization

The chemical compatibility of the bentonite with the HD was investigated by using FTIR spectroscopy technique.

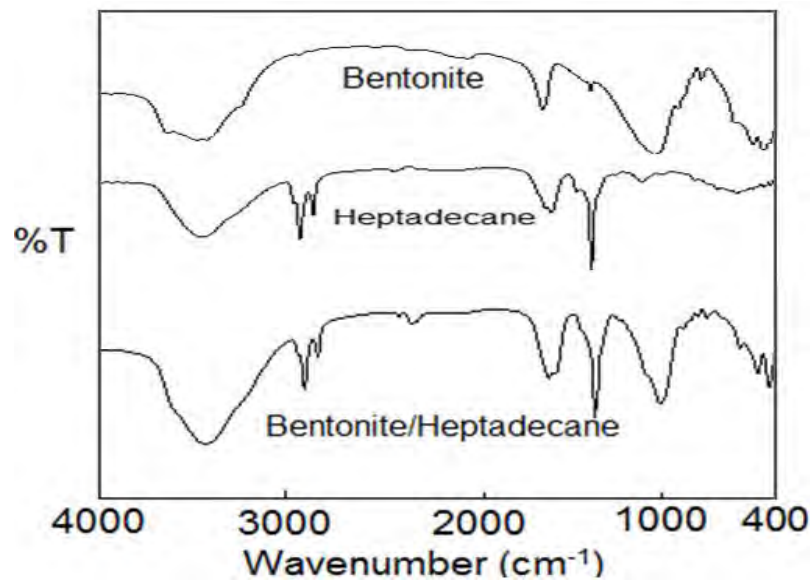


Figure 2. FT-IR spectra of the bentonite, heptadecane and the produced F-SPCM

As seen from the FTIR spectrum of HD and bentonite in Figure 2, its stretching vibration bands of $-CH_2$ groups are recorded in the close ranges of about $2800-2950\text{ cm}^{-1}$ for HD. The main peaks shown between 3235 cm^{-1} and 3617 cm^{-1} and around 1637 cm^{-1} are attributed to the stretching vibration and bending vibration regarding with water in the structures of bentonite. It has also other characteristic bands such as Si-antisymmetric vibration and bending vibrations at 1039 cm^{-1} and 460 cm^{-1} and 1045 cm^{-1} and 463 cm^{-1} , respectively. On the other hand, in the spectrum of the F-SCPCM, it can be easily detected all of the bands obtained for HD and bentonite. However, after impregnation process, the absorption peaks regarded with the main characteristic bands of the F-SCPCM showed only little shifts, which were due to the physical interactions. In addition to these results, non-observation of any new absorption peak in the spectrum of the composites confirmed the chemical inertness property of bentonite against the selected organic PCMs.

3.3. TES Properties

A building composite PCM should have proper phase transition temperature and adequately high phase transition enthalpy for heating, ventilating and air conditioning (HVAC) applications in building envelopes. As seen the DSC curve given in Figure 3, the bentonite/HD composite prepared in form-stable form show a melting phase change at 22.07°C and solidification phase change at 21.43°C . These values are suitable for HVAC applications in buildings depending on the climatic conditions. On the other hand, by comparing the phase change temperatures of the pure HD, it can be observed little decreases in case of prepared F-SCPCM, which are due to weakly attractive interactions among the components of the composite.

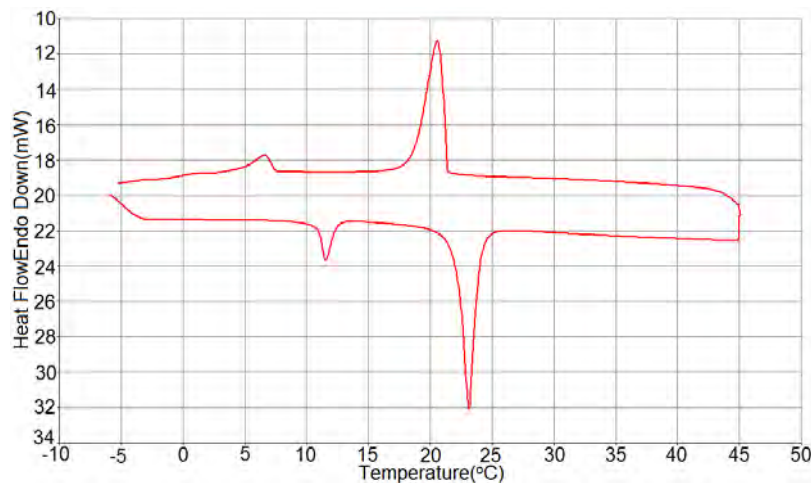


Figure 3. DSC curves of the produced F-SPCMs.

On the other, the produced F-SCPCM has a melting and solidification enthalpy as 38.42 J/g and -38.63 J/g, respectively. These properties also make them promising candidate composites for solar passive TES purposes in buildings. Additionally, by dividing the measured enthalpy value for the melting transition to the corresponding value of pure PCM the theoretical holding ratio of PCM by bentonite was calculated as 17.8 wt% which is close to real impregnation mass fractions of 18wt%. However, lower real mass fraction could be owing to the non-free of phase transition of the PCM hold between inner layers of bentonite [12].

3.4. TES reliability and Chemical Stability

A new F-SCPCM should be dependable in term of its TES properties after long-term use. With this regard, TES dependability of the prepared F-SCPCM was determined by measuring after treatment of heating/cooling cycles repeated for 1000 times. It is possible to observe very little amount of decrease in its melting and solidification temperature as 0.06 and 0.02°C, respectively. Moreover, after thermal cycling, the corresponding enthalpy values of the F-SCPCM were reduced as little as 8.6% and 12.8% for freezing period, respectively. However, it can be concluded that the prepared F-SCPCM has good TES dependability for solar passive thermal applications in buildings.

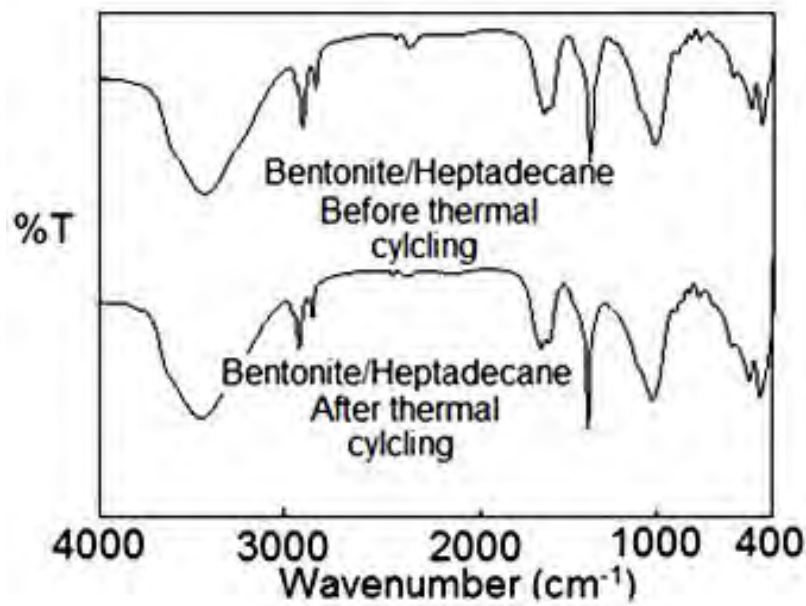


Figure 4. FT-IR spectra of the produced F-SPCMs after thermal cycling.

On the other hand, a newly prepared composite PCM should be stable chemically after thermal cycling treatment. As clearly perceived from the FT-IR spectrums in Figure 4, the profile and wavenumbers of the characteristic absorption bands of the prepared F-SCPCM were kept without change after 1000 cycling. These results mean that the prepared F-SCPCM has good chemical stability.

3.5. Thermal Resistance

A freshly produced PCM should show good thermal resistance against high temperature. In this regard, the TG analysis of HD and the prepared F-SCPCM were carried out in the temperature range of 50-500°C.

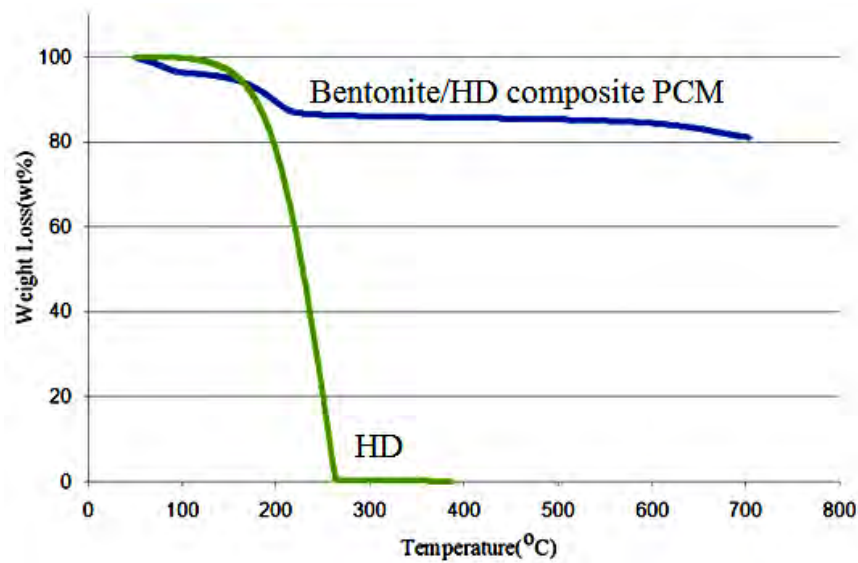


Figure 5. TG curves of pure HD and produced F-SPCMs.

As seen from Figure 5, about 3%-part of total weight of pure HD loses by evaporation at 150°C and its weight loss actions was ended at about 255°C. As also seen from the TG curve, the HD were evaporated in the temperature range of 165-255°C, which is corresponded to the percentages of weight loss of 19wt%. These results indicated that the degradation temperatures of the HD hold into composite are extremely over its phase change temperatures. Thus, it can be concluded that the prepared F-SCPCM have high thermal resistant and thus good thermal stability.

3.6. Thermal Conductivity Enhancement

Thermal conductivity of a PCM is one of the factors which remarkably affect the heat charging/discharging transfer rates to/from TES systems. In this respect, the thermal conductivity of the pure HD and bentonite were measured as 0.17, and 0.82 W/m.K. Afterwards, EG (thermal conductivity value: 4.26 W/mK) was added to the prepared F-SCPCM in mass fraction of 5%wt and its thermal conductivity was measured as 0.56 W/m.K. This means that the thermal conductivities of prepared F-SCPCM was increased approximately as 47%.

3.7. Effect of Thermal Conductivity Enhancement on Total Heating Time

Figure 6 shows the effect of enhanced thermal conductivity on the total heating times of the prepared F-SCPCM. The temperature differences (ΔT) between the sublimit and upper limit values during the completion of heating period of the composite PCM were also shown on 19.8°C.

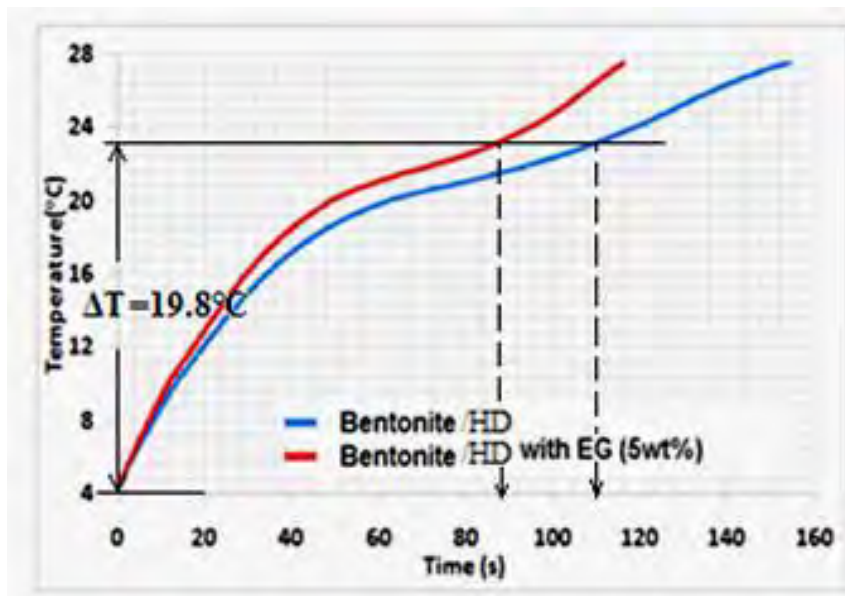


Figure 6. Temperature history vs time obtained for the heating period of the produced F-SCPMs.

After EG addition to the composites, the amount reduction occurred in their total heating times corresponded to the ΔT values are measured as 12 s. These results showed that the total heating times of the F-SCPCM with EG additive was diminished as about 11%, because of the increasing effect of the enhanced thermal conductivity on the heat transfer rate.

4. CONCLUSIONS

This study is focused on preparation, characterization and investigation of TES properties of bentonite/HD composite PCM. According to the leakage test, the maximum absorption ratio of HD was found to be 18wt%. The FT-IR and SEM results exposed the presence of good physical compatibility. The DSC measurements indicated that the prepared F-SCPCM has suitable phase change temperature and good latent heat capacity for solar HVAC applications for buildings envelopes depending on climatic conditions. Thermal cycling test showed that the prepared F-SCPCM has good TES dependability and chemical stability. TG analysis exhibited that the F-SCPCM had considerably high thermal resistance. Furthermore, after 5 wt% EG addition, the thermal conductivities of the produced bentonite/HD composite was increased approximately as 47%. The enhancement to be occurred in the thermal conductivity values of the composite was also confirmed by the reduction taken place in its total heating time. By taking account of all results, it can be also deduced that the prepared F-SCPCM can be considered as promising construction materials for building envelopes, thermal insulation/coatings of interior/exterior wall, plasterboards, and building bricks.

REFERENCES

- [1] Parameshwaran R, Kalaiselvam S. Sustainable thermal energy storage technologies for buildings: review, *Renew. Sustain. Energy Rev.* 2012;16:2394-2433.
- [2] Pomianowski M, Heiselberg P, Zhang Y. Review of thermal energy storage technologies based on PCM application in buildings. *Energy Build* 2013;67:56-69.
- [3] Memon SA, Lo TY, Cui H, Barbhuiya S. Preparation, characterization and thermal properties of dodecanol/cement as novel form-stable composite phase change material. *Energy Build*, 2013;66:697-705.
- [4] Rozanna D, Salmiah A, Chuah TG, Medyan R, Thomas choong SY, Sa'ari M. A study on thermal characteristics of phase change material (PCM) in gypsum board for building application. *J. Oil Palm Res.* 2005;17:41-46.
- [5] Pielichowski K, Kinga F. Differential scanning calorimetry study of blends of poly(ethylene glycol) with selected fatty acids. *Macromol Mater Eng* 2003;288:259-264.
- [6] Li C, Fu L, Ouyang J, Yang H. Enhanced performance and interfacial investigation of mineral-based composite phase change materials for thermal energy storage, *Sci Rep* 2013;3:1-7.
- [7] Sari A, Alkan C, Biçer A, Bilgin C. Latent heat energy storage characteristics of building composites of bentonite clay and pumice sand with different organic PCMs. *Int J Energy Res* 2014;38:1478-1491.
- [8] Jiao C, Ji B, Fang D. Preparation and properties of lauricacid-stearicacid/expanded perlite composite as phase change materials for thermal energystorage. *Mater Lett* 2012; 67:352-354.
- [9] M. Li, H. Kao, Z. Wu, J. Tan, Study on preparation and thermal property of binary fatty acid and the binary fatty acids/diatomite composite phase change materials. *Appl Energy* 88;2011:1606-1612.
- [10] Karaipekli A, Sari A. Capric-myristic acid/vermiculite composite as form stable phase change material for thermal energy storage. *Sol. Energy* 83;2009:323-332.
- [11] Sarier N, Onder E, Ozay S, Ozkilig Y. Preparation of phase change material-montmorillonite composites suitable for thermal energy storage. *Thermochim. Acta* 2011;524:39-46.
- [12] Fang X, Zhang Z. A novel montmorillonite-based composite phase change material and its applications in thermal storage building materials. *Energy Build* 38;2006:377-380.
- [13] Sari A, Tuzen M. Cd(II) adsorption from aqueous solution by raw and modified bentoniteite. *Appl. Clay Sci* 2014; 88-89:63-72.

Performance Analysis of Organic Rankine Cycle with R744 and N₂O

Fatih Yılmaz¹⁶, Reşat Selbaş², Arif Emre ÖZGÜR², Mustafa Tolga Balta³

Abstract

In this study deal with performance analyses of the supercritical organic Rankine cycles (ORC) with have been conducted using carbon dioxide (CO₂) and nitrous oxide (N₂O). Also these refrigeration's compared with each other based on various performance indicators. The energy and exergy efficiencies of the ORC are calculated various conditions.

Keywords: energy, exergy, organic Rankine cycle, CO₂, N₂O

36. INTRODUCTION

Global warming and ozone depletion of fossil fuels are two main concerns of energy producers. And also with living standards are increasing, the global population growth results in the energy demand acceleration. The energy demand is predicted to increase faster [1]. The utilizations of fossil fuels has caused serious environmental problems.

Low temperature applications (350 °C) for electricity generation conventional steam power of using water is become uneconomically and less efficient [2]. Thus situated Organic Rankine Cycle (ORC) may generally preferred for the processes having low temperature. Because of the usage of organic fluid as working fluid instead of water and high pressure steam, this process named as ORC. The ORC-based plants have been successfully adopted in recovering the solar energy [3]. The systems have been proven promising in converting low-grade heat into power.

The working principle of the ORC is the same as that of the steam Rankine cycle: the working fluid is pumped to a boiler where it is evaporated, passed through an expansion device (turbine or other expander), and then through a condenser heat exchanger where it is finally re-condensed. The main drawback of the ORC technology of the thermal efficiency is often lower than that of the steam Rankine cycle.

Many papers had examined ORC system for electrical power production, in the open literature [4-10]. Quoilin et al. [4] have presented techno-economic survey of various ORC applications. In this study, a market review has been introduced, technological constraints and optimization methods have been described and argued. Hettiarachchi et al. [5] studied the performance of ORC using different pure working fluids. Li et al. [6] assessed the performance of their system for both power and water production through reverse osmosis (RO) and their system had efficiency between %18 and % 20. Badr et al. [7] studied the characteristics of ideal working fluid for an ORC operating

¹⁶ Corresponding author: Aksaray University, Department of Technical Science of Vocational School, 68100, Aksaray, Turkey.
fatiyilmaz7@gmail.com

²Suleyman Demirel University, Departman of Energy System Engineering, 32100, Isparta Turkey

³ Aksaray University, Departman of Energy Mechanical Engineering, Engineering Faculty, 68100, Aksaray, Turkey

between 120 oC and 40 °C. Some researchers are analyzed of the geothermal ORC systems, economically and exergoeconomically [8, 9, 10]. They studied the effect of different operating parameters of the ORC and the geothermal fluid conditions on the cost rates associated with the energy and exergy streams through the system.

Amongst the natural refrigerants, the suggested of the use of CO₂ seems to be the most promising especially as the natural refrigerant. The CO₂ including that non-toxic, easily available, excellent thermophysical properties and not explosive. N₂O refrigerant, which is alternative of CO₂ in terms of thermophysical properties. N₂O refrigerants' disadvantage is, its global warming potential (GWP) is higher than CO₂.

In this study performance analyses of the supercritical organic Rankine cycles (ORC) with have been conducted using carbondioxide (CO₂) and nitrous oxide (N₂O). The energy and exergy efficiencies of the ORC cycle are calculated according to various conditions and both fluids.

2. PERFORMANCE ANALYSES OF ORC CYCLE

An ORC system consists of a working fluid, pump, an evaporator, a turbine and a condenser. As a working fluid selected CO₂ and N₂O. The schematic diagram of the ORC cycle give in the Fig. 1. T-s diagram of ORC cycle with working fluids seen that Fig.2

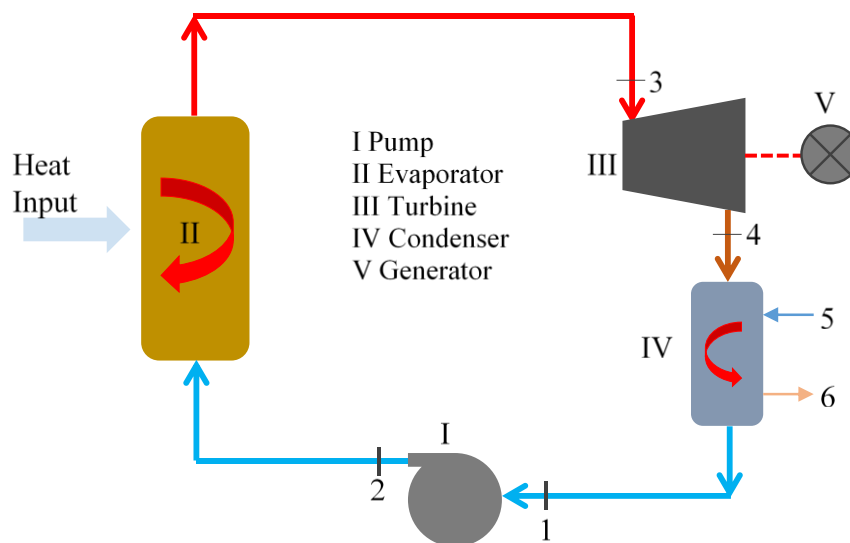


Fig. 1 Schematic diagram of ORC cycle

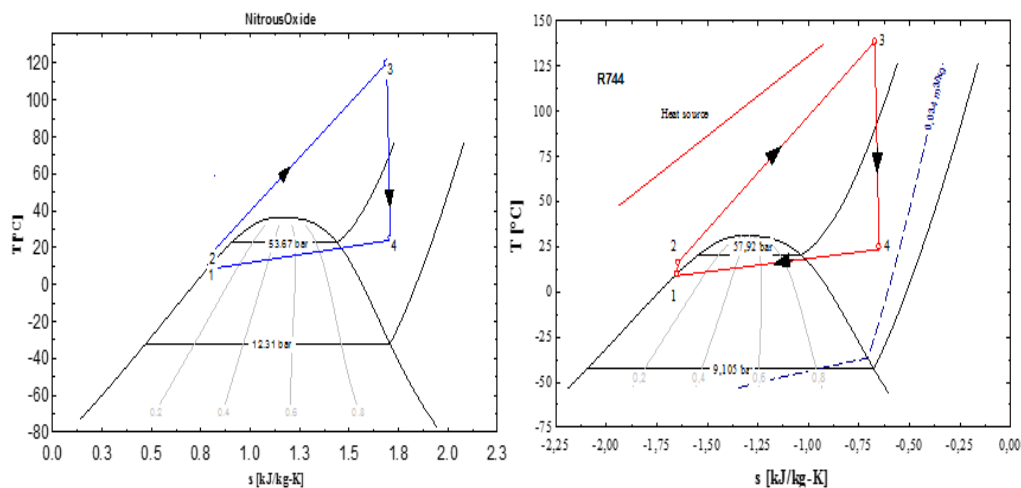


Fig. 2. T-s diagram of ORC cycle with CO₂ and N₂O

The natural fluid N₂O has a triple point -90.82 °C. Furthermore similarity between critical temperature N₂O and CO₂. Table 1 given in thermodynamic properties of CO₂ and N₂O.

Table 1 Thermodynamic properties of CO₂ and N₂O.

Property	CO ₂	N ₂ O
Critical pressure (Bar)	73.77	72.45
Critical temperature (°C)	30.98	36.37
Triple point temperature (°C)	-56.56	-90.82
Molecular weight(kg/kmol)	44.01	44.01

The thermodynamic modeling of the ORC system considered is presented in this section. The equations developed is programmed using Engineering Equation Solver (EES) software. The input data used in this ORC system is given in Table 2.

Table 2. Input data for ORC system

ORC pump isentropic efficiency	85%
ORC turbine isentropic efficiency	85 %
Evaporator output temperature	100-200 °C
Working fluids	CO ₂ -N ₂ O
Reference temperature (T0)	21 °C
Reference pressure (P0)	1 Bar

For a general steady-state, steady-flow process, the three balance equations, namely mass, energy and exergy balance equations, are employed to find the work input, the rate of exergy destruction, energy and energy efficiencies.

For the steady-state process, the mass, energy and exergy balance for the each control volume can be expressed as follows:

$$\sum \dot{m}_{in} = \sum \dot{m}_{out} \quad (1)$$

where \dot{m} is the mass flow rate, and the subscript in stands for inlet and out for outlet. The general energy balance can be expressed in the rate form as;

$$\dot{E}_{in} - \dot{E}_{out} = \Delta \dot{E}_s \quad (2)$$

which becomes [11];

$$\dot{Q} - \dot{W} = \sum \dot{m}_{out} \cdot h_{out} - \sum \dot{m}_{in} \cdot h_{in} \quad (3)$$

$$\dot{W}_p = \dot{m} * (h_2 - h_1) \quad (4)$$

$$\dot{Q}_{ev} = \dot{m} * (h_3 - h_2) \quad (5)$$

$$\dot{W}_T = \dot{m} * (h_4 - h_3) \quad (6)$$

$$\dot{Q}_{kon} = \dot{m} * (h_4 - h_1) \quad (7)$$

Exergy analysis can be used beneficially to analyze and improve the efficiency. The exergy

balance for a process can be written as;

$$\Delta \dot{E}x_{sys} = \sum \dot{E}x_{in} - \sum \dot{E}x_{out} - \sum \dot{E}x_{dest} \quad (8)$$

where $\dot{E}x_{in}$ and $\dot{E}x_{out}$ are the rate of net exergy transferred by heat, work and mass, and $\dot{E}x_{dest}$ is the rate of exergy destruction. For a steady-state system, $\Delta \dot{E}x_{sys}$ is zero, so Eq. (8) becomes;

$$\dot{E}x_Q - \dot{E}x_W + \dot{E}x_{mass,in} - \dot{E}x_{mass,out} = \dot{E}x_{dest} \quad (9)$$

The exergy of heat, work and mass flow are defined as follows [12];

$$\dot{E}x_Q = \dot{Q} \left(1 - \frac{T_0}{T} \right) \quad (10)$$

$$\dot{E}x_W = \dot{W} \quad (11)$$

$$ex = (h - h_0) - T_0(s - s_0) \quad (12)$$

$$\dot{E}x_{mass} = \dot{m} ex \quad (13)$$

The energy efficiency of the overall system can be defined by;

$$\eta_{\text{sys}} = \frac{\dot{W}_{\text{net}}}{\dot{Q}_{\text{in}}} \quad (14)$$

The exergy efficiency of the overall system can be defined by;

$$\Psi_{\text{sys}} = \frac{\dot{W}_{\text{net}}}{\dot{Q}_{\text{in}} \left(1 - \frac{T_0}{T_{\text{evap}}}\right)} \quad (15)$$

3. RESULTS AND DISCUSSION

Fig.3. illustrated that variations of net power output of the ORC system with turbine inlet pressure. For a constant turbine inlet temperature at 120 °C, when the turbine inlet pressure is increases the system of net power output increases as can be seen in this figure. The ORC system of net power output with CO₂ fluid higher than N₂O fluid at same conditions.

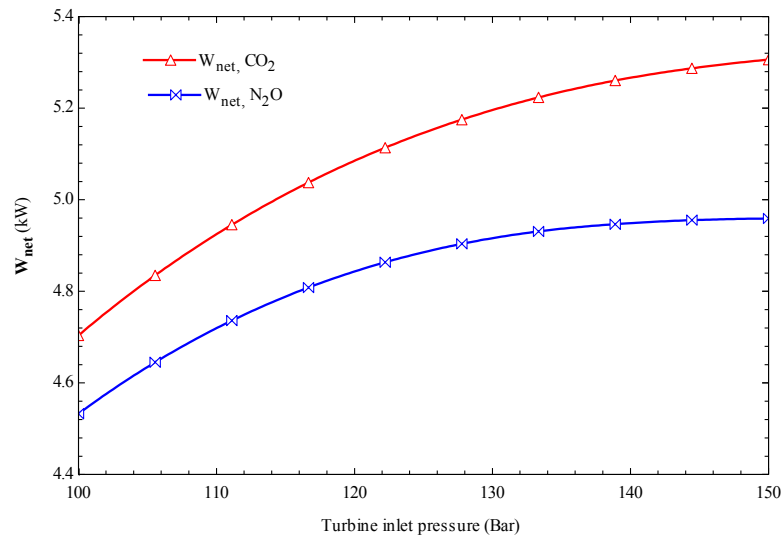


Fig. 3. Variations of net power output with inlet turbine pressure

The effect of the evaporation temperature on the net output power of the ORC system is presented in Fig 4. The net output power increases with evaporation temperature increases while the evaporation temperature constant 100 bar. The maximum net output power of ORC system is obtained CO₂ fluid at same conditions.

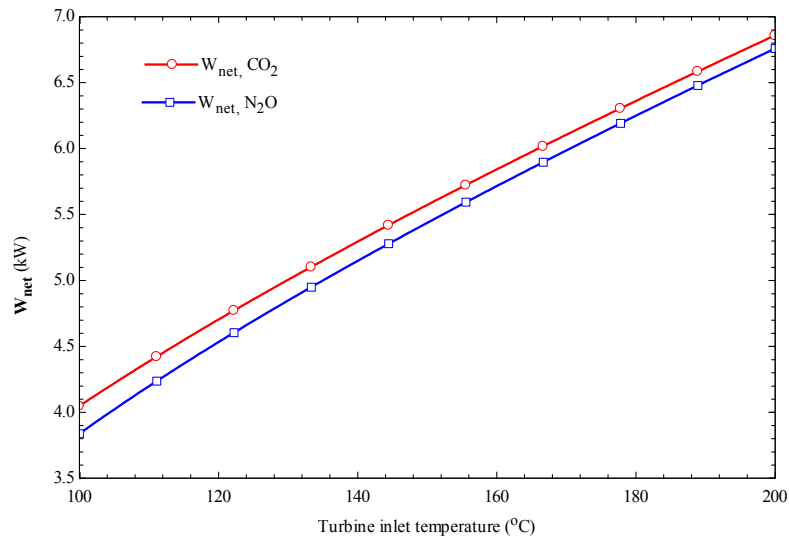


Fig. 4. Variations of net power output with inlet turbine temperature

Fig. 5. show that the effect of evaporator temperature on energy efficiency of ORC system. While the evaporator pressure constant 100 bar, when the evaporator temperature increases from 100 °C to 200 °C the system of energy efficiency increases from 14.5% to 17.2%.

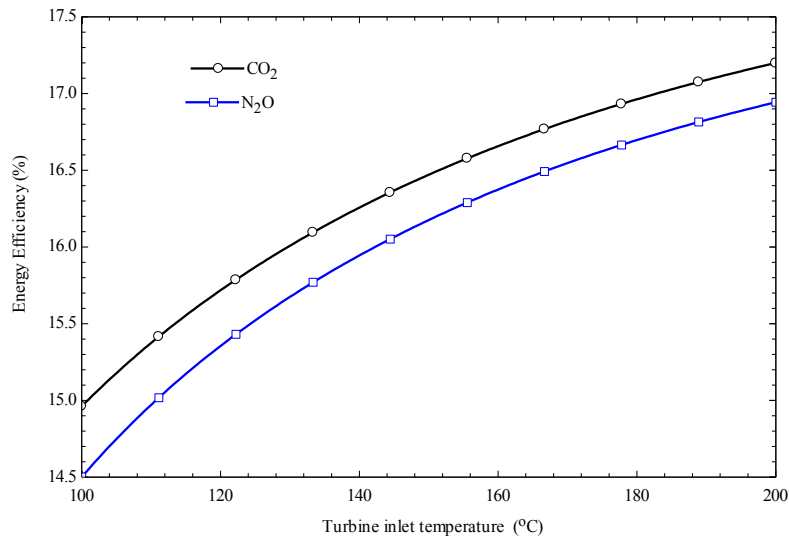


Fig. 5. The effect of evaporation temperature on energy efficiency

The exergy destruction for each components of ORC system as can be seen in Fig 6. While evaporator temperature and pressure are fixed 150 °C and 100 bar, respectively, exergy destruction of pump, evaporator, turbine and condenser are calculated as 0.2749 kW, 5.747 kW, 0.6451 kW and 0.4688 kW, respectively.

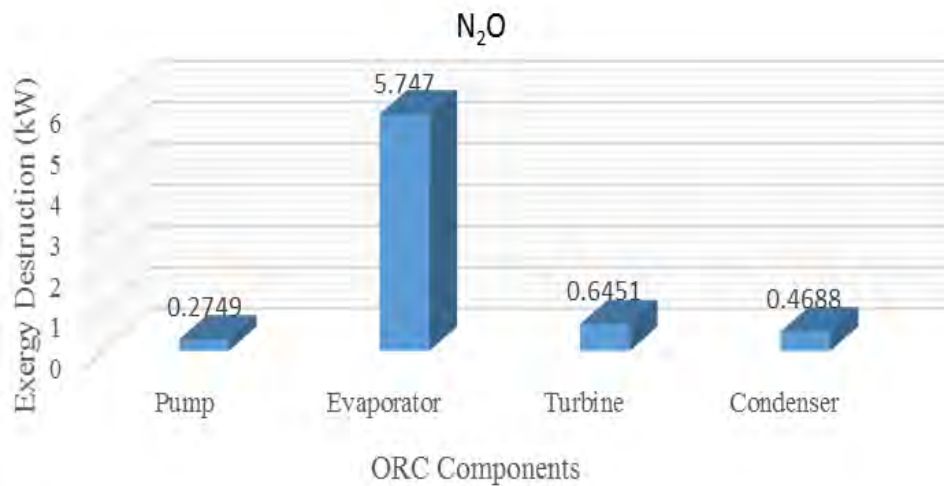


Fig. 6. Exergy destruction for each components of ORC with N_2O

Fig. 7, illustrated that the exergy destruction for each components of ORC system. While evaporator temperature and pressure are fixed $150\text{ }^\circ\text{C}$ and 100 bar , respectively, exergy destruction of pump, evaporator, turbine and condenser are calculated as 0.3297 kW , 6.107 kW , 0.6592 kW and 0.966 kW , respectively.

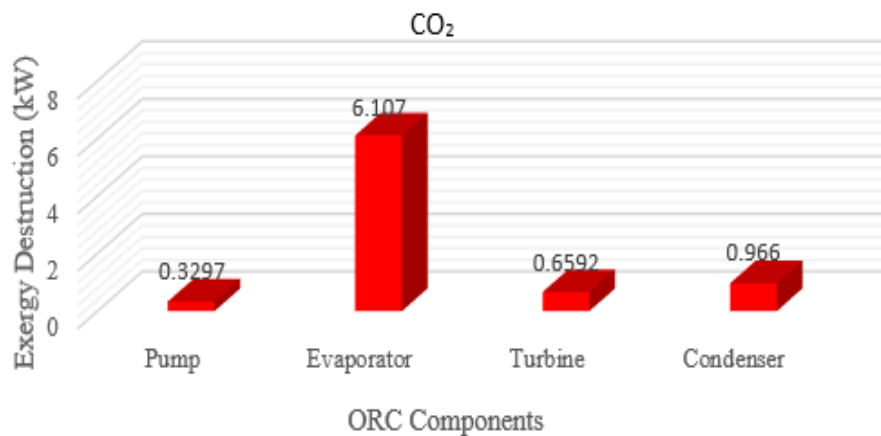


Fig. 7. Exergy destruction for each components of ORC with CO_2

The effect of turbine inlet temperature on the exergy efficiency of the ORC system is demonstrated at Fig.8. The exergy efficiency decreases with turbine inlet temperature increases. From Fig. 8, it can be calculated that the exergy efficiency of ORC system with CO_2 higher than with N_2O .

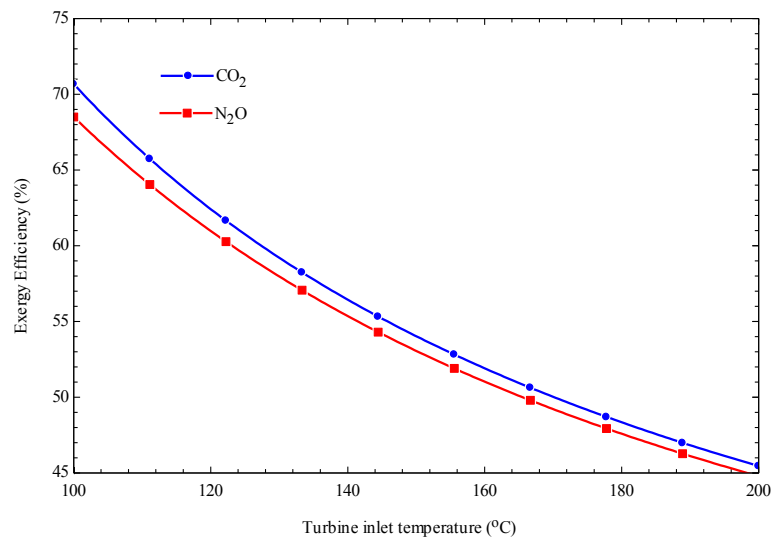


Fig. 8. The effect of turbine inlet temperature on exergy efficiency

3. CONCLUSION

An ORC cycle with CO₂ and N₂O as working fluid is studied performance assessment, based on energy and exergy concepts. We assumed the ORC system of evaporator temperature variation from 100 °C to 200 °C. The following remarks can be extracted from this study;

- The net output power ORC system CO₂ and N₂O as working fluids are calculated 4.704 kW and 4.533, respectively, at 120 °C fixed turbine inlet temperature.
- The net output power ORC system CO₂ and N₂O as working fluids are calculated 4.048 kW and 3.838, respectively, at 100 bar constant turbine inlet temperature
- The energy efficiency ORC system with CO₂ higher than N₂O, at same conditions.
- The exergy efficiency ORC system with CO₂ higher than N₂O, at same conditions.
- It is demonstrated that by increasing the turbine inlet temperature, the ORC energy efficiency increases.

It can be concluded that power generation with ORC using renewable heat sources like solar or geothermal systems and low-temperature industrial waste heat would significantly reduce CO₂ emissions and offsets grid consumption

REFERENCES

- [1] U.S. Energy Information Administration. International energy outlook 2011, Washington, DC. 2011.
- [2] T. Marciniak, J. Krazinski, J. Bratis, H. Bushby, E. Buyco, Comparison of Rankine-cycle Power Systems: Effects of Seven Working Fluids, 1981.
- [3] Quoilin S, Orosz M, Hemond H, Lemort V. Performance and design optimization of a low-cost solar organic Rankine cycle for remote power generation. *Sol Energy*, 2011;85:955-66.
- [4] Quoilin S, Van Den Broek M, Declaye S, Dewallef P, Lemort V. Technoeconomic survey of organic Rankine cycle (ORC) systems. *Renew Sustain Energy Rev* 2013; 22:168–86.
- [5] H.D. Madhawa Hettiarachchi, M. Golubovic, W.M. Worek, Y. Ikegami, Optimum design criteria for an Organic Rankine cycle using low-temperature geothermal heat sources, *Energy* 2007; 32 1698-1706.
- [6] Li C, Kosmadakis G, Manolakis D, Stefanakos E, Papadakis G, Goswami DY. Performance investigation of concentrating solar collectors coupled with a transcritical organic Rankine cycle for power and seawater desalination cogeneration. *Desalination* 2013; 318:107–17.
- [7] O. Badr, S.D. Probert, P.W. O'Callaghan, Selecting a working fluid for a Rankine-cycle engine, *Applied Energy* 1985; 21, 1-42.
- [8] S. Quoilin, S. Declaye, B.F. Tchanche, V. Lemort, Thermo-economic optimization of waste heat recovery organic Rankine cycles, *Applied Thermal Engineering* 2011; 31 2885-2893.

- [9] F. Heberle, P. Bassermann, M. Preiinger, D. Bruggemann, Exergoeconomic optimization of an organic Rankine cycle for low-temperature geothermal heat sources, *International Journal of Thermodynamics* 2012; 15 119-126.
- [10] A.S. Nafey, M.A. Sharaf, L. García-Rodríguez, Thermo-economic analysis of a combined solar organic Rankine cycle-reverse osmosis desalination process with different energy recovery configurations, *Desalination* 2010; 261,138-147.
- [11] Cengel, Y.A. and Boles, M.A. 2008. *Thermodynamics: An Engineering Approach*, 6th edition, McGraw-Hill, NY.
- [12] Dincer, I. and Rosen, M. A. 2007. *EXERGY: Energy, Environment and Sustainable Development*. Elsevier Science; 1st ed., 472, Oxford, UK.

Using cluster analysis method for multivariate mapping

Burak Çağlar¹⁷, Hüseyin Zahit Selvi¹⁸

Abstract

Multivariate mapping is the graphic display of more than one variable or attribute of geographic phenomena. Multivariate mapping integrates computational, visual, and cartographic methods to develop a visual approach for exploring and understanding spatiotemporal and multivariate patterns. More than one attribute can be visually explored and symbolized using numerous statistical classification systems or data reduction techniques. In this sense, clustering analysis methods can be used for multivariate mapping. In this study Agglomerative Hierarchical Clustering method which is one of the clustering analysis methods was analyzed. Classes and multivariate maps created with this method from traffic accident data of two different years in Turkey were presented. In addition usability of such maps in risk management and planning was discussed.

Keywords: multivariate mapping; data mining; cluster analysis; visualization

37. INTRODUCTION

Multivariate mapping is the graphic display of more than one variable or attribute of geographic phenomena. The simultaneous display of sometimes multiple features and their respective multivariate attributes allows for estimation of the degree or spatial pattern of cross-correlation between attributes. Multivariate mapping integrates computational, visual, and cartographic methods to develop a visual approach for exploring and understanding spatiotemporal and multivariate patterns [1].

A fundamental issue in multivariate mapping is whether individual maps should be shown for each attribute or whether all attributes should be displayed on the same map ([2], p.327). Producing separate maps for each attributes would make it difficult to compare two objects which have various attributes. Therefore methods in which various attributes are shown in the same map are preferred more. In this sense, Trivariate Choropleth Map which is created by overlapping of two colored choropleth map [3-6], Multivariate Dot Maps method in which specific color or symbol is used for each attribute in the map [7], Multivariate Point Symbol methods which are used when multivariate data can be shown with point symbols [8-15], method in which combining different type of symbols is used for representing multivariate data [16] and method of separating different attributes from integral symbols [17] can be listed.

Different from the methods above, in order to represent many attributes in the same map, classification method based on clustering methods in data mining can be used as well. With the use of clustering methods, similar aspects of different spatial objects can be revealed by considering more than one attribute [18-19]. In this sense, spatial analyses that would make important contributions for risk analysis, planning etc. can be done. In this study, Agglomerative Hierarchical Clustering method which is one of the clustering analysis methods that could be applied within the scope of multivariate mapping is examined. This method will be used in extracting profile

of traffic accidents in Turkey; result maps produced with data of two different years will be compared. Cluster Analysis and Agglomerative Hierarchical Clustering method in the second section, application in the third section will be explained in details, results and suggestions will be shared in last section.

38. CLUSTER ANALYSIS

Cluster analysis is the process of grouping information in a data set according to specific proximity criteria. Similarity of element in the same cluster should be high, similarity between clusters should be low [20]. In the process of classification, classes are determined before. In clustering method, classes are not determined before. Data are separated different classes according to the similarity of data obtained.

Cluster methods are classified in different ways in various resources. In general sense, cluster methods can be classified as hierarchical and non-hierarchical methods [2].

¹⁷ Çorum Special Provincial Administration Directorate of Roads and Transportation Services, Çorum, bcaglar19@gmail.com

¹⁸ Corresponding author: Necmettin Erbakan University Geomatic Engineering Department Division of Cartography, Konya, hyselvi@konya.edu.tr

- **Non-hierarchical Methods:** In non-hierarchical methods, n objects are divided into k clusters according to k number ($k < n$) given before. This method divides data in a way that there will be at least one object in each cluster and each object will be included at least in one cluster [21].
- **Hierarchical Methods:** Hierarchical clustering methods group data objects in tree structure. Hierarchical clustering methods are classified as agglomerative or divisive according to hierarchical division being bottom-up or top-down [22].

In this study, Agglomerative and Divisive Hierarchical Clustering method from hierarchical methods will be analyzed.

38.1. Agglomerative and Divisive Hierarchical Clustering Method

AGNES (AGglomerative NESTing) follows bottom-up strategy. In the beginning each object is accepted as a separate cluster. In each step of algorithm, similar clusters are agglomerated until they are a single cluster or enable expected properties. Most of the hierarchical clustering methods are included in this category. On the other hand, DIANA (Divisive ANALysis) follows top-down strategy. In the beginning the entire data object is accepted as one cluster. In each step of algorithm, the most similar objects are merged together; large cluster is divided into smaller clusters. This clustering method continues until each object composes a cluster on its own or any expected condition is enabled [22] (Figure 1).

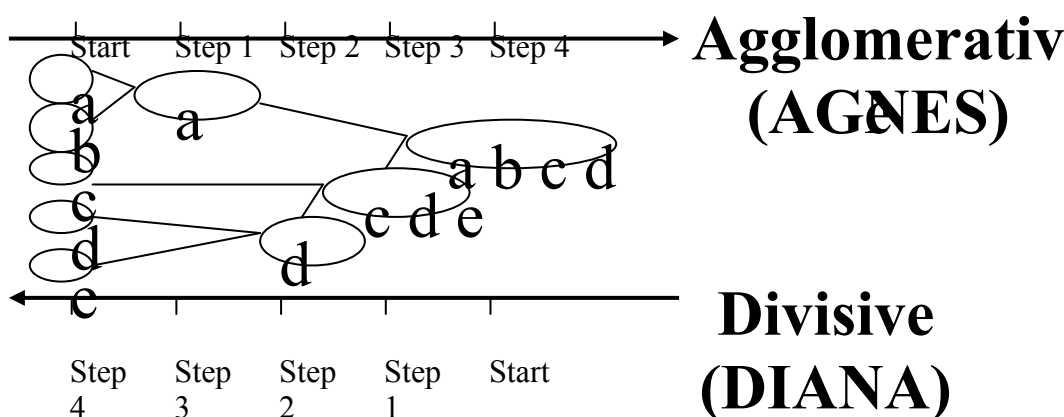


Figure 10. Agglomerative and Divisive Hierarchical Clustering on {a,b,c,d,e}

Tree structures named as dendrogram is used for stating the process of hierarchical clustering. Dendrogram shows how objects are grouped step by step (Figure 2).

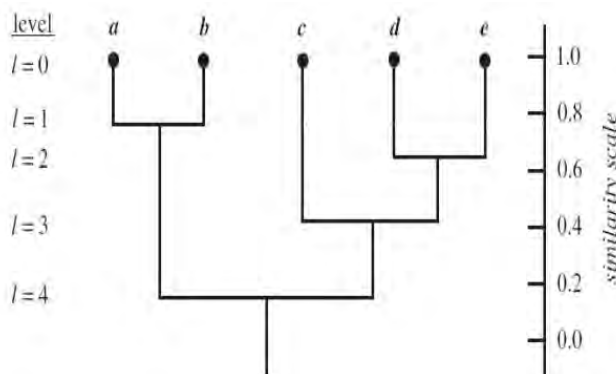


Figure 2. Dendrogram for Hierarchical Clustering of {a,b,c,d,e}

Although hierarchical clustering method is thought to be simple, there are some difficulties in choosing agglomeration or division points. Choice of these points is quite important because further steps will be carried out through new clusters formed by agglomeration or division of an object group. It is neither possible to change previous processes or objects between clusters. Therefore not taking agglomeration or division decisions in specific steps would cause formation of low qualified clusters.

39. APPLICATION

Casualties, injuries and financial damages as a result of traffic accidents are among the most important problems of Turkey. When data of the last 5 years are analyzed, it is seen that there have been more than 1.000.000 traffic accidents, 145.000 of them ended up with death and injury, and nearly 1.060.000 of them results with financial damage. 4000 people lose their life on average in these accidents and nearly 250.000 people are injured. It is quite important to make use of more than one current

traffic accidents attributes and determine similarity of traffic data on city basis in order to detect measures to be taken for traffic security in Turkey and future investments to be done. For this aim, in this study, clustering analysis will be made with AGNES method by using number of motor land vehicles based on city, number of traffic accidents resulting in death and injury, number of casualties and injuries (4 different values) for the years 2011 and 2012 prepared by Turkish Statistical Institute (TUIK) and multivariate maps will be produced according to analysis results.

In the application of clustering analysis method, IBM SPSS (Statistical Package for the Social Sciences) developed by IBM Company, was used. Multivariate maps were designed by ArcGIS software developed by ESRI group.

39.1. Multivariate Map Design with AGNES Hierarchical Clustering Method

In application of AGNES method, Euclidean distances were used in determination of similarity of i and j elements that would form the cluster. Euclidean distance of two elements that would form the cluster was calculated with the equation:

$$d_{ij} = \sqrt{(X_i - X_j)^2 + (Y_i - Y_j)^2} \quad (1)$$

In determination of the most suitable cluster number that would be formed in AGNES method, tree structure named dendrogram which is explained in 2nd section is used. Large jumps on dendrogram show the clusters to be formed. However, since the aim is to generate actually homogeneous and different from the other groups in clustering, it is necessary to analyze dendrogram with an auxiliary axis and determine homogeneous groups. SPSS software was used in AGNES Hierarchical Clustering process. Dissimilarity matrix used in clustering process, dendrogram used in determination of cluster numbers and cluster elements were attained with the help of this software. Each node on which tree structure on dendrogram intersects with auxiliary axis represents a cluster. In this way, 5 clusters were determined for both 2011 and 2012 data (Figure 3). Centroid Tables of clusters generated as a result of clustering process are given in Table 1 and Table 2.

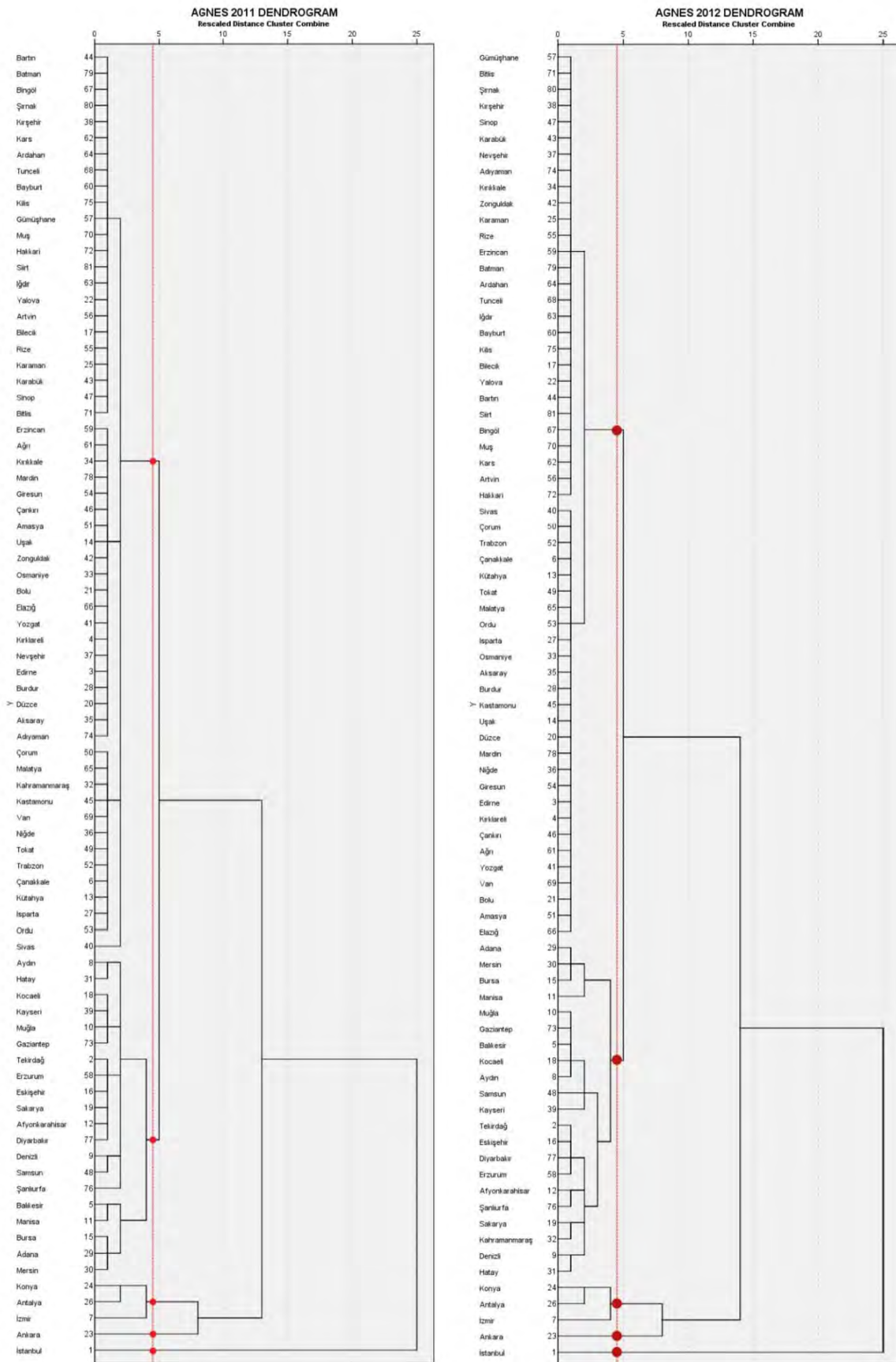


Figure 3. Expression of 2011 and 2012 traffic accident data on dendrogram

Table 3. Centroid values of clusters generated with AGNES method for 2011 data

AGNES CENTROID TABLE (2011)					
	Cluster 1	Cluster 2	Cluster 3	Cluster 4	Cluster 5
Number of Motor Land Vehicle	2927650	1367427	763392.6	289374.5	66371.1
Number of Traffic Accidents with Death – Injury	13887	10318	6210.6	2535,3	683.9
Number of Death	226	164	147.6	79.9	25.1
Number of Injuries	21388	17251	9957.6	4553.5	1401.6

Table 2. Centroid values of clusters generated with AGNES method for 2012 data

AGNES CENTROID TABLE (2012)					
	Cluster 1	Cluster 2	Cluster 3	Cluster 4	Cluster 5
Number of Motor Land Vehicle	3065465	1436349	803977.3	300970	69078.1
Number of Traffic Accidents with Death – Injury	15082	11772	7607.6	2954.7	760.5
Number of Death	247	205	160.3	66	26
Number of Injuries	22772	19466	11899	5130.2	1498.4

Again with the help of classes obtained by using 4 different values in clustering processes with AGNES method, multivariate maps were designed for the years 2011 and 2012 (Figure 4).

40. CONCLUSIONS

In the scope of multivariate mapping, more than one attribute can be displayed in separate maps or in the same map. Designing separate maps for each attribute would make it difficult to compare two objects which have various attributes. Therefore methods in which various attributes are shown in the same map are preferred more. One of the methods in which various attributes are displayed in the same map is to generate thematic map classes by determining the effect of different attributes with clustering analysis. In this sense, in this study, considering traffic accidents in 2011 and 2012 in Turkey, number of vehicles in traffic in these years, number of traffic accidents resulting in death and injuries, number of casualties and injuries parameters, multivariate maps were designed with cluster analysis method.

When designed maps (Figure 4) and clusters and cluster elements determined on dendrogram were analyzed, it is seen that 2011 and 2012 maps designed with AGNES method were the same except for one city (K.maraş). This result shows that multivariate maps designed with AGNES method were quite important in the sense of risk management. Because, risk regions predicted with 2011 data were confirmed in 2012 data.

With this study it was shown that by using clustering method, similar aspects of different spatial objects can be presented by considering more than one attribute. It is thought that by using multivariate maps designed with clustering method, spatial analyses which have important contributions for practices such as risk management, planning etc. can be made.

ACCORDING TO THE ROAD TRAFFIC ACCIDENT STATICS CLUSTERING OF CITIES USING AGNES ALGORITHM

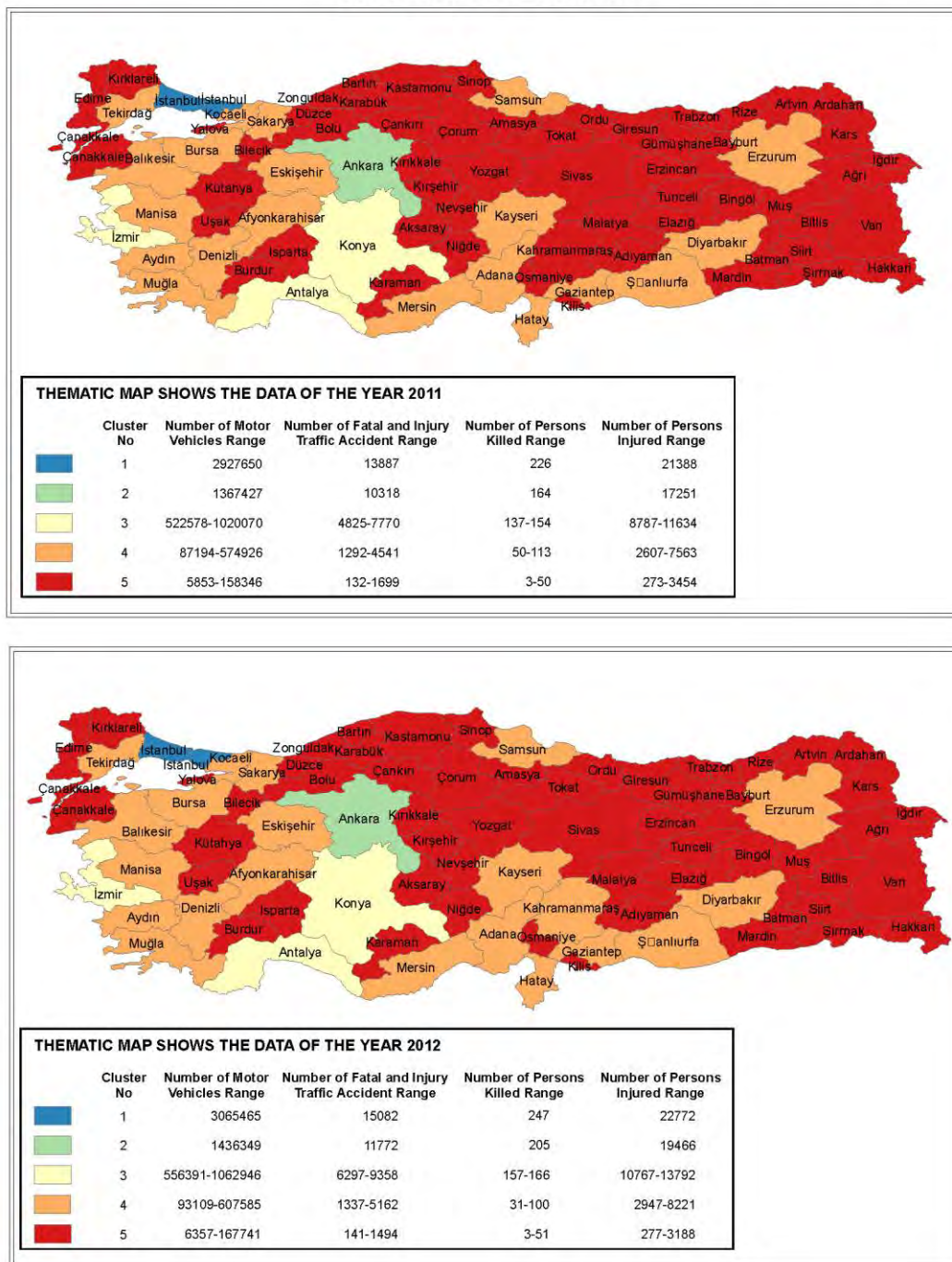


Figure 4. Multivariate maps designed with AGNES method for the years of 2011 (above) and 2012 (below)

REFERENCES

- [89]. A. Buckley, "Multivariate mapping," In *Encyclopedia of Geographic Information Science* edited by Kemp K., 2008, 300-303.
- [90]. T.A. Slocum, R.B. McMaster, F.C. Kessler and H.H. Howard, *Thematic Cartography and Geovisualization*, Pearson Education Inc. Third Edition, USA, 2009.
- [91]. C.A. Brewer, "Color Use Guidelines for Mapping and Visualization", In *Visualization in Modern Cartography* edited by MacEachren A.M. and Taylor D.R.F., 1994, 123-147.

- [92]. G. Metternicht and J. Stott, "Trivariate Spectral Encoding: A Prototype System for Automated Selection of Colours for Soil Maps Based on Soil Textural Composition," *Proceedings of the 21st International Cartographic Conference*, Durban, CD, 2003.
- [93]. J. R. Byron, "Spectral Encoding of Soil Texture: A New Visualization Method," *GIS/LIS Proceedings*, Phoenix, Ariz., 1994, 125-132.
- [94]. V. Interrante, "Harnessing Natural Textures for Multivariate Visualization," *IEEE Computer Graphics and Applications*, 2000, 20(6), 6-11.
- [95]. G. F. Jenks, "Pointillism as a Cartographic Technique," *The Professional Geographer*, 1953, 5, 4-6.
- [96]. D.J. Cox (1990), "The Art of Scientific Visualization," *Academic Computing*, 1990, 4, 20-22, 32-34, 36-38.
- [97]. R. Ellson, "Visualization at Work," *Academic Computing*, 1990, 4(6), 26-28, 54-56.
- [98]. D. Dorling, "The visualization of local urban change across Britain," *Environment and Planning B: Planning and Design*, 1995, 22, 269 - 290.
- [99]. G. Grinstein, J.C.J. Sieg, S. Smith and M.G. Williams, "Visualization for Knowledge Discovery," *International Journal of Intelligent Systems*, 1992, 7, 637-648.
- [100]. C.G. Healey and J.T. Enns, "Large Datasets at A Glance: Combining Textures And Colors In Scientific Visualization," *IEEE Transactions on Visualization and Computer Graphics*, 1999, 5(2), 145-167.
- [101]. J.R. Miller, "Attribute Blocks: Visualizing Multiple Continuously Defined Attributes," *IEEE Computer Graphics and Applications*, 2007, 27(3), 57-69.
- [102]. X. Zhang and M. Pazner, "The Icon Imagemap Technique for Multivariate Geospatial Data Visualization: Approach and Software System," *Cartography and Geographic Information Science*, 2004, 31(1), 29-41.
- [103]. E. S. Nelson and P. P. Gilmartin, "An evaluation of multivariate, quantitative point symbols for maps," In *Cartographic Design: Theoretical and Practical Perspectives* edited by C. H. Wood and C. P. Keller, 1996, 191-203.
- [104]. D. DiBiase, "Designing Animated Maps for A Multimedia Encyclopedia," *Cartographic Perspectives*, 1994, 19, 3-7.
- [105]. E.S. Nelson, "Designing Effective Bivariate Symbols: The Influence of Perceptual Grouping Processes," *Cartography and Geographic Information Science*, 2000, 27(4), 261-78.
- [106]. A. T. Murray and T. H. Grubestic, "Exploring spatial patterns of crime using non-hierarchical cluster analysis," In *Crime modeling and mapping using geospatial technologies*, 2013, 105-124, Springer Netherlands.
- [107]. T. H. Grubestic, R. Wei and A.T. Murray, "Spatial Clustering Overview and Comparison: Accuracy, Sensitivity, and Computational Expense," *Annals of the Association of American Geographers*, 2014, 104(6), 1134-1156.
- [108]. E.Ş. Dinçer, "Veri Madenciliğinde K-means Algoritması ve Tıp Alanında Uygulanması," M. Eng. Thesis, Kocaeli University Institute of Science, Kocaeli, 2006 (in Turkish).
- [109]. J. Han, J.G. Lee and M. Kamber, "An Overview of Clustering Methods in Geographic Data Analysis," In *Geographic Data Mining and Knowledge Discovery* edited by Miller H.J. and Han H., Taylor & Francis Group, LLC, 2009.
- [110]. J. Han and M. Kamber, *Data Mining: Concepts and Techniques*, San Francisco, 2006

Effects of TEMPO, PINO and Periodate on Kraft Pulp Fibers

Ayhan Tozluoğlu¹⁹

Abstract

Cellulose, in the form of fibers or derivatives, is the most abundant and renewable biopolymer resources utilized to produce a wide spectrum of materials. The oxidation of cellulosic materials is a gripping and challenging topic due to the presence of multiple reactive sites causing specific reactions. These pivotal reactions result in materials having superior and diversified properties. In this study, oxidations agents of 2,2,6,6-tetramethylpiperidine-1-oxyl radical (TEMPO), N-hydroxyphthalimide (PINO) and sodium periodate was used to compare structural (FT-IR, ¹³C-NMR), thermal (TGA, DSC) and morphological properties (SEM) of bleached kraft pulp. Homogeneity and surface area were increased with treatments. TEMPO oxidized pulps had the highest thermal stability. Periodate oxidation led significant degradation and glycosidic cleavage in the structure. TEMPO and PINO oxidation affected the viscosity and the lowest viscosity was observed in TEMPO oxidation.

Keywords: Cellulose, kraft, periodate, PINO, TEMPO.

41. INTRODUCTION

Generally, the conventional regenerated cellulose fibers are prepared either by indirect viscose process (viscose fibers) or fibers are modified with the basic procedures. The chemical and physical properties of regenerated fibers can be improved by treatment processes. Some of these processes are alkaline washing, slack-mercerization and bleaching. In addition, oxidation is a method to modify cellulose fibers. Oxidization of cellulose increases the adsorption capability and surface charge density resulting in more accessible negative fiber groups. Oxidized materials are bioresorbable and easily degradable under physiological conditions. These are mostly being used as absorbable hemostatic scaffolding material [1] and as a postsurgical adhesion prevention layer [2]. These materials are in addition used as carrier material for agricultural, cosmetic and pharmaceutical applications [3].

Nitroxides, NO₂ and N₂O₄ have been used for the selective oxidation of primary hydroxyl group of cellulose [4]. NaNO₂ and NaNO₃ are other selective reagents for oxidation of OH group bonded at C6. Alcohols in ionic liquid media are utilized as a mild and an efficient method to oxidize the primary OH groups with [5]. At present, the most studied system to oxidize primary OH group for a wide range of polysaccharides is 2,2,6,6-tetramethyl-1-piperidinyloxy radical (TEMPO) / NaBr / NaOCl [6]. In this system, the actual oxidizing species is the nitrosonium ion [6], the oxidized form of TEMPO. The generation of nitrosonium ion takes place in situ, through the reaction of TEMPO with hypobromide ions, which in turn are produced from bromide salt and NaOCl. The use of non persistent phthalimide-N-oxy (PINO) radical generate in situ from N-hydroxyphthalimide (NHPI) [7]-[10] has been reported for the oxidation of cellulose fibers, at room temperature, pH=10.5 in the presence of NaBr / NaOCl [9]. Another oxidizing agents are periodates which is a specific oxidant. this is able to oxidize the vicinal hydroxyl groups at carbon atoms 2 and 3 in an anhydroglucose unit of cellulose and forms two aldehyde groups. Concomitantly, the carbon-carbon bonds between two carbon atoms of 2 and 3 is broken [11].

In this study, bleached kraft fibers were oxidized by different oxidizing agents. Cellulose modifications are assumed to be advantageous for following nanoscale cellulose production. The chemical, reological, morphological as well as thermal properties of oxidized fibers were examined in this study.

2. MATERIALS AND METHODS

2.1. Materials

For this study, freshly cut logs of a 16-year-old river red gum tree (*Eucalyptus camaldulensis*) collected from Tarsus, Turkey, was used as a raw material. The bark and cambium were carefully removed the logs, which were reduced to chips suitable size for the subsequent kraft pulping operations. The chips were air-dried and screened to establish a uniform size throughout pulping.

¹⁹Corresponding author: Duzce University, Department of Forest Industry Engineering, 81620, Düzce, Turkey. ayhantozluoglu@duzce.edu.tr

2.2. Methods

2.2.1. Pulping and Bleaching

Kraft pulp was produced using 500 g of chips (o.d.). The cook was made in a 10 L rotating digester (Uniterm Rotary Digester, Uniterm Lab.) at 150 °C for 150 min after reaching the maximum temperature in 30 min. The calculated H-factor was 410. The cook was achieved at 18% active alkali and 28% sulphidity charges, and the liquor-to-wood ratio (L/kg) was 5:1. The produced pulp was disintegrated and washed with hot tap water, and then screened using a flat laboratory screen (Somerville Flat Screen, Techlab Systems) with a slot width of 0.15 mm (Tappi T275). The pulp yield (screened/unscreened) and rejects were determined according to Tappi T210 via gravimetric measurements in the laboratory environment. The pulp was bleached using Elemental Chlorine Free (ECF) processes (ODEP: oxygen-chlorine dioxide-alkaline-peroxide). Oxygen (O₂) bleaching was conducted in a digester using 2% NaOH (as Na₂O-o.d. pulp) and 0.5% MgSO₄ (as carbohydrate stabilizer-o.d. pulp) at a pressure of 6 kgf cm⁻² (90 °C for 60 min). The consistency was 10%. The chlorine dioxide (D) bleaching was performed in a plastic bag placed in a water bath (GFL 1023 Water Bath, GFL Lab.) (60 °C for 60 min) and each pulp (10 g, o.d.) was treated with 100 mL ClO₂ (1%) consisting of 3 mL H₂SO₄ (98%) solution. The alkaline extraction (E) was also performed in a water bath at 60 °C for 60 min and each pulp (10 g, o.d.) was treated with 100 mL NaOH solution (2%). The hydrogen peroxide bleaching (P) was conducted at 10% pulp consistency using 4% H₂O₂, 0.5% Na₂SiO₃ (as hydrogen peroxide stabilizer), 0.1% MgSO₄ and 1.5% NaOH (o.d. pulp). The process was carried out at 105 °C for 120 min in a digester. After each bleaching operation, the pulps were washed with water, squeezed and crumbled.

2.2.2. Pretreatments

TEMPO Oxidation

TEMPO-mediated oxidation methodology was applied at neutral pH, as reported by Besbes et al. [12]. 5 g of bleached hardwood Eucalyptus kraft pulp (H1) was suspended in 0.05 M sodium phosphate buffer solution (500 mL, pH 7) that contained TEMPO (25 mg) and NaBr (250 mg). The suspension was stirred to ensure good dispersion of all reagents. Sodium chlorite solution (1.13 g, 10 mM) and sodium hypochlorite solution (1.13 g, 10 mM) were added to the suspension. Then, the mixture was stirred at 500 rpm and 60 °C for 2 h. Oxidation was terminated by adding 100 mL of ethanol. The oxidized fibers (H1O1) were filtered and washed two times and prepared for further analysis.

PINO oxidation

PINO-mediated oxidation methodology was applied as reported by Biliuta et al. [13]. 16 g of bleached hardwood Eucalyptus kraft pulp fibres (H1) were placed in a 3 L two-necked flask, containing 1.4 L deionised water:acetonitrile (6:1 vol), equipped with a balloon filled with O₂. NHPI together with anthraquinone (3.2 mmol of each) were added, and the resulted suspension was kept at room temperature under stirring for 5 days. The reaction was quenched by adding 100 mL ethanol, and the oxidized fibres (H1O2) were filtered off. The recovered fibres were washed with acetone and deionised water and prepared for further analysis.

Periodate Oxidation

Periodate-mediated oxidation methodology was applied as reported by Yang [14]. 4 g of bleached hardwood Eucalyptus kraft pulp fibres (H1) were thoroughly dispersed by a disintegrator, and then filtered to remove extra water from the pulp. Next 5.33 g NaIO₄ and 15.6 g NaCl were dissolved in water, and the wet pulp was added to this solution. The total volume of water was 266 mL, including the moisture from the wet pulp. The oxidation reaction was performed at room temperature stirring at a speed of 105 rpm. The reaction beaker was wrapped with several layers of aluminum foil to prevent entry of any light. At each designed reaction time (10 h, 16 h, 24 h, 96 h), one fourth of the mixture was taken out of the beaker, and ethylene glycol was added into this mixture to quench the reaction by removing the residual periodate. The oxidized pulp (H1O3) was washed thoroughly with water by filtration.

2.2.3. Analytical Methods

FTIR (Fourier transform infrared) Spectroscopy: The IR spectra were taken via an attenuated total reflectance (ATR)-FTIR device (Shimadzu IR Prestige-21, Shimadzu Corp.). Sample suspensions of 0.5 ml were prepared in a concentration of 2% (w/w). The samples were gently dropped in a diamond attachment using an automatic pipette (0.1-1 ml). In order to elucidate molecular vibration signals in the range of 4000-600 cm⁻¹, 20 scans with a resolution of 4 cm⁻¹ were taken.

¹³C CP/MAS NMR (Cross Polarization Magic Angle Spinning Nuclear Magnetic Resonance) Spectroscopy: The solid state ¹³C CP/MAS NMR spectra of the samples were recorded using an Advance III 300-MHz NMR instrument (Bruker Corp.). The operating frequency was fixed at 75.385 MHz. A double air-bearing probe and a zirconium oxide rotor (4 mm) were used in the analysis. The MAS rate was 8500 Hz. A CP pulse was ramped at a contact pulse of 100 μs with the rotation of 4 μs proton at 90° pulse (294.8 °K). The delay between repetitions was 2.5 s.

Rheological Measurements: In order to determine the rheological properties of the samples, a RST-CPS Rheometer (Brookfield Corp.) was used. The measurements were made at the 37.5 mm diameter cone-plate and the 25 mm diameter parallel plate. The gap was fixed at 1 mm. Before the measurements, the shearing was applied to the materials at 20,000 rpm for 2 min (IKA T18 homogenizer, IKA Lab.) to disrupt any flocculated aggregates, and the samples were then allowed to rest for 3 min.

SEM (Scanning Electron Microscopy): The morphological properties of the samples were analyzed by taking SEM (FEI Quanta FEG 250, FEI Corp.) images. The samples were first dried at 105 °C overnight, and then coated up to 5 nm with a gold-palladium composite. Pictures were taken for all samples at 1-15 kV using a field emission gun equipped with a compacted secondary electron detector. Scales were selected as 100 μm for fiber materials and 1 and 100 μm for MFC and NFC. In addition, SEM analysis were carried out for MFC or NFC films.

Thermal Analysis: The thermal properties of the materials were examined using differential scanning calorimetry (DSC) and thermogravimetric analysis (TGA). For the DSC, samples of approximately 3-5 mg of material were first squeezed, and then placed in an aluminum pan. In device chamber the sample was heated from room temperature to 500 °C at the rate of 10 °C min⁻¹. All measurements were carried out under nitrogen flow (75 mL min⁻¹) using a Shimadzu DSC-60 Plus (Shimadzu Corp.) equipped with a thermal analysis data station. The mass of the material was recorded as a function of the temperature. For the TGA, a Shimadzu DTG 60 (Shimadzu Corp.) equipped with a thermal analysis data station was utilized. The material samples were first dried at room temperature overnight. Approximately 5 mg of the material was placed in a platinum pan and heated from room temperature to 650 °C at a rate of 20 °C/min. Measurements were carried out under nitrogen flow (75 mL min⁻¹). The mass of the material was recorded as a function of the temperature.

3. RESULTS AND DISCUSSION

3.1. FTIR Analyzes

FTIR spectra were investigated to elucidate molecular interactions of kraft pulp (H1) and oxidized kraft pulp samples (H1O1, H1O2 and H1O3) (Figure 1). The broad O-H peaks, matched to the free OH groups on the cellulose molecules corresponding to intra and intermolecular H-bonds, which were observed at around 3330 cm⁻¹ (Figure 1a) ([15]- [17]). Treatments of oxidizing agents on kraft pulping creased O-H peaks intensity of all samples due to increasing of O-H concentrations ([16], [18], [19]). This phenomenon could be explained by the cellulose disintegration, reduction of fiber dimensions and more specific surface area ([18], [20]).

C-H asymmetric vibrations, stemming from methylene groups, were observed at around 2895 cm⁻¹. These peaks also indicated crystallinity as well as 1370 cm⁻¹ giving C-H symmetric bending [21]. Intensity of these peaks and some minor shifts, especially for H1O3, were increased after treatments due to increasing surface area and decreasing crystallinity ratio (H1370/H2900) (Figure 1b). Peaks at around 1160cm⁻¹ were related to C₁-O-C₅ asymmetric stretching vibrations of the intra-molecular pyranose rings ([15], [21]). The peak observed at 1025 cm⁻¹ revealed the glycosidic (C₁-O-C₄) deformation of cellulose. H1O3 from periodate treatment resulted in minor shifts on both C₁-O-C₅ in intra-molecular and C₁-O-C₄ in inter molecular interactions (Figure 1c). These shifts were caused due to the glycosidic cleavage and resulted in increased surface area.

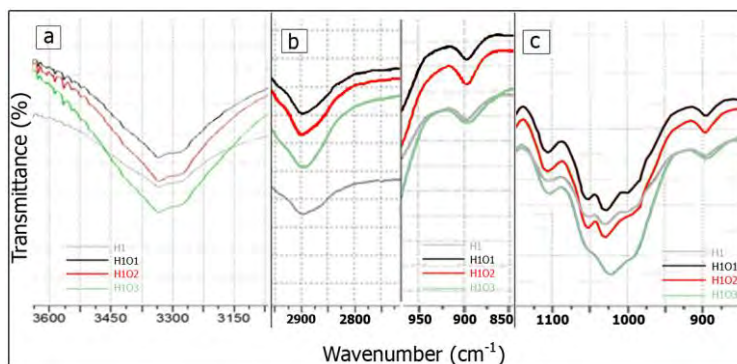


Figure 1. FT-IR spectras of bleached kraft pulp (H1) and its oxidizing samples (H1O1= TEMPO oxidized bleached kraft pulp , H1O2= PINO oxidized bleached kraft pulp and H2O3= Periodate oxidized bleached kraft pulp)

3.2. ^{13}C CP/MAS NMR Analyzes

The chemical structures of the samples were analyzed by CP/MAS ^{13}C -NMR (Figure 2). Some chemical shifts observed could be attributed to the packing effect of the supramolecular structures due to applied treatments as well as specific chemical processes [22]. Lower intensity regarding C peaks compared to other samples were observed in H1O3 that is probably related to more glycosidic cleavage of the cellulose. C4 and C6 peaks give insights about crystalline and non-crystalline forms. They were seen as doubled-collateral peaks at 62 ppm-74 ppm and 40 ppm-48 ppm, respectively. The former (left) peak displayed the crystalline character, whereas the latter (right) showed the amorphous character for both C4 and C6 [23]. In H1O3, some minor alterations has been observed for C4 amorph region and C6 amorph region compared to other oxidized kraft pulp samples. This findings monitored that H1O3 structure had more amorph character by substantiated FTIR and DSC. As of carbonyl peaks, findings were in agreement with the report by Codou et al. [24] and Kim et al. [25]. The report indicated that carbonyl resonance has not been observed in the 175–210 ppm region. The peaks were explained in hemiacetal cross-linkings either within the same cellulose or with adjacent ones.

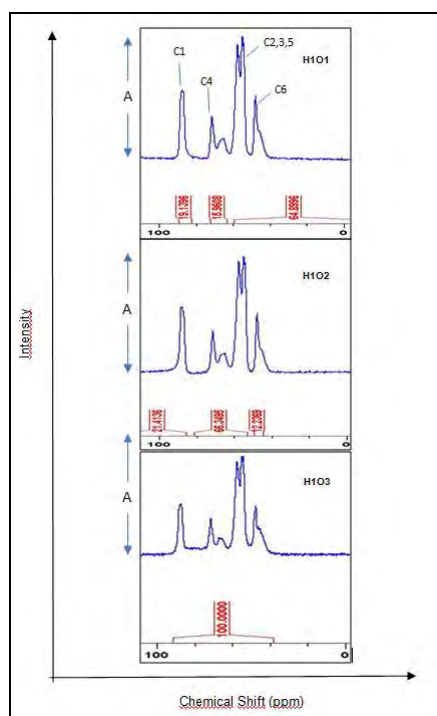


Figure 2. ^{13}C CP/MAS NMR spectras of oxidized samples (H1O1= TEMPO oxidized bleached kraft pulp, H1O2= PINO oxidized bleached kraft pulp and H2O3= Periodate oxidized bleached kraft pulp)

3.3. Rheological Properties

It is known that the rheological behaviour, highly related to the viscosity, depends on shear stress, which is of great importance to predict the usage of the materials. The viscosity as a function of shear rate was depicted in Figure 3. All of suspensions displayed the shear-thinning properties, i.e. viscosity decreased with increasing shear rate. Shear thinning property of cellulose was not changed after all oxidizing treatments. This behavior is known as pseudoplastic characteristic. The high viscosity at low shear rate could be related to the morphology of the samples with exceeding several μm diameter. This circumstance led to the entanglement of the fibrils which caused a strong network structure ([12], [23]). Lower viscosity was obtained in TEMPO-oxidized bleached kraft pulp and this could be explained by the electrostatic repulsion resulting from the presence of a high level of ionized carboxyl groups on the surface of the fibrils. This diminished the extent of the interaction among TEMPO-oxidized kraft pulp. Also, PINO oxidation had no significant effect on the viscosity.

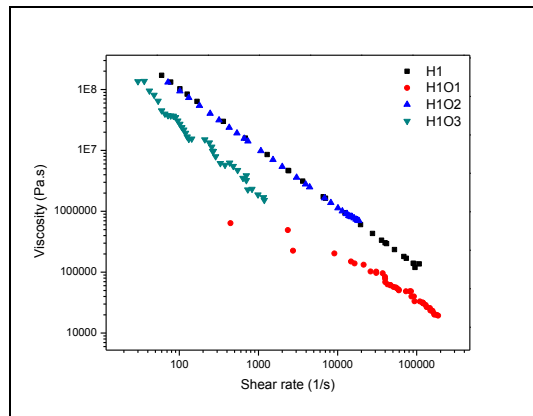


Figure 3. Viscosity as a function of the shear rate for bleached kraft pulp (H1) and its oxidizing samples (H1O1= TEMPO oxidized bleached kraft pulp, H1O2= PINO oxidized bleached kraft pulp and H1O3= Periodate oxidized bleached kraft pulp)

3.4. Morphological (Structural) Properties

SEM morphological analysis was carried out to investigate surface alterations as well as fibril dimensions (Figure 4). Oxidized kraft pulp (H1O1, H1O2 and H1O3) had almost similar fibril diameter (8-12 μm). In addition, the more homogenous structure was observed when compared to bleached kraft pulp. In the process, C6 carboxylated groups were probably formed in cellulose microfibrils surface which were negatively charged. Electrostatic repulsion and/or osmotic effects between anionically-charged cellulose microfibrils caused completely individualized nanofibrils which were dispersed in water by mechanical disintegration followed by TEMPO-PINO-Periodate oxidations [26]. In addition, some damaged zones were observed in oxidized samples especially sample oxidized with periodate. In addition, sample oxidized with periodate had much more complex structure as observed in the DSC analysis. Obtained results are in good agreement with literature [12].

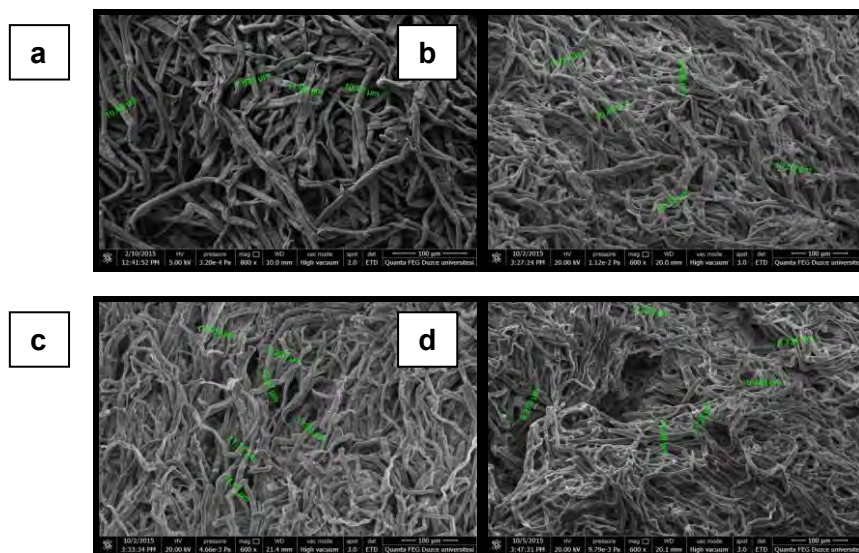


Figure 4. SEM images: a) H1, b) H1O1, c) H1O2, d) H1O3 (H1=bleached kraft pulp, H1O1= TEMPO oxidized bleached kraft pulp, H1O2= PINO oxidized bleached kraft pulp and H1O3= Periodate oxidized bleached kraft pulp)

3.5. Thermal Characterization

3.5.1. DSC Analyses

DSC curves for kraft pulp and oxidized samples (H1O1, H1O2 and H1O3) were given in Figure 5. Mainly two considerable endothermic peaks were observed at around 25°C-150°C and 350°C-380°C. Exception observed with H1O3. The first observed peak could be attributed to the loss of water in the samples. The later peaks observed at around 350-380 °C indicated the degree of cellulose decomposition. The first endothermic peaks for all oxidized samples were shifted to the higher temperature because of increasing hydroxyl groups formed with new surface area. Sample treated with TEMPO (H1O1) displayed higher thermal stability compared other samples. These thermal behaviors associated with crystallinity and TEMPO-oxidization increased the crystallinity ([27], [28]). Besides periodate treatment, kraft pulp revealed much more amorph structure as substantiated by FT-IR and ¹³C-NMR. This is probably due to cleavage of glycosidic bonds during the treatments.

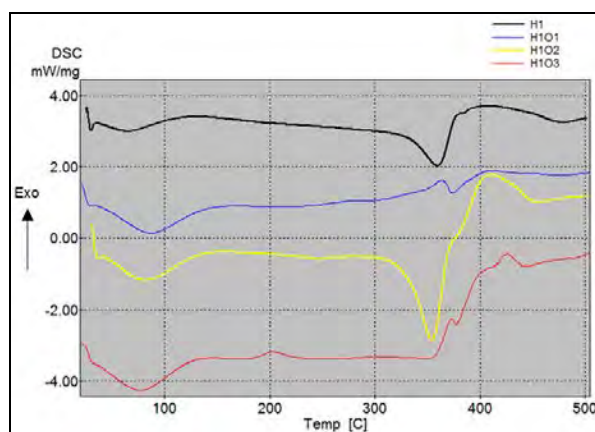


Figure 5. DSC curves registered at a range of room temperature to 500 °C for bleached kraft pulp (H1) and its oxidizing samples (H1O1= TEMPO oxidized bleached kraft pulp , H1O2= PINO oxidized bleached kraft pulp and H2O3= Periodate oxidized bleached kraft pulp)

3.5.2. TGA Analyses

The TGA thermograms of kraft pulp and oxidized samples were given in Figure 6. A small weight loss (5-8%) in the first range ascribed with the removal of humidity and some low molecular weight compounds from the structure (25-150 °C) [29]. Compared to kraft pulp, oxidized samples revealed higher decomposition in first range. This could be due to the increase in aspect ratio and surface area that caused faster heat transfer and diminished the thermo stability ([30]-[32]). A significant weight loss, higher decomposition related to cellulose and hemicellulose removal, was observed between 300-380 °C (around 70% by mass). However, the degradation started earlier for H1O3 and this finding was explained with the cleavage of glycosidic as well as other covalent bonds ([8], [33]). This situation was more pronounced for H1O3 that periodate oxidation posed more amorphous alteration that made easier to decompose through thermo oxidative reactions. Conversion to amorphous structure were substantiated by DSC, FT-IR and ¹³C-NMR. Also, this behavior showed that glycosidic cleavage of the cellulose reduced the polymerization degree leading to the formation of CO₂, H₂O and variety of hydrocarbon derivatives (H1O2) [21]. The weight loss associated with the char decomposition was the highest for the H1O1.

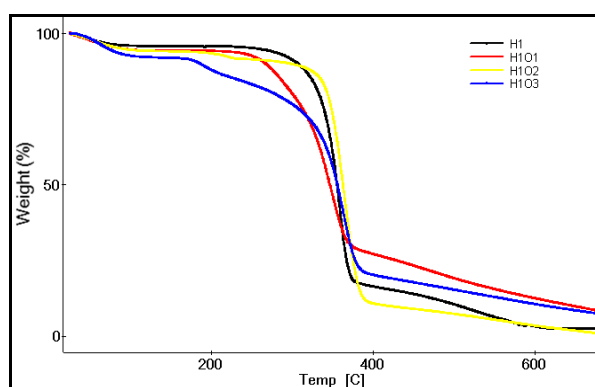


Figure 6. TGA curve of bleached kraft pulp (H1) and its oxidizing samples (H1O1= TEMPO oxidized bleached kraft pulp , H1O2= PINO oxidized bleached kraft pulp and H2O3= Periodate oxidized bleached kraft pulp)

4. CONCLUSIONS

The main aim of this study was to determine structural, thermal, viscoelastic and morphological properties of bleached kraft pulp that was oxidized with TEMPO, PINO and periodate. Oxidation efficiency of samples were evaluated regarding O-H, C-O, C-O-C, and ¹³C-NMR resonances, crystallinity, thermal stability, viscosity and fibrils textures. It could be concluded that periodate mostly induced the structural degradation due to the cleavage of glycosidic bonds. It formed other cellulose derivatives.

Oxidization improved the surface area having more hydroxyl groups. The crystallinity of the samples were altered and TEMPO oxidized sample had the highest crystallinity. The morphology of the samples were mostly unaffected in TEMPO and PINO, however considerable damage zones and fragmentations were observed when bleached kraft pulp was oxidized with periodate. The lower viscosity value was obtained with TEMPO oxidation, whereas no significant alteration was observed with PINO oxidation.

ACKNOWLEDGEMENT

This work was supported by The Scientific and Technological Research Council of Turkey (TUBITAK Project: 114O022).

REFERENCES

- [1]. G. J. Dias, P. V. Peplow, and F. Teixeira, "Osseous regeneration in the presence of oxidized cellulose and collagen," *Journal of Materials Science: Materials in Medicine*, vol. 14, pp. 739-745, Sep. 2003.
- [2]. D. M. Wiseman, L. Saferstein, and S. Wolf, "Bioresorbable oxidized cellulose composite material for prevention of postsurgical adhesions," U.S. Patent 6 500 777, Dec. 31, 2002.
- [3]. B. Jin, and W.-T. Wu, "Compositions for veterinary and medical applications". PCT WO/2005/020997 (2005).
- [4]. D. S. Zimnitsky, T. L. Yurkshtovich, and P. M. Bychkovsky, "Synthesis and characterization of oxidized cellulose," *J. Polym. Sci., Part A: Polym. Chem.*, vol. 42, pp. 4785-4791, Aug. 2004.
- [5]. J. Safaei-Ghomi, A. R. Hajipour, and M. Esmaeili, "Mild and efficient method for oxidation of alcohols in ionic liquid media," *Digest journal of nanomaterials and biostructures*, vol. 5, pp. 865-871, Oct. 2010.
- [6]. P. L. Bragd, H. Bekkum, and A. C. Besemer, "TEMPO-Mediated Oxidation of Polysaccharides: Survey of Methods and Applications," *Top. Catal.*, vol. 27, pp. 49-66, Feb. 2004.
- [7]. S. Coseri, "Phthalimide-N-oxyl (PINO) Radical, a Powerful Catalytic Agent: Its Generation and Versatility Towards Various Organic Substrates," *Catal. Rev.*, vol. 51, pp. 218-292, May 2009.
- [8]. S. Coseri, "A New and Efficient Heterogeneous System for the Phthalimide N-Oxyl (PINO) Radical Generation," *Eur. J. Org. Chem.*, vol. 2007, pp. 1725-1729, Apr. 2007.
- [9]. S. Coseri, G. Nistor, L. Fras, S. Strnad, V. Harabagiu, and B. C. Simionescu, "Mild and selective oxidation of cellulose fibers in the presence of N-hydroxyphthalimide," *Biomacromolecules*, vol. 10, pp. 2294-2299, Aug. 2009.
- [10]. S. Coseri, "N-Hydroxyphthalimide (NHPI)/lead tetraacetate reactions with cyclic and acyclic alkenes," *J. Phys. Org. Chem.*, vol. 22, pp. 397-402, Dec. 2008.
- [11]. S. Coseri, G. Biliutaa, B.C. Simionescua, K. Stana-Kleinschekc, V. Ribitschd, and V. Harabagiu, "Oxidized cellulose-survey of the most recent achievements," *Carbohydrate Polymers*, vol. 93, pp. 207-215, Mar. 2013.
- [12]. I. Besbes, M. Rei Vilar, S. Boufi, "Nanofibrillated cellulose from Alfa, Eucalyptus and Pine fibres: Preparation, characteristics and reinforcing potential," *Carbohydrate Polymers*, vol. 86, pp. 1198-1206, Aug. 2011.
- [13]. G. Biliuta, L. Fras, V. Harabagiu, and S. Coseri, "Mild oxidation of cellulose fibers using dioxygen as ultimate oxidizing agent," *Digest Journal of Nanomaterials and Biostructures*, vol. 6 pp. 291- 297, Jan. 2011.
- [14]. Yang, "Investigation and characterization of oxidized cellulose and cellulose nanofiber films," Msc thesis, Department of Chemistry, McGill University, Montreal, Quebec, Canada, Aug. 2011.
- [15]. A. Mandal, and D. Chakrabrty, "Isolation of nanocellulose from waste sugarcane bagasse and its characterization," *Carbohydrate Polymers*, vol. 86, pp. 1291-1299, Aug. 2011.
- [16]. E. Abraham, B. Deepa, L. A. Pothen, J. Cintil, S. Thomas, M. J. John, R. Anandjiwala, and S. S. Narine, "Environmental friendly method for the extraction of coir fibre and isolation of nanofibre," *Carbohydrate Polymers*, vol. 92, pp. 1477-1483, Feb. 2013.
- [17]. M. C. Popescu, C. M. Popescu, G. Lisa, and Y. Sakata, "Evaluation of morphological and chemical aspects of different wood species by spectroscopy and thermal methods," *Journal Molecular Structure*, vol. 988, pp. 65-72, Mar. 2011.
- [18]. H. M. Ng, L. T. Sin, T. T. Tee, S. T. Bee, D. Hui, C. Y. Low, and A. R. Rahmat, "Extraction of cellulose nanocrystals from plant sources for application as reinforcing agent in polymers," *Compos Part B Eng.*, vol. 75, pp. 176-200, Jun. 2015.
- [19]. F. Jiang, and Y. L. Hsieh, "Chemically and mechanically isolated nanocellulose and their self-assembled structures," *Carbohydrate Polymers*, vol. 95, pp. 32-40, Jun. 2013.
- [20]. T. N. Ang, G. C. Ngoh, A. S. M. Chua, and M. G. Lee, "Elucidation of the effect of ionic liquid pretreatment on rice husk via structural analyses," *Biotechnology for Biofuels*, vol. 5, pp. 67-77, Aug. 2012.
- [21]. M. Poletto, V. Pistor, and A. J. Zattera, "Structural characteristics and thermal properties of native cellulose," *Materials*, vol. 7, pp. 6105-6119, 2014.
- [22]. G. Zuckerstätter, G. Schild, P. Wollboldt, T. Röder, H. Weber, and H. Sixta, "The elucidation of cellulose supramolecular structure by ¹³C CP-MAS NMR," *Lenzinger Berichte*, vol. 87, pp. 38-46, 2009.
- [23]. M. Pääkko, M. Ankerfors, H. Kosonen, A. Nykänen, S. Ahola, M. Österberg, J. Ruokolainen, J. Laine, P.T. Larsson, O. Ikkala, and T. Lindström, "Enzymatic hydrolysis combined with mechanical shearing and high- pressure homogenization for nanoscale cellulose fibrils and strong gels," *Biomacromolecules*, vol. 8, pp. 1934-1941, May.2007.
- [24]. A. Codou, N. Guigo, L. Heux, and N. Sbirrazzuoli, "Partial periodate oxidation and thermal cross-linking for the processing of thermoset all-cellulose composites," *Composites Science and Technology*, vol. 117, pp. 54-61, Sep. 2015.
- [25]. U.J. Kim, S. Kuga, M. Wada, T. Okano, and T. Kondo, "Periodate oxidation of crystalline cellulose," *Biomacromolecules*, vol. 3, pp. 488-492, Jul. 2000.
- [26]. A. Isogai, T. Saito, and H. Fukuzumi, "TEMPO-oxidized cellulose nanofibers," *Nanoscale*, vol. 3, pp. 71-85, Oct. 2011.
- [27]. S. F. S. Draman, R. Daik, F. A. Latif, and S. M. El-Sheikh, "Characterization and thermal decomposition kinetics of kapok (Ceibapentandra L.)-based cellulose," *BioResources*, vol. 9, pp. 8-23, 2014.
- [28]. T. Hosoya, and S. Sakaki, "Levoglucosan formation from crystalline cellulose: importance of a hydrogen bonding network in the reaction," *ChemSusChem*, vol. 6, pp. 2356-2368, Dec. 2013.
- [29]. W. Chen, H. Yu, Y. Liu, P. Chen, M. Zhang, and Y. Hai, "Individualization of cellulose nanofibers from wood using high-intensity ultrasonication combined with chemical pretreatments," *Carbohydrate Polymers*, vol. 83, pp. 1804-1811, Feb. 2010.

- [30]. M. G. Thomas, E. Abraham, P. Jyotishkumar, H. J. Maria, L. A. Pothen, and S. Thomas, "Nanocelluloses from jute fibers and their nanocomposites with natural rubber: Preparation and characterization," *International Journal of Biological Macromolecules*, vol. 81, pp. 768–777, Nov. 2015.
- [31]. P. Lu, and Y. L. Hsieh, "Preparation and properties of cellulose nanocrystals: Rods, spheres, and network," *Carbohydrate Polymers*, vol. 82, pp. 329–336, Sep. 2010.
- [32]. Y. Shimazaki, Y. Miyazaki, Y. Takezawa, M. Nogi, K. Abe, S. Ifuku, and H. Yano, "Excellent thermal conductivity of transparent cellulose nanofiber/epoxy resin nanocomposites," *Biomacromolecules*, vol. 8, pp. 2976–2978, Aug. 2007.
- [33]. W. S. Chen, H. P. Yu, and Y. X. Liu, "Preparation of millimeter-long cellulose I nanofibers with diameters of 30–80 nm from bamboo fibers," *Carbohydrate Polymers*, vol. 86, pp. 453–461, Aug. 2011.

Flexural properties of micro-size Oak wood and correlation with standard-size samples

Ümit Büyüksarı²⁰

Abstract

*Structural-size and standard-size have been used to determine the mechanical properties of wood. In recent years, micro-sized samples have been used to evaluate the mechanical properties of wood. The aim of this study was to investigate flexural properties of micro-size Oak wood (*Quercus petraea* Lieb.) and to compare with standard-size test specimens values. Bending strength and modulus of elasticity in bending were determined using standard-size and micro-size test samples. In the standard- and micro-size samples, bending strengths were evaluated as 99.4 and 71.2 N/mm² and modulus of elasticity in bending as 11394.1 and 2741.3 N/mm², respectively. The results showed that the bending strength and modulus of elasticity of the micro samples were lower compared to the standard samples. Furthermore, regression analyses indicated a positive linear regression between the micro- and standard-size samples. When it is not possible to obtain standard size samples, micro- size samples can be used to determine mechanical properties of wood.*

Keywords: flexural properties, micro-size, standard size, oak wood, correlation.

42. INTRODUCTION

Structural-size with defects and standard-size (small-size clear samples) have been used to determine the mechanical properties of wood. In recent years, microscale-sized samples have been used to evaluate the mechanical properties of earlywood and latewood sections, wood strands, and fibers [1-7]. The using of micro-size test samples will provide facility to determine mechanical properties of wood when it is not possible to obtain standard size samples in structural areas such as wooden bridge, historic buildings etc. Strength loses depending on time can be determined by using micro-size samples in the structural using areas of wood. Periodically, test samples from structural wood materials can be taken and mechanical properties of them would be determined. Also, changes in the mechanical properties of the wood over time could be observed. Especially, historical wooden buildings would be effectively evaluated.

There is no standard about the micro-size test samples. Therefore, sample dimensions and loading rates vary according to the purpose of the study. Different dimensions and loading rates were used by several researchers. The bending properties of red oak, white oak, and sweetgum flakes dried at 20, 150, and 350 °C investigated by Plagemann [8]. The size of the specimens was 0.5 × 3.8 × 14.2 mm and loading rate was 0.029 mm/min. It was reported that the modulus of rupture and modulus of elasticity values of the flakes dried at 20 °C were 91 and 4068 MPa for white oak, 102 and 4799 MPa for red oak and 101 and 5281 MPa for sweetgum, respectively. Hindman and Lee [6] measured the bending and tensile properties of both earlywood and latewood sections of loblolly pine (*Pinus taeda*) strands. Dimensions were used 33.0 × 11.0 × 0.68 mm in the bending test and 60 × 0.66 × 4.58 mm for earlywood, and 60 × 0.66 × 3.3 mm for latewood in

the tension test. The loading rate was selected as 0.127 mm/min. Deomano and Zink-Sharp [7] investigated the bending properties of wood flakes. The size of the specimens was 25 × 5.0 × 0.6 mm and loading rate was 2.54 mm/min. It was determined that the modulus of rupture and modulus of elasticity values to be 66.0 and 4086.9 MPa for southern pine, 78.6 and 4430.6 MPa for sweetgum, and 89.0 and 5829.4 MPa for yellow poplar, respectively.

There is limited information concerning the comparison of flexural properties of micro- and standard-size samples. Moreover, in previous studies, authors have compared their findings for micro-size samples with the published values for the standard-size samples in the Wood Handbook [9]. This is not true way to get information about whether there is correlation between micro-size and standard-size samples or not. Because it is well known that tree age and growth conditions such as climate, soil characteristics, slope and altitude affects mechanical properties of wood. This paper aims to evaluate the mechanical properties of Oak wood (*Quercus petraea* Lieb.) using micro-size samples and to compare with standard-size samples.

²⁰Corresponding author: Duzce University, Department of Forest Industry Engineering, 81620, Düzce, Turkey. umitbuyuksari@duzce.edu.tr

2. MATERIALS AND METHODS

2.1. Materials

Sample trees were harvested from the Duzce Forest Enterprises in the northwestern part of Turkey. Six trees having straight stems were selected as sample trees. Table 1 presents the properties of the sample trees. Logs of 3 m in length were cut from each tree. Micro- and standard-size test samples were prepared from lumber cut from these logs.

Table 1. Properties of the sample trees

Tree species	Tree no.	Diameter of tree at 1.30 m (cm)	Tree age (year)	Altitude (m)	Direction	Slope (%)
Oak	1	34	203	670	East	60
	2	39	207			
	3	38	138			
	4	40	193			
	5	41	214			
	6	40	204			

The cutting plan of the test samples is shown in Figure 1. All specimens were conditioned in a climate chamber at a temperature of 20 °C and a relative humidity of 65% for three weeks before testing.

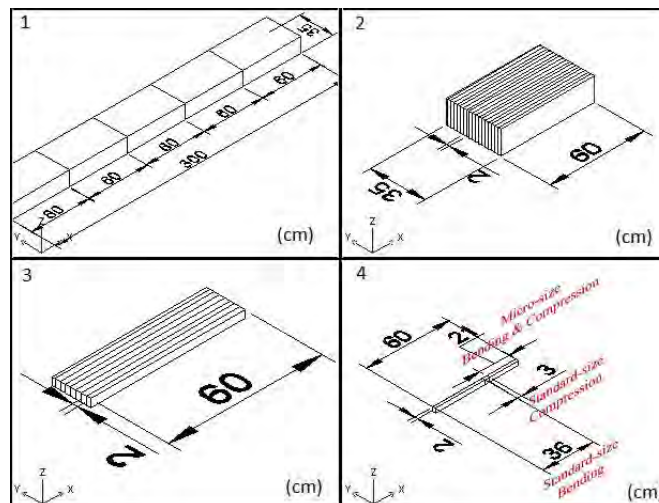


Figure 1. Cutting plan of bending test samples at standard- and micro-size

2.2. Methods

Standard-size test specimens were cut according to International Organization for Standardization (ISO) in order to determine the bending strength (ISO 13061-3) [10] and modulus of elasticity in bending (ISO 13061-4) [11]. A Lloyd universal test machine with a 10 kN load cell was used for the standard-size tests.

Micro-size tests were performed with a Zwick universal test machine using a 100 N load cell for bending tests. The same standards were used as a guide for the micro-size samples. The micro-size bending test samples were approximately 50.0 × 5.0 × 1-1.3 mm. The tests were performed with a three-point bending fixture. The same span/thickness ratio was used for both the micro-size and standard-size bending tests. The testing speed of the bending test for the micro-size samples were 1.2 mm/min. Number of test specimens were 400 for both standard-size and micro-size. The micro-size and standard-size bending test sample and test setup is shown in Figure 2 (a) and Figure 2 (b).



Figure 2. (a) Standard-size bending test sample and test setup (b) Micro-size bending test sample and test setup

2.3. Data analyses and statistical methods

For the bending strength and modulus of elasticity in bending, all multiple comparisons were first subjected to an analysis of variance (ANOVA) at $p < 0.05$ considering two factors (sample size and tree number) and interactions. Post-hoc comparisons were conducted using Duncan's multiple range test. Regression analysis was used to determine the relationship between standard- and micro-size samples.

3. RESULTS AND DISCUSSION

3.1. Bending strength

Figure 3 shows the average bending strength values the standard- and micro-size Oak wood. The average bending strength of micro-size samples was found to be 71.2 MPa. Plagemann [8] determined that the bending strength of white oak and red oak were 91 MPa and 102 MPa, respectively. In this current study, lower bending strength for white Oak wood was determined compared to Plagemann [8] results. This could be attributed to the dimensions of the specimens, the loading speed, the ratio of earlywood and latewood and span/thickness ratio. Jeong [1] pointed out that the results of previous studies are not directly comparable because of different loading conditions and different wood species.

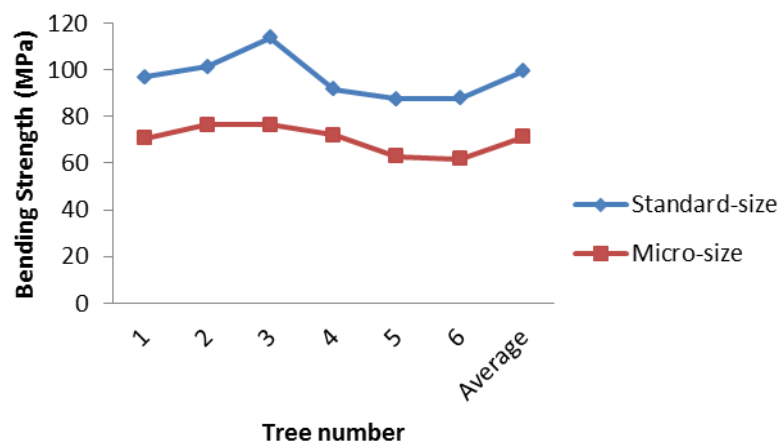


Figure 3. The average bending strength values the standard- and micro-size Oak wood

The average bending strength of standard-size samples was found to be 99.4 MPa. The results showed that the bending strength value of the standard-size samples was 39.6% higher compared to the micro-size samples. Deomano and Zink-Sharp [7] compared their findings for micro-size samples with the published values in the Wood Handbook [9] for standard specimens. They found that the bending strength values of the standard specimens were higher by 25.0% for southern yellow pine and 8.9% for sweetgum, while they were lower by 27.1% for yellow poplar. Zink-Sharp and Price [12] pointed out that comparison of experimentally determined values with standard handbook values was often useful, but not all-encompassing. This current study provides more effective comparison than previous studies because of using wood samples from the same trees.

3.2. Modulus of elasticity in bending

Figure 4 shows the average modulus of elasticity in bending values of the standard- and micro-size Oak wood. The average modulus of elasticity of micro-size Oak wood was determined as 2883.9 MPa. Deomano and Zink-Sharp [7] found that the modulus of elasticity of southern pine, sweet gum, and yellow poplar were 4086.9, 4430.6, and 5829.4 MPa, respectively. Plagemann [8] determined that the MOE values of white oak, red oak and sweetgum in micro-size samples were 4068, 4799 and 5281 MPa. In this current study, lower modulus of elasticity for white Oak wood was determined compared to previous studies results. This could be attributed to the dimensions of the specimens (especially thickness of specimens), the loading speed and span/thickness ratio. Plagemann [8] used samples with $0.5 \times 3.8 \times 14.2$ mm dimensions and applied loading rate of 0.029 mm/min. In this current study, samples dimensions were $1-1.3 \times 5.0 \times 50.0$ mm dimensions and the loading rate was 1.2 mm/min.

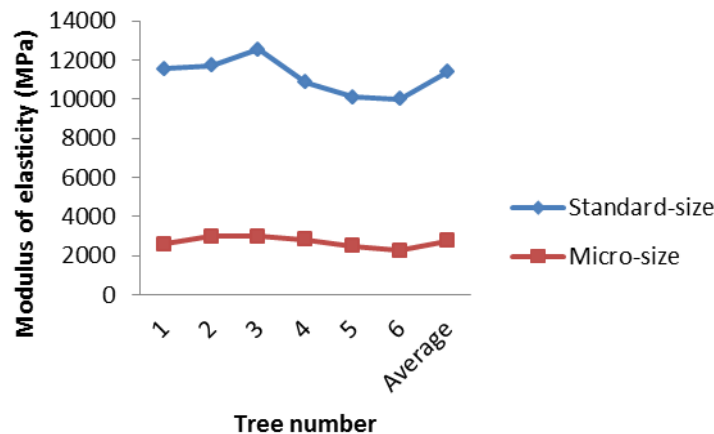


Figure 4. The average modulus of elasticity values the standard- and micro-size Oak wood

The average modulus elasticity was found to be 11394.1 MPa for standard-size samples. The results showed that the modulus of elasticity value of the micro-size samples was 74.7 % lower compared to the standard-size samples. Similar lower modulus of elasticity values was observed for different wood species in micro-size samples by Deomano and Zink-Sharp [7]. They found that the modulus elasticity values of micro-size specimens were lower by 66.9% for southern yellow pine, 60.8% for sweetgum and 46.5% for yellow poplar.

Statistical comparisons of the entire data set were made with regard to the main effects of sample size (micro- and standard-size) and tree number. For the bending strength and modulus of elasticity, all factors were significantly different ($p < 0.000$). Regression analyses graphics for the bending strength and modulus of elasticity of the micro-size and standard-size wood samples are shown in Figures 5 and 6, respectively.

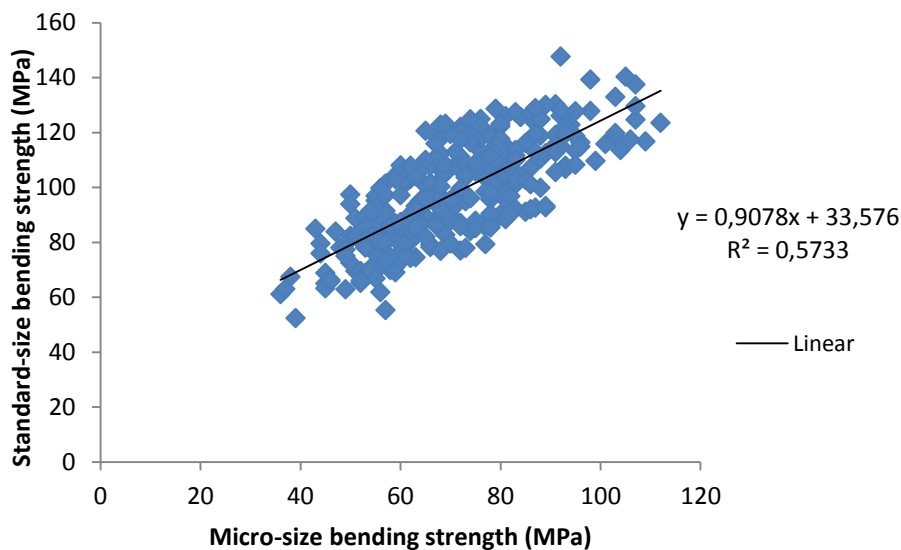


Figure 5. Regression analyses results for bending strength of the micro and standard wood samples

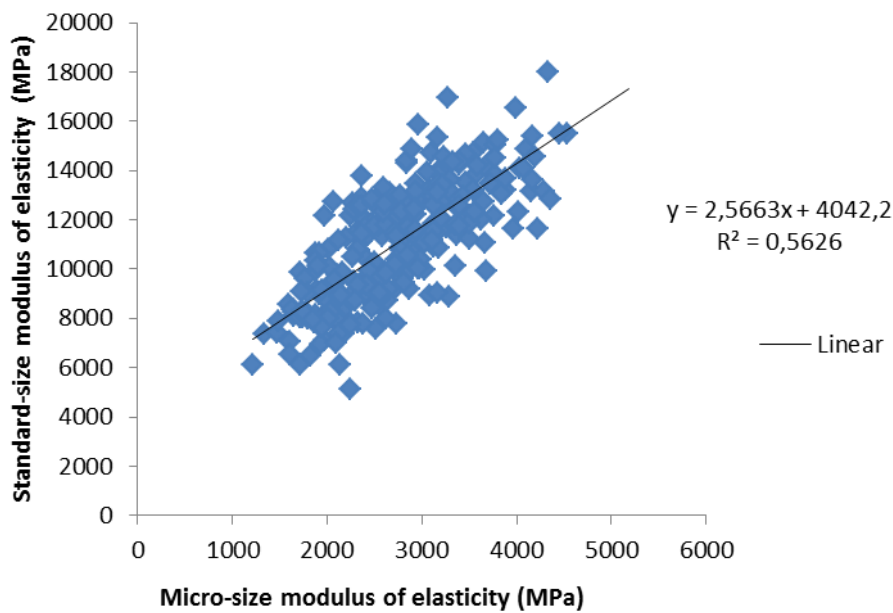


Figure 6. Regression analyses results for modulus of elasticity of the micro and standard wood samples

The regression analyses indicated that flexural properties of the micro-size samples were significantly correlated with the standard samples ($p < 0.000$). The correlation between bending strength and modulus of elasticity values of the standard-size and micro-size samples showed a positive linear relation, presenting an R^2 of 0.573 and 0.563, respectively.

4. CONCLUSIONS

From this study, the following conclusions can be drawn:

1. The bending strength and modulus of elasticity values of the micro-size samples were lower compared to the standard-size samples.
2. The bending strength and modulus of elasticity values of the standard-size and micro-size samples of Oak wood were statistically significant.
3. The regression analyses indicated that flexural properties of the micro-size samples were significantly correlated with the standard samples.

ACKNOWLEDGEMENT

This work was supported by The Scientific and Technological Research Council of Turkey (TUBITAK Project: 112O815).

REFERENCES

- [34]. G. Y. Jeong, "Tensile properties of loblolly pine strands using digital image correlation and stochastic finite element method", Doctoral dissertation, Virginia Polytechnic Institute & State University, 2008.
- [35]. G. Y. Jeong, A. Zink-Sharp, and D. P. Hindman, "Tensile properties of earlywood and latewood from loblolly pine (*Pinus taeda*) using digital image correlation", *Wood Fiber Sci*, vol. 41, pp. 51-63, 2009.
- [36]. L. Groom, S. Shaler, and L. Mott, "Mechanical properties of individual southern pine fibers. Part III. Global relationships between fiber properties and fiber location within an individual tree", *Wood Fiber Sci*, vol. 34, pp. 238-250, 2002.
- [37]. L. Mott, L. Groom, and S. Shaler, "Mechanical properties of individual southern pine fibers. Part II. Comparison of earlywood and latewood fibers with respect to tree height and juvenility", *Wood Fiber Sci*, vol. 34, pp. 221-237, 2002.
- [38]. D. E. Kretschmann, S. M. Cramer, R. Lakes, and T. Schmidt, "Selected mesostructure properties in loblolly pine from Arkansas plantations. In: Stokke DD, Groom LH (eds) Characterization of the cellulosic cell wall. Blackwell, pp. 149 – 170, 2006.
- [39]. D. P. Hindman, and J. N. Lee, "Modeling wood strands as multi-layer composites: bending and tension loads", *Wood Fiber Sci*, vol. 39, pp. 516-526, 2007.
- [40]. E. C. Deomano, and A. Zink-Sharp, "Bending properties of wood flakes of three southern species", *Wood Fiber Sci*, vol. 36, pp. 493-499, 2004.

- [41]. W. L. Plagemann, "The response of hardwood flakes and flakeboard to high temperature drying". Master's thesis, Washington State University, 1982.
- [42]. D. W. Green, J. E. Winandy, and D.E. Kretschman, "Mechanical properties of wood. In: Wood handbook-Wood as an engineering material, Gen. Tech. Rep. FPL-GTR-113, Chapter 12. U.S. Department of Agriculture, Forest Service, Forest Products Laboratory: Madison, WI, 463 p., 1999.
- [43]. ISO 13061-3, "Physical and mechanical properties of wood -- Test methods for small clear wood specimens -- Part 3: Determination of ultimate strength in static bending", International Organization for Standardization, Geneva, Switzerland, 2014.
- [44]. ISO 13061-4, "Physical and mechanical properties of wood -- Test methods for small clear wood specimens -- Part 4: Determination of modulus of elasticity in static bending", International Organization for Standardization, Geneva, Switzerland, 2014.
- [45]. A. Zink-Sharp, and C. Price, "Compression strength parallel to the grain within growth rings of low density hardwoods", Maderas: Ciencia y Tecnologia, vol. 8, pp. 117-126, 2006.

The Kinematic Structures of Gülbahçe Fault (İzmir, Western Anatolia)

Oya Pamukçu¹, Ayça Çirmik¹, Fikret Doğru²¹

Abstract

In this study, the kinematic structures of Gülbahçe fault (İzmir, Western Anatolia) were examined by using GNSS data. The southern side of N-S directional Gülbahçe fault is located in Sığacık Bay which is seismically active region. It has emerged the necessity to investigate the structure, features and continuity of this fault for determining its contribution to seismic activity on its southern region. In the scope of this study, for examining these mentioned subjects, GNSS data obtained from the measurements realized in İzmir between the years 2009 and 2011 were used. The GNSS stations located near to the fault were chosen and relatively GNSS solutions were done by using GAMIT/GLOBK software. Then, Gülbahçe fault was modeled within Coluomb 3.3 software by using the velocities obtained from relatively solutions. The fault parameters of model given best fitting between the obtained and calculated velocities were reached and compared with the geological knowledge. Consequently, the structural features of Gülbahçe fault parameters which have not been known so far were discussed within this study in the literature as the first time.

Keywords: coulomb, fault parameters, GNSS, Gülbahçe Fault, Western Anatolia

43. INTRODUCTION

Gülbahçe fault is one of the faults located on south of İzmir which is coastal city of Western Anatolia. This fault is an important border which separates İzmir bay and Karaburun Peninsula due to their structural and morphological differences (Figure 1). The continental part of the fault extends through Gülbahçe Bay and Sığacık Bay. Both ends of the N-S directional fault are located beneath these bays. The total length of the fault with submarine sides is approximately 70 km [1].

In the previous study [1], it was pointed out that the strike-slip sense was dominant at Gülbahçe fault. It was defined that the fault was oriented to the west by Karaburun. Additionally, reverse fault components were determined at north side of the fault, but these components were not detected at the south side. It was indicated that detailed researches were required for explaining the regional morphotectonically structure and general geometry of the fault.

The kinematic structures of Western Anatolian grabens were investigated by GNSS relatively solutions and fault modeling in the study of [2]. In the scope of this study, Gülbahçe fault was examined with the same methods.

²¹ DOKUZ EYLUL UNIVERSITY, ENGINEERING FACULTY DEPARTMENT OF GEOPHYSICAL ENGINEERING, TINAZTEPE CAMPUS, 35160, Buca/İzmir, Turkey. oya.pamukcu@deu.edu.tr

In this study, GNSS data obtained in the scope of The Scientific and Technological Research Council of Turkey (TUBITAK) Project (No: 108Y285), realized in İzmir and its surroundings between the years 2009 and 2011, were used. The GNSS data of the stations located near to Gülbahçe faults were processed and relatively calculations were obtained due to the fault by using GAMIT/GLOBK (GG) software ([3], [4]). In the second part of the study, the fault was modelled and theoretical velocity vectors were obtained with the help of geological parameters of the fault by using Coulomb 3.3 software ([5], [6]).

At the last part of the study, the fault model given the best coherence between the velocities which obtained and calculated by GG and Coulomb 3.3, respectively, was reached. Consequently, the fault parameters of the fault model, which give the best coherence between the obtained and calculated velocities, were compared with the geological knowledge. By this study, the detailed findings related to the kinematic structures of the Gülbahçe fault were presented as the first time at the literature.

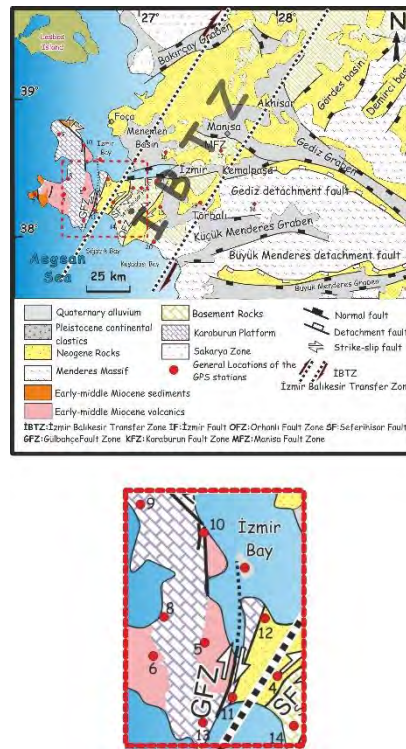


Figure 1. The location of Gülbahçe Fault and main tectonic structure of its surrounding(modified from [7]).

2. APPLICATIONS

As the first step, relatively calculations were realized by using GG with GNSS data of the stations (UZUN, DU05, DU11, DU12, DU13) located near to Gülbahçe fault (Figure 2). Then, several models were created for different kinematic cases of the fault and velocities were calculated with these models. The models which give the best coherence between the observed and calculated velocities are given at Figure 3, Figure 4 and Figure 5.

In Coulomb calculations firstly, Gülbahçe fault was modelled as 3 fault parts (Figure 3 and Figure 4). In Figure 3, the senses of the faults numbered as 1, 2 and 3 were normal right-lateral oblique, normal right-lateral oblique and right-lateral strike slip, respectively. The fault parameters used in modelling (Figure 3) were given in Table 1.

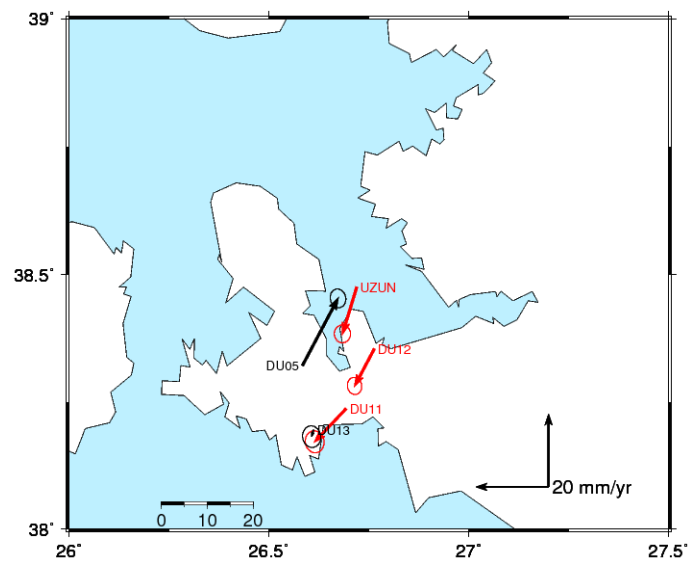


Figure 2. The velocities near to Gulbahce Fault observed by relatively calculations.

Table 1. The parameters used in fault modeling in Figure 3.

Component of Gulbahce	Rake (°)	Netslip	Dip angle (°)	Top (km)	Bottom (km)
1	-120	0.45	90	0.0	4.0
2	-110	0.80	100	0.0	4.0
3	160	1.00	100	0.0	4.0

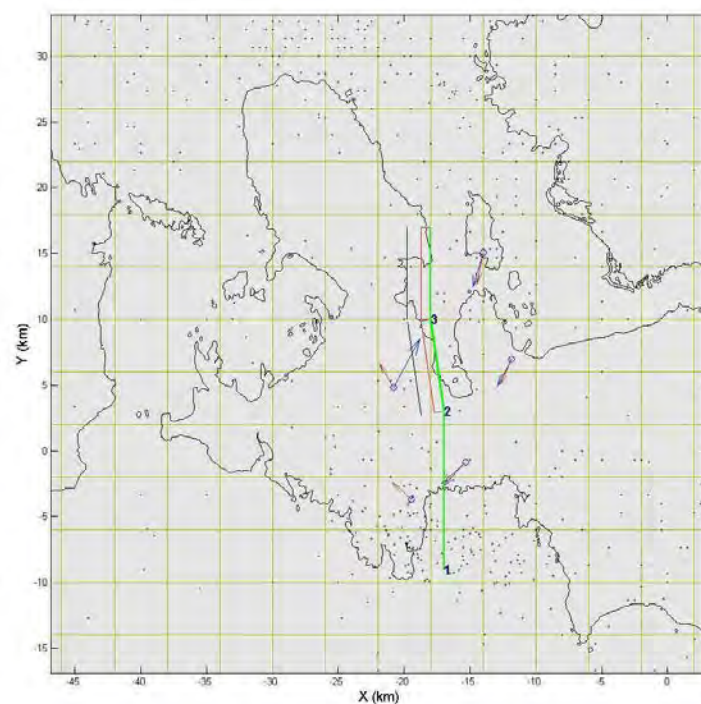


Figure 3. Gulbahce fault model using the parameters given in Table 1. Blue vectors represent the obtained velocities; red vectors represent the calculated vectors. The dots show the focal mechanism calculated earthquakes occurred in the region.

In Figure 4, the senses of the faults numbered as 1, 2 and 3 were normal right-lateral oblique, pure strike-slip and reverse right-lateral oblique, respectively. The fault parameters used in modelling (Figure 4) were given in Table 2.

Table 2. The parameters used in fault modeling in Figure 4.

Component of Gulbahce	Rake (°)	Netslip	Dip angle (°)	Top (km)	Bottom (km)
1	-110	0.50	80	0.0	10.0
2	180	0.50	80	0.0	10.0
3	140	0.80	70	0.0	10.0

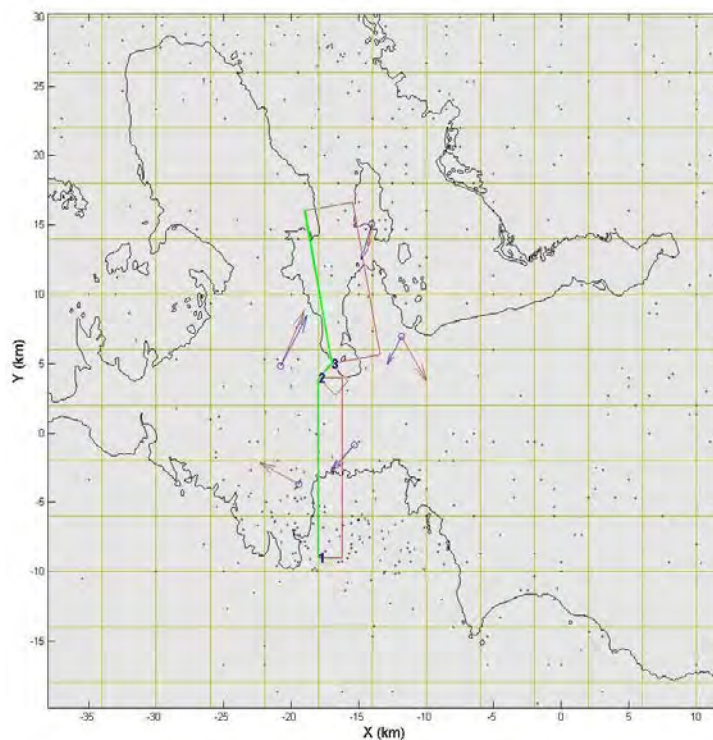


Figure 4. Gulbahce fault model using the parameters given in Table 2. Blue vectors represent the obtained velocities; red vectors represent the calculated vectors. The dots show the focal mechanism calculated earthquakes occurred in the region.

In Figure 5, Gulbahce fault was divided into 2 fault parts and the senses of both parts numbered as 1 and 2 were pure strike-slip. The fault parameters used in modelling were given in Table 3.

Table 3. The parameters used in fault modeling in Figure 5.

Component of Gulbahce	Rake (°)	Netslip	Dip angle (°)	Top (km)	Bottom (km)
1	180	0.5	80	0.0	10.0
2	180	0.4	80	0.0	10.0

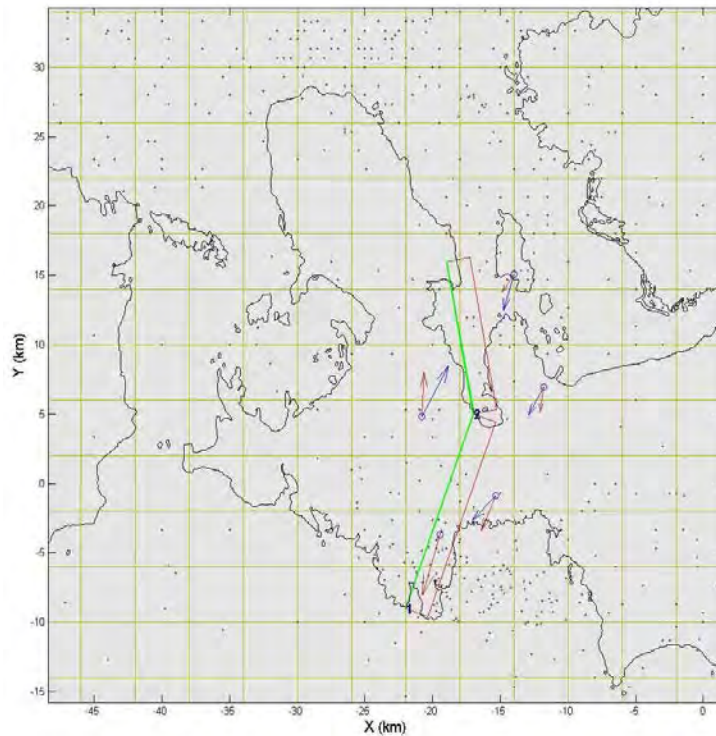


Figure 5. Gülbahçe fault model using the parameters given in Table 3. Blue vectors represent the obtained velocities; red vectors represent the calculated vectors. The dots show the focal mechanism calculated earthquakes occurred in the region.

RESULTS

This study is the first investigation for examining the features of Gülbahçe fault by using GNSS data. As the results of the GG relatively calculations, the sense of Gülbahçe fault was determined as right-lateral strike-slip fault. This result was consistent with the results defined in the previous study [1] which was the unique research for this fault in the literature. According to the modelling studies, it was pointed out that Gülbahçe fault was not consist of only one part (segment). Additionally, Gülbahçe fault presents different kinematic structures for these segments. The relatively calculations were not observed any velocity for the GNSS station located in the south-western of the fault. This result pointed out that there is an effect of a distinct kinematic structure in this part.

ACKNOWLEDGEMENTS

This study has been achieved under the scope of (No. 108Y285) The Scientific and Technological Research Council of Turkey (TUBITAK) project.

REFERENCES

- [1]. Ö. Emre, S. Özalp, A. Doğan, V. Özaksoy, C. Yıldırım and F. Göktaş, Active faults and earthquake potential of Izmir and its surroundings. MTA Report No:10754 (in Turkish), 80p. 2005. (not published).
- [2]. A. Çırmık, "Determining the deformations in Western Anatolia with GPS and gravity measurements," Ph.D. Thesis, Dokuz Eylül University, The Graduate School of Natural and Applied Sciences, Izmir, Turkey, 2014.
- [3]. T. A. Herring, R.W. King and S.C. McClusky, GAMIT reference manual: GPS analysis at MIT, Release 10.4: MIT, Cambridge, USA., 2010a.

- [4]. T. A. Herring, R.W. King and S.C. McClusky, GLOBK global Kalman filter VLBI and GPS analysis program, Release 10.4: MIT, Cambridge, USA., 2010b.
- [5]. S. Toda, R. S. Stein, K. Richards-Dinger and S. Bozkurt, "Forecasting the evolution of seismicity in southern California: Animations built on earthquake stress transfer," *Journal of Geophysical Research*, vol. 110, B05S16, 2005.
- [6]. J. Lin and R.S. Stein, "Stress triggering in thrust and subduction earthquakes and stress interaction between the southern San Andreas and nearby thrust and strike-slip faults," *Journal of Geophysical Research*, vol. 109, B02303, 2004.
- [7]. B. Uzel, H. Sözbilir and Ç. Özkaymak, "Neotectonic evolution of an actively growing superimposed basin in western Anatolia: The inner bay of Izmir, Turkey", *Turkish Journal of Earth Science*, vol. 21, pp. 439-471, 2012.

Compared of Crustal Parameters of Eastern Anatolia Using Different Approaches

Oya Pamukçu¹, Fikret Doğru¹

Abstract

The tectonics of the Eastern Anatolia is dominated by the collision between the Arabian and Eurasian plates. The region, demonstrates a very complicated tectonic structure, because marine and continental basins seem to have played a very significant role in the evolutionary process of the region. These processes presented different crustal structures and physical parameters. The crustal thickness and isostatic model of Eastern Anatolia are very important subjects for discussing the crustal form. The actual isostasy studies are related with loads and their compensations with strong part of lithosphere. Thus compensation type and strong layer of crust play very important role to interpret the crustal structure and isostatic model of the region. Under the guidance of these, in this study, using Global Crustal Model, the crustal thickness and isostasy of Eastern Anatolia were investigated. As a result, it was found that the moho depth of East Anatolian region was not coherent with Airy theory crustal model which was obtained from Global Crustal Model. The crustal thicknesses which were obtained from Global Crustal Model and ground gravity data compared with each other. In addition, the effective elastic thickness as one of the isostatic model parameter was determined from ground gravity data and compared with the result of Airy theory crustal model.

Keywords: Crustal depth, Eastern Anatolia, gravity, isostasy.

44. INTRODUCTION

A number of geodynamics models were presented to determine the dynamics of the collision and to define the collision zone which is between Arabian and Anatolian plate (Figure 1) ([1], [2], [3], [4], [5], [6], [7], [8], [9], [10], [11], [12], [13]).

The crustal thickness is about 45 km on the average ([12], [13]) and the topography is approximately 2 km in the Eastern Anatolia. Additionally, there is asthenospheric upwelling in the study area ([14], [15], [16]). A probable isostatic model of the East Anatolian Region was examined by [17] with effective elastic thickness (T_e).

In this study, the crustal, sediment thickness and moho depth were calculated using Global Crustal Model and Airy moho depth model was calculated using Airy isostatic model [18]. Also the results compared with previous studies. Consequently, it was found that Airy isostatic model was not coherent with Eastern Anatolian isostatic model.

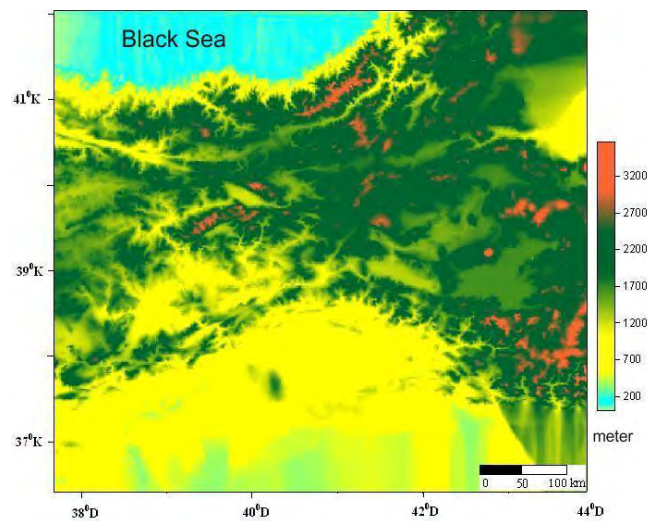


Figure 1. The location of Eastern Anatolia Region and its topographic map.

45. APPLICATION

In the scope of this study, the sediment thickness, moho depths and crustal thickness were obtained by Global Crustal model (<http://igppweb.ucsd.edu/~gabi/crust2.html>) ([19]), moho depths were calculated also using Airy isostatic model. All the results were shown in the Figure 2. These results were compared with the structural depths map of the region created in the previous study ([13]). It was noticed that the values of crust and moho depth with Crust 2.0 seen in Figure 2 were coherent with the structural depths values in Figure 3. However, it was found that the results of moho depth obtained by Airy model (Figure 2) were not coherence with the depths distributions of the region.

Therefore, existence of a compense mechanism which was pointed out by [17] corrected by this study. This mechanism can be explained by the admittance calculations based on effective elastic thickness (T_e) investigations (Figure 4). The admittance values for the compensation depth (t_c) of 40 km were calculated from gravity and topographic data using,

$$Z(k) = \frac{\sum_{r=1}^N G_r(k) T_r^*(k)}{\sum_{r=1}^N T_r(k) T_r^*(k)} \quad (1)$$

this function ([20]). Here, $G(k)$ and $T(k)$ are the discrete Fourier transforms of gravity and topography, N is the number of data. For comparing the result with the theoretical admittance,

$$Z_c(k) = 2\pi G \rho_c (1 - (\exp(-kt_c)) / A \quad (2)$$

where

$$A = 1 + \frac{Dk^4}{g(\rho_m - \rho_c)} \quad D = E \frac{T_e^3}{12(1 - \sigma^2)}$$

is used ([21]). D is rigidity, k ($= 2\pi / \text{wavelength}$) is wave-number, G is gravitational constant, E is Young's modulus, σ is Poisson's ratio, g is the gravity acceleration, ρ_c is average crustal density, ρ_m is density of material below the assumed flexed elastic plate, t_c is effective depth of compensation, T_e is the effective elastic thickness, $Z_c(k)$ is theoretical admittance function.

The Airy model was not valid for the study area seen as in the T_e values obtained by on ground gravity data calculations (Figure 4).

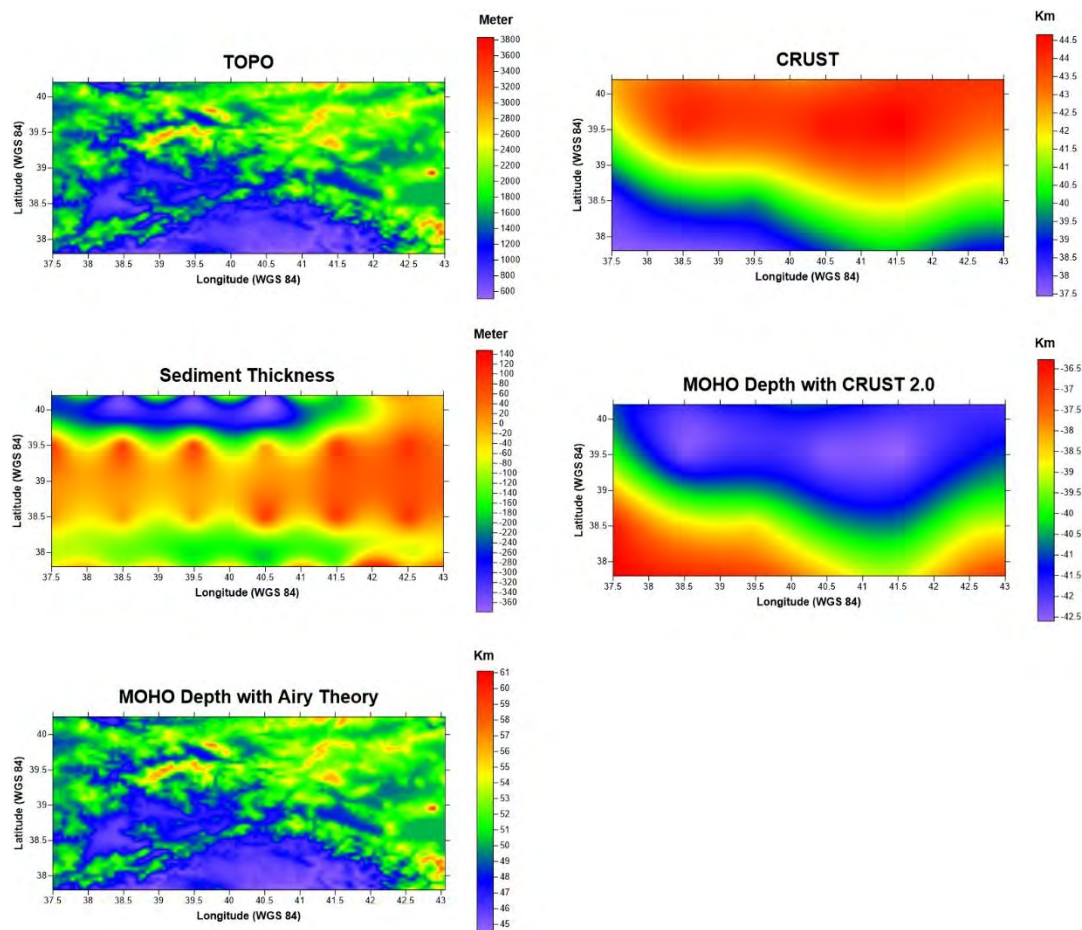


Figure 2. The results of the sediment thickness, Airy model, crustal thickness and moho depths obtained by Global Crustal Model.

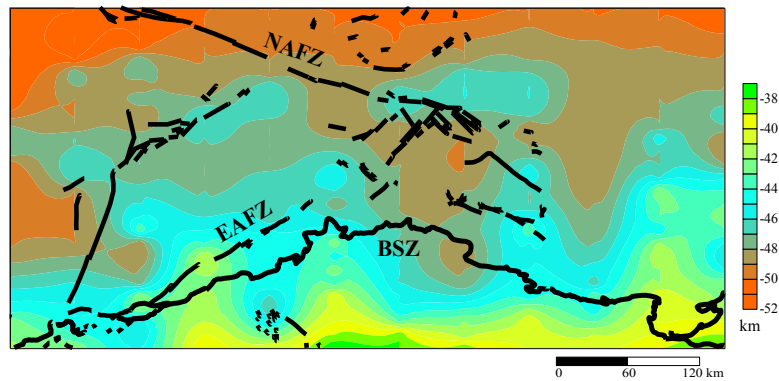


Figure 3. The structural depths of Eastern Anatolia, using power spectrum method on Bouguer gravity data (modified from [13]).

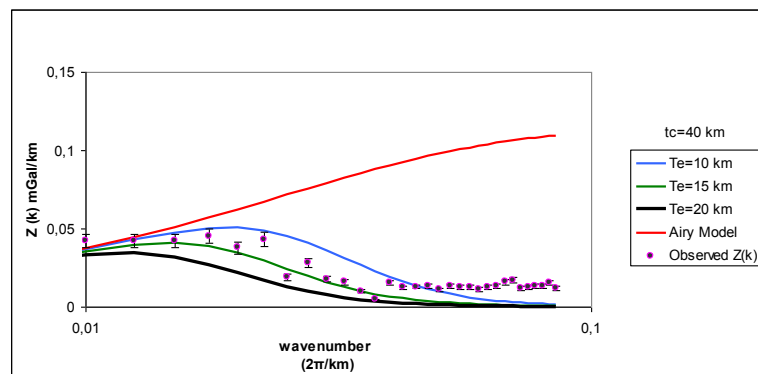


Figure 4. Observed admittance (from Eq. 1), calculated admittances $Z(k)$ (from Eq. 2) for different T_e value and Airy Model ($T_e=0$) (modified from [17]).

RESULTS

The values of the crust and moho depth with Crust 2.0 obtained by Global Crustal Model and the structural depths obtained by on ground measurements were found coherent with each other for Eastern Anatolia Region. Additionally, it can be said that the isostatic mechanism of the region is not represented by Airy model obtained by Global Crustal model. Besides, the Airy model results obtained by T_e values calculated with on ground gravity data are not coherent with the isostatic model of the region. Consequently, for this region the isostatic model can be named as flexural model wherein loadings are supported by the elastic stresses in lithospheric layer lying over the fluid and weak asthenosphere. The boundary in this lithospheric layer between brittle and ductile parts is characterized by the effective elastic thickness. The difference of Airy model from flexure model is the flexural rigidity is accepted as zero.

REFERENCES

- [1]. D.P. Mckenzie, *Active tectonics of the Mediterranean region*, The Geophysical Journal of the Royal Astronomical Society, 30, 109-185, 1972.

- [2]. Y. Rotstein, and A.L. Kafka, *Seismotectonics of the southern boundary of Anatolia, eastern Mediterranean region: subduction, collision, and arc jumping*, Journal of Geophysical Research, 87, 7694-7706, 1982.
- [3]. F. Innocenti, P. Manetti, R. Mazzuoli, G. Pasquare and L. Villari, *Anatolia and north-western Iran*, Andesites: Orogenic andesites and related rocks, 327-349, 1982.
- [4]. J.F. Dewey, M.R. Hempton, W.S.F. Kidd, F. Şaroğlu and A.M.C. Şengör, *Shortening of continental lithosphere: the neotectonics of eastern Anatolia- a young collision zone*, in: Coward M.O., Ries A.C.(Eds.), *Collisional Tectonics*, Geological Society Special Publication, Geological Society London 19, 3-36, 1986.
- [5]. J.A. Pearce, J.F. Bender, S.E. De Long, W.S.F. Kidd, P.J. Low, Y. Güner and J.G. Mitchell, *Genesis of collision volcanism in Eastern Anatolia, Turkey*, Journal of Volcanology and Geothermal Research, 44(1), 189-229, 1990.
- [6]. M. Keskin, J.A. Pearce and J.G. Mitchell, *Volcano-stratigraphy and geochemistry of collision-related volcanism on the Erzurum-Kars Plateau, northeastern Turkey*, Journal of Volcanology and Geothermal Research, 85(1), 355-404, 1998.
- [7]. J. Mitchell and R. Westaway, *Chronology of Neogene and Quaternary uplift and magmatism in the Caucasus: constraints from K-Ar dating of volcanism in Armenia*. Tectonophysics, 304(3), 157-186, 1999.
- [8]. A.I. Al- Lazki, D. Seber, E. Sandvol, N. Turkelli, R. Mohamad and M. Barazangi, *Tomographic Pn velocity and anisotropy structure beneath the Anatolian plateau (eastern Turkey) and the surrounding regions*. Geophysical Research Letters, 30(24), 2003.
- [9]. R. Gök, E. Sandvol, N. Türkelli, D. Seber and M. Barazangi, *Sn attenuation in the Anatolian and Iranian plateau and surrounding regions*, Geophysical Research Letters, 30(24), 2003.
- [10]. N. Turkelli, E. Sandvol, E. Zor, R. Gok, T. Bekler, A. Al- Lazki and S. Bayraktutan, *Seismogenic zones in eastern Turkey*, Geophysical Research Letters, 30(24), 2003.
- [11]. E. Sandvol, N. Turkelli, E. Zor, R. Gok, T. Bekler, C. Gurbuz and M. Barazangi, *Shear wave splitting in a young continent- continent collision: An example from eastern Turkey*, Geophysical Research Letters, 30(24), 2003.
- [12]. E. Zor, E. Sandvol, C. Gürbüz, N. Türkelli, D. Seber and M. Barazangi, *The crustal structure of the East Anatolian plateau (Turkey) from receiver functions*, Geophysical Research Letters, 30(24), 2003.
- [13]. O.A. Pamukçu, Z. Akçığ, Ş. Demirbaş and E. Zor, *Investigation of crustal thickness in Eastern Anatolia using gravity, magnetic and topographic data*, Pure and Applied Geophysics, 164(11), 2345-2358, 2007.

- [14]. A.M.C. Şengör, S. Özeren, T. Genç and E. Zor, *East Anatolian high plateau as a mantle-supported, north-south shortened domal structure*, Geophysical Research Letters, 30, 24, 8045, 2003.
- [15]. M. Keskin, *Magma generation by slab steepening and breakoff beneath a subduction-accretion complex: An alternative model for collision-related volcanism in Eastern Anatolia, Turkey*, Geophysical Research Letters, 30, 24, 8046, 2003.
- [16]. O. Pamukçu, T. Gönenç, A.Y. Çirmik, Ş. Demirbaş and S. Tosun., *Vertical and horizontal analysis of crustal structure in Eastern Anatolia Region*. Bulletin of the Mineral Research and Exploration, (151), 2015.
- [17]. O.A. Pamukçu, Z. Akcig, *Isostasy of the Eastern Anatolia (Turkey) and discontinuities of its crust*, Pure Applied Geophysics, 168/901-917, 2011.
- [18]. G.B. Airy, *On the computation of the effect of the attraction of mountain-masses, as disturbing the apparent astronomical latitude of stations in geodetic surveys*, Philosophical Transactions of the Royal Society of London, 145, 101-104, 1855.
- [19]. M. Kuhn and W. E. Featherstone, *On the construction of a synthetic Earth gravity model*, Gravity and Geoid, 189-194, 2002.
- [20]. D.P. Mckenzie and C.O. Bowin, *The relationship between bathymetry and gravity in the Atlantic Ocean* Journal of Geophysical Research, 81, 1903–1915, 1976.
- [21]. D. Mckenzie and D. Fairhead, *Estimates of the effective elastic thickness of the continental lithosphere from Bouguer and free air gravity anomalies*, Journal of Geophysical Research, 102, 27523–27552, 1997.

Numerical Modeling Studies for Different Temperatures on Extensional Region

Ayça Çirmik²²

Abstract

Numerical modeling by using finite elements can be used for determining forces, deformations, stresses and strains throughout a dependent structure. These can be made at any point in the structure including within the related layer. Besides, the element mesh can accurately describe the geometry of the bond line so the influence of geometrical features, such as the shape of model and boundaries. The spatial discretization of the medium finite element associated with the time discretization is used to give a digital nature to equations. The deformation modeling on the lithosphere as a continuous medium is mainly based on the equilibrium equations of the environment, the laws of behavior of this medium, the boundary conditions of the environment as well as some initial conditions. In this study, numerical modeling was used to investigate the deformation during the geological scales by using the finite elements. In this scope, a theoretical structure was modeled from south to north for modeling the extension. The topography and crust-mantle interface values which were represented the Moho depth of the study area were used as surface and subsurface limits of the boundary conditions on the model. Therefore, the models were created for different temperature values, geological scales, therefore, deformed areas were occurred. Consequently, the numerical models how effected by these parameters were determined.

Keywords: Deformation, extensional region, finite elements, numerical modeling.

46. INTRODUCTION

Numerical models are mathematical models which use several numerical time-stepping for obtaining the models behavior over the time. On deformation modeling on a permanent medium is mainly based on the equilibrium equations, medium behavior laws the boundary conditions. The medium is imagined as permanent lets using the mechanical continuum concepts for obtaining the equilibrium of the system. Discontinuities corresponding the faults modeled this behavior by law Coulomb friction-type are treated as a boundary condition of a particular type [1].

In this study, theoretical structure was modeled from south to north for investigating the deformation on an extensional area at different temperature values during the geological scales. Therefore, the finite element modeling software, namely, ADELI ([2]) which was developed by using theoretical equations given in [3], [4], [5], [1] was used for modeling the deformation.

47. APPLICATIONS

In large-scale deformation for 3D modeling by using ADELI software, the medium is modeled by tetrahedral finite elements with four nodes. The terms are obtained by assembling the contribution of each element, with the M mass

²² Dokuz Eylul University, Engineering Faculty, Department of Geophysical Engineering, 35160, Buca/Izmir, Turkey.

Corresponding author: ayca.yurdakul@deu.edu.tr.

matrix, F_{ext} the vector of external forces, F_{int} the vector of internal forces, F_{cont} the contact force vector and the vector accelerations \ddot{u} are given as [6].

$$M\ddot{u} = F_{ext} + F_{int} + F_{cont} \quad (1)$$

Before starting the modeling with finite elements, for generating the meshes a three-dimensional finite element mesh generator tool, namely, ‘Gmsh’ ([7]) was used. Then, for viewing the outputs a parallel visualization application tool, namely, ‘Paraview’ ([8]) was used.

In this study, theoretical structure was modeled from south to north for modeling the extension. The length of the model, the weight and the depth were; 250 km, 20 km and 30 km, respectively (Figure 6.9). In the modeling, the continental crust was modeled up to 30 km and the model was divided into 3 layers at the vertical direction. The first layer depth was 4 km, second layer depth was 7 km for modeling the crust up to Moho depth. 3 weakness zones were given in the initial model at the first layer, (Figure 1).

For continental crust, rheologic parameters of [9] based on wet quartzite were used. As elastic parameters; Young modulus $E = 10^{11}$ Pa and Poisson ratio $\nu = 0.25$ ([10]) and as density 2.4 g/cm^3 for first layer, 2.9 g/cm^3 for second layer and 3.1 g/cm^3 for third layer were given. The densities of the weakness zones at the first layer shown as No:1, 2 and 3 in Figure 1, were chosen as 2.4 g/cm^3 . For giving extension to the model, the forces as 3 mm/yr were given to N-S direction (x-axis). The all parameters used in the modeling were given at Table 1.

Table 1. Physical parameters used in the numerical modeling.

Parameters	Values
Young Modulus (Pa)	10^{11}
Poisson ratio	0.25
Viscosity Parameter ($\text{Pa}^{-n} \text{s}^{-1}$)(A)	1.10^{-28}
Activation Energy (kJ/mol)	223
Stress Exponent (n)	4
Frictional Coefficient	0.3
Pressure (Pa)	0.e25

In the first application, 200°K was given at the top of the model and 500°K was given at the bottom of the model as temperature values. As a result, temperature distributions, finite strain fields and the velocity fields of the model which were obtained after 5 Myr were shown in the Figure 2, Figure 3 and Figure 4.

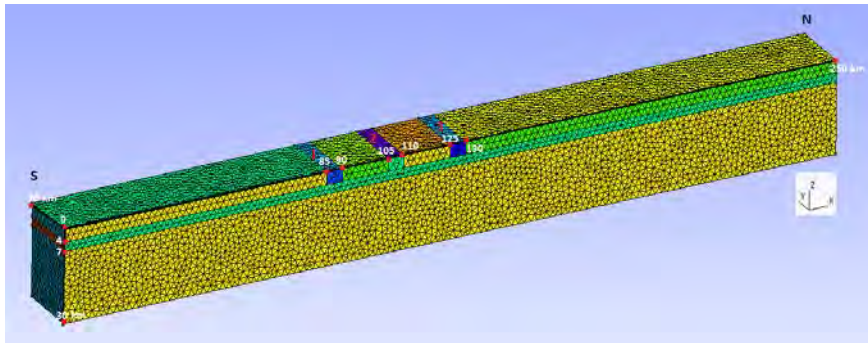


Figure 1. The initial view of the model. No:1, No:2 and No:3 represent the weakness zones.

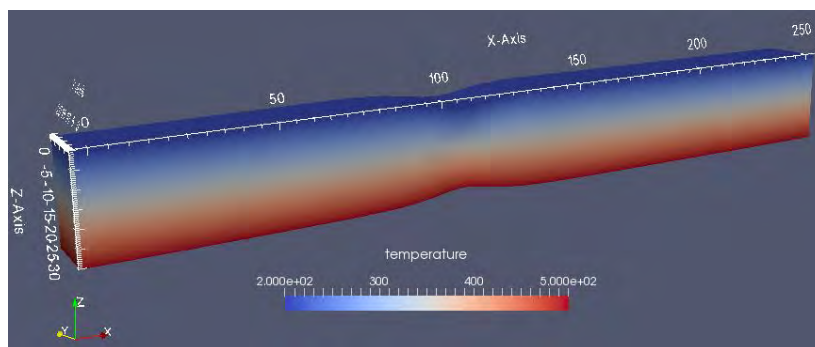


Figure 2. The temperature distributions on model after 5 Myr for 200°K-500°K

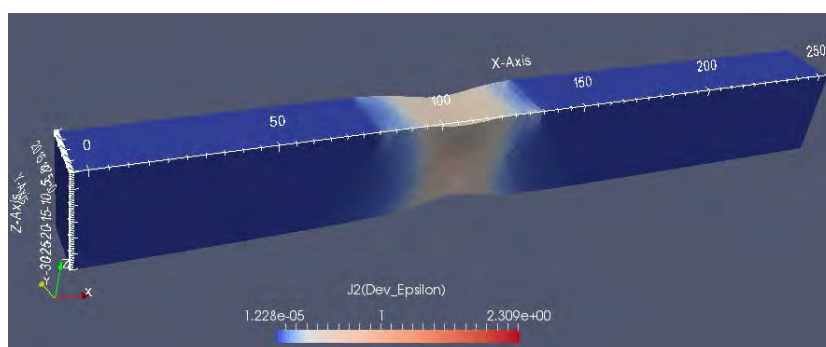


Figure 3. The finite strain fields on model after 5 Myr for 200°K-500°K

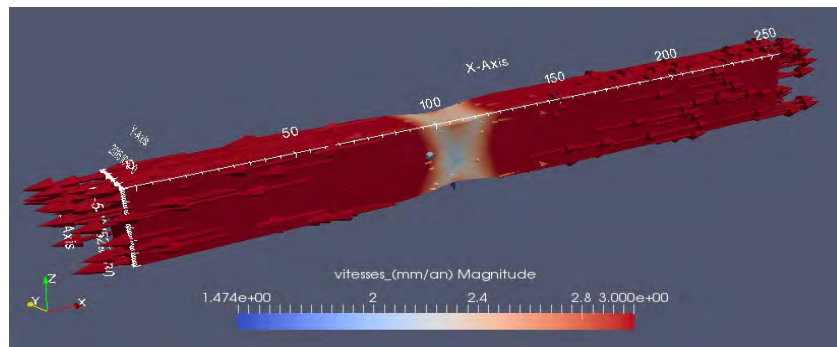


Figure 4. The velocity fields with vectors on model after 5 Myr for 200°K-500°K

In the second application, 273°K was given at the top of the model and 1400°K was given at the bottom of the model as temperature values. As a result, the finite strain fields and the velocity fields which were obtained after 5 Myr were shown in Figure 5 and Figure 6.

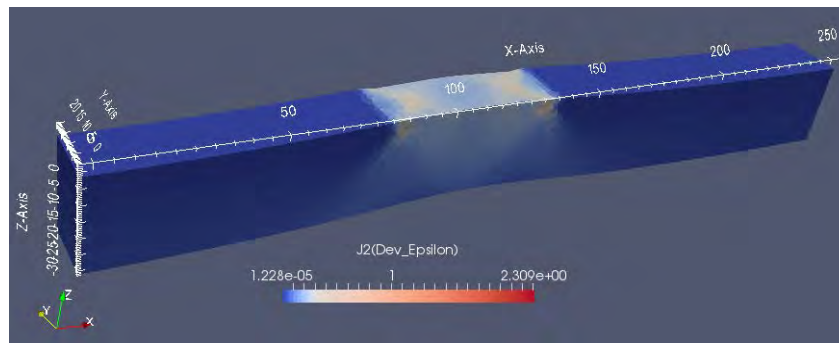


Figure 5. The finite strain fields on model after 5 Myr for 273°K-1400°K

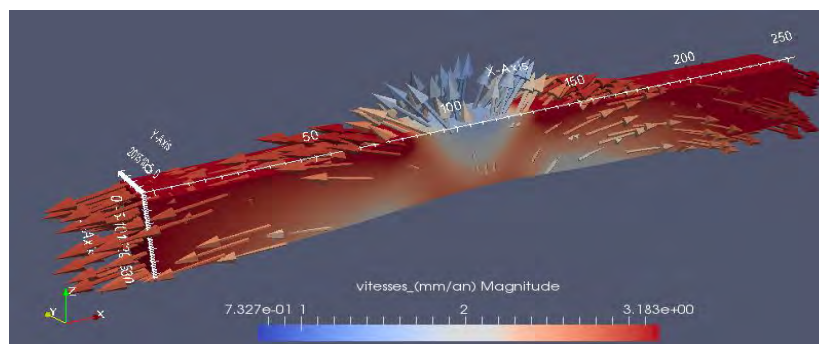


Figure 6. The velocity fields with vectors on model after 5 Myr for 273°K-1400°K

RESULTS

In this study for investigating the effects of the temperature changes on deformation, a theoretical model was created by using finite elements modeling. For giving extension to the model, forces were added to the borders. According to different temperature values, it was noticed that the finite strain fields enlarged on N-S direction (x-axis) along depth by increasing the temperature of Moho from 500 °K to 1400°K (Figure 3 and Figure 5). On the other hand, it was noticed that the velocities decreased, in the other words

the low velocity fields extended at the bottom of the model (at Moho depth) while increasing the temperature (Figure 6). Additionally, while giving the same velocity values to the models (Figure 4 and Figure 6), the velocity vector directions changed by increasing the temperature particularly in the middle of the model (Figure 6).

REFERENCES

- [111]. J. Salençon, *Mécanique du continu*. Paris: Ellipses, 1995.
- [112]. J. Chery and R. Hassani, *ADELI user's guide: A 2D and 3D finite element software for thermomechanical modeling of geological deformation*, 2002.
- [113]. O. Zienkiewicz, *The finite element method*, NY: McGraw-Hill, 1977.
- [114]. D. R. J. Owen and E. Hinton, *Finite elements in plasticity: theory and practice*, 1st ed., Swansea : Pineridge, 1980.
- [115]. G. Dhatt and G. Thouzot, *Une présentation de la méthode des éléments finis*, 1st ed., Paris: Maloine, 1981.
- [116]. P. Vernant, *Cinématique actuelle et dynamique de l'Iran: GPS et modélisation numérique*, Ph.D. Thèse, Université de Montpellier II, Montpellier, 2003.
- [117]. C. Geuzaine and J.-F. Remacle, Gmsh: "a three-dimensional finite element mesh generator with built-in pre- and post-processing facilities," *International Journal for Numerical Methods in Engineering*, vol. 79(11), pp. 1309-1331, 2009.
- [118]. K. Moreland, *The ParaView Tutorial, Version 4.0.*, Technical Report SAND 2013-6883P, Sandia National Laboratories, 2013.
- [119]. G. C. Gleason and J. Tullis, "A flow law for dislocation creep of quartz aggregates determined with the molten salt cell," *Tectonophysics*, vol. 247, pp. 1–23, 1995.
- [120]. D. L. Turcotte and G. Schubert, *Geodynamics*, 2nd ed., NY: Cambridge University Press, 2002.

Evaluation of Various Models Based on Sunshine Duration to Estimate Monthly Average Daily Global Solar Radiation

Ali Etem Gürel²³, Yunus Biçen²⁴

Abstract

In this study, some empirical models based on sunshine duration in literature were evaluated for estimating monthly average daily global solar radiation on horizontal surface in Rize, Turkey. Data provided by Turkish State Meteorological Service relating to the time period of 2004-2009 were employed in the study and regression coefficients were determined for the used models. Selected models were compared by using the statistical methods of mean bias error (MBE), root mean square error (RMSE), mean absolute percentage error (MAPE) and coefficient of determination (R^2). The cubic model which proposed by bahel et al. showed high performance in estimating monthly average daily global solar radiation on horizontal surface in Rize, Turkey.

Keywords: Solar radiation, Sunshine duration, Empirical models

48. INTRODUCTION

Solar energy is being seriously considered for satisfying an important part of energy demand in Turkey, as is in the world. Solar energy potential is very high in Turkey. Turkey is located at the Mediterranean at 36 and 42°N latitudes and has a typical Mediterranean climate. The yearly average solar radiation is 3.6 kWh/m² day, and the total yearly radiation period is ~2610 h. [1]. Therefore, solar energy systems are widely used in Turkey.

Knowing solar radiation intensity of the region in designing a solar energy system is very important for performance of the system. This data is used in estimating cost and efficiency of the project. Further, monthly mean daily data are needed for the estimation of long-term solar systems performances. However, the instruments designed for measuring solar radiation cannot be used easily in many developing countries due to the reasons like high cost, faults and calibration requirements. Therefore, it is important to elaborate methods to estimate the solar radiation based on readily available meteorological data. This allows determining solar radiation intensity in places in which measurement tools are not easily available [2, 3].

Many empirical models have been used to calculate solar radiation, utilizing the available data on meteorological parameters, including sunshine duration, ambient temperature, cloudiness, relative humidity for estimating solar radiation have been proposed and tested in various locations [4-12]. Among them, those models based on sunshine duration are widely used and generally more accurate.

The first model for estimating solar radiation from sunshine duration was proposed by Ångström. The model bases on the global solar radiation for cloudless day. To solve the difficulty in obtaining the cloudless day solar radiation data, Prescott suggested the use of extraterrestrial radiation to replace it.

In this way, the modification resulted in the formation of the Ångström-PreScott (Å-P) model, which has been the most convenient and widely used correlation [13].

²³ Corresponding author: Duzce University, Department of Electrical and Energy, 81010, Merkez/Duzce, Turkey. etemgurel@gmail.com

²⁴ Duzce University, Department of Electronics and Automation, 81010, Merkez/Duzce, Turkey. yunusbicen@gmail.com

This study is focused on comparison of various models based on sunshine duration in estimating monthly average daily global solar radiation.

49. METHODOLOGY

The seven models, which are recommended in the literature for estimating monthly average daily global solar radiation on horizontal surface, are seen in Table 1. In Table 1, H is the monthly average daily global solar radiation, H_o is the monthly average Daily extraterrestrial radiation, S_o is the day length, and a , b , c and d are the empirical coefficients.

Eq. (1) was used to calculate the monthly average daily extraterrestrial radiation H_o .

$$H_o = \frac{24}{\pi} I_{sc} \left[1 + 0.033 \cos\left(\frac{360D}{365}\right) \right] \times \left[\cos(\varphi) \cos(\delta) \sin(\omega_s) + \frac{\pi \omega_s}{180} \sin(\varphi) \sin(\delta) \right] \quad (1)$$

$$\delta = 23.45 \sin\left(360 \frac{284 + D}{365}\right) \quad (2)$$

$$\omega_s = \cos^{-1}[-\tan(\varphi) \tan(\delta)] \quad (3)$$

Eq. (4) was used to calculate day length S_o .

$$S_o = \frac{2}{15} \cos^{-1}[-\tan(\varphi) \tan(\delta)] = \frac{2}{15} \omega_s \quad (4)$$

Table 1. Regression models proposed in the literature

#	Model	Expression	References
1	Linear	$H / H_o = a + b(S / S_o)$	Ångström and Prescott [14], [15]
2	Quadratic	$H / H_o = a + b(S / S_o) + c(S / S_o)^2$	Akınoğlu and Ecevit [16]
3	Cubic	$H / H_o = a + b(S / S_o) + c(S / S_o)^2 + d(S / S_o)^3$	Bahel et al. [17]
4	Logarithmic	$H / H_o = a + b \log(S / S_o)$	Ampratwum and Dorvlo [18]
5	Linear logarithmic	$H / H_o = a + b(S / S_o) + c \log(S / S_o)$	Newland [19]
6	Linear exponential	$H / H_o = a + b(S / S_o) + c \exp(S / S_o)$	Bakırcı [20]
7	Exponential	$H / H_o = a + b \exp(S / S_o)$	Almorox et al. [10]

50. STATISTICAL ANALYSIS METHODS

Statistical indicators of mean bias error (MBE), root mean square error (RMSE), mean absolute percentage error (MAPE) and the coefficient of determination (R^2), which are commonly used in statistical applications, were used to compare estimated and measured monthly average Daily global solar radiation values.

MBE, RMSE and MAPE values were calculated with the help of the following equations.

$$MBE = \frac{1}{n} \sum_{i=1}^n (y_i - x_i) \quad (5)$$

$$RMSE = \left(\frac{1}{n} \sum_{i=1}^n (y_i - x_i)^2 \right)^{1/2} \quad (6)$$

$$MAPE = \frac{1}{n} \sum_{i=1}^n \left| \frac{y_i - x_i}{y_i} \right| \times 100 \quad (7)$$

where x_i is the i th measured value, y_i the i th calculated value, and n the total number of observation. The MBE provides information on the long-term performance of an equation. A positive MBE represents an overestimation while a negative MBE shows an under estimation. The RMSE provides information on the short-term performance of an equation. [20].

The coefficient of determination, R^2 can be calculated from the following equation [2, 20]:

$$R^2 = [(S_t - S_r) / S_t]^{1/2} \quad (8)$$

where S_t is the standard deviation and S_r the deviation of the calculated value from the measured one. S_t and S_r are defined as follows:

$$S_t = \sum_{i=1}^n (x_a - x_i)^2 \quad (9)$$

$$S_r = \sum_{i=1}^n (x_i - y_i)^2 \quad (10)$$

where x_a is the average of the measured values and is given by

$$x_a = \frac{1}{n} \sum_{i=1}^n x_i \quad (11)$$

For better data modeling, MAPE, MBE and RMSE should be closer to zero, but R^2 should approach 1.0 as closely as possible [13].

51. RESULTS AND DISCUSSION

Data provided by Turkish State Meteorological Service relating to the time period of 2004-2009 were employed in the study and regression coefficients were determined for the used models and monthly average daily global solar radiation on horizontal surface for the year of 2010 were estimated with the models, which had been developed based on these coefficients. The obtained results were compared with the meteorological measurements for the year of 2010. Coefficient values were calculated from regression analysis between H/H_o and S/S_o for a long period and each month.

Regression coefficients determined for the models under evaluation, R^2 , MBE, RMSE and MAPE values are given in Table 2. According to the table, correlation coefficients of all of the developed seven models are quite close to 1. This indicates that these models may be used efficiently in estimating monthly average daily global solar radiation on horizontal surface in Rize. MBE, RMSE and MAPE values of the equation, which had been produced by Model 3, were determined as 0.595, 0.722 and 7.27% respectively. Performance of Model 6 is the closest one to the Model 3 MBE, RMSE and MAPE values of Model 6, were determined as 0.663, 0.773 and 9.56% respectively. This result evidences that both of the models have high performance. However, Model 3 having the value of $R^2 = 0.9849$ and low MBE, RMSE and MAPE values is recommended as the most suitable estimation model for Rize.

Table 3 shows the estimated values of monthly average daily global solar radiation on horizontal surface values based on the models and the real values provided by Turkish State Meteorological Service.

Table 2. Regression coefficients and statistical data for used models

Model	a	b	c	d	R^2	MBE	RMSE	MAPE
1	0.2556	0.3893	-	-	0.9818	0.675	0.779	7.91
2	0.4199	-0.6945	1.7106	-	0.9750	0.823	0.906	11.1
3	-0.0431	3.919	-13.18	15.63	0.9849	0.595	0.722	7.27
4	0.5157	0.2684	-	-	0.9802	0.678	0.810	7.28
5	-0.4235	1.3901	-0.7112	-	0.9784	0.724	0.844	10.7
6	-2.104	-3.06	2.509	-	0.9819	0.663	0.773	9.56
7	-0.0132	0.285	-	-	0.9618	1.024	1.118	11.9

Table 3. Measured and estimated monthly average daily global solar radiation (MJ/m²) values

Month	Measured	Model 1	Model 2	Model 3	Model 4	Model 5	Model 6	Model 7
January	4	4.42	5.12	4.12	4.15	5.44	5.06	4.67
February	6.32	6.62	6.91	6.74	6.56	6.88	6.84	6.89
March	9.48	9.79	9.81	9.81	9.85	9.66	9.67	10.12
April	11.2	12.33	12.38	12.39	12.4	12.2	12.21	12.75
May	14.78	15.45	15.52	15.14	15.5	15.27	15.19	15.93
June	15.03	15.88	15.85	15.57	15.98	15.61	15.55	16.38
July	14.45	15.32	15.28	15.05	15.43	15.04	14.99	15.81
August	13.02	13.44	13.39	13.3	13.55	13.19	13.17	13.87
September	9.67	10.98	10.93	10.86	11.03	10.77	10.75	11.33
October	6.12	7.39	7.71	7.52	7.31	7.67	7.63	7.69
November	5.12	5.26	5.52	5.35	5.19	5.51	5.47	5.48
December	3.89	4.24	4.48	4.3	4.17	4.48	4.44	4.42

It was seen at the end of the study that the measured and estimated monthly average daily global solar radiation values are very close to each other. The most important point indicating coherence between a mathematical model and measured data is its long-term performance. The seven different models under the use were statistically analyzed for their long-term performance and as a result, it was found that Model 3 has the best long-term performance (MBE=0.595).

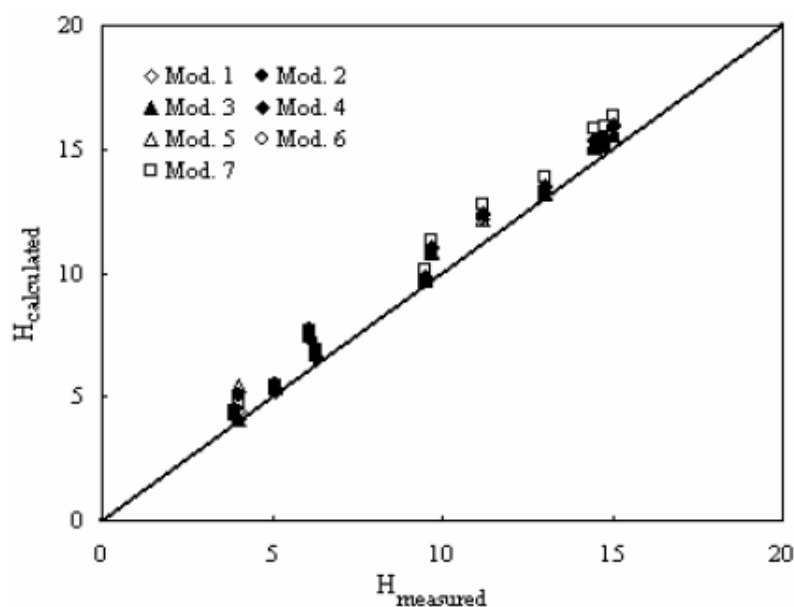


Fig. 1. Comparison of the used models.

Comparison of the used models and variation measured and estimated monthly average daily global solar radiation values in given Fig. 1 and Fig. 2., respectively. Monthly average daily global solar radiation values estimated by using the developed models are higher than those measured. This may be understood from the fact that MBE values obtained from the models were found positive. According to Figure 1, measured and estimated values are very close to each other. At the end of the study, it was seen that all

the models produced reliable estimation results but the cubic model is the most convenient method according to the measured values.

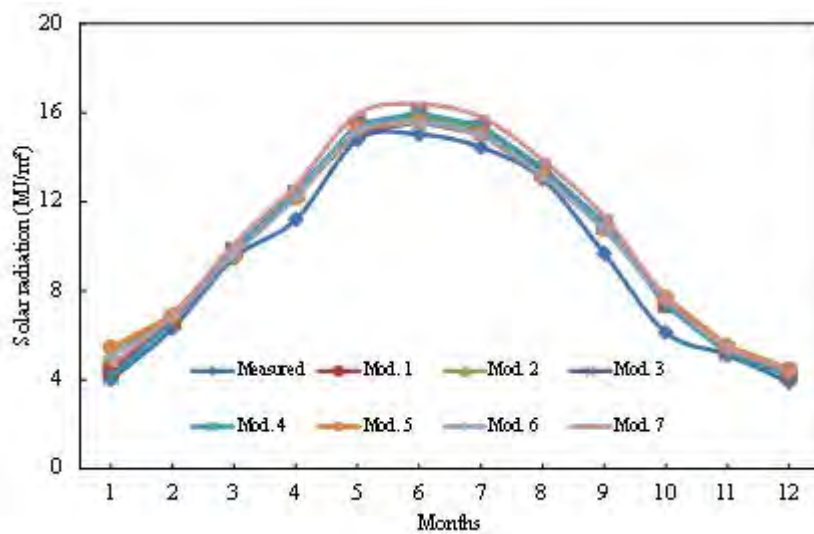


Fig. 2. Variation measured and estimated monthly average daily global solar radiation values

52. CONCLUSION

Knowing solar radiation intensity of the region in designing a solar energy system is very important. This knowledge allows making efficiency analyses and cost determination for the system. However, the use of the instruments measuring solar radiation is very limited in many regions. Therefore, designing mathematical models based on meteorological and/or geographic data is a method, which is very prevalently practiced in estimating solar radiation. This allows determining solar radiation with high accuracy with no need for measurement instruments.

In the conducted study, seven different models recommended in the literature were compared for estimating monthly average daily global solar radiation on horizontal surface in Rize, Turkey. Mean bias error (MBE), root mean square error (RMSE), mean absolute percentage error (MAPE) and correlation coefficient statistical expressions were used in evaluating models performance.

At the end of the study, a cubic model was proposed by referencing Bahel et. al. $H/H_o = -0.0431 + 3.919(S/S_o) - 13.18(S/S_o)^2 + 15.63(S/S_o)^3$ The model showed highest performance for Rize, Turkey.

NOMENCLATURE

a, b, c, d	regression constants of empirical models
D	number of days of the year starting from the first of January
H	monthly average daily global radiation (MJ/m ²)
H_o	monthly average daily extraterrestrial radiation (MJ/m ²)
I_{sc}	solar constant (=1353 W/m ²)
MBE	mean bias error
MAPE	mean absolute percentage error

RMSE	root mean square error
S	sunshine duration (h)
S_o	day length (h)
δ	declination angle (deg)
φ	latitude of site (deg)
ω_s	mean sunrise hour angle for the month (deg)

REFERENCES

- [1] Şenkal, O., & Kuleli, T. (2009). Estimation of solar radiation over Turkey using artificial neural network and satellite data. *Applied Energy*, 86(7), 1222-1228.
- [2] Muzathik, A. M., Ibrahim, M. Z., Samo, K. B., & Nik, W. W. (2011). Estimation of global solar irradiation on horizontal and inclined surfaces based on the horizontal measurements. *Energy*, 36(2), 812-818.
- [3] Bakirci, K. (2009). Models of solar radiation with hours of bright sunshine: a review. *Renewable and Sustainable Energy Reviews*, 13(9), 2580-2588.
- [4] Rehman, S., & Mohandes, M. (2008). Artificial neural network estimation of global solar radiation using air temperature and relative humidity. *Energy Policy*, 36(2), 571-576.
- [5] Deniz, E., & Atik, K. (2007). Investigation of using regression analysis and artificial neural network methods in estimate of solar radiation. *Journal of Thermal Science Technology* 27(2): 15-20. (In Turkish).
- [6] Mubiru, J., & Banda, E. J. K. B. (2008). Estimation of monthly average daily global solar irradiation using artificial neural networks. *Solar Energy*, 82(2), 181-187.
- [7] Ulgen, K., & Hepbasli, A. (2009). Diffuse solar radiation estimation models for Turkey's big cities. *Energy Conversion and Management*, 50(1), 149-156.
- [8] Jin, Z., Yezheng, W., & Gang, Y. (2005). General formula for estimation of monthly average daily global solar radiation in China. *Energy Conversion and Management*, 46(2), 257-268.
- [9] Sabziparvar, A. A., & Shetaee, H. (2007). Estimation of global solar radiation in arid and semi-arid climates of East and West Iran. *Energy*, 32(5), 649-655.
- [10] Almorox, J. Y., & Hontoria, C. (2004). Global solar radiation estimation using sunshine duration in Spain. *Energy Conversion and Management*, 45(9), 1529-1535.
- [11] Yelmen, B., & Cakir, M. T. (2011). Total for the horizontal surface of the city of Konya solar radiation comparison of predicted and test values. *Energy Education Science and Technology Part A* 28: 211-220.
- [12] Yelmen, B., Ustuner, T., & Ustuner, M. (2011). Determining the potential of solar energy and benefiting from this potential using photovoltaic system in Turkey. *Energy Education Science and Technology Part A* 27: 347-358.
- [13] Li, H., Ma, W., Lian, Y., Wang, X., & Zhao, L. (2011). Global solar radiation estimation with sunshine duration in Tibet, China. *Renewable Energy*, 36(11), 3141-3145.
- [14] Angstrom, A. (1924). Solar and terrestrial radiation. Report to the international commission for solar research on actinometric investigations of solar and atmospheric radiation. *Quarterly Journal of the Royal Meteorological Society*, 50(210), 121-126.
- [15] Prescott, J. A. (1940). Evaporation from a water surface in relation to solar radiation. *Transactions of the Royal Society of South Australia*, 64, 114-118.
- [16] Akinoğlu, B. G., & Ecevit, A. (1990). Construction of a quadratic model using modified Ångström coefficients to estimate global solar radiation. *Solar Energy*, 45(2), 85-92.
- [17] Bahel, V., Bakhsh, H., & Srinivasan, R. (1987). A correlation for estimation of global solar radiation. *Energy*, 12(2), 131-135.
- [18] Ampratwum, D. B., & Dorvlo, A. S. (1999). Estimation of solar radiation from the number of sunshine hours. *Applied Energy*, 63(3), 161-167.
- [19] Newland F.J. (1989). A study of solar radiation models for the coastal region of South China. *Solar Energy*, 43, 227-235.
- [20] Bakirci K. (2009). Correlations for estimation of daily global solar radiation with hours of bright sunshine in Turkey. *Energy*, 34, 485-501.

Accuracy Investigation of Scientific and Commercial GPS Processing Software: A case study within European Reference (EUREF) Permanent Network

İbrahim KALAYCI²⁵, Bekir YÜKSEL²⁶, Sermet ÖĞÜTCÜ¹

Abstract

This paper deals with the accuracy comparison of scientific and commercial GPS processing software for varying length of baselines. European Reference (EUREF) Permanent Network Stations were used for the processing. GAMIT/GLOBK scientific GPS processing software (version 10.6) and Leica Geo Office (version 8.4) commercial GPS processing software were chosen for the experiment. TUBO EUREF station was taken as a known station whose three-dimensional (3D) coordinates are known before the processing and the other stations were taken as unknown points whose 3D coordinates are calculated after the processing. In this way, minimally constrained adjustment was performed for each unknown station and their coordinates were calculated w.r.t. TUBO station with using each software. Only independent (non-trivial) baselines are formed between known station and unknown stations. Processing was conducted for 10 different days with 24 hours rinex data of the stations. After the processing, difference between the calculated 3D coordinates of stations and the published true coordinates of the stations were resolved to topocentric coordinates (north, east, up) to observe the error direction more conveniently in 3D space. Results show that vertical accuracy obtained from commercial software is significantly low comparing with the scientific software. There is no significant difference observed for horizontal accuracy between the software but the horizontal accuracy obtained from the scientific software is slightly better than commercial one. There is no deterministic correlation is found between the baseline distance and accuracy for each software. Calculated RMS errors for the farthest (BZRG) and nearest (BIST) station w.r.t. control station (TUBO) for each software as follows; 5mm (north), 5mm (east), 48mm (up) for Leica Geo Office and 3mm (north), 2mm (east), 5mm for GAMIT/GLOBK software and 2mm (north), 3mm (east), 70mm (up) for Leica Geo Office and 2mm (north), 2mm (east), 6mm (up) for GAMIT/GLOBK software respectively.

Keywords: Adjustment, Baseline, GAMIT, GLOBK, GPS

53. INTRODUCTION

The Global Positioning System becomes a common technique for surveyors. Determination of three-dimensional coordinates based on determination distance between satellites and receiver. Measurement requires high accuracy and precision, generally carried out with using static relative positioning technique. Static relative positioning employs at least two GPS receivers (base receiver and roving receiver) simultaneously tracking the same satellites to determine their relative coordinates. Base receiver remains stationary at a site with accurately known coordinates while the remaining receivers occupy the points whose coordinates are unknown [1].

Generally, carrier phase measurements are chosen for precise static relative positioning [2], [3]. GPS carrier phase processing can be performed with commercial and scientific software. The three-dimensional accuracy obtained after the processing depends on several factors. One of the most important factor is baseline distance between the known and unknown points especially for commercial software. Scientific software is rather less dependent on the baseline distance than commercial software for point accuracy. This is one of the main advantage of scientific software comparing the commercial software.

In this paper, varying length of baselines are processed with using commercial and scientific GPS processing software in order to investigate the accuracy differences as a function of baseline for each software. European Reference Permanent (EUREF) Network is chosen for processing. Leica Geo Office (version 8.4) commercial GPS processing software and GAMIT/GLOBK

²⁵ Corresponding author: Necmettin Erbakan University, Department of Surveying Engineering, 42090, Konya /Turkey. sermetogutcu@konya.edu.tr

²⁶ Republic Of Turkey Ministry Of Food, Agriculture And Livestock, by_harita@hotmail.com

scientific GPS processing software (version 10.6) were chosen for processing. 6 points were chosen southwest-northwest direction w.r.t. the known point TUBO station for forming 6 baselines varying from 131 to 495 km (Table 1). Location of these stations are shown in Figure 1.

Table 1: Baseline Distance

Baseline	Baseline Length (km)
TUBO-BISK	131
TUBO-LINZ	196
TUBO-SBG2	300
TUBO-LODZ	351
TUBO-BOGO	480
TUBO-BZRG	495

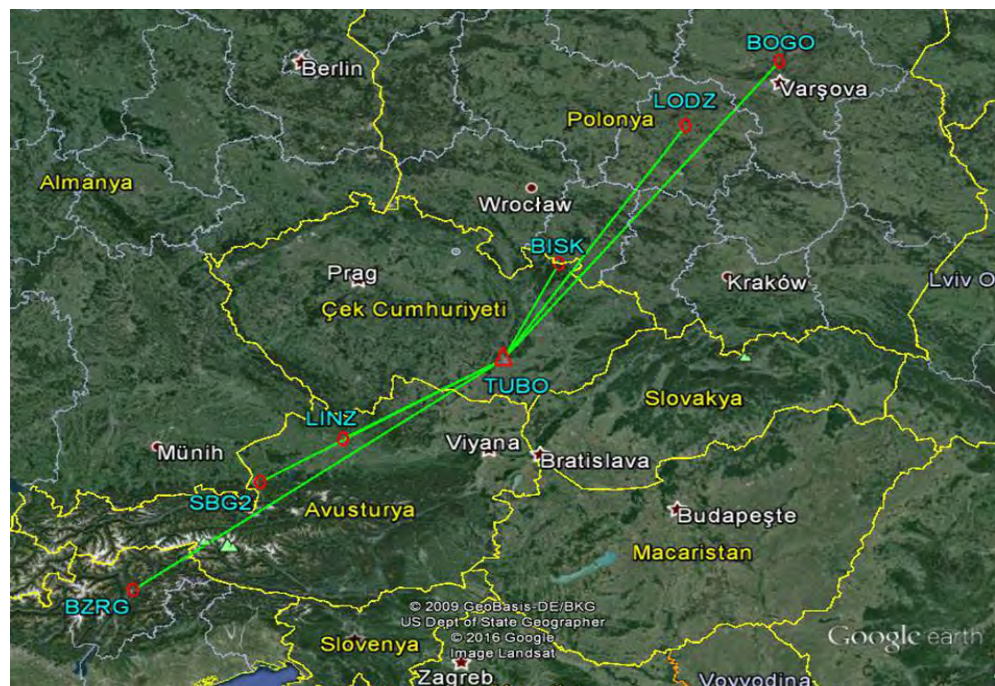


Figure 1: Location of the stations and baselines

10 different days (from March 03 to March 16 in 2015) were chosen to conduct experiment. Due to the data shortage of some stations, 4 consecutive days between March 08 and March 13 cannot be processed.

Constrained adjustment are quite common in the processing of GPS data enables a new survey can be fitted to existing control points. In general, unknown parameters in the constrained adjustment are the coordinates of points. It is generally necessary to fix coordinates of at least one point to determine the coordinate of unknown point w.r.t. the control point [4]. When only one point used as a fix station for the adjustment, this is called minimally constrained adjustment. In this experiment, minimally constrained adjustment is performed while fixing the TUBO station as a control point. After the processing, difference between coordinates of the unknown points obtained from the adjustment and published true coordinates of the unknown points were calculated in order to investigate accuracy analysis.

54. METHODOLOGY AND DATA PROCESSING

24 hour rinex data of each station was downloaded from EUREF network. GPS precise ephemerides data [5] was downloaded from IGS (International GNSS Service). Only GPS satellites were used for processing. Baseline processing was performed with using 30 second sampling rate and 15 degrees of elevation mask angle for each software. Tropospheric models used for processing are different for each software. Hopfield tropospheric model [6] and Global Mapping Function (GMT) [7] were used for Leica Geo Office and GAMIT/GLOBK software respectively. The ionospheric effect was mitigated by forming the linear combination of two carrier phase frequency for each software.

The same processing steps were carried out by each software. For each baseline, assumed true ECEF (Earth Centered Earth Fixed) Cartesian coordinates of TUBO station are held fixed then baseline between TUBO station and unknown stations were processed. Only the phase ambiguity fixed solutions are accepted from the baseline processing for each day and each software. After the baseline processing, minimally constrained adjustment was performed for each day.

Leica Geosystems is a Swiss company founded in 1819 with the name Kern & Co. There are several software and survey devices are available in the company. Leica Geo Office GPS software is among them. By the help of user friendly graphical interface, GPS data can be easily processed without spending long time to apprehend the usage of the software. GLONASS data can also be processed with or without GPS data.

GAMIT/GLOBK is a comprehensive GPS analysis package developed at MIT, the Harvard-Smithsonian Center for Astrophysics (CfA), and the Scripps Institution of Oceanography (SIO) for estimating station coordinates and velocities, stochastic or functional representations of post-seismic deformation, atmospheric delays, satellite orbits, and Earth orientation parameters. Considerable time is necessary to apprehend the concept and usage of the software. There is no graphical user interface available for the software. Users who want to use the software need to know basic bash scripting. There are several analysis related to the GPS survey quality can be performed in GAMIT after the processing. Cycle slip analysis and the phase ambiguity resolution are among them. These parameters cannot be determined in Leica Geo Office which are very essential to interpret the processing quality.

There are several limitations associated with this study. The processing data only involves GPS observations by the fact that for some baselines phase initial ambiguities associated with GLONASS satellites could not be fixed especially for long baselines. Therefore to maintain the consistency between the software, GLONASS satellites were removed from the processing. Only ten days of data during March 2015 was processed thus seasonal, long-term effects and precision are not considered in this study. Only 24 hour rinex data was processed of the stations therefore the processing accuracy of short observation times and the effect of dilution of precision (GDOP) were not investigated.

The obtained three-dimensional coordinates of the unknown points after the minimally constrained adjustment are taken as final coordinates. Adjustment was performed in IGS08 coordinate system. Survey epoch (2015.19) coordinates are used for the control point instead of reference epoch (2005.00) coordinates. To investigate the accuracy of the adjustment, the differences between three-dimensional coordinates of unknown stations obtained after the adjustment and already established three-dimensional coordinates (assumed true) of the unknown stations were resolved into topocentric coordinates (north, east, up) components for all processed data for each software. With the help of topocentric coordinates, direction of the errors can be investigated more clearly.

55. RESULTS

With the help of calculated north east up coordinates, root mean square (rms) errors of each component was calculated as follows;

$$rms_{north} = \sqrt{\frac{\sum_{i=1}^{10} (x_{north(i)} - t_{north})^2}{10}} \quad (1)$$

$$rms_{east} = \sqrt{\frac{\sum_{i=1}^{10} (x_{east(i)} - t_{east})^2}{10}} \quad (2)$$

$$rms_{up} = \sqrt{\frac{\sum_{i=1}^{10} (x_{up} - t_{up})^2}{10}} \quad (3)$$

$$rms_{3D} = \sqrt{\frac{((rms_{north})^2 + (rms_{east})^2 + (rms_{up})^2)}{3}} \quad (4)$$

Here, x_{north} , x_{east} and x_{up} , represent the topocentric coordinates of the unknown stations obtained after the minimally constrained adjustment; t_{north} , t_{east} and t_{up} represent the assumed true published coordinates of the unknown stations. rms_{north} , rms_{east} , rms_{up} and rms_{3D} represent the rms error of north, east, up and three-dimensional components respectively. 10, represents the total number of days for processing. Calculated rms errors for each station and each software w.r.t. the baseline distance were tabulated in Table 2.

Table 2: RMS analysis of each software

ACCURACY ANALYSIS								
GAMIT/GLOBK					LEICA			
Baseline	rms_{north} (mm)	rms_{east} (mm)	rms_{up} (mm)	rms_{3D} (mm)	rms_{north} (mm)	rms_{east} (mm)	rms_{up} (mm)	rms_{3D} (mm)
TUBO-BISK (131 km)	2.4	2.3	6.6	7.4	2.9	1.7	70	70.1
TUBO-LINZ (196 km)	4.3	2.3	6.0	7.7	3.0	2.4	56	56.1
TUBO-SBG2 (300 km)	3	1.2	13	13.4	4.4	3.7	98	98.2
TUBO-LODZ (351 km)	0.5	0.7	5.5	5.6	3.0	3.7	42	42.3
TUBO-BOGO (480 km)	1.5	1.1	7.6	7.8	4.9	3.1	44	44.4
TUBO-BZRG (495 km)	1.7	3.2	5.2	6.3	4.6	5.4	48	48.5

56. CONCLUSIONS AND RECOMMENDATIONS

As it is seen from the rms analysis, up component accuracy of Leica commercial GPS processing software is significantly low comparing the GAMIT/GLOBK scientific software. Maximum error in up component was calculated 15cm and 1.8cm for SBG2 station from Leica and GAMIT/GLOBK software respectively. The differences of two-dimensional accuracy between the software are in the order of mm level but for the most baselines, obtained accuracy from GAMIT/GLOBK is slightly much better.

Tropospheric model used in the software would be responsible for the significant difference in up component between the software. Scientific GPS software use sophisticated tropospheric model thus up component of the station can be determined more accurately even for long baselines. There is no trend was observed between baseline distance and positioning accuracy for each software but the lowest two-dimensional accuracy is observed the longest baseline for Leica software.

It should be emphasized that minimally constrained adjustment with fixing one station was performed in this study. Constrained adjustment results with fixing several stations for the same length of baselines would be different from the minimally constrained adjustment. Accuracy of fiducial (fixed) stations coordinates and quality of raw observations play considerable role for accuracy in minimally constrained and constrained adjustment. If fiducial stations coordinate in constrained adjustment is not enough accurate, all errors in these stations degenerate the unknown points' coordinates. In this situation, minimally constrained adjustment can give more accurate results than constrained adjustment. One would take into account this tradeoff when performing adjustment in the GPS network.

ACKNOWLEDGMENT

This work is supported by scientific research development department of Necmettin Erbakan University.

REFERENCES

- [121]. M. Berber, A Üstün, M Yetkin., "Comparison of accuracy of GPS techniques", *Measurement*. 45: 1742-1746, 2012.
- [122]. J. Wang, C. Satirapod, C. Rizos., "Stochastic Assessment of GPS carrier phase measurements for precise static relative positioning". *Journal of Geodesy* 76: 95-104, 2001.
- [123]. P. Teunissen., "GPS Carrier Phase Ambiguity Fixing Concepts". *GPS for Geodesy* 319:388, 1998.
- [124]. Schwarz C.R., "The Trouble with Constrained Adjustment". *Surveying and Land Information Systems*. 54: 202-209, 1994.
- [125]. Dow JM, Neilan RE, Gendt G, "The International GPS Service: celebrating the 10th anniversary and looking to the next decade". *Advance Space Research* 36: 320-326, 2005.
- [126]. Hopfield, H.S, "Two-quartic tropospheric refractivity profile for correcting satellite data", *Journal of Geophysical Research*. 74: 4487-4499, 1969.
- [127]. Boehm J, Niell A, Tregoning P, Schuh H., "Global Mapping Function (GMF): A new empirical mapping function based on numerical weather model data", *Geophysical Research Letters*. 33, 2006.

Performance Analysis of Gravity Concentration Methods at Narrow Particle Size Fractions

Murat KADEMLİ²⁷

Abstract

We investigated effects of the particle size distribution on the performance of gravity concentration methods used in mineral processing and measured the recovery differences between a whole size distribution and narrow size fractions. Three different gravity concentration methods (jig, spiral, and shaking table) were tested using two different artificial feed samples comprising Hematite (Fe_2O_3) and Quartz (SiO_2) (Sample A), and Calcite ($CaCO_3$) and Lignite (Sample B). The operational conditions followed typical industrial operational limits. The performance of the three methods was compared at narrow particle size fractions. The findings showed that the performance of all three methods increased with narrow size fractions. However, the jig method showed the strongest effect for both artificial samples, with recovery increases of 16.94% for Sample A and 21.60% for Sample B.

Keywords: *particle size effect, performance analysis, gravity concentration*

57. INTRODUCTION

Gravity concentration is the best known and oldest method of mineral processing and uses the differences in density between minerals to separate them. Yet, despite its long and widespread use, it is not yet entirely understood [1]. The gravity separation process has been used in the mineral industry to separate particles under the action of hydrodynamic and gravitational forces [2]. It uses their relative movement in response to gravity and other forces, and is broadly related to the resistance to motion offered by a viscous fluid [3]. Gravity concentration offers advantages such as small capital requirements, low operating costs, and high efficiency (depending on the feed size). As it does not require the use of chemicals or excessive heating, it is usually considered to be environmentally friendly [3],[4],[5],[6],[7],[8],[9].

The efficiency of gravity concentration falls at particle sizes below 100 μm . At these sizes separation is difficult without imparting an extra force to the particles. This led to the development of enhanced gravity separators [8],[10],[11],[12],[13].

²⁷ Corresponding author: Hacettepe University, Hacettepe Vocational School, 06931, Sincan/Ankara, Turkey. kademli@hacettepe.edu.tr

The two principal factors affecting gravity concentration are the differences in density and particle size between the minerals being separated. When there are large particle size distributions in the feed, the separation performance is badly affected because of the loss of small heavy particles, which act like light coarse particles in the process.

All gravity concentration devices function more efficiently with prepared feeds, in which the particles are within a comparatively narrow size range [1]. The separation process takes advantage of density differences between minerals, but often there are no large density differences between the minerals to be separated. In such cases, narrow particle size distributions should be considered as a way of improving the efficiency of the separation process.

In this research, whole particle size distributions and narrow size fractions were compared, and the behavior of gravity concentration methods at narrow particle size fractions was investigated in detail. The equipment used in the research was as follows:

57.1. Jig Concentrator

This is a device that is used in mineral processing to separate the particles in the feed based on their specific gravity. The separation of particles is effected in a bed resting on a ragging screen. The bed is fluidized by a vertical pulsating motion created by a diaphragm and an incoming flow of hutch water [7]. The particles are introduced to the jig bed (usually a screen) where they are thrust upward by a pulsing water column or body, causing the particles to become suspended in the water. To allow stratification of the material into fractions of different settling velocity in the jig, the particles must be able to move freely between each other [14]. The jiggling action causes the heavier particles (of high specific gravity and size) to sink into the underflow, and the lighter and smaller particles to form a tailing overflow.

57.2. Spiral Concentrator

This is a device used for separating particles in a slurry, based upon a combination of the solid particle density and the hydrodynamic properties of the particles, such as drag force and centrifugal force. The device has a tower and sluice. Slots or channels are placed in the base of the sluice to extract heavy particles that have settled out of suspension. As larger and heavier particles migrate to the inside of the sluice faster and experience more drag from the inside, they travel more slowly and thus move toward the center of the spiral.

57.3. Shaking Table

This is used to separate minerals using the combined effect of mechanical motion and a thin water layer on the sloping table. The surface of the table oscillates backward and forward, causing the particles on the table to arrange themselves in different layers and zones. The minerals are then separated according to their densities.

58. MATERIALS AND METHODS

Two test material samples were used. Sample A was a mix of quartz (SiO_2) and hematite (Fe_2O_3), prepared by magnetic separating, and with particle densities of 2.65 g/cm^3 and 4.9 g/cm^3 , respectively. The samples comprised 20% hematite and 80% quartz by weight. Sample B, a calcite and lignite feed, was prepared in a float–sink bath, with particle densities of 2.7 g/cm^3 and 1.5 g/cm^3 , respectively. All samples were sieved at the same sieving size to obtain four different narrow fractions ranging from 1.6 mm to 0.106 mm.

Three concentration methods (shaking table, spiral, and jig) were tested using the same narrow size fractions, different solid contents, and different feed rates (except in the case of the jig). The artificial feed

was introduced in four steps and the performance was analyzed and compared. Three operational parameters were tested for the spiral concentrator and shaking table methods to determine the best feed rates. For all three methods, two further parameters were investigated: the particle size and the solids contents of the feed. Eighty different conditions were tested using the spiral and shaking table methods and 20 different conditions were tested using the jig. In total, 360 different conditions were tested. The test conditions for the spiral concentrator and shaking table are given in Table 1.

Table 1. Test Conditions for Spiral Concentrator and Shaking Table

Number of Tests	Particle Size (mm)	Solids,%	Feed Rate (l/s)
1-16	1.6 + 1.18	15	1/1.5/2/2.5
		20	1/1.5/2/2.5
		25	1/1.5/2/2.5
		30	1/1.5/2/2.5
17-32	1.18 + 0.6	15	1/1.5/2/2.5
		20	1/1.5/2/2.5
		25	1/1.5/2/2.5
		30	1/1.5/2/2.5
33-48	0.6 + 0.3	15	1/1.5/2/2.5
		20	1/1.5/2/2.5
		25	1/1.5/2/2.5
		30	1/1.5/2/2.5
49-64	0.3 + 0.106	15	1/1.5/2/2.5
		20	1/1.5/2/2.5
		25	1/1.5/2/2.5
		30	1/1.5/2/2.5
65-80	1.6 + 0.106 (Whole distribution)	20	1/1.5/2/2.5
		25	1/1.5/2/2.5
		30	1/1.5/2/2.5

First, the spiral and shaking table methods were tested at different feed rates. The test conditions are shown in Table 1 for the spiral concentrator and shaking table and Table 3 for the jig.

Table 2. Feed Rate Results for Spiral Concentrator and Shaking Table (15% Solids)

Spiral		Shaking Table		
Recoveries (%)				
Sample A		Sample B		
Feed Rate (l/s)	Total of Narrow Fractions	Whole Distribution	Total of Narrow Fractions	Whole Distribution
1	97.40	81.64	89.76	71.98
1.5	94.80	79.71	86.98	69.87
2	93.45	79.08	58.52	69.09
2.5	91.45	78.05	83.39	67.86

Table 2. Test Conditions for Jig

Number of Tests	Particle Size (mm)	Solids, %
1-4	1.6 + 1.18	15/20/25/30
5-8	1.18 + 0.6	15/20/25/30
9-12	0.6 + 0.3	15/20/25/30
13-16	0.3 + 0.106	15/20/25/30
17-20	1.6 + 0.106 (Whole distribution)	15/20/25/30

All tests were operated as batch processes. Two discharge units were used, the positions of which were fixed. Samples were fed directly into the separators and the products were collected as concentrates and tailings. The hematite was separated by a magnetic separator, and the lignite was separated using a float-sink bath. The products were dried and weighed out; they were finally analyzed, and their recovery rates calculated.

Samples of the concentrates and tailings were taken simultaneously during the tests. In each new test, the equipment was cleaned, calibrated and operated in a manner appropriate to the new test conditions. To allow comparisons to be made between the methods at whole particle size distributions from 1.6 mm to 0.106 mm and at four narrow size fractions, the concentrates from all the methods were treated in the same way.

59. RESULTS AND DISCUSSIONS

The particle size distributions were set between $-1.6 + 1.18$ mm and $-0.3 + 0.106$ mm, and the solids% ranged from 30% to 15% by weight for all methods. All these ranges were within typical industrial operational limits. The relationships between particle size and recovery rates are given in Figures 1 to 3, and the differences in recovery rates between the methods are given in Figure 4, for both samples A and B.

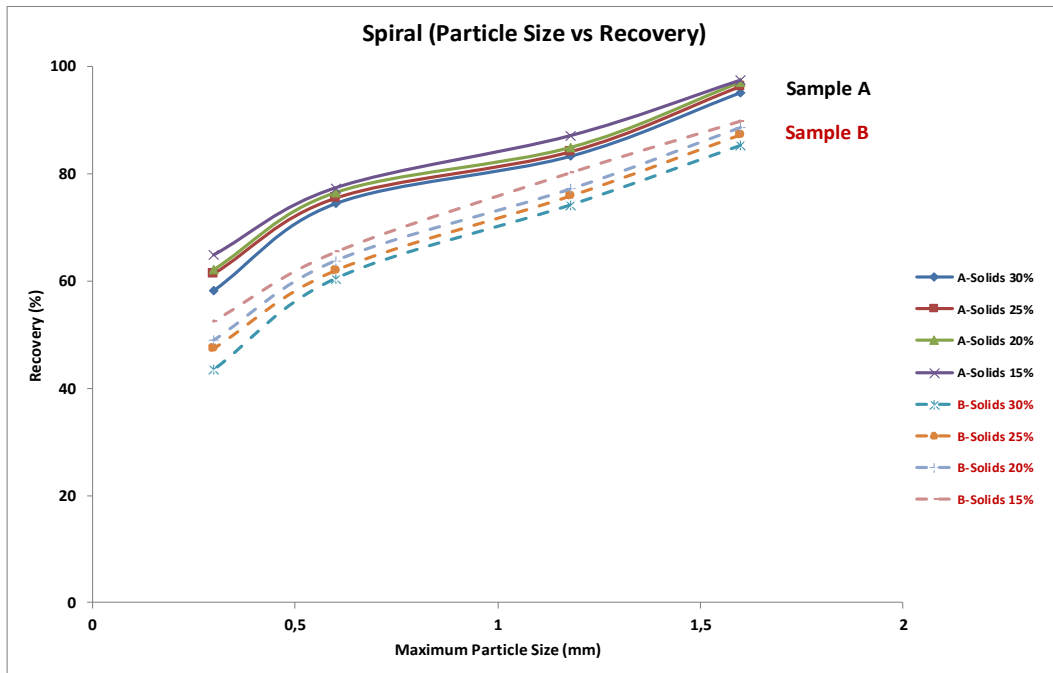


Figure 1. Spiral Recovery versus Particle Size for Both Samples

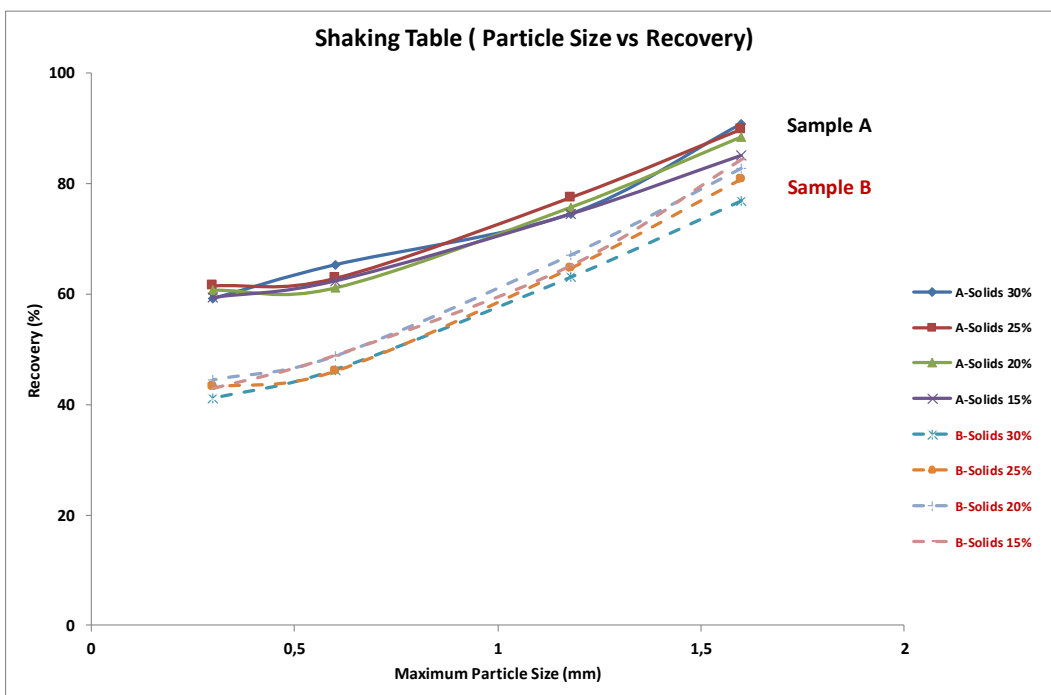


Figure 2. Shaking Table Recovery versus Particle Size for Both Samples

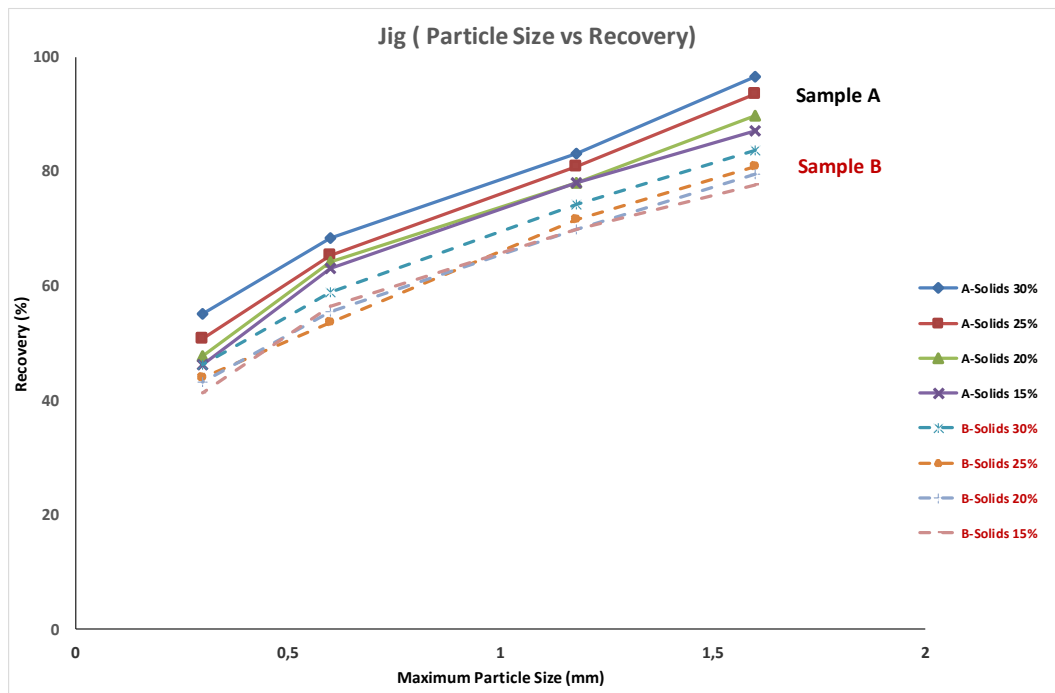


Figure 3. Jig Recovery versus Particle Size for Both Samples

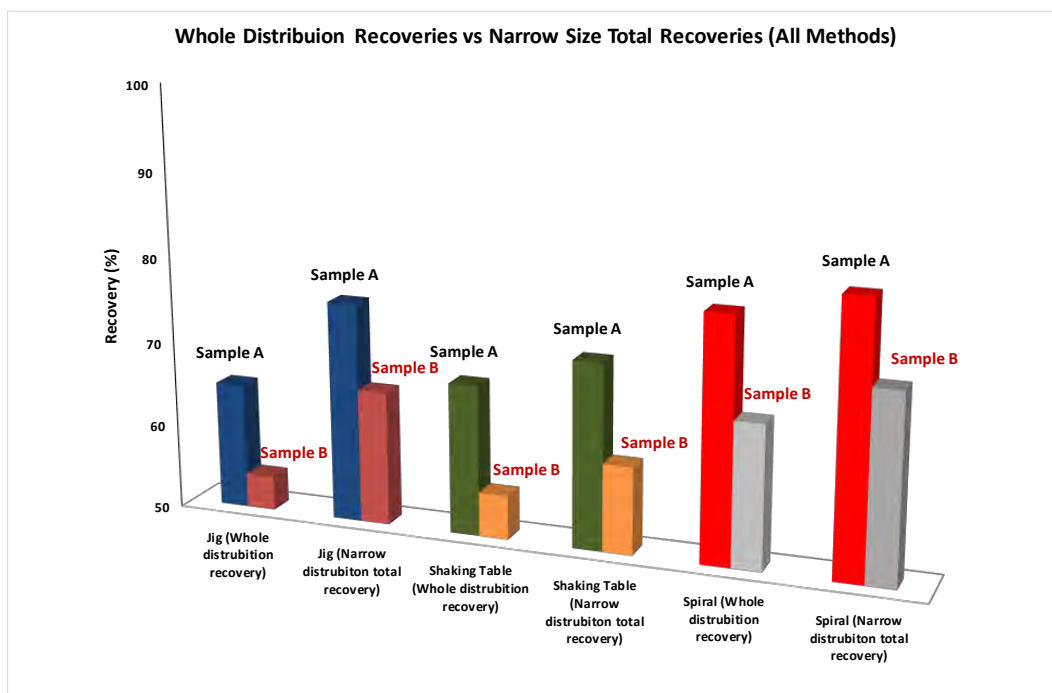


Figure 4. Recovery Differences between Whole Distribution and Total Fractional Particle Size for Both Samples

The results for both samples showed that the best recovery rates were obtained at a 1 l/s feed rate for all solids contents. The recoveries at 15% solids contents are given in Table 2.

In the spiral and shaking table concentrators, slight differences in recoveries were observed for different solids contents of the feed. As can be seen from Figures 1, 2, and 3, however, the recoveries were more strongly affected by increases in the particle size.

The recoveries using the shaking table were lower than those from the spiral concentrator, but the results showed the same overall trend of increasing with particle size. A direct relationship with the particle size distribution was found in both concentrations for both samples. The jig recoveries showed the most significant increase as the maximum particle size increased, as shown in Figure 4. The total recoveries were calculated using Equation 1.

$$\text{total recovery, \%} = \sum_{i=1}^n \frac{C_i \cdot c_i}{F \cdot f} \cdot 100 \quad (1)$$

where C_i is the amount of feed fraction, c_i is the grade of hematite at fraction, F is the total feed amount, f , is the grade of total feed, and n is the number of fractions.

The results suggested that the performance of all methods increased as the feed departed from narrow size fractions. The jig performance increased by 16.94% for sample A and 21.60 for sample B, the shaking table performance increased by 6.08% for sample A and 9.20% for sample B, and the spiral concentrator performance increased by 3.98% for sample A and 7.79% for sample B.

60. CONCLUSION

In this study, the effect of the particle size distribution on the separation performance of gravity concentrators was investigated. The experiments tested four narrow fractions of $-1.6 + 1.18$ mm, $-1.18 + 0.6$ mm, $-0.6 + 0.3$ mm, and $-0.3 + 0.106$ mm and with whole fractions, comprising all four, of $-1.6 + 0.106$ mm, with four different solids contents. The performance of the concentrators was demonstrated to be directly related to the particle size distribution. The performance of all methods increased as the feed departed from narrow size fractions.

The effect of particle size was greater for Sample B than Sample A. All three concentrators showed improved total recovery performance using prepared feeds with particles falling into a comparatively narrow size range.

The effect of the prepared feed on the concentrator was different for the different methods. The most significant improvement in performance was recorded for the jig, with recovery increases of 16.94% for Sample A and 21.60% for Sample B.

REFERENCES

- [1]. Burt, R.O. 1984. *Gravity Concentration Technology*. Elsevier Science Publishers: B.V, 80 – 81 p.
- [2]. Umucu, Y. 2015. Investigation of Separation Performance of Dense Medium Cyclone Using Computer Simulation. *Physicochem. Probl. Miner. Process.* 51(1), pp. 303–314.
- [3]. Burt, R. 1999. The role of gravity concentration in modern processing plants. *Minerals Engineering* 12 (11), pp. 1291 – 1300.
- [4]. Turner, J.F. 1991. Gravity concentration, past, present and future. *Minerals Engineering*, 4 (3–4), pp. 213 – 223.
- [5]. Luttrell et al. 1995 – Luttrell, G.H., Honaker, R.Q. and Phillips, D.I. 1995. Enhanced gravity separators: new alternatives for fine coal cleaning. *12th International Coal Preparation Conference*. Lexington, KT, pp. 281 – 292.

- [6]. Laplante, A.R. and Spiller, D.E. 2002. Bench-scale & Pilot plant test work for gravity concentration circuit design. *Society for Mining, Metallurgy and Exploration Inc. Min. Process. Plant Des., Practice Control Proc* (1), pp.160–175.
- [7]. Falconer, A. 2003. Gravity separation: old technique/new methods. *Phys. Sep. Sci. Eng.* 12 (1), pp. 31 – 48.
- [8]. Oruc et al. 2010 – Oruc, F., Ozgen, S. and Sabah, E. 2010. An enhanced-gravity method to recover ultrafine coal from tailings: Falcon Concentrator. *Fuel* (89), pp. 2433 – 2437.
- [9]. El-Midany, A.A. and Ibrahim, S.S. 2011. Does calcite content affect its separation from celestite by Falcon concentrator. *Powder Technology* 213 (1–3), pp. 41– 47.
- [10]. Traore et al. 1995 – Traore, A., Conil, P., Houot, R. and Save, M. 1995. An evaluation of the Mozley MGS for fine particle gravity separation. *Minerals Engineering* 8 (7), pp. 767–778.
- [11]. Burt et al. 1995 – Burt, R.O., Korinek, G., Young, S.R. and Deveau, C. 1995. Ultrafine tantalum recovery strategies. *Minerals Engineering* 8 (8), pp. 859 – 870.
- [12]. Honaker et al. 1996. – Honaker, R.Q., Wang, D. and Ho, K. 1996. Application of the Falcon concentrator for fine coal cleaning. *Minerals Engineering* 9 (11), pp. 1143–1156.
- [13]. Honaker, R.Q. 1998. High capacity fine coal cleaning using an enhanced gravity concentrator. *Minerals Engineering* 11 (12), pp. 1191 – 1199.
- [14]. Surowiak, A. and Brozek, M. 2016. A Physical Model of Separation Process by Means of Jigs. *Physicochem. Probl. Miner. Process.* 52(1), pp.228–243.

BIOGRAPHY

He is graduated from Hacettepe University, Department of Mining Engineering at the date of 2001. He had M.Sc. and Ph.D. degrees from the mineral processing section of same department at 2004 and 2009 respectively. He has been working at Hacettepe Vocational School since 2002. He is head of Alternative Energy Sources Program, his professions are mineral processing, coal cleaning and industrial raw materials.

Prediction of Surface Roughness in Milling Compacted Graphite Iron with Artificial Neural Network and Regression Analysis

Şener Karabulut²⁸, Murat Sarıkaya²⁹, Abdulkadir Güllü³⁰

Abstract

In the present study, it was investigated machinability of compacted graphite iron by using various lead angles and chip thickness and cutting speeds. Analytical models were developed for the prediction of surface roughness (Ra) values after face milling process. Experimental results have been modeled by using artificial neural networks and variance (ANOVA) analysis results and developed a prediction model. A comparison of ANN model with regression model is also carried out. Variance analysis results showed that a strong correlation between the lead angle, chip thickness and surface quality. The surface roughness values were improved while increasing the lead angle value from 45° to 88° in dry and wet milling of compacted graphite iron. The experimental results showed surface quality was improved between 3.0% - 38% at the all lead angles when cutting oil was used in the experiments.

Keywords: Compacted Graphite Iron, lead angle, face milling, surface roughness, artificial neural network, regression model.

61. INTRODUCTION

Compacted graphite iron (CGI) is accepted nowadays as an important manufacturing material widely used in the automotive industry for the production of many parts such as engine heads, diesel engine blocks, exhaust manifolds and brake discs instead of gray cast iron (GCI) due to its performance. Due to its increased strength compared to grey cast iron (CI) it allows an increase in the cylinder-pressures and, therefore, a better fuel economy and a higher power output would also be possible. However, the machinability of CGI is poor when compared to grey cast iron [1-3] Heck et al. [4] machined CGI in high cutting speeds (800 m/min) and obtained a rougher surface compared with the surface quality of GCI. Munoz et al. [5] investigated the surface milling of the material of A1 7075-T7351 in experiments and modelled the experimental results by using artificial neural networks. Their experiments have shown that there is a strong correlation between chip thickness and surface roughness. Yalçın et al. [6] carried out a surface milling processing on the material SAE 1050 and modelled the experimental data by using artificial neural networks (ANN) at the end of the experiment. While chip thickness and the rate of feed were the most effective parameters on the model, the cutting speed and cutting oil were the least effective parameters. Chien and Chou [7] developed a mathematical model for the machinability of stainless steel of type 304 in an experiment. They predicted the surface roughness, cutting power and tool life as 4,4 %, 5,3 % and 4,2 % respectively. Sağlam [8] applied and evaluated artificial neural networks in his experiment to establish an observation system for a smart tool status based on the results of cutting powers in face milling operations. Test results indicated that tool wear and surface roughness were predicted with a success rate of 77 % and 79 %. Lo [9], indicated that ANNs had been very effective in metal

cutting applications and radius of cutting tool edge, feed rate, cutting speed and the heat and vibrations were the main elements having an effect on the surface roughness. Zain et al. [10] used an artificial neural network model to predict the parameters effecting surface roughness during milling. The analysis of the results of their experiment showed that the best surface roughness value could be obtained by means of high speed, low feed and radial chip angle. Öktem et al. [11] investigated the surface roughness values obtained in milling the steel of the type AISI 1040 in wet cutting with carbide tools by establishing a mathematical model with artificial neural networks. Marimuthu and Chandrasekaran [12] used multi layered feed forward ANN to predict the surface roughness and tool wear during turning process of stainless steels. Palanisamy et al. [13] and Kalidas et al. [14] used feed forward back propagation ANN along with regression analysis for a proposed design of experiments to predict

¹Hacettepe University, Department of Mechanical program, 06935, Ankara Turkey senerkarabulut@hacettepe.edu.tr

²Sinop University, Department of Mechanical Engineering, Sinop Turkey msarikaya@sinop.edu.tr

³Gazi University, Faculty of Technology, Manufacturing Engineering Department, 06500, Ankara Turkey agullu@gazi.edu.tr

tool wear and the predicted values were found within the trained range. Asiltürk et al. [15] studied the effect of the cutting parameters on the surface roughness (Ra) on the machining of hardened steel of AISI 1040. The experimental results showed the feed rate was the most important parameter of those which had an effect on surface roughness. Kivak [16] studied to determine the effects of the machining parameters on surface roughness and flank wear by using Analysis of variance (ANOVA). The analysis results showed that the feed rate was the dominant factor affecting surface roughness and cutting speed was the dominant factor affecting flank wear. Vrabel et al. [17] developed a control strategy by using ANN to predict surface roughness and tool wear. Experimental data collected from tests were used as input parameters into ANN to identify the sensitivity among cutting conditions, tool wear and monitoring parameters and surface roughness. Rao et al. [18], studied the effect of cutting parameters on the surface roughness, tool wear and work piece vibrations by using ANN which were trained by using experimental results. They developed a predict model and used to predict the surface roughness, tool wear and work piece vibration. They found good correlation between the predicted values and experimental data. Benardos and Vosniakos [19] presented a neural network modeling approach for the prediction of surface roughness for a Taguchi design of experiments (DOE) method.

In this study, the effects of lead angle variation and cutting parameters on the surface roughness are studied and developed a new approach based on ANNs and regression analysis to determine the effect of lead angle and maximum chip thickness on the surface roughness when machined CGI various cutting parameters such as cutting speed, feed rates and constant depth of cut.

62. MATERIAL AND METHODS

The milling experiments were carried out in dry and wet cutting conditions using a very rigid Jhonford VMC550 model three axis CNC milling machine tool. Rectangular CGI blocks of 100 x 100 x 100 mm³ were used in the experiments. The chemical compositions of the specimens were obtained during the casting process in the factory is given in Table 1 and mechanical properties are indicated in Table 2. Sandvik coromant GC3040 quality carbide inserts mounted on the tool holder and two inserts were used in the experiments. CastrolHysol G thinned at the rate of 5.0% was used as cutting liquid. The average surface roughness (Ra) of the workpiece was measured by a MAHR-Perthometer M1 portable surface roughness device Every surface was machined with a separate set of tools and surface roughness was measured by machining the samples along 100 mm and also their averages were calculated by measuring the rate of surface roughness on 4 different points. Maximum chip thickness value (h_{ex}) was taken as variance instead of fixed feed rate values in the experiments. Reducing the lead angle (K_r) increases the feed rate f_z in connection with the equation $h_{ex} = f_z \times \sin \kappa_r$. The cutting parameters used in the experiments are shown in Table 3.

Table 1. Chemical composition of CGI

C	Si	Mn	P	S	Cr	Ni	Mo
3.82	1.804	0.337	0.031	0.015	0.074	0.013	0.002
Cu	Mg	Sn	Ti	Al	Zn	Bi	Fe
0.879	0.014	0.092	0.0203	0.008	0.082	0.007	Kalan

Table 2. Mechanical properties of CGI

Ultimate Tensile Strength (MPa)	% 0.2 Yield Strength (MPa)	Elongation (%)	Typical Hardness, HV	Impact test (Joule)
502.7	284.3	1.8	280.0	8.6

63. MODELLING OF SURFACE ROUGHNESS VALUE

63.1. Estimation of surface roughness value by ANN

Multilayer ANN model with back-propagation was taken in this experiment because of its wide application and usage and Levenberg-Marquardt algorithm was preferred. The learning algorithm of Levenberg-Marquardt, a very successful optimization method, is one of the different learning techniques

of back-propagation algorithm used in learning. LM algorithm is based on a great number of neighborhood areas; it is a method of least squares. One of the most important advantages of LM algorithm lies in its characteristic feature of rapid convergence. A feed forward four layered back propagation neural network is constructed in Fig.2. The network is constructed with four layers including with input, output and hidden layers. The input neurons are cutting speed, lead angles, chip thickness and output neuron is surface roughness (Ra).The prediction performance of ANN model developed in the experimental study was specified by using coefficient of determination (R^2), root mean square error (RMSE) and mean absolute percentage error (MAPE).

$$R^2 = 1 - \left(\frac{\sum (Ra_i - Ra_{ANN,i})^2}{\sum (Ra_{ANN,i})^2} \right) \quad (1)$$

$$RMSE = \sqrt{\left(\frac{1}{n} \sum_{i=1}^n |Ra_{ANN,i} - Ra_i|^2 \right)} \quad (2)$$

$$MAPE = \sqrt{\left(\frac{1}{n} \sum_{i=1}^n \left| \frac{Ra_{ANN} - Ra}{Ra_{ANN}} \right| \times 100 \right)} \quad (3)$$

Pythia software was used for training of this network and the ANN was trained with back propagation algorithm. Weights of network connections are randomly selected by the software. Neural network was trained with 31 experimental data and tested 17 experimental data for each of the dry and wet cutting conditions. Pythia software uses Fermi function as transfer function. Fermi transfer function can be measured using equality (4).

$$N(z) = \frac{1}{1 + e^{-4(z-0.5)}} \quad (4)$$

The experimental results were trained with ANN and investigated with the most appropriate network structures, different cycle and neuron counts. Firstly, a network structure with the lowest deviation value was selected by getting the programme automatically optimized. After specifying such network structure, it was trained up to the smallest deviation value by changing the deviation count and training values of the programme. After these operations, a network structure comprised of four layers and twelve neurons was selected for the experiments made in dry conditions. On the other hand, a network structure constructed of four layers and seventeen neurons as selected for the experiments made with cutting liquid. Maximum and minimum values of the cutting values used in the experiment for normalization are shown in Table 4. Real values were compared with the results of the network structure obtained in order to test the reliability of the network structure and it was observed thereby that there was no explicit error in the deviation rate. After this phase, weight values in neurons were imported into excel software and analytical model was developed by using these weight values so as to predict the average surface roughness value (Ra).

Table 4. The limit values for ANN software

Inputs			
	Lead angle (κ_r) degree	Cutting speed (Vc) m/min	Table feed speed (Vf)
Maximum	88	290	995
Minimum	45	180	291

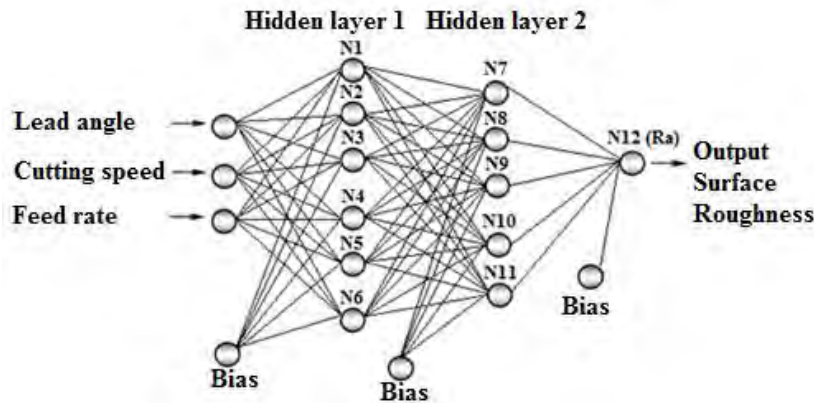


Figure 2. ANN structure in LM algorithm with twelve neurons in dry machining

Each input value is multiplied with the weight values connected with it. Weighted input values are added linearly, thus transforming into output values. As it is shown in Figures 2 and 3, these output values are used as input values for other neurons. Equation 5 was acquired by using the weight values of the neurons in the ANN network structure obtained in dry milling conditions. This equality can be used for the prediction of the surface roughness value (Ra) when milling compacted graphite iron by using the parameters of lead angle, cutting speed and chip thickness

$$N_{12}(Ra) = \frac{1}{1+e^{-4(1,898239*N_7+1,214437*N_8-0,476672*N_9-1,760697*N_{10}+0,848790*N_{11}-0,5)}} \quad (5)$$

Fermi transfer function,

$$N(i) = \frac{1}{1+e^{-4*(E_i-0,5)}} \quad (6)$$

Table 5. Constants used in eq.7 from neurons 1–6.

<i>i</i>	Constants		
	w_{1i}	w_{2i}	w_{3i}
1	-1.068314	0.830852	-0.252841
2	-0.235084	-0.131288	0.939488
3	0.027382	-1.092550	0.274929
4	0.589768	-0.194317	0.063548
5	-0.211420	-0.550743	0.799970
6	-1.429907	0.464325	0.673908

E_i value was calculated using the equation (7) for the neurons between N1–N6. i represents the neuron numbers in the equation. Obtained weights are shown in **Table 5**.

$$E_i = w_{1i} * V_c + w_{2i} * \kappa_r + w_{3i} * V_f \quad (7)$$

E_i value for the neurons between N7–N11 was calculated using the equation (8). Obtained weights are shown in Table 6.

$$E_i = w_{1i} * N_1 + w_{2i} * N_2 + w_{3i} * N_3 + w_{4i} * N_4 + w_{5i} * N_5 + w_{6i} * N_6 \quad (8)$$

Table 6. 7–11 Constants used in eq. (8) from neurons 7–11.

i	Constants					
	w1i	w2i	w3i	w4i	w5i	w6i
7	0.850954	0.604835	-0.107952	0.223413	0.368959	-0.380113
8	-0.460165	-0.719499	0.892320	0.177093	-0.559321	0.024755
9	-1.100507	-0.186601	-0.567789	0.565843	0.440070	-0.323774
10	0.790632	-1.428010	-0.885115	1.311894	-1.960543	0.402976
11	-0.503508	-1.020433	0.603632	0.050887	-0.234520	-0.471311

After that the experimental data obtained using cutting liquid were trained in ANN software, the network structure shown in Fig. 2 was obtained.

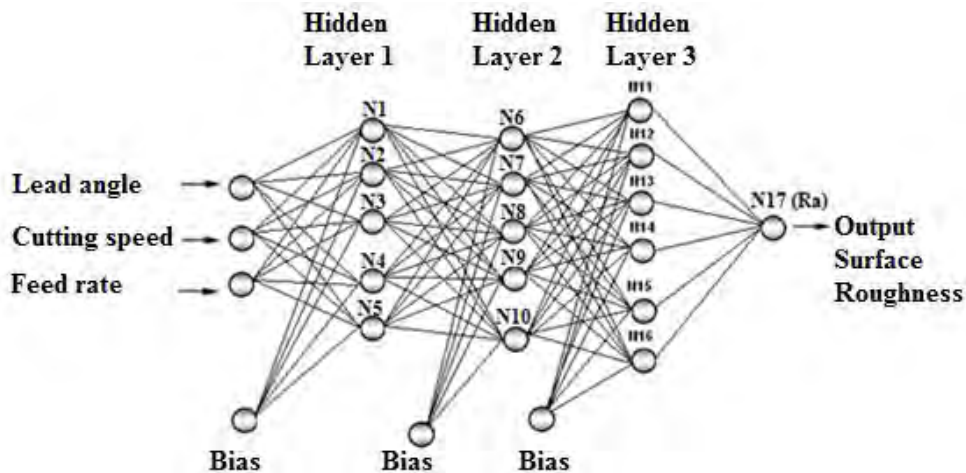


Figure 3. ANN structure in LM algorithm with seventeen neurons in machining with cutting fluid

The prediction model in the equation 9 was produced by using the weight values of the neurons in the ANN network structure obtained in wet cutting conditions.

$$N_{17}(Ra) = \frac{1}{1 + e^{-4(1.026041 * N_{11} + 1.366720 * N_{12} + 0.849316 * N_{13} + 1.614065 * N_{14} - 0.361943 * N_{15} - 0.991599 * N_{16} - 0.5)}} \quad (9)$$

E_i value for the neurons between $N_1 - N_5$ was calculated using the equation 10. i represents here the neuron numbers in the equality. The obtained weights are shown in **Table 7**.

$$E_i = w_{1i} * V_c + w_{2i} * \kappa_r + w_{3i} * V_f \quad (10)$$

Table 7. 1-5 Constants used in eq. (10) from neurons 1-5.

<i>i</i>	Constants		
	w_{1i}	w_{2i}	w_{3i}
1	0.223671	-0.528556	1.271025
2	0.741552	0.359002	-0.716669
3	-0.274169	0.097705	0.391986
4	1.176485	-2.398944	-0.218577
5	0.004250	0.385007	-1.839784

E_i value for the neurons between $N_6 - N_{10}$ was calculated using the equation (11). The obtained weights are shown in Table 8.

$$E_i = w_{1i} * N_1 + w_{2i} * N_2 + w_{3i} * N_3 + w_{4i} * N_4 + w_{5i} * N_5 \quad (11)$$

Table 8. Constants used in eq. (11) from neurons 6-10.

<i>i</i>	Constants				
	w_{1i}	w_{2i}	w_{3i}	w_{4i}	w_{5i}
6	0.382548	-0.699944	-0.590017	0.646119	-0.471840
7	-0.164589	1.136325	-1.322452	-0.196480	-1.308185
8	-0.931087	-1.173439	0.869143	-0.192901	0.105950
9	0.456575	-0.151332	0.532153	-0.215186	1.210140
10	-1.203295	0.661660	-1.116207	1.346328	-0.778138

E_i value for the neurons between $N_{11} - N_{16}$ was calculated using the equation no. (12). the weights obtained are shown in Table 9.

$$E_i = w_{1i} * N_6 + w_{2i} * N_7 + w_{3i} * N_8 + w_{4i} * N_9 + w_{5i} * N_{10} \quad (12)$$

Table 9. Constants used in eq. (11) from neurons 11-16.

<i>i</i>	Constants				
	w_{1i}	w_{2i}	w_{3i}	w_{4i}	w_{5i}
11	-0.433657	-0.458551	-0.643912	0.522064	-0.442472
12	-0.734969	0.368748	-0.025489	-0.167362	-0.531363
13	-0.885300	-0.783036	0.571686	-0.602674	0.488736
14	0.771363	-0.730785	-0.986845	0.840777	0.634347
15	-0.275527	0.661349	0.770736	-0.818973	-0.795326
16	-0.428654	-0.114545	-0.298867	-0.864344	1.521841

63.2. Estimation of surface roughness by regression analysis

In this study regression analysis was also used for the modelling and analysing of several cutting variables where there is relationship between dependent and independent variables. In the experiments dependent variable is surface roughness (R_a) whereas the independent variables are lead angle (K_r), cutting speed (V_c) and maximum chip thickness (h_{ex}). In obtaining predictive equations for the surface roughness, regression analysis was used. The predictive equations which were obtained by the linear regression model of surface roughness in dry and wet cutting conditions are given below. The linear regression model

was generated under the main effects of control factors realised in dry cutting conditions. The coefficient of determination of this equation was calculated as $R^2 = 0.95$.

$$R_a = 0,617096 - 0,0034838 \times K_r - 0,000717807 \times V_c + 0,00042847 \times V_f \quad (13)$$

The linear regression model obtained in wet cutting conditions was calculated as $R^2 = 0.90$. This result was realised under 95% confidence level. Hence the predictive equations for the quadratic regression of surface roughness was calculated with factor interactions.

$$R_a = 0,533 - 0,00257 \times K_r - 0,000727 \times V_c + 0,000368 \times V_f \quad (14)$$

The coefficient of determination of quadratic equation was calculated as $R^2 = 0.9686$ and is given below:

$$R_a = 0,23095 + 0,0122182 \times K_r - 0,00252211 \times V_c + 0,000527258 \times V_f + 0,00000673564 \times K_r \times V_c - 0,00000127682 \times K_r \times V_f - 0,0000006148 \times V_c \times V_f - 0,000116653 \times K_r^2 + 0,0000033134 \times V_c^2 + 0,0000000970135 \times V_f^2 \quad (15)$$

64. RESULTS AND DISCUSSIONS

In the experiments, the surface roughness was affected by the cutter lead angle and maximum chip thickness. All the experimental results indicated that the surface roughness value improved as the lead angle increased from 45° towards 88° in dry and wet cutting conditions. The highest surface roughness value in dry cutting conditions was obtained as $R_a=0.69 \mu\text{m}$ when the cutting parameters are $K_r 45^\circ$, $V_c=290 \text{ m/min}$ and $V_f=994 \text{ mm/min}$ the highest feed speed in experimental parameters. In the same cutting conditions by using cutting liquid surface roughness value $R_a=0.58 \mu\text{m}$ was obtained. The best surface roughness value $R_a=0.29 \mu\text{m}$ was obtained in lead angle of 88° , cutting speed of $V_c=215 \text{ m/min}$ and feed speed of $V_f=348 \text{ mm/min}$. In the same cutting conditions by using cutting liquid $R_a=0.21 \mu\text{m}$ was obtained. It was observed in all the experiments that cutting liquid made a positive contribution in a manner that surface roughness values got better at the rates 3% up to 38%. Main effects of control factors were evaluated in variance analysis. The effect of control factors on surface roughness in experiments made under dry conditions was as follows: lead angle (K_r) 72.75%, feed rates (V_f) 21.64% and cutting speed (V_c) 0.533%. The results of the variance analysis showed that the lead angle had the greatest effect on surface roughness when processed with different lead angles and the cutting speed had the least effect thereby. While feed rate value increased in connection with the maximum chip thickness, surface roughness value increased as well. The results obtained in experimental studies were realised in parallel to the related literature. Although it can be expected that an increase in the cutting speed could better the surface quality, the increase in feed rate neutralized the effect of cutting speed. It was observed for this reason that the equation of second degree was more effective in the prediction model and the evaluation of variance analysis was realised based on the independent variables and the interactions of these variables. The effect of control factors on surface roughness was as follows: lead angle (K_r) 65.96%, feed speed (V_f) 23.92% and cutting speed (V_c) 5.77%. An examination of variance analysis indicated that lead angle had the most effect on surface roughness in dry and wet cutting conditions and cutting speed had the least effect in this sense (Figure 4). While decreasing the lead angle from 88° towards 45° for a given chip thickness, increased the feed rates and the cutting edge contacted the machined material on a wider surface during the cutting process. As a result of this, high feed cutting forces were produced during the process because of the friction [20,21] and thus the value of surface roughness got higher.

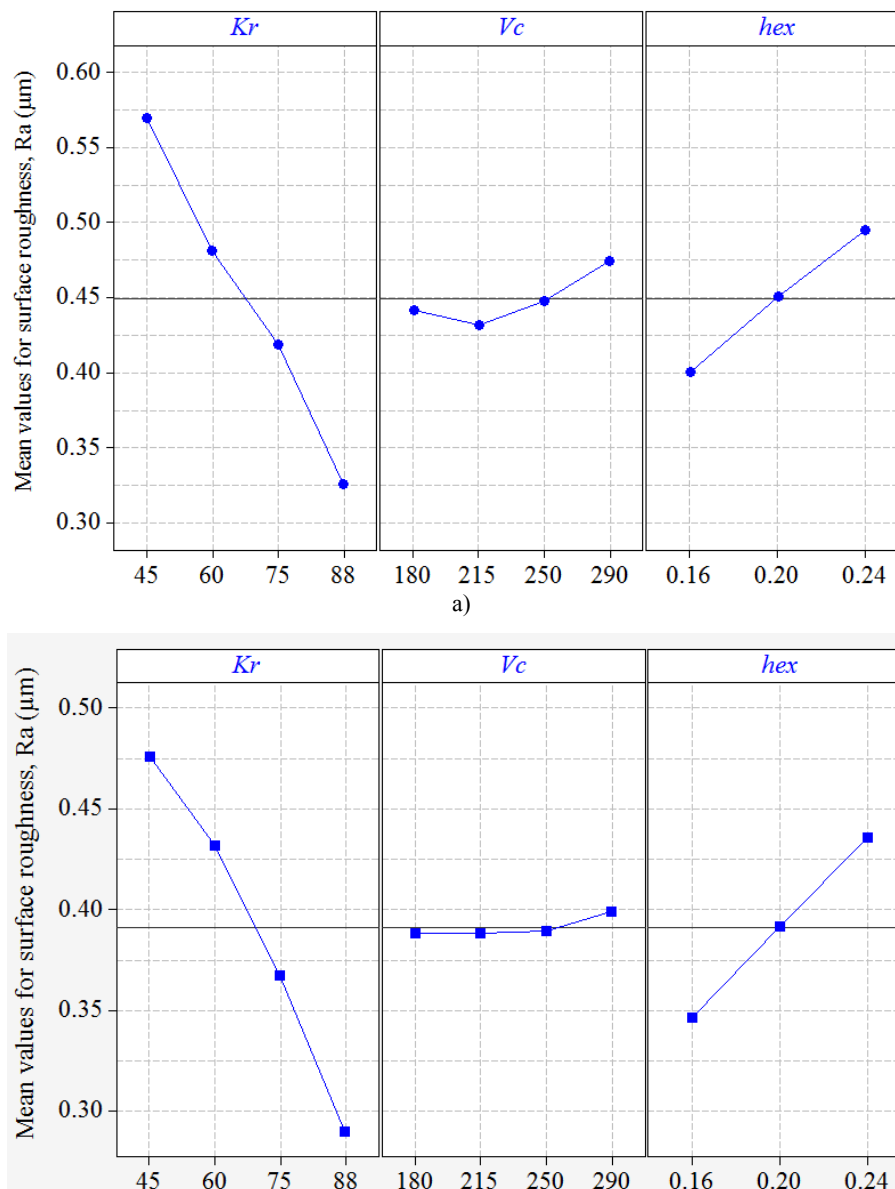


Figure 4. The effects of the cutting parameters on the surface roughness a) in dry machining b) in machining with cutting fluid

Variance analysis results regarding to dry cutting conditions are shown in Table 10, on the other hand Table 11 indicates the variance analysis concerning processing realised with cutting liquid.

Table 10. Analysis of Variance (ANOVA) in dry cutting conditions.

Control factors	Degree of freedom	Sum of squares	Mean squares	F	P
Dry conditions					
Kr	3	0.23981	0.06479	168.603	0.00
Vc	2	0.00176	0.01634	104.741	0.00000
Vf	2	0.07133	0.07133	26.411	0.0000210
Total	31	0.32959			
Wetting conditions					
Kr	1	0.148062	0.0041762	124.232	0.002012
Vc	1	0.000174	0.0010481	31.178	0.091979
Vf	1	0.053707	0.0006098	18.139	0.192401
Kr*Vc	1	0.000405	0.0000923	0.2746	0.605751
Kr*Vf	1	0.001174	0.0000194	0.0577	0.812540
Vc*Vf	1	0.000602	0.0000215	0.0641	0.802653
Kr*Kr	1	0.012967	0.0100923	300.220	0.000020
Vc*Vc	1	0.000306	0.0002409	0.7165	0.406835
Vf*Vf	1	0.000014	0.0000138	0.0409	0.841597
Total	30	0.224471			

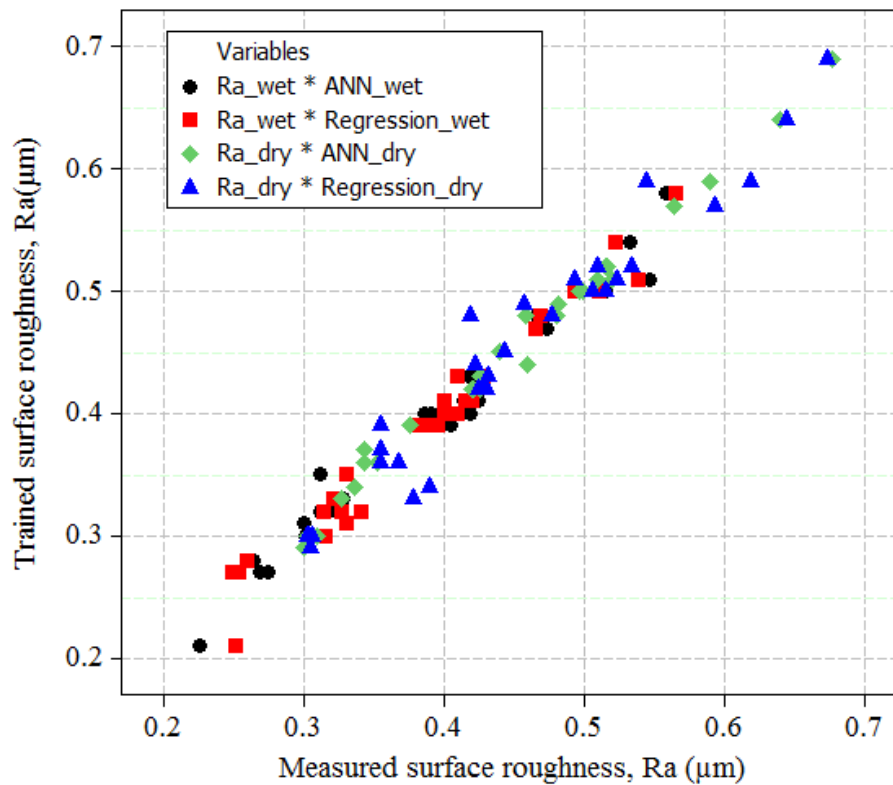


Figure 5. Comparison of training data result with the ANN model and regression model

Figure 5 shows the results obtained with the measured and trained surface roughness value by using ANN and regression analysis models. In order to test the reliability levels of obtained mathematical models, it was carried out 17 confirmation test in dry and wet cutting conditions with respect to the control factors of lead angle, cutting speed and feed rate. The comparison of actual test result and predicted values which were obtained by ANN and regression models in dry and wet machining conditions are given in Fig.6. It was found that predicted values are very close to the experimental values. The prediction rate in the developed model by ANN has been 99.1% in dry cutting conditions and in wet cutting conditions the prediction rate has realised 97.4%. R^2 values of the equations which were obtained by regression model for Ra were calculated 94.9% in dry cutting and 96.8% in wet cutting. R^2 values of the equations which were obtained by ANN and regression models for Ra were found to be 96.9% for ANN and 94.7% for regression respectively in dry cutting conditions. ANN model was produced a prediction rate of 95.1% and regression model was produced a prediction rate of 97.2% in wet cutting conditions.

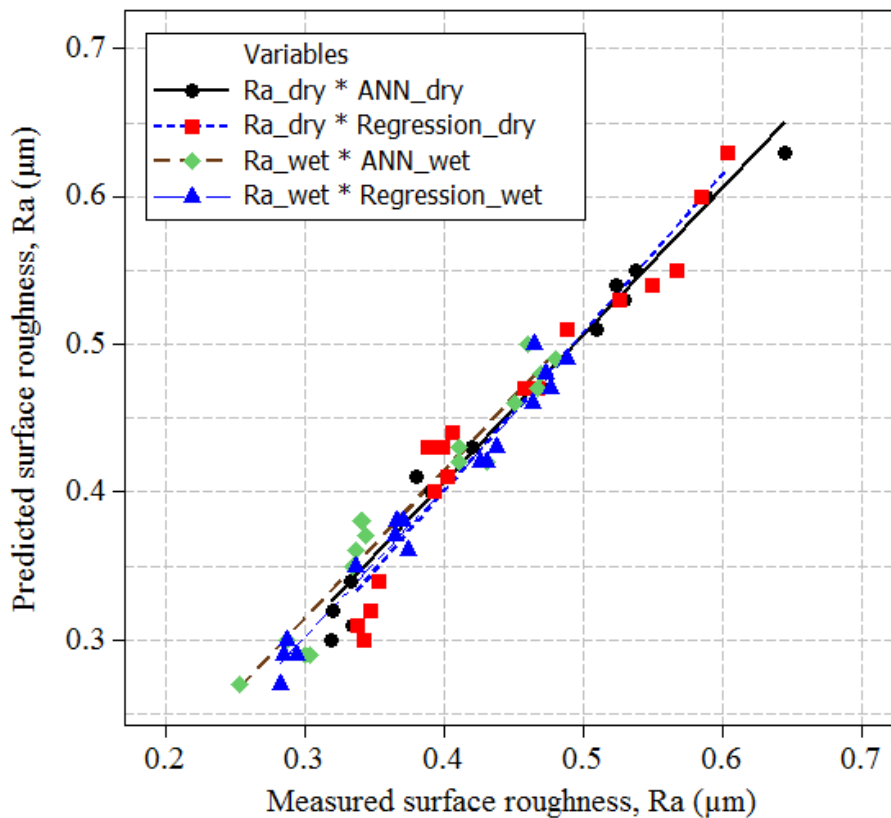


Figure 6. Comparison of test data with the prediction model.

5 CONCLUSIONS

CGI was machined in dry and wet cutting conditions in milling machine with various lead angle and cutting parameters. The ANN was trained with 31 experimental data and tested with 17 experimental data for dry and wet cutting conditions. The experimental results also were evaluated using ANOVA. The following conclusions may be drawn:

- In each trial of experiment, a strong correlation surface roughness value and lead angle. The experimental results have shown that surface roughness values decreased when the lead angle increased in dry and wet cutting conditions. While decreasing the lead angle from 88° towards 45° , feed rate and the removed chip volume were increased, this situation had a negative effect on the surface roughness. Cutting liquid caused an improvement in rates between 3% and 38% on surface roughness values.
- The mathematical models showed that there is agreement between experimental data and predicted values for surface roughness.
- According to the result ANOVA, it was found that the lead angle was the most significant parameter for surface roughness with a percentage contribution of 72.75% in dry cutting conditions and 65.96% in wet cutting conditions.
- According to confirmation test results, measured values were within the 95% confidence interval. The R2 values for confirmation data were calculated as 96.9% with ANN and 94.7% with regression analysis in dry cutting conditions. In wet cutting conditions, the R2 values for confirmation data were calculated as 95.1% with ANN and 97.2% with regression analysis

All of these results showed that the ANN and regression method were reliable methodology for the reducing of machining time and costs in milling CGI.

Acknowledgments

The authors would like to thank TUBİTAK and Compenanta DÖKTAŞ for their support in this work.

REFERENCES

- [1]. W. Guesser, T. Schroeder, and S. Dawson, Production Experience with compacted graphite iron automotive components, AFS Transactions, DesPlaines, 2001.
- [2]. E. Abele, B. Schramm, Wear behavior of PCD in machining, Proceedings of the 2nd industrial diamond conference, Rome, 2007.
- [3]. M. Heck, H. M. Ortner, S. Flege, U. Reuter, W. Ensinger, Analytical investigations concerning the wear behaviour of cutting tools used for the machining of compacted graphite iron and grey cast iron, International Journal of Refractory Metals & Hard Materials 26, 197–206 2008.
- [4]. U. Şeker, A. Kurt, and I. Çiftçi, Design and construction of a dynamometer for measurement of cutting forces during machining with linear motion, Materials and Design, 23, 355-360 2002.
- [5]. P. Munoz-Escalona, and P. G Maropoulos, Artificial neural networks for surface roughness prediction when face milling Al 7075–T7351, Journal of Materials Engineering and Performance, 19, 185–193 2010.
- [6]. U. Yalcin, A.D. Karaoglan, I. Korkut, Optimization of Cutting Parameters in Face Milling with Neural Networks and Taguchi based on Cutting Force, Surface Roughness and Temperatures, International Journal of Production Research, 51, 3404–3414 2013.
- [7]. W. Chien, The predictive model for machinability of 304 stainless steel”, Journal of Materials Processing Technology, 118, 442-447 2001.
- [8]. H. Sağlam, Frezeleme yapay sinir ağları kullanarak, çok-elemanlı kuvvet ölçümlerine dayalı takım durumu izleme”, Doktora Tezi, Selçuk Üniversitesi Mühendislik Fakültesi, Konya, 2000.
- [9]. S. Lo, “An adaptive-network based fuzzy inference system for prediction of workpiece surface roughness in end milling”, Journal of Materials Processing Technology, 142, 665-675 2003.
- [10]. Zain Mohd, H. Haron and S. Sharif, Prediction of surface roughness in the end milling machining using Artificial Neural Network, Expert Systems with Applications, 37, 1755–1768 2010.
- [11]. H. Öktem, ve F. Erzincanlı, AISI 1040 çelik malzemenin CNC frezeleme ile işlenmesi sırasında oluşan yüzey pürüzlülüğünün yapay sinir ağıyla modellenmesi, 2. Ulusal Tasarım İmalat ve Analiz Kongresi, (2010) 221-229.
- [12]. P. Marimuthu, K. Chandrasekaran, Experimental study on stainless steel for optimal setting of machining parameters using Taguchi and neural network, ARPN J. Eng. Appl. Sci. 6, 119–127 2011.
- [13]. P. Palanisamy, I. Rajendran, S. Shanmugasundaram, Prediction of tool wear using regression and ANN models in end-milling operation, Int. J. Adv. Manuf. Technol. 37, 29–41 2008.
- [14]. S. Kalidass, P. Palanisamy, V. Muthukumaran, Prediction of tool wear using regression and artificial neural network models in end milling of AISI 304 austenitic stainless steel, Int. J. Eng. Innovative Technol. 1, 29–36 2012.
- [15]. Asiltürk, T.M. Demirci, Karbür kesici kullanarak sertleştirilmiş AISI 1040 çeliklerin frezelemeindeki yüzey pürüzlülüğünün regresyonla modellenmesi, 2. Ulusal Tasarım İmalat ve Analiz Kongresi, 20-30 2010.
- [16]. T. Kivak, Optimization of surface roughness and flank wear using the Taguchi method in milling of Hadfield steel with PVD and CVD coated inserts, Measurement 50, 19–28 2014.
- [17]. M.Vrabel, I. Mankova, J. Beno, J. Tuharsky, Surface roughness prediction using artificial neural networks when drilling Udimet 720, Procedia Eng. 48, 693–700 2012.

- [18]. K. Venkata Rao, B.S.N. Murthy, N. Mohan Rao, Prediction of cutting tool wear, surface roughness and vibration of work piece in boring of AISI 316 steel with artificial neural network, *measurement* 51, 63-70 2014.
- [19]. P.G. Bernardos, G.C. Vosniakos, Prediction of surface roughness in CNC face milling using neural networks and Taguchi's design of experiments, *Robot. Cim.-Int. Manuf.* 18 (5-6), 343-354 2002.
- [20]. Ş. Karabulut, A. Güllü, An investigation of cutting forces and analytical modelling in milling compacted graphite iron with different lead angles, *Journal of the Faculty of Engineering and Architecture of Gazi University*, 28, 135-143 2013.
- [21]. Ş. Karabulut, A. Güllü, Wear Model in Milling Compacted Graphite Iron with Different Lead Angle Using Ceramic Cutting Tools, *Solid State Phenomena*, 199, 371-376 2013.

Alleration of Volume Increment According to Basal Area and Social Stem Classes on Brutian Pine(*Pinus Brutia Ten.*) in Burdur Region

Serdar CARUS³¹

Abstract

*In even aged stands, some trees may be higher crown layer, and others may be lower crown layer. Thus, social classes between trees were resulted in a stand. The distribution of trees for social tree class affects the quantity and quality of tree stock diversity, and the determination of this distribution is important for forest management. In this study, the distribution of social tree classification in Schadelin (1931) was obtained and also the effect of this distribution on thinning severity (lightly, moderately and heavily) and years (2007-2010) and stand volume increment was examined for a plantation and thinning Brutian pine (*Pinus brutia Ten.*) stands in spring 2007. The material was obtained from Ağlasun Forest Enterprise, Burdur Forest District Directorship. The results showed that better tree attributes in Schadelin gived higher average stand volume increments for Brutian pine plantations. Dominant and co-dominant trees constitute the largest part of the volume increment in a stand.*

Keywords: Brutian pine, thinning heavy, volume increment, social stem class.

1. INTRODUCTION

Brutian pine (*Pinus brutia Ten.*) is one the main species in commercial plantations as a resource of the short- rotation forestry in western Turkey. It also provides a variety of end uses such as poles, pulpwood and saw logs. Presently there are 700.000 ha of Brutian pine plantations and because of its productive, ecological and protective roles [1]. The silvicultural regime of this species (determined by its ecological and technical characteristics) has to allow for the optimization of social needs while avoiding putting stand survival and stability at risk. As a species of intolerant temperament, Brutian pine plantation is fast growing in its early stages, and completes its current volume increment at 20-30 years of age, depending on site quality [1].

Thinning may also have negative effects. Too heavy thinning may result in biotic and abiotic damage as well as have undesirable effects on wood quality. In addition, heavy thinnings may considerably reduce the total yield obtained during a stand rotation. However, a slight growth reduction may be acceptable if it is more than compensated by larger stem diameters and earlier income from thinnings [2]. These relationships are difficult to generalize because increment responses are often highly variable depending on differences in stand density, origin, tree species, site quality, stand age and different thinning [3]. Consequently, regional studies are required for thinning impact assessment in geographically distinct forest area with different silvicultural practices.

On plantations, the effects of juvenile spacing do not last long because of the competition of the roots and crowns of the younger trees beginning at the onset of crown closure. Crowded trees have to compete for light, water and nutrients, resulting in slower growth or even death of some trees [1]. Moreover, some weak trees also become vulnerable to insect and disease. To avoid overcrowding and competition, trees are often thinned to increase the growing space available to the remaining trees. Enhancing growth on final crop trees by removing other trees has long been recognized and practiced in commercial thinning.

Thinning was also found to necessary to reduce the competition for sunlight, soil water and nutrients, as these requirements become critical as the trees get larger. If the stand remains unthinned the growth rate slows down, stagnation develops, and many dead trees eventually occur. As a result, tree growth is usually increased after thinning. Growth responses to thinning have been modeled to provide increased knowledge to be applied in forestry [4]. Thinning effects on tree growth are usually studied in terms of tree diameter, height, volume growth and canopy expansions of the remaining trees have been studied as well. Thinning in plantation has improved the diameter growth of individual trees. Diameter growth response of residual trees increases with increasing intensity of thinning. However, thinning may lower stand density the point where basal area growth and volume growth of the residual stand are greatly reduced and recovery of the stand to a fully stocked condition is much delayed. Most

³¹ Corresponding author: Suleyman Demirel University, Department of Forest Engineering, 32260, Çünür/Isparta, Turkey. serdarcarus@sdu.edu.tr

research on thinnings of this species has been carried out in Central Europe, where there have been thinning experiments since the beginnings of the 20th century [5]. In Turkey, the general application of thinning in variety pine stands began later, well in to century. Approximately 40% of the plantation area was covered by Brutian pine, therefore, its silviculture practice is of great importance. Forest managers need practical guidelines on thinning. Unfortunately, individual tree and stand level response to thinning in Brutian pine plantations are largely unknown, and few guidelines currently exist for successful management of these plantations. The purpose of this study was to investigate each year in 4 year response to alternative thinning regimes on the volume growth and stand structure in a 32 year old Brutian pine plantation in Burdur.

2. MATERIALS AND METHODS

2.1. Study Area

The study was conducted in an even-aged, Brutian pine plantation in Burdur. The sample plots were established within the boundary of Burdur Forest districts in the western Turkey (37° 40' 12'' N latitude, 30° 33' 15'' E longitude). The plantation with 1.5m x 3.0m spacing was established in 1980 with an area of 600 ha. Its exposure is north, the altitude is 1175 m asl and the mean slope is 10%. The meteorological station at Isparta, located at 997m asl, 40 km from the study area, recorded precipitation and temperature values for the period 1940-2010. These values were transformed for study area. Average annual total precipitation and mean annual temperature are 770 mm and 10.0 C, respectively. The research area is in an arid (must be semi-humid) zone water deficiency is observed during the June-August period of the year [6]. The bedrock is limestone and soil is rather shallow, sandy-loam with a high stone content. In spring of 2007, the main silvicultural characteristics of after thinning are: mean density, 1075 trees per hectare; quadratic mean diameter, 17.36 cm, mean height, 7.72 m, stand basal area 17.10 m²/ha and the stand was expected to achieve a yield class of 3.6 m³/ha/yr (poor site quality).

2.2. Measurements of Growth and Thinning

The design of experiment was random incomplete blocks, with two blocks and three treatments. The plot size was 25m x 25m (625 m²) and buffers were 10 m wide. Treatments applied consisted in comparing two degrees of thinning intensity with control. The thinning experiment was carried out during the spring of 2007. This trial consists of sixteen plots in two blocks. Three treatments were tested: lightly thinning (10% of basal area removal), moderately thinning (11- 20%) and heavily thinning (21- 40%). This trial consists of light, moderately and heavily thinning plots 3, 9 and 4, respectively.

At the beginning of the experiment, all the standing stems were included in the inventory and all stems were permanently numbered. In each plot, the following measurements were made diameter at breast height (diameter) and height for all trees. Within with tree growth and stand structure were measured immediately before and annually after the thinning in 2007-2010.

For data gathering all trees in the sixteen plots are identified by a number and marked at a height of 1.3 m with an upside down T- shape in order to ensure that diameters are always measured at the same point. This greatly increased the accuracy of stem diameter increments determined from repeated measurements. Thinned trees were felled to waste using chainsaws. The thinning type was from low, eliminating small trees, trees with badly shaped crowns, twisted stems, diseased trees, etc. Inventories were carried out 4 years, (2007, 2010) and the following data collected: diameter at breast height of all trees to the nearest millimeter, heights of all trees in each plot to the nearest 0.25m.

The following characters were used for further comparisons and analyses: diameter, height, volume and remaining basal area. The relative values were calculated for each plot. Basal area calculations were made using the diameter measurements for each tree and these calculations were summarized for each plot. Total stem outside bark volume calculations for trees were made using the double entry volume table of [1]. All calculations were then averaged for plots contained in each thinning category. These calculations were performed before treatment, immediately after treatment and 4 years after treatment. We treated plots as our experimental units. Crown classes were assessed on all trees within each measurement plot. In each plot, individual tree volume was calculated using the diameters and heights at 2007- 2010. This was converted to stand volume increment (m³/ha/yr) for the treatments.

$$I_v = V_e - V_b \quad (1)$$

Where V_e = stand volume at the end of period; V_b = stand volume at the beginning of period, data were analyzed to evaluate the effect of silvicultural treatments on stand volume increment (I_v) of trees using the analysis of factorial variance. Stand volume increment values were compared with the Duncan's test (2 tailed) at a 5% level of significance to analyze significant differences between each silvicultural treatment.

2.3. Statistical Analysis

Effects of thinning on stem volume growth rates were tested by an analysis of covariance of individual tree growth rates using initial volume as a covariate. The model 2 was used in the analysis of factorial variance (FANOVA) which this statistical method was recommended by [7].

$$x_{ij} = \mu + \alpha_i + \beta_j + (\alpha\beta)_{ij} + \varepsilon_{ijk} \quad (2)$$

Where, x_{ij} = is variable analyzed, μ = is the overall mean effect, α_i = is the effect of thinning, β_j = is the effect of years, $(\alpha\beta)_{ij}$ = is the mixed effect of thinning and years and ε_{ijk} = is assumed independently with random distribution. Duncan's test of multiple ranges was used to analyze the differences among treatments for the main stand variables (95% of significance level). Analyses were performed with the SPSS Ver. 17.0 statistical package.

To again a better understanding of the effects of the thinning treatments on those trees most likely to become final crop trees, we assessed volume increment responses of the dominant and codominant trees only. However, the mean annual increment of volume was calculated for each year after thinning in period. The ratio of the volume growth rate in the moderately thinned and heavily thinned to lightly thinned plots were analyzed.

3. RESULTS AND DISCUSSON

The statistical analyses showed that the thinning treatments were no significant at 0.05 level for volume growth (Tables 1 and 2). But volume increment differences were statistically significant (Tables 2 and 3). As a result, thinning is an important silvicultural treatment for establishing the new stand and development of quality and quantity, and it must be done in timely manner. In order to determine the appropriate silvicultural treatment, the production target and rotation age must be taken into consideration. It is apparent from this study that different volume growth of young Brutian pine stands occurs at different levels of thinning.

Table 1. Stand volume increment statistics according to thinning severity and years

		Thinning Severity					
		Lightly		Moderately		Heavily	
Years	n	\bar{x}	n	\bar{x}	n	\bar{x}	
2007	3	3.624	9	4.528	4	4.312	
2008	3	4.008	9	4.669	4	4.113	
2009	3	4.496	9	5.277	4	5.216	
2010	3	4.989	9	5.450	4	5.251	

Table 2. FANOVA results according to thinning severity (A) and years (B) on stand volume increment

Source	df	Mean square	F	p
A	2	2.258	1.861	0.166
B	3	3.676	3.030	0.037
AxB	6	0.115	0.095	0.997
Error	52	1.213		
Total	63			

Table 3. Duncan's multiple results comparisons according to years (B) on stand volume increment

		Groups	
		1	2
	n		
2007	16	4.304	
2008	16	4.406	
2009	16	5.116	5.116
2010	16		5.314

The volume growth rate ratios were $i = 4.406/4.304 = 1.024$, $j = 5.116/4.304 = 1.189$ and $k = 5.314/4.304 = 1.235$. These results proved that growth rate of the stand volume increment for 2008, 2009 and 2010 years, respectively.

For volume increments for thinning were no significant ($F_{2,52} = 1.861$, $p = 0.166$). Relative volume increment had to be lower in lightly thinned plots, as we found, since absolute volume growth was affected by thinning whilst initial basal area was much reduced by it. Average annual volume growth averaged 4.279, 4.981 and 4.723 in the lightly thinned, moderately thinned and heavily thinned plots, respectively.

Thinning did increase the volume increment of the dominant/co-dominant component of the plantation (Tables 5-7). Thinning treatments increased each year volume growth of individual dominant and co-dominant trees, dominated and suppressed were significant differences among the three levels of thinning could be detected ($F_{3,252} = 131.604$, $p = 0.000$). Upper crown class in the lightly thinned plot grew 2.424 m³/ha/yr and 1.450 m³/ha/yr in stand volume increment in 4 yr, whereas those in low crown classes grew 0.749 m³/ha/yr and 0.170 m³/ha/yr, respectively. This poor volume growth within the dominant/co-dominant component of the lightly thinned plot will likely lead to further reductions in the density of upper crown class trees as marginally healthy trees drop to the intermediate and suppressed classes. Continued poor volume growth of dominant and codominant trees in the lightly thinned plot is expected to continue in the future, such that the differences in volume growth among the three thinning treatments plots will likely continue to widen.

Table 4. Stand volume increment statistics according to social stem classes and years

		Social Stem Classes							
		Dominant		Co-dominant		Dominated		Suppressed	
Years	n	\bar{x}	n	\bar{x}	n	\bar{x}	n	\bar{x}	
2007	16	2.188	16	1.290	16	0.675	16	0.151	
2008	16	2.188	16	1.342	16	0.710	16	0.166	
2009	16	2.588	16	1.560	16	0.786	16	0.182	
2010	16	2.730	16	1.609	16	0.825	16	0.183	

Table 5. Stand volume increment statistics according to social stem classes

		Social Stem Classes							
		Dominant		Co-dominant		Dominated		Suppressed	
		n	\bar{x}	n	\bar{x}	n	\bar{x}	n	\bar{x}
		64	2.424	64	1.450	64	0.749	64	0.170

Table 6. ANOVA results according to social stem classes on stand volume increment

Source	df	Mean square	F	p
Between groups	3	60.223	131.604	0.000
Within groups	252	0.458		
Error	255			

Table 7. Duncan's multiple results comparisons according to social stem classes on stand volume increment

		Groups				
Social stem class	n	1	2	3	4	
Suppressed	64	0.170				
Dominated	64		0.749			
Codominant	64			1.450		
Dominant	64				2.424	

Dominant and co-dominant trees accounted for 79% of the total volume growth in the moderately thinned plot and 77% of the total volume growth in the heavily thinned plot, whereas only 91% of the total volume in the lightly thinned plot was distributed among upper crown class tree (Table 8). Consequently, both thinning treatments allowed a much greater proportion of the totals wood production of the stand to be concentrated in those trees most likely to produce high quality sawtimber as final crop trees.

Table 8. Stand volume increment percent distribution according to social stem classes and number of trees

Social Stem Class	Thinning Severity					
	Lightly		Moderately		Heavily	
	Trees (%)	Iv (%)	Trees (%)	Iv (%)	Trees (%)	Iv (%)
Dominant	49	54	51	49	51	51
Codominant	40	37	30	30	27	26
Dominated	8	8	14	16	18	20
Suppressed	3	1	5	5	4	3

Brutian pine responded to thinning differently according to tree size. In absolute terms, growth of large stems was stimulated by thinning more than that of smaller trees. Large trees probably have a greater capacity for resources acquisition, and are thus more able to take advantage of the increase of resources availability that takes place after thinning, and to eventually use these resources for growth [8]. In these cited studies size and differences between diameter classes were statistically significant for the study period. More specifically, a higher uptake of water and nutrients from a larger root system are probably involved in this response.

Brutian pine showed a positive growth response to thinning, as evidenced by enhanced growth rates for volume. Consistent with these results, similar work by [9] and [10] with Lebanon cedar and Calabrian pine showed increases no significant in tree growth (diameter, height and volume) and stand growth after thinning.

Among the treatments evaluated in this study, heavily thinning produced the most desirable combination of individual tree volume growth. Reducing basal area proves to be effective in increasing the growth rates of red maple, however, caution should be taken not to open the site too much. These results expand and substantiate the work of [11-12] in which he concluded Brutian pine volume growth increased after thinning.

Basal area increment is greater with heavily thinned plot than in the lightly thinned plot and with moderately thinned, and behaves differently than increment in volume [13]. The results indicate differences in mean volume increment between treatments. This volume increases with intensity of thinning as a result of removing the thinning type was from low, eliminating small trees, trees with badly shaped crowns, twisted stems, diseased trees, etc., through this difference is statistically significant (Table 2). In very even-aged and homogeneous stands height usually varies little with diameter, which means that sometimes, even with moderate thinning, mean height significantly vary. This strong competition has meant that after 25 years practically all dominated trees and very suppressed have died, resulting in a more regular stand. In other words, the strong differentiation of sociological classes is found in the early years, while after 30-40 years, low thinning helps to achieve greater uniformity.

Heavily thinned plots grew more in diameter than the lightly thinned plots. We found that periodic annual increment was no significant for stand volume increment among tree thinning levels and among years 2007 and 2010 (Tables 2 and 3). As we expected, heavily thinned plots increased more in stand volume increment than the lightly thinned plots (Table 2). The same trends occurred for annual volume increment; trees accelerated in volume growth more in the heavily thinned plots than trees in the lightly thinned plots. This trend may continue until the onsets of self thinning with strong inter tree competition. Thinning enhances the growth of not only small trees, but also the dominant trees [14-15].

Among the many aims of thinning, one of the most important is that of producing larger trees in order to increase the stand' s yield quality. Table 2 and 3 shows the greater increment in volume of the average tree in the most intensive thinning regime. Though seemingly trivial, this fact is of great practical importance from the silvicultural point of view, since it enables the entire productive capacity of the site to be concentrated on the production of trees of greater girth and higher quality, already selected for their better technical characteristics. If as is often the case, the final rotation of Brutian pine is determined by technical criteria, intensive thinning helps to reduce the length of rotation by 20-25 years in comparison with barely treated or lightly thinned stands, particularly in high quality sites.

The results of this study indicate that moderately and heavily thinning had effect on the growth rates of Brutian pine plantation. Therefore, thinning is necessary to avoid growth rate slow down and the death of too many trees. In the moderately thinned plots, there is a slight fall in increment by basal area and volume with respect to the lightly plots. However, this regime thus exceeds the density limit below which there is loss of yield by volume. Acceptable basal area reduction is compensated by the positive effect of intensive low thinning on volume increment, resulting in larger size timber.

4. CONCLUSIONS

The four years results of this study showed that the highest increment in volume was obtained from heavily thinning. The effect treatment was not significant on stand volume increment. However, in order to obtain most conclusive results, it will be necessary to carry out long term studies for getting the actual forest yields.

Low thinning naturally increases mean tree size in the main crop, the more so the more intensive the thinning on the one hand crop growth becomes concentrated on fewer individuals, while on the other the extraction of smaller tree brings up the mean (technical growth). The first is one of the aims of thinning, and in order to evaluate it is necessary to analyze current increment in diameter, a true indicator of mean tree growth.

In the moderately thinned plot, there is a slight fall in increment by basal area and volume with respect to the lightly plots. However, this regime thus exceeds the density limit below which there is loss of yield by volume. Acceptable basal area reduction is compensated by the positive effect of intensive low thinning on diameter resulting in larger size timber. This regime also produces noticeable improvement in the vigour of the stand and its resistance to abiotic damage. In middle to high quality sites, we propose an early initial age and heavily low thinnings.

ACKNOWLEDGEMENTS

This study was supported by the grant of Süleyman Demirel University BAPYB (Project number 2871-M-11). The author wish to extend their thanks to the authorities of the Regional Forest Service of Isparta for the valuable assistance provided during the ground survey.

REFERENCES

- [1] Usta, H.Z., *A study on the yield of Pinus brutia plantations*. Turkish Forestry Research Institute Publication, Ankara, 1991
- [2] Makinen, H., and A. Isomaki, "Thinning intensity and growth of Scots pine stands in Finland". *For. Ecol. Manage.*, vol. 201, pp. 311-325, 2004.
- [3] Nowak, C.A., "Wood volume increment in thinned, 50 to 55 year-old, mixed species Allegheny hardwoods". *Can. J. For. Res.*, vol. 26, pp. 819-835, 1996.
- [4] Hamilton, G.H., "The effects of high intensity thinning on yield". *For.*, vol. 54, pp.1-15, 1981.
- [5] Assmann, E., *The principles of forest yield study*. Pergamon, Oxford, 1970.
- [6] Çepel, N., *Forest ecology*. Istanbul University Publication, Istanbul, 1978.
- [7] Kalıpsız, A., *Statistical methods, Istanbul University publication*, 1981.
- [8] Pukkala, T. J. Miina, and S.Kellomaki, "Response to different thinning intensities in young *Pinus sylvestris*". *Scandinavian Journal of Forestry Research*, vol.13, pp.141-150, 1998.
- [9] Eler, Ü., "*Effects of delayed thinning on the development of natural Lebanon cedar (Cedrus libani A. Rich.) stands in Antalya region*". Turkish Forestry Research Institute Publication, Ankara, 1990.
- [10] Eler, Ü., and S. Keskin, "*Effects of silvicultural treatments applied on delayed first thinning of Calabrian pine (Pinus brutia Ten.) plantations in Antalya region*". Turkish Forestry Research Institute Publication, Ankara, 1991.
- [11] Usta, H.Z., "*Effects of initial thinnings on the growth of Pinus brutia plantations in the southwest Turkey*". Turkish Forestry Research Institute Publication, Ankara, 1996.
- [12] Eler, Ü., "*Effects of silvicultural treatments applied on delayed first thinnings of Calabrian pine (Pinus brutia Ten.) plantations in Antalya region*". Turkish Forestry Research Tech. Bulletin, Ankara, 1991.
- [13] Zhang, J., and W.W. Oliver, "Stand structure and growth of *Abies magnifica* responded to five thinning levels in northeastern California, USA", *Forest Ecology and Management*, vol. 223, pp. 275-283, 2006.
- [14] Carus, S., and Y. Çatal, "Response to different thinning intensity in Calabrian pine (*Pinus brutia* Ten.) plantations in Turkey". *International Journal of Natural and Engineering Sciences*, vol. 3, pp.126-131, 2009.
- [15] Çatal, Y., "West Mediterranean region brutian pine (*Pinus brutia* Ten.) stands increment and growth". Suleyman Demirel University, Graduate school of natural and applied sciences, Doctoral thesis, Isparta. 2009.

BIOGRAPHY

Serdar Carus was born at Istanbul in 1966. Academic education at the University of Istanbul in Turkey was completed in 1988. Faculty of Forestry at the same University's academic work began in 1990. Then, Süleyman Demirel University was trying to associate professor in the Faculty of Forestry in 2001. He has served as a faculty member here. Still the same university ' is continuing his academic career as Professor. He has 11 articles in the Science Citation Index and a total of 90 articles or papers. He is married and has two children.

Analytic Hierarchy Process Extended with Internal Type-2 Fuzzy Sets to Assess Potential Environmental Impacts of Ship Recycling Process

Erkan Celik³², Emre Akyuz³³

Abstract

Ship recycling is one of the core topics in maritime industry since the process has a great impact on the environment. Overaged ships may contain environmentally hazardous substances that may severely affect human life and marine environment. Therefore, researchers have been performing utmost effort by seeking creative solutions for protection of environment and improvement of safety standards in ship recycling industry. The purpose of this paper is to evaluate potential environmental impacts in the process of ship recycling. Thus, potential hazards which may seriously affect marine environment are analysed to enhance safety control level in ship recycling industry. To achieve this purposes, the paper takes benefit of analytic hierarchy process (AHP) extended with interval type-2 fuzzy sets (IT2FSs). Since AHP method is used for prioritizing the potential hazards that may impact on environment, the IT2FSs deal with uncertainty and vagueness in the process of obtaining expert decision. Hence, the potential environmental impacts of ship recycling process can be evaluated. In conclusion, the paper outcomes encourage the maritime safety researcher and environmental protection agency to focus on the main points in terms of pollution prevention.

Keywords: IT2FSs, decision-making, ship recycling, maritime safety, environment protection

65. INTRODUCTION

Ship recycling industry has been gradually growing in the global world since it has considerable economic contributions [1]. There are numerous countries that are dealing with ship recycling process. Most of them carry out some manual techniques such as labour-intensive manner. Therefore, most of developed countries left and tried to find different countries such as India, Bangladesh, Vietnam, China, Turkey, etc. where labours are relatively cheap. Currently, almost fifteen million tons of overaged ship were recycling in aforementioned countries per year [2]. Since it has a considerable amount of contribution to the economy and is considered one of the most environmentally friendly way of disposal of the overaged ships, the ship recycling process has a great impact on the environment. Therefore, the International Maritime Organisation (IMO) adopted Safe and Environmentally Sound Recycling of Ships in Hong Kong Convention. The aim of this convention is to provide safe progress throughout the ship recycling [3]. Thus, facilities do not pose any unnecessary risks to human health, safety and to the environment.

³² Corresponding author: Tunceli University, Department of Industrial Engineering, 62000 Tunceli, Turkey. erkancelik@tunceli.edu.tr

³³ Bursa Technical University, Department of Maritime Management, Osmangazi 16190, Bursa, Turkey. emreakyuz@hotmail.com.tr

Although there are rigid rules and regulations adopted by maritime regulatory bodies, ship recycling process poses acute hazards to the environment and human life. Therefore, maritime safety researchers and environmental protection agencies have been proposing alternative creative solutions to minimize potential environmental impacts and enhance safety levels in ship recycling industry. For instance, Chang et al. [4] discussed historical development, structure and enforcement of Hong Kong Convention. In the paper, potential effects and contributions of convention in the view of maritime pollution is widely discussed. Likewise, a study which is analysing ship recycling industry was presented in order to reduce the risk and damage to the environment. In light of the findings, a preventive plan for the safe scrapping of ships is introduced [5]. Furthermore, another study related to ship recycling industry was presented to focus on narrowing differences between the European Union and South Asian ship recycling industry [6]. A similar study was performed to compare ship recycling among Chinese Law and Hong Kong Convention [7].

In the view of above, most of papers apparently focus on ship recycling legislation and Hong Kong Convention rather than technical analysis. Recently, some researchers have attempted to extend their interests in the analysing of risk in ship recycling industry. For instance, Garmer et al. [8] performed a risk assessment for ship recycling sector. The authors adopt three-step risk assessment method which was conducted in 35 ship recycling facilities through questionnaire surveys in order to reduce risk and improve safety. A different perspective in the view of ship-specific recycling plan has been recently proposed to enhance safety and prevent environment in ship recycling facilities [9]. The findings show that there is lack of research in the ship recycling industry to evaluate potential environmental impacts as the consequences may become extremely damaging. Therefore, this paper attempts to assess potential environmental impacts of ship recycling by using IT2FSs AHP which is evaluating the relative importance of multiple criteria. Thus, potential hazards associated with ship recycling are evaluated. In this context, the paper organised as follows. This part gives motivation, a brief literature and the aim of study. The next part outlines methodology. Part three shows how adopted method will assess potential environmental impacts. The final part gives conclusion remark and contribution of this study into maritime industry.

2. METHODOLOGY

This part expresses the method used in the paper to evaluate potential environmental impacts of ship recycling process.

2.1 IT2FSs AHP

Type-2 fuzzy sets are developed by Zadeh [10] as an extension of the concept of a type-1 fuzzy sets [11, 12, 13]. It is usually applied in different applications [14]-[15] which contains more uncertainty [16]-[18] and produces more accurate and robust results [19]. Various literature reviews for IT2FSs are presented as industrial applications [15], design and optimization of IT2FSs controllers [20], optimization of IT2FSs based on bio-inspired methods [21], classification and pattern recognition [22], MCDM approaches based on IT2FSs [23]. We first presented some definitions about type-2 fuzzy sets and IT2FSs [17], [24]-[30].

Definition 1: A type-2 fuzzy set \tilde{A} in the universe of discourse X can be represented by a type-2 membership function $\mu_{\tilde{A}}$, shown as follows:

$$\tilde{A} = \{((x,u), \mu_{\tilde{A}}(x,u)) | \forall x \in X, \forall u \in J_x \subseteq [0,1], 0 \leq \mu_{\tilde{A}}(x,u) \leq 1\}$$

where J_x denotes an interval in $(0, 1)$. Moreover, the type-2 fuzzy set \tilde{A} also can be showed as follows:

$$\tilde{A} = \int_{x \in X} \int_{u \in J_x} \mu_{\tilde{A}}(x,u) / (x,u)$$

where $J_x \subseteq [0,1]$ and \int denotes union over all admissible x and u .

Definition 2 : Let \tilde{A} be a type-2 fuzzy set in the universe of discourse X presented by the type-2 membership function $\mu_{\tilde{A}}$. If all

$\mu_{\tilde{A}}(x,u) = 1$, then \tilde{A} is called as an IT2FSSs. An IT2FSSs \tilde{A} can be regarded as a special case of a type-2 fuzzy set, presented as follows:

$$\tilde{A} = \int_{x \in X} \int_{u \in J_x} 1 / (x,u) \text{ where } J_x \subseteq [0,1]$$

Definition 3: The upper and the lower membership function of an IT2FS are type-1 membership functions, respectively. Figure 1 shows a trapezoidal IT2FSSs $\tilde{A}_i = (\tilde{A}_i^U, \tilde{A}_i^L) = \left((a_{i1}^U, a_{i2}^U, a_{i3}^U, a_{i4}^U; H_1(\tilde{A}_i^U), H_2(\tilde{A}_i^U)), (a_{i1}^L, a_{i2}^L, a_{i3}^L, a_{i4}^L; H_1(\tilde{A}_i^L), H_2(\tilde{A}_i^L)) \right)$, where \tilde{A}_i^U and \tilde{A}_i^L are type-1 fuzzy sets, $a_{i1}^U, a_{i2}^U, a_{i3}^U, a_{i4}^U, a_{i1}^L, a_{i2}^L, a_{i3}^L, a_{i4}^L$ are the reference points of the IT2FSSs \tilde{A}_i ; $H_j(\tilde{A}_i^U)$ denotes the membership value of the element $a_{i(j+1)}^U$ in the upper trapezoidal membership function \tilde{A}_i^U ; $1 \leq j \leq 2$, $H_j(\tilde{A}_i^L)$ denotes the membership value of the element $a_{i(j+1)}^L$ in the lower trapezoidal membership function \tilde{A}_i^L ; $1 \leq j \leq 2$, $H_1(\tilde{A}_i^U) \in [0,1]$, $H_2(\tilde{A}_i^U) \in [0,1]$, $H_1(\tilde{A}_i^L) \in [0,1]$, $H_2(\tilde{A}_i^L) \in [0,1]$ and $1 \leq i \leq n$.

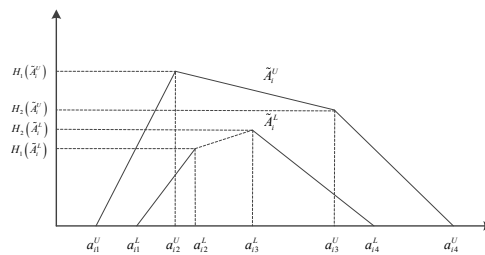


Figure 1. The membership function

AHP, developed by Saaty [31], is applied to various and almost all application [32]. It contains hierarchy structure, ranking criteria and consistency of the comparison. Buckley [33] integrating interval type-1 fuzzy sets with AHP. While Abdullah and Najib [34] developed a new type-2 fuzzy set of linguistic variables, Kahraman et al. [18] also proposed a new ranking method for AHP. Celik et al. [25] also applied AHP under IT2FSSs for evaluating critical success factors in humanitarian relief logistics. Gul et al. [35] applied AHP based on IT2FSSs for determining important criteria in emergency department. In this paper, we employed AHP based on IT2FSSs to obtain importance weights of hazards to assess potential environmental impacts of ship recycling process. The steps of applied method are presented as follows.

Step 1: Construct the pair wise comparison matrix under IT2FSSs among all hazards. The linguistic terms are presented in Table 1.

$$\tilde{M} = \begin{pmatrix} 1 & \tilde{a}_{12} & \dots & \tilde{a}_{1m} \\ \tilde{a}_{21} & 1 & \dots & \tilde{a}_{2m} \\ \vdots & \vdots & \ddots & \vdots \\ \tilde{a}_{m1} & \tilde{a}_{m2} & \dots & 1 \end{pmatrix} = \begin{pmatrix} 1 & \tilde{a}_{12} & \dots & \tilde{a}_{1m} \\ \tilde{1} / \tilde{a}_{12} & 1 & \dots & \tilde{a}_{2m} \\ \vdots & \vdots & \ddots & \vdots \\ \tilde{1} / \tilde{a}_{1m} & \tilde{1} / \tilde{a}_{2m} & \dots & 1 \end{pmatrix} \quad (1)$$

$$\text{where } \tilde{1} / \tilde{a}_{ij} = \left(\left(\frac{1}{a_{ij4}^U}, \frac{1}{a_{ij3}^U}, \frac{1}{a_{ij2}^U}, \frac{1}{a_{ij1}^U}; H_1(a_{ij}^U), H_2(a_{ij}^U) \right), \left(\frac{1}{a_{ij4}^L}, \frac{1}{a_{ij3}^L}, \frac{1}{a_{ij2}^L}, \frac{1}{a_{ij1}^L}; H_1(a_{ij}^L), H_2(a_{ij}^L) \right) \right)$$

Table 1. Linguistic terms for importance weights of factors

Linguistic variables	IT2FSSs	Reciprocal IT2FSSs
Extremely more important (EMI)	((8;9;9;10;1;1),(8.5;9;9;9.5;0.9;0.9))	((0.1;0.11;0.11;0.13;1;1),(0.11;0.11;0.11;0.12;0.9;0.9))
Intermediate value (IV)	((7;8;8;9;1;1),(7.5;8;8;8.5;0.9;0.9))	((0.11;0.13;0.13;0.14;1;1),(0.12;0.13;0.13;0.13;0.9;0.9))
Very strong more important (VSMI)	((6;7;7;8;1;1),(6.5;7;7;7.5;0.9;0.9))	((0.13;0.14;0.13;0.14;1;1),(0.13;0.14;0.13;0.13;0.9;0.9))
Intermediate value (IV)	((5;6;6;7;1;1),(5.5;6;6;6.5;0.9;0.9))	((0.14;0.17;0.17;0.2;1;1),(0.15;0.17;0.17;0.18;0.9;0.9))
Strongly more important (SMI)	((4;5;5;6;1;1),(4.5;5;5;5.5;0.9;0.9))	((0.17;0.2;0.2;0.25;1;1),(0.18;0.2;0.2;0.22;0.9;0.9))
Intermediate value (IV)	((3;4;4;5;1;1),(3.5;4;4;4.5;0.9;0.9))	((0.2;0.25;0.25;0.33;1;1),(0.22;0.25;0.25;0.29;0.9;0.9))
Moderately more important (MMI)	((2;3;3;4;1;1),(2.5;3;3;3.5;0.9;0.9))	((0.25;0.33;0.33;0.5;1;1),(0.29;0.33;0.33;0.4;0.9;0.9))
Intermediate value (IV)	((1;2;2;3;1;1),(1.5;2;2;2.5;0.9;0.9))	((0.33;0.5;0.5;1;1;1),(0.4;0.5;0.5;0.67;0.9;0.9))
Equally important (EI)	((1;1;1;1;1;1),(1;1;1;1;0.9;0.9))	((1;1;1;1;1;1),(1;1;1;1;0.9;0.9))

Step 2: Analyze the consistency of the fuzzy pair wise comparison. In this step, if the result of the A is consistent, then the result of the \tilde{A} is also consistent. A CR of 0.1 or less is considered as acceptable.

Step 3: Apply the geometric mean technique to obtain the fuzzy geometric mean as follows.

$$\tilde{r}_i = (\tilde{a}_{i1} \times \tilde{a}_{i2} \times \dots \times \tilde{a}_{im})^{1/m} \quad (2)$$

$$\text{where } \sqrt[n]{\tilde{a}_{ij}} = \left(\begin{array}{l} \left(\sqrt[n]{a_{ij1}^U}, \sqrt[n]{a_{ij2}^U}, \sqrt[n]{a_{ij3}^U}, \sqrt[n]{a_{ij4}^U}; H_1(a_{ij}^U), H_2(a_{ij}^U) \right), \\ \left(\sqrt[n]{a_{ij1}^L}, \sqrt[n]{a_{ij2}^L}, \sqrt[n]{a_{ij3}^L}, \sqrt[n]{a_{ij4}^L}; H_1(a_{ij}^L), H_2(a_{ij}^L) \right) \end{array} \right)$$

Step 4: The fuzzy weights of each criterion is calculated as follows.

$$\tilde{w}_i = \tilde{r}_i \times (\tilde{r}_1 + \tilde{r}_2 + \dots + \tilde{r}_m)^{-1} \quad (3)$$

Step 5: Defuzzify the IF2FSs using center of area method [18] obtaining weights of each hazard.

$$\text{Defuzzified}(\tilde{w}_i) = \frac{\frac{(a_{i4}^U - a_{i1}^U) + (H_1(\tilde{A}_i^U) * a_{i2}^U - a_{i1}^U) + (H_2(\tilde{A}_i^U) * a_{i3}^U - a_{i1}^U)}{4} + a_{i1}^U + \frac{(a_{i4}^L - a_{i1}^L) + (H_1(\tilde{A}_i^L) * a_{i2}^L - a_{i1}^L) + (H_2(\tilde{A}_i^L) * a_{i3}^L - a_{i1}^L)}{4} + a_{i1}^L}{2} \quad (4)$$

Step 6: Normalized the crisp weights of potential hazards.

$$w_i = \text{Defuzzified}(\tilde{w}_i) / \sum_{i=1}^n \text{Defuzzified}(\tilde{w}_i) \quad (5)$$

3. ASSESSMENT ENVIRONMENTAL IMPACTS OF SHIP RECYCLING PROCESS

In this part, environmental impacts of recycling process are assessed by employing AHP method under IT2FSs environment.

3.1. Problem Description

Since increased ship recycling (either performing at beaching, slipway, alongside or dry dock) activities provide a wide range of economic benefits to country, the consequences of process could potentially harm for environment. Implementation of the Safe and Environmentally Sound Recycling of Ships regulation addresses some concerns raised about the environmentally hazardous substances. However, there still exists a gap, in particular practical application on facilities. The potential hazards which may seriously affect marine environment have not been analysed yet. To remedy this gap, a comprehensive evaluation related to potential hazards to the environment are performed.

3.2. Potential Hazards Related to Ship Recycling Process

The potential hazards related to ship recycling process have great impact to the environment. The list of potential hazards, their resultants and environmental effects are shown in Table 2.

Table 2. Hazards related to ship recycling process.

	Potential hazard	Resultant	Environmental impact
H ₁	Pollutants disposed by ship breaking	Organ tins, arsenic, zinc, cadmium and chromium	Air, soil, water
H ₂	Persistent organic pollutants	Hexabromocyclododecane, tetraBDE	Soil and water
H ₃	Asbestos	Dust and fibbers	Air and soil
H ₄	Heavy metal residues	Chromium, iron, nickel, zinc, lead	Soil, air, water
H ₅	Oil /bunker pollutants	Hydrocarbons	Water and soil
H ₆	Toxins	Lead, asbestos, Freon	Soil, air, water
H ₇	Coating and paint residues	Clor, Zinc, Copper, Lead	Water, soil, air

H ₈ Ballast water pollutants	Aquatic organisms, non-indigenous species	Water and soil
---	---	----------------

3.3 Assessment of Hazards to the Environment

In order to evaluate potential hazards, an extensive questionnaire surveys were performed with occupational health and safety experts who have been working for one of the leading ship dismantling and recycling companies in Turkey. In this paper, the evaluation of potential hazards is applied with respect to three experts. Each expert was asked to compare hazard on the basis of Saaty's linguistic scale that is presented in Table 1. The interval type-2 fuzzy pair wise comparison matrix among all hazards is constructed in step 1 by using Eq. (1). Then, the aggregated IT2FSs of pair wise comparison for three experts is calculated and it is presented in Table 3.

Table 3. The aggregated IT2FSs of pair wise comparison

H ₁	...	H ₈
H ₁ ((1;1;1;1;1;1),(1;1;1;1;0.9;0.9))	...	((0.33;0.5;0.5;1;1;1),(0.4;0.5;0.5;0.67;0.9;0.9))
H ₂ ((0.5;0.56;0.56;0.67;1;1),(0.52;0.56;0.56;0.6;0.9;0.9))	...	((0.25;0.33;0.33;0.5;1;1),(0.29;0.33;0.33;0.4;0.9;0.9))
H ₃ ((0.23;0.32;0.32;0.53;1;1),(0.27;0.32;0.32;0.39;0.9;0.9))	...	((0.2;0.25;0.25;0.33;1;1),(0.22;0.25;0.25;0.29;0.9;0.9))
H ₄ ((3;4;4;5;1;1),(3.5;4;4;4.5;0.9;0.9))	...	((0.17;0.2;0.2;0.25;1;1),(0.18;0.2;0.2;0.22;0.9;0.9))
H ₅ ((0.31;0.44;0.44;0.83;1;1),(0.36;0.44;0.44;0.58;0.9;0.9))	...	((0.14;0.17;0.17;0.2;1;1),(0.15;0.17;0.17;0.18;0.9;0.9))
H ₆ ((1.33;2;2;2.67;1;1),(1.67;2;2;2.33;0.9;0.9))	...	((0.13;0.14;0.13;0.14;1;1),(0.13;0.14;0.13;0.13;0.9;0.9))
H ₇ ((0.31;0.44;0.44;0.83;1;1),(0.36;0.44;0.44;0.58;0.9;0.9))	...	((0.11;0.13;0.13;0.14;1;1),(0.12;0.13;0.13;0.13;0.9;0.9))
H ₈ ((3.67;4.67;4.67;5.67;1;1),(4.17;4.67;4.67;5.17;0.9;0.9))	...	((0.1;0.11;0.11;0.13;1;1),(0.11;0.11;0.11;0.12;0.9;0.9))

Then, the consistency ratios of each expert and aggregated evaluation matrix for potential hazards are computed in step 2 as 0.091, 0.068, 0.085, and 0.090, respectively. The comparison results of the aggregated comparison matrix are consistent because of CR value is 0.09. The aggregated type-2 fuzzy evaluation matrix for the factors weights is obtained. The type-2 fuzzy geometric means of the factors are calculated in step 3 using Eq. (2). The type-2 fuzzy weights are computed in step 4 using Eq. (3) and it is presented in Table 4.

Table 4. The importance weight of potential hazards

IT2FSs	Defuzzify the IF2FSs	Normalized the crisp weights
H ₁ ((0.06;0.09;0.09;0.12;1;1),(0.08;0.09;0.09;0.1;0.9;0.9))	0.087	0.120
H ₂ ((0.04;0.06;0.06;0.08;1;1),(0.05;0.06;0.06;0.06;0.9;0.9))	0.056	0.077
H ₃ ((0.04;0.05;0.05;0.08;1;1),(0.05;0.05;0.05;0.06;0.9;0.9))	0.054	0.074
H ₄ ((0.08;0.11;0.11;0.15;1;1),(0.09;0.11;0.11;0.13;0.9;0.9))	0.109	0.149
H ₅ ((0.06;0.08;0.08;0.11;1;1),(0.07;0.08;0.08;0.09;0.9;0.9))	0.078	0.106
H ₆ ((0.11;0.15;0.15;0.2;1;1),(0.13;0.15;0.15;0.18;0.9;0.9))	0.151	0.207
H ₇ ((0.08;0.11;0.11;0.15;1;1),(0.1;0.11;0.11;0.13;0.9;0.9))	0.111	0.152
H ₈ ((0.07;0.08;0.08;0.11;1;1),(0.07;0.08;0.08;0.1;0.9;0.9))	0.084	0.115

In step 5, the importance weights based on IT2FSs of 8 potential hazards are defuzzified using center of area method [18] of each hazard. In last step, the normalized crisp importance weights of potential hazards are calculated that is presented in last column of Table 4. According to the three experts' evaluation, the toxins (H₆=0.207) is determined as the first potential hazard of ship recycling process. While coating and paint residues (H₇=0.152) is evaluated as the second, Heavy metal residues (H₄=0.149) is determined as the third potential hazard. Also, based on the results, the least potential hazard is determined as persistent organic and pollutants (H₂=0.077) and asbestos (H₃=0.074).

4. CONCLUSION

Ship recycling industry has considerable impact upon economy since a wide range of overage ships have to be recycled. During the recycling, a number of hazards could appear as ships are built with hazardous materials, including heavy metals and asbestos. These substances may severely affect environment and cause serious damages. In this context, it is critical to assess potential environmental impacts of ship recycling process. To achieve this purpose, this paper prompts a methodological approach integrating

AHP with IT2FSs. Thus, potential hazards which may severely affect environment are analysed to improve safety awareness in ship recycling industry. In the view of comprehensive evaluation, Toxins (H_6) is found the most contributory factors to environmental hazards. Thereafter, coating and paint residues (H_7) and heavy metal residues (H_4) are ranging as prominent hazards that may affect environment. The study is expected to assist maritime safety researchers and environmental protection agencies for protecting environment and enhancing safety standards in ship recycling industry.

REFERENCES

- [1]. BIMCO, 2013. Ship recycling markets. Bulletin vol. 108 by Dr. Nikos Mikelis.
- [2]. TSWM (Turkish Shipping World Magazine), 2015. Turkish Ship Recycling Industry. Istanbul, Turkey.
- [3]. IMO, 2009. Final Act of the International Conference on the safe and environmentally sound recycling of ships, 2009. Certified True Copy signed on August 18th, 2009. London, IMO.
- [4]. Chang, Y.C., Wang, N., & Durak, O.S., (2010). Ship recycling and marine pollution. *Marine Pollution Bulletin* 60: 1390 – 1396.
- [5]. Welaya, Y. M. A., Naby, M. M. A., Tadros, M. Y. Technological and economic study of ship recycling in Egypt. *International Journal of Naval Architect Ocean Engineering* 4: 362 – 373.
- [6]. Yujuico, E., 2014. Demandeur pays: The EU and funding improvements in South Asian ship recycling practices. *Transportation Research Part A* 67: 340 – 351.
- [7]. Zhao, Y., Chang, Y.-C., 2014. A comparison of ship-recycling legislation between chinese law and the 2009 Hong Kong Convention. *Ocean Development & International Law* 45:53 – 66.
- [8]. Garmer, K., Sjöström, H., Hiremath, A. M., Tilwankar, A. K., Kinigalakis, G., & Asolekar, S. R., 2015. Development and validation of three-step risk assessment method for ship recycling sector. *Safety Science* 76: 175 – 189.
- [9]. Hiremath, A. M., Pandey, S. K., & Asolekar, S. R., 2016. Development of ship-specific recycling plan to improve health safety and environment in ship recycling yards. *Journal of Cleaner Production* 116: 279 – 298.
- [10]. Zadeh, L. A. (1975). The concept of a linguistic variable and its application to approximate reasoning—II. *Information Sciences*, 8(4), 301-357.
- [11]. Karnik, N. N., & Mendel, J. M. (2001). Operations on type-2 fuzzy sets. *Fuzzy sets and systems*, 122(2), 327-348.
- [12]. Mendel, J. M. (2007). Type-2 fuzzy sets and systems: an overview. *Computational Intelligence Magazine, IEEE*, 2(1), 20-29.
- [13]. Mendel, J. M. (2007). Advances in type-2 fuzzy sets and systems. *Information sciences*, 177(1), 84-110.
- [14]. Mendel, J. M. (2009). On answering the question “Where do I start in order to solve a new problem involving interval type-2 fuzzy sets?”. *Information Sciences*, 179(19), 3418-3431.
- [15]. Dereli, T., Baykasoglu, A., Altun, K., Durmusoglu, A., & Türksen, I. B. (2011). Industrial applications of type-2 fuzzy sets and systems: a concise review. *Computers in Industry*, 62(2), 125-137.
- [16]. Mendel, J. M., & John, R. I. B. (2002). Type-2 fuzzy sets made simple. *Fuzzy Systems, IEEE Transactions on*, 10(2), 117-127.
- [17]. Mendel, J. M., John, R., & Liu, F. (2006). Interval type-2 fuzzy logic systems made simple. *Fuzzy Systems, IEEE Transactions on*, 14(6), 808-821.
- [18]. Kahraman, C., Öztaysi, B., Sarı, İ. U., & Turanoğlu, E. (2014). Fuzzy analytic hierarchy process with interval type-2 fuzzy sets. *Knowledge-Based Systems*, 59, 48-57.
- [19]. Dereli, T., & Altun, K. (2013). Technology evaluation through the use of interval type-2 fuzzy sets and systems. *Computers & Industrial Engineering*, 65(4), 624-633.
- [20]. Castillo, O., & Melin, P. (2012). A review on the design and optimization of interval type-2 fuzzy controllers. *Applied Soft Computing*, 12(4), 1267-1278.
- [21]. Castillo, O., & Melin, P. (2012). Optimization of type-2 fuzzy systems based on bio-inspired methods: a concise review. *Information Sciences*, 205, 1-19.
- [22]. Melin, P., & Castillo, O. (2013). A review on the applications of type-2 fuzzy logic in classification and pattern recognition. *Expert Systems with Applications*, 40(13), 5413-5423.
- [23]. Celik, E., Gul, M., Aydin, N., Gumus, A. T., & Guneri, A. F. (2015). A comprehensive review of multi criteria decision making approaches based on interval type-2 fuzzy sets. *Knowledge-Based Systems*, 85, 329-341.
- [24]. Chen, S. M., & Lee, L. W. (2010). Fuzzy multiple attributes group decision-making based on the interval type-2 TOPSIS method. *Expert systems with applications*, 37(4), 2790-2798.
- [25]. Celik, E., Gumus, A. T., & Alegoz, M. (2014). A trapezoidal type-2 fuzzy MCDM method to identify and evaluate critical success factors for humanitarian relief logistics management. *Journal of Intelligent & Fuzzy Systems: Applications in Engineering and Technology*, 27(6), 2847-2855.
- [26]. Celik, E., Aydin, N., & Gumus, A. T. (2014). A multiattribute customer satisfaction evaluation approach for rail transit network: A real case study for Istanbul, Turkey. *Transport Policy*, 36, 283-293.
- [27]. Celik, E., & Gumus, A. T. (2015). An assessment approach for non-governmental organizations in humanitarian relief logistics and an application in Turkey. *Technological and Economic Development of Economy*, 1-26. DOI:10.3846/20294913.2015.1056277.
- [28]. Akyuz, E. & Celik, E. (2016). A modified human reliability analysis for cargo operation in single point mooring (SPM) off-shore units. *Applied Ocean Research*. 58, 11-20.
- [29]. Celik, E., Bilisik, O. N., Erdogan, M., Gumus, A. T., & Baraclı, H. (2013). An integrated novel interval type-2 fuzzy MCDM method to improve customer satisfaction in public transportation for Istanbul. *Transportation Research Part E: Logistics and Transportation Review*, 58, 28-51.
- [30]. Celik, E., Gumus, A. T., & Erdogan, M. (2016). A new extension of the ELECTRE method based upon interval type-2 fuzzy sets for green logistic service providers evaluation. *Journal of Testing and Evaluation* 44 (5), 1-15.
- [31]. Saaty, T. L. 1980. *The analytic hierarchy process*, New York: McGraw-Hill.
- [32]. Ho, W. (2008). Integrated analytic hierarchy process and its applications—A literature review. *European Journal of operational research*, 186(1), 211-228.
- [33]. Buckley, J.J. 1985. Fuzzy hierarchical analysis, *Fuzzy Sets and Systems* 17:233–247. [http://dx.doi.org/10.1016/0165-0114\(85\)90090-9](http://dx.doi.org/10.1016/0165-0114(85)90090-9)
- [34]. Abdullah, L., & Najib, L. (2014). A new type-2 fuzzy set of linguistic variables for the fuzzy analytic hierarchy process. *Expert Systems with Applications*, 41(7), 3297-3305.

- [35]. Gul, M., Celik, E., Gumus, A. T., & Guneri, A. F. (2016). Emergency Department Performance Evaluation by an Integrated Simulation and Interval Type-2 Fuzzy MCDM Based Scenario Analysis. *European Journal of Industrial Engineering*, 10(2), 196-223.

Effects of Different Reaping Periods on Volatile Oil Components of endemic *Phlomis leucophracta* P. H. Davis & Hub.-Mor. (Lamiaceae)

Ayşe Gul SARIKAYA³⁴, Huseyin FAKIR³⁵

Abstract

Specimens of *Phlomis leucophracta* P. H. Davis & Hub.-Mor. which is endemic taxa were collected in 3 different reaping periods that are pre-flowering, flowering and post flowering periods between 2012 and 2015 in the Lakes District of Turkey. A total of 70 volatile components were determined by SPME analyses. Among of them, (E)-2-Hexenal, Limonene and β -Caryophyllene were found as main components. In pre-flowering period, ratios of β -Caryophyllene, Limonene and (E)-2-Hexenal were determined as 22.32%, 13.64% and 7.50% respectively. The ratios were found as 22.45%, 14.56% and 8.74% in flowering period and 20.12%, 10.93% and also 6.10% in post flowering period respectively.

Keywords: *Phlomis leucophracta*, volatile oil, collecting period, the Lakes District, Turkey

66. INTRODUCTION

Turkey flora has approximately 11.466 plant taxon [1]. Turkey is rich in species variety is the gen center of several plants, also there are many endemic species in different geographical regions of country [2,3]. *Phlomis* taxon has an important place among the medical plants and one of the species which has most type quantity of Lamiaceae family. It has got about 100 species all around the world. This species distributed in Asia, South Europe and Northern Europe [4,5]. Heights of species could vary between 30 cm and 2 meters. Sides of leaves are jagged and opposing aligned but not in bulk condition. Feathers covering the surface of plant are stellate. Flowers are purple, pink, white or yellow colored [6]. Leaves and flowers are used as appetizing, anti-allergic, diuretic, diarrhea preventive, getter, against stomach aches, pain seeker, anti-diabetic, herbal tea and tonic. At the same time it is known that plant is used for respiratory tract diseases and hemorrhoid problems in colloquially [7].

The *Phlomis* taxa have been picked in three different time period as pre-flowering period, flowering period, and post flowering period annually and volatile oil components were determined by using SPME analyze.

67. MATERIAL AND METHODS

67.1. Material

Material of research is consisting of *Phlomis* samples which were picked from Akbelenli province of Isparta-Aşağıgökdere in the Lakes District between the years 2012-2015 (Figure 1). *Phlomis* samples have been reaped in three different time period as pre-flowering period, flowering period, and post flowering period annually.

³⁴ Corresponding author: Suleyman Demirel University, Atabey Vocational School, Isparta/Turkey. aysegulsarikaya@sdu.edu.tr

³⁵ Suleyman Demirel University, Faculty of Forestry, Isparta/Turkey, huseyinfakir@sdu.edu.tr

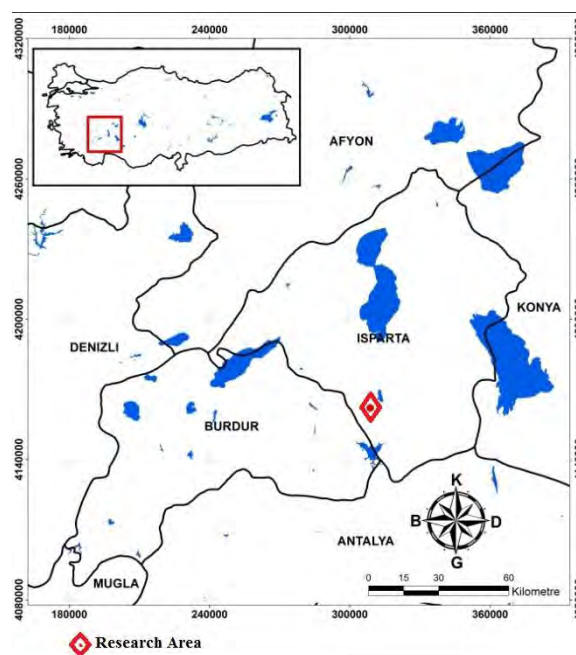


Figure 1. Collecting site of *Phlomis leucophracta*

67.2. Method for determination to volatile compounds of leaf and flower

Samples belonging to 3 different vegetation periods such as pre-flowering period, flowering period and post-flowering period from the determined areas. Collected leaves and flower samples have been transported to laboratory by putting in to paper packages and without waiting and exposing to sunlight. After drying the plant materials in room temperature (25 °C), 2 grams from each sample were bottled and heated 15 minutes in 60 °C. Proper edge injector sank to bottle and absorbed for 30 minutes. Compounds hold to fiber edge injected to GC injection block and waited 5 minutes for desorbing.

Shimadzu Qp 5050 brand GC-MS device has been used in order to determined volatile compounds. HP-5 MS (30 m x 0.25 mm length and 0.25 µm film) was used in device and helium was used as column and carrier gas (10 psi flow rate). Temperature of injection block was 240 °C and detector temperature was 250 °C.

68. RESULTS

Leaf and flower volatile compounds of taxon distributed in the Lakes District such as *Phlomis leucophracta* has been determined by SPME analyze (solid based micro extraction method). By SPME analysis, 70 volatile compound of *Phlomis leucophracta* determined and results were given in Table 1.

Table 1. Volatile compounds of *Phlomis leucophracta*

<i>Phlomis leucophracta</i>					
	Compounds	R.T.	Pre-flowering period	Flowering period	Post flowering period
1.	Acetaldehyde	1.135	-	-	0.77
2.	Dimethyl sulfide	1.320	-	-	0.26
3.	2-Methylpropanal	1.470	-	-	0.14

4.	2-Butenal	1.874	1,09	1,00	0.67
5.	3-Methylbutanal	1.920	0,38	0,39	1.67
6.	2-Methylbutanal	1.997	0,52	0,61	1.12
7.	Ethyl vinly ketone	2.184	0,34	0,12	0.66
8.	Pentanal	2.322	0,54	0,47	-
9.	2-Ethylfuran	2.344	0,35	0,30	2.09
10.	trans-3-Penten-2-one	2.885	0,16	0,18	-
11.	(E)-2-Pentenal	3.166	0,18	0,20	0.75
12.	3-Methyl-2-butenal	3.821	-	-	0.37
13.	Hexanal	4.090	4,89	3,54	3.27
14.	(E)-2-Hexenal	5.515	7,50	8,74	6.10
15.	(Z)-3-Hexenol	5.576	0,22	0,44	1.91
16.	Hexanol	6.015	0,16	0,25	0.51
17.	Heptanal	7.015	0,92	0,85	2.30
18.	2,4-Hexadienal	7.278	0,42	0,56	0.20
19.	Sorbaldehyde	7.369	-	-	2.15
20.	α - Thujene	7.835	0,54	0,51	-
21.	α -Pinene	8.060	2,85	2,72	1.92
22.	(E)-2-Heptenal	8.939	1,33	1,26	0.25
23.	Benzaldehyde	9.042	2,50	1,98	2.77
24.	β -Pinene	9.508	0,15	0,22	0.10
25.	Amyl vinyl ketone	9.716	0,24	0,23	0.39
26.	Amyl vinly carbinol	9.869	1,06	0,83	0.70
27.	Hept-5-en-2-one <6-methyl->	10.013	0,42	0,44	1.00
28.	Myrcene	10.206	2,15	2,28	1.76
29.	2-Isopropyl-5-oxohexanal	10.297	-	-	0.57
30.	Octanal	10.708	2,24	2,11	1.71
31.	α -Phellandrene	10.760	0,44	0,64	-
32.	2,4-Heptadienal, (E,E)	10.969	1,18	1,48	5.17
33.	α -Terpinene	11.176	0,68	1,00	-
34.	para-Cymene	11.469	1,03	1,29	-
35.	Limonene	11.693	13,64	14,56	10.93
36.	(E)-3-Octen-2-one	12.014	0,75	0,61	-
37.	Phenylacetaldehyde	12.134	0,63	0,71	-
38.	(E)- β -Ocimene	12.368	0,24	0,39	-
39.	(E)-2-Octenal	12.764	0,93	0,98	0.63

40.	3,5-Octadien-2-one	13.198	0,36	0,34	-
41.	Octanol	13.338	0,10	0,19	-
42.	Terpinolene	13.811	1,55	2,29	0.50
43.	Dimethylstyrene < α -para->	13.971	0,10	0,21	-
44.	Methyl benzoate	14.102	0,26	0,27	-
45.	Linalool	14.410	-	-	1.04
46.	Nonanal	14.609	3,44	3,61	3.32
47.	(E)-2-Nonenal	16.674	0,30	0,50	0.59
48.	Methyl salicylate	17.927	-	-	0.60
49.	Decanal	18.450	0,62	0,86	0.30
50.	(E)-2-Decenal	20.477	0,24	0,46	0.10
51.	Hendecanal	22.141	0,13	0,24	-
52.	α - Cubebene	23.507	3,55	-	-
53.	α -Copaene	24.468	0,96	0,79	2.78
54.	β -Bourbonene	24.734	0,79	0,17	1.92
55.	β - Cubebene	24.897	0,89	0,20	-
56.	β -Elemene	24.960	0,19	0,14	-
57.	β -Caryophyllene	26.000	22,32	22,45	20.12
58.	β - Cedrene	26.279	0,23	-	-
59.	Aromadendrene	26.887	1,17	0,56	0.77
60.	(E)- β -Farnesene	27.104	3,77	3,96	2.40
61.	α -Humulene	27.114	-	-	0.90
62.	Cadina-1(6),4-diene <10 β H->	27.321	0,40	0,21	0.10
63.	Epi-bicyclosesquiphellandrene	27.444	-	-	0.39
64.	Germacrene D	27.956	6,46	8,32	7.47
65.	β - Bisabolene	28.908	-	0,22	-
66.	γ -Cadinene	28.975	0,38	0,24	0.20
67.	δ -Cadinene	29.163	0,71	0,82	1.18
68.	Caryophyllene oxide	31.090	0,17	0,47	-
69.	(2-Ethylhexyl)Ether	31.344	-	-	1.32
70.	Nonadecane	40.184	0,44	0,72	-

(E)-2-Hexenal, Limonene and β -Caryophyllene have been determined as the essential compound of *P. leucophracta*. It has been determined, E)-2-Hexenal (7.50%), Limonene (13.64%) and β -Caryophyllene (22.32%) in pre-flowering period; (E)-2-Hexenal (8.74%), Limonene (14.56%) and β -Caryophyllene (22.45%) in flowering period and (E)-2-Hexenal (6.10%), Limonene (10.93%) and β -Caryophyllene (20.12%) in post flowering period.

69. DISCUSSION

70 volatile compound of *Phlomis leucophracta* have been determined by the SPME analysis and essential compounds have been determined as (E)-2-Hexenal (8.74%), Limonene (14.56%) and β -Caryophyllene (22.45%). Çelik et al. [8] determined β -Caryophyllene (20.2%), α -pinen (19.2%) and limonen (11%) in *P. leucophracta* in Turkey. β -Caryophyllene and limonene were determined as essential compounds. Result of this research supports our study. Apart from our researches, (E)-2-Hexenal compound has been determined between the dominant compounds.

As a result, it is significantly important to reaping of *P. bourgaei*, *P. leucophracta*, *Phlomis lycia* taxon in flowering period of *P. bourgaei* and *Phlomis lycia* taxon in respect to volatile compound productivity. In the light of these determined information it is considered that the locals and traders will become conscious and slapdash plant picking and economic losses will be prevented. These kinds of researches and studies should increase in order to show the plants used for medicine raw material or food and cosmetic products and use them more consciously.

5. ACKNOWLEDGMENTS

This study was a part of PhD thesis of first author Ayse Gul SARIKAYA. We express our sincere appreciation to Suleyman Demirel University for their financial support by project which numbered as 3360-D2-12.

REFERENCES

- [128]. A. Güner, A Checklist of the Flora of Turkey (Vascular Plants). Nezahat Gökyiğit Botanical Garden Press., 1290 p., Istanbul, 2012.
- [129]. A. Tan, Plant Genetic Resources and Conservation in turkey, *Anadolu Journal of AARI*, 2: 50-64, MARA, 1992.
- [130]. P.H. Davis, Flora of Turkey and East Aegean Islands 7, Edinburg University Press., 948 p, Edinburg, 1982.
- [131]. Dadandı, M.Y., The Revision of the genus *Phlomis* L. (Lamiaceae) of Turkey, PhD Thesis, Gazi University, Ankara, 2002.
- [132]. C. Mathiesen, A. C. Scheen, C. Lindqvist,. Phylogeny and biogeography of the lamioid genus *Phlomis* (Lamiaceae). *The Board of Trustees of the Royal Botanic Gardens, Kew*, Vol: 66: 83-89, 2011
- [133]. A. Huber-Morath, *Phlomis* L. in Flora of Turkey and East Aegean Islands, Davis, P. H. (Ed.), Edinburg University Press., Vol: 7, Edinburg, 1965-1982, s: 102-126, 1982.
- [134]. Ü. Ş. Harput, İ. Çalış, İ. Saraçoğlu, A.A. Dönmez, A. Nagatsu, "Secondary Metabolites from *Phlomis syriaca* and Their Antioxidant Activities", *Turkish Journal of Biology*, 30: 383-390, 2006.
- [135]. S. Çelik, R.S. Göktürk, G. Flamini, P.L. Cioni, I. Morelli, Essential oils of *Phlomis leucophracta*, *Phlomis chimerae* and *Phlomis grandiflora* var. *grandiflora* from Turkey. *Biochem Syst Eco*, 33: 617-623, 2005.

Position Control of Servo Motor by Use of Matlab OPC Tools with PLC

Ali SAYGIN¹, Yücel BEŞYAPRAK²

Abstract

The study has performed the position control of the servo motors moving independently in two axes. The motor position data have been calculated from Matlab program whereas transferred to PLC via OPC tools. The communication between Matlab and PLC has been realized by using KEPServerEX OPC software. The variables of KEPServerEX OPC interface are processed in the software, the real positions are read and the desired new position information are sent using Matlab OPC tools. The new position data arriving to PLC via OPC tools are transferred to the servo motor driver through CanOPEN protocol whereas the motor position controls are then performed. The driver and the functions of motor power, home, absolute position, sudden stop and error correction are controlled from Matlab. The practice included the use of Schneider brand LMC058 PLC, Lexium servo motor driver and servo motor.

Keywords: KEPServerEX, Matlab, OPC, PLC

1. INTRODUCTION

The servo motor control is separated in the motor speed control, motor moment control or motor position control classes depending on the purpose of use. The servo motor position control includes the speed, moment and position controls depending on the data and resolution of the position sensor encoder located on the motor. In motor and driver compatible systems, the motion realizes in form of commands sent to the driver. The computer user interface prepared for the driver marks the digital entry and exit addresses and the analogous entry and exit addresses. Moreover, considering the logic level status data, the functioning of the commands are coded. After adjusting the encoder resolution and existing controller gains, the driver acts in line with the commands to arrive from PLC. Optionally, the temporary panels installed may be used for manual control. The robotic practices, CNC lathe implementations and sensitive position requiring systems all utilize servo motors commonly in the present day. Again in a common manner, new generation PLC infrastructures do support the drivers and PLC hardware up to 64 axes. PLC may operate the servo motors using the installed program or may do the same in line with the external commands arriving. In the second option, the commands arrive from a remote access centre. OPC (Ole for Process Control) is a standard formed for real time data communication and functions as a protocol for the communication between the computer and external devices. PLC companies require the use of their own remote control and data acquisition (Supervisory Control And Data Acquisition – SCADA) software or the utilization of OPC software. The SCADA systems within the OPC limits the software designer however direct OPC use provides flexibility. Işık and et. al. have performed a study named “The Control and Monitoring of PLC based Motion Control System via Device-Net” and used Device Net communication protocol for the motor control whereas a SCADA software developed by OMRON Company for the communication between PLC and computer[1]. Wei Mo and et. al. have performed AC servo motor speed control using PLC based control system for winding machine[2]. Prabhavath has written an article in 2014 and claimed that power production, fuel and gas industry, automotive industry etc. sectors’ complex sub-system analyses may be realized whereas related system controls may be performed with a program written with LABVIEW[3]. Huidong Li and et. al. have conducted an article study in 2014 and based on the fuzzy logic controller design and control systems in Matlab whereas served the results which ease the communication between Matlab and PLC for online controls[4]. W. Zhang and et.al. have used PLC for the asphalt machine and controlled the servo and step motors. They have not used any OPC interface in implementation[5]. Jasmin Velagic and et.al. have conducted their study named “Networked based control and supervision of induction motor using OPC server and PLC” and used Siemens WinCC protocol for successful Profinet based control[6]. Teresa Devesa and et. al. have claimed in 2009 that when the Matlab function blocks are converted in PLC program (Matlab/Simulink) they can operate the simulation system[7]. Kenichi NAKAGAWA and et.al. have measured the interface characteristics of high-speed PLC modem use in case of narrow band signal utilization. They have calculated the measured values with Matlab/Simulink. The results they have obtained made them claim such data may be used in future[8]. Gülden and et. al. have compared the Matlab/Simulink models that have been converted to CFC programming language through different PLCs having IEC 61131-3 protocol[9].

Most of applications have been given motion control of servo motor with PLC. But Matlab applications are limited. So, In this study has been used LMC058 model PLC produced by Schneider company. The selected PLC has the capacity to be used for position control up to 8 axes. Together with PLC, Lexium 32MU90M2' series servo driver and servo motor (BMH0701T16A1A) are preferred to be tested in real practice. The PLC programming is written with CFC language. Matlab has been communicated with PLC via versa KEPServerEX OPC tools.

2. CONTROL DIAGRAM

The operational diagram of the system consists of three stages. PC, PLC and Servo Group. PC side used Matlab/Simulink and Matlab OPC tools. The data access from Matlab program has been performed with KEPServerEX software. The KEPServerEX software is used for data transfer between Matlab and PLC. The Ethernet protocol is used for communication between PC and PLC. The values and commands coming from Matlab/Simulink interface are transferred to PLC. The PLC and servo motor drives communicate through CanBUS protocol. The PLC, as in line with the commands and position data arriving from Matlab program, operates the AC servo motors. The motion is controlled in line with the control method and using the digital entry and exit addresses on the server. The encoder on the servo engine reads the real position and driver status data and the same are transferred to Matlab/Simulink interface from PLC in real time using the same communication protocol. The control scheme of above designated system is given below under Figure 1.

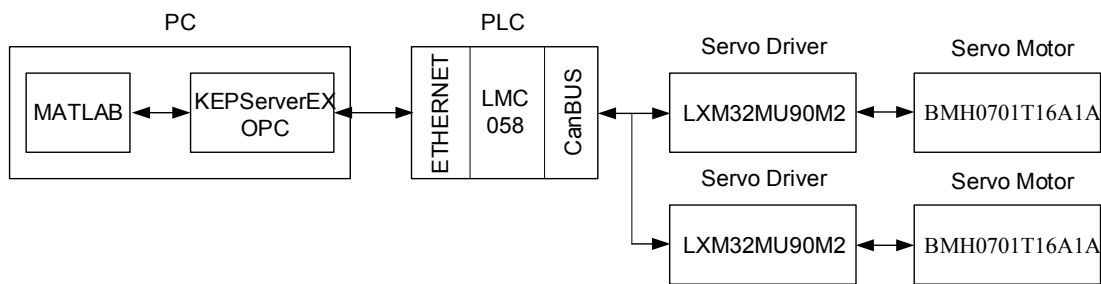


Figure 1. System Control Scheme

OPC flow algorithm of the system has been given under Figure 2. The flow scheme includes the selection, call and, when necessary, termination of the OPC objects in Matlab/Simulink interface however here only the communication section has been drawn. The new variables may be added in case required by the software.

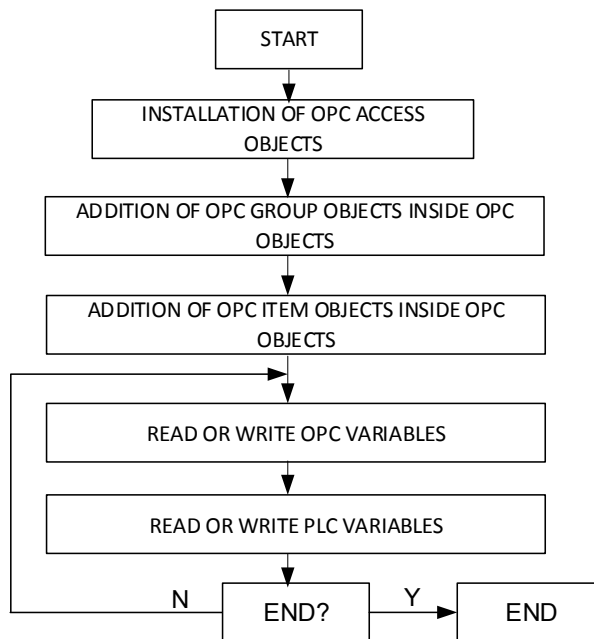


Figure 2. Matlab OPC flow diagram

3. OPC IMPLEMENTATION and KEPServerEX

OPC allows client and server applications to communicate with each other. OPC is designed to be an abstraction layer between industrial networks and proprietary PLC drivers. The OPC standard specifies the behavior that the interfaces are expected to provide to their clients; and the clients receive the data from the interfaces using standard function calls and methods. Consequently, as long as a computer analysis or data acquisition program contains an OPC client protocol, and an industrial device driver has an associated OPC interface, the program can communicate with the device. The specification also includes a protocol for working with data control systems and application databases, as well as online data access, alarm and event handling, and historical data access for all of these data sources[10].

KEPServerEX, independently from the system type in use, uses a single type server interface and eases the project development. KepserverEX enables more than one device drivers to an application, the centralization of the communication and reduction of the user load. KEPServerEX provides single structuring mode and strong program development tools to the user. The function of Kepware is to present an OPC server with unique compatibility and performance. KEPServerEX is a 32/64 bit windows application whereas enables to transfer the data and information from many industrial devices to the client application in your computer. The OPC type to function for communication shall be selected from KEPServerEX. The device is added to the selected communication protocol. The reading and writing variables of the device are adjusted. The marked or unmarked status of the variables are important whereas the correctness of the sent or received data depends on the same. The Figure 4 provides the interface of the variables used in the article.

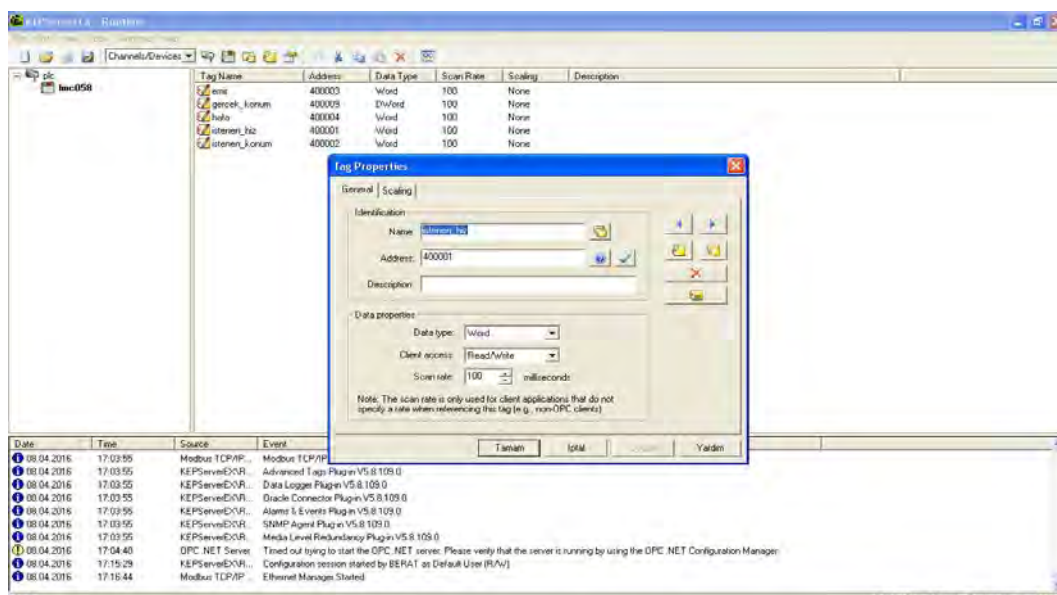


Figure 3. KEPServerEX OPC tools

4. MATLAB/SIMULINK OPC TOOLS

The communication settings are performed from the OPC tools menu in the Matlab/Simulink. For the communication settings, first perform the appointment "localhost/Kepware.KEPServerEX.V5 [Timeout = 10, Connected]" in OPC client page. Define each "plc.lmc058.gercek_konum" variable etc. in Items/ID section. The graphic screen displays the real time position, motor speed etc. values being read from PLC. For the position control, only the motor real positions are monitored in Matlab interface. The figure 4 provides the Matlab/Simulink interface.

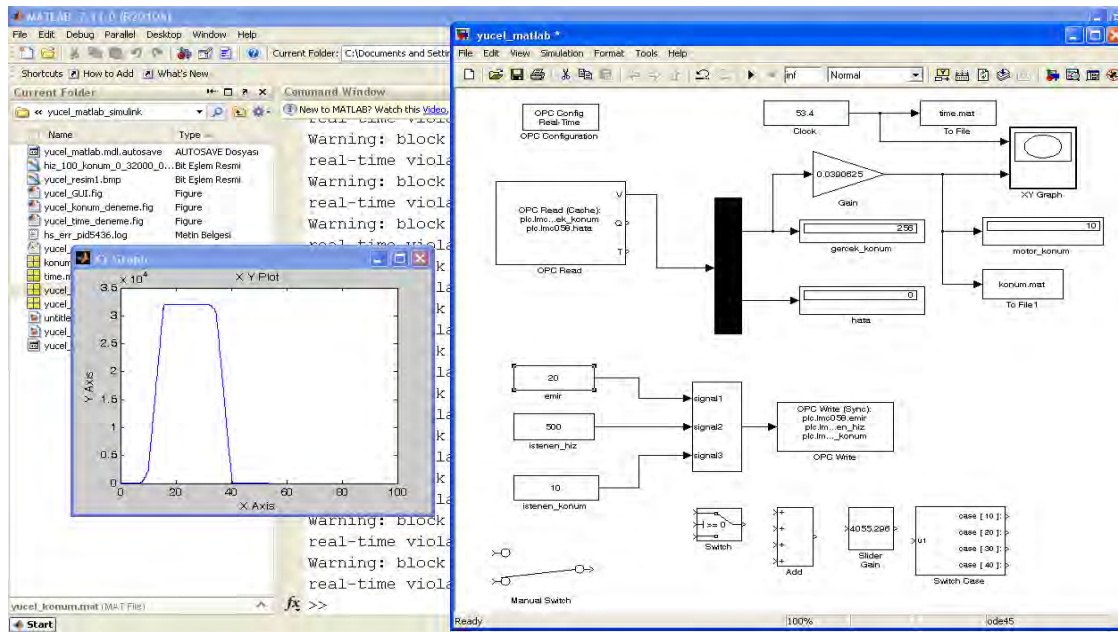


Figure 4. Matlab/Simulink OPC tools

5. EXPERIMENTAL RESULTS

Through the experimental works performed, the motion of the motors to the various positions is conducted. The analyses about the motion of the motor to the desired position at desired speed are performed. The reach of servo motor to home, to the desired position or sudden stop have been coded in Matlab interface. The servo driver used (+) limit switch, (-) limit switch and home digital input entries. When the home information arrives in Matlab program, the motor starts motion and the motion is completed when corresponds (hits) the home switch. Thus, the encode value becomes zero and the system stands by as ready for absolute position. The figure 5 provides the speed information of the motor while proceeding to the home position. While controlling the position information in Matlab interface, the speed realized on the path to desired position are read from the driver.



Figure 5. Servo motor reference and actual speed

The motor slows down while proceeding to the desired position and the speed becomes zero at that desired position. The desired speed and the real speed have been shown in Figure 6 as read from the driver.

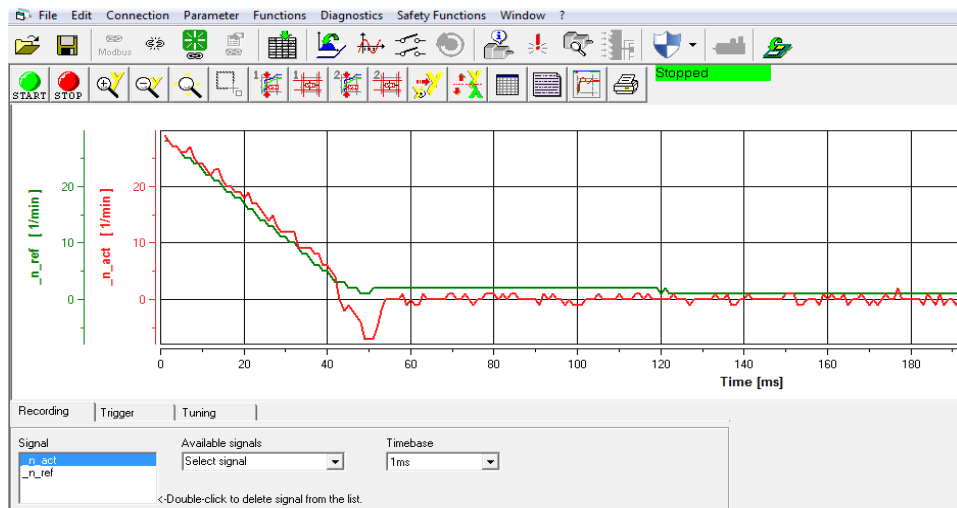


Figure 6. Desired speed and real speed curve while approaching to the desired position

The Figure 7 provides the change from rated speed of the motor under ramp/slope function and reduction of the same towards the desired position. The speed up curve of the motor in reverse direction against the desired position has been provided under Figure 8. The rising slope has been calculated in connection with the trained PI controller coefficient on the driver as well as reference speed curve. The servo motor shall follow the same curve in real speed. The reference speed goes from -540 r/m to 620 r/m under Figure 8 whereas it has been sampled instantaneously. The instantaneous load changes have been realized while the motor is in operation. The samples obtained from servo driver are real time and accordingly not filtered. LexiumCT licenced software for Schneider is used servo motor driver

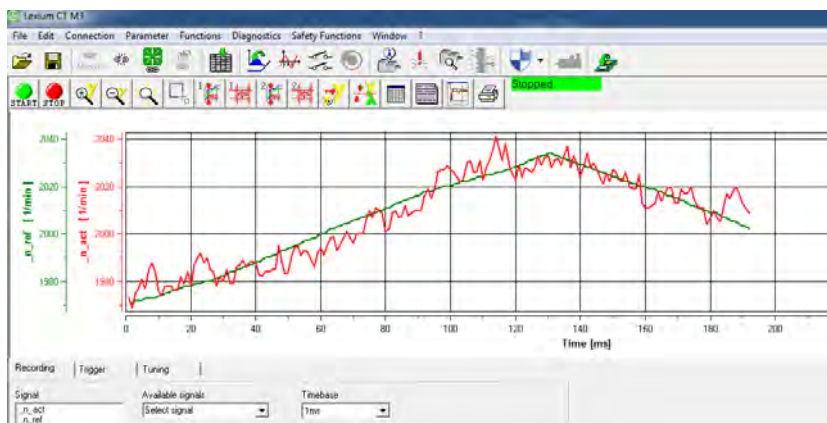


Figure 7. Ramp Function Response

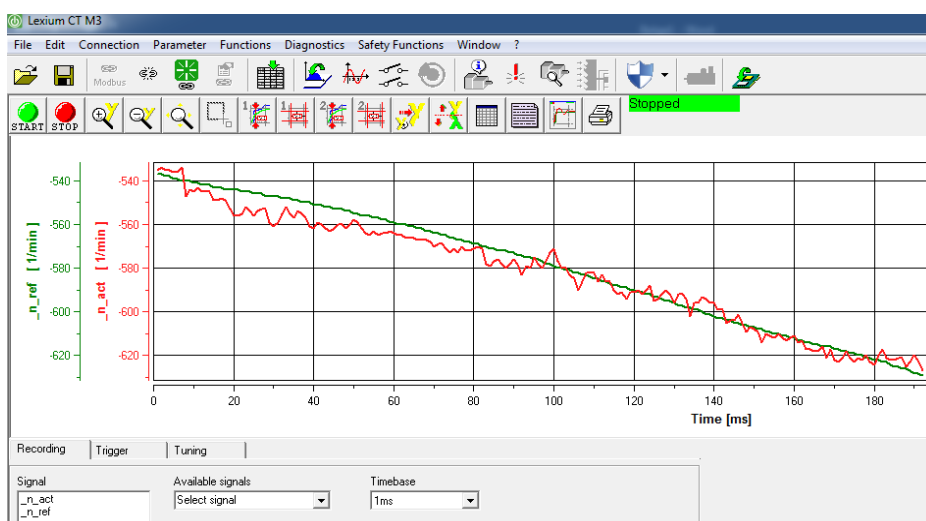


Figure 8. Reverse Speed Up Curve

6. CONCLUSION

This study has made use of KEPServerEX OPC for the communication between Schneider brand PLC and PC i.e. two directional data transfer. The bit and communication parities are adjusted in OPC interface as in line with data type whereas the PC and PLC communication synchronization has been established without any interruption in Real-Time.

Matlab/Simulink program has been used whereas the position and speed control of serve motors operating at two axes has been performed. The variables in Matlab are transferred to Schneider brand LMC058 PLC using KEPServerEX OPC software; accordingly the desired position and speed are controlled in serve motors. The obtained real value are resent to the Matlab program by PLC. The desired and realized motion are verified under the Matlab interface. The user experiment (testing) platforms are developed for the 2 and more axes using target monitoring platforms widely used in defence industry, as with a similar pitch and roll angle control; i.e. for the guided or non-guided missile launch platforms and for other industrial related practices requiring 2 or more axes motion control abilities.

REFERENCES

- [1]. M. F. Işık; M. R. Haboğlu; H. Yanmaz “Monitoring and control of PLC based motion control systems via device-net” Power Electronics and Motion Control Conference and Exposition (PEMC), 2014 16th International, DOI: 10.1109/EPEPEMC.2014.6980632, 2014 IEEE Conference Publications, 21-24 Sept 2014 Antalya, Turkey. Pages: 963 - 966,
- [2]. W. Mo; M. Wang; J. S. Lin; H. Zan; G. Sun, “Control System Based on PLC for Winding Machine” Computer, Consumer and Control (IS3C), 2014 International Symposium on Computer, Consumer and Control, DOI: 10.1109/IS3C.2014.31 IEEE Conference Publications. Pages: 74 - 77
- [3]. M. Prabhavathy; B. Ramesh; T. Kalpalatha Reddy, “An alternative distributed control using Labview”, 2014 International Conference on Computation of Power, Energy, Information and Communication (ICCPEIC), DOI: 10.1109/ ICCPEIC.2014.6915361, IEEE Conference Publications.,Pages: 174 – 180.
- [4]. H. Li; L. Yang., “The Application of Fuzzy Control in PLC Temperature Control System Based on OPC Technology”, 2014 Seventh International Symposium on Computational Intelligence and Design (ISCID), DOI: 10.1109/ISCID.2014.260 IEEE Conference Publications, Pages: 288 – 291.
- [5]. W. Zhang; B. Liu; D. Li; J. Yang., “The control system research of paving machine for the modified asphalt coiled material”, 2011 International Conference on Mechatronics and Automation (ICMA), DOI: 10.1109/ICMA.2011.5986333, August 7 - 10, Beijing, China, Pages: 2433 – 2437.
- [6]. J. Velagic; A. Kaknjo; N. Osmic; T. Džananovic., “Networked based control and supervision of induction motor using OPC server and PLC”, ELMAR, 2011 Proceedings 2011, 14-16 September 2011, Zadar, Croatia, Pages: 251 – 255.
- [7]. T. Deveza; J. F. Martins., “PLC control and Matlab/Simulink simulations. A translation approach”, IEEE Conference on Emerging Technologies & Factory Automation, 2009. ETFA 2009. DOI: 10.1109/ETFA.2009.5347138 Cited by: Papers (2) , Pages: 1 – 5.
- [8]. K. Nakagawa; S. Hosoya; M. Tokuda; Y. Igata, “Narrowband interference characteristics of high-speed power line communication based on Wavelet-OFDM”, 2009 20th International Zurich Symposium on Electromagnetic Compatibility, , DOI: 10.1109/EMCZUR.2009.4783493, Pages: 473 – 476.
- [9]. G. Bayrak; P. J. Murr; S. Ulewicz; B. Vogel-Heuser, “Comparison of a transformed Matlab/Simulink model into the programming language CFC on different IEC 61131-3 PLC environments”, 2012 IEEE 17th Conference on Emerging Technologies & Factory Automation (ETFA), DOI: 10.1109/ETFA.2012.6489667, Pages: 1 - 8
- [10]. H. Li; L. Yang, “The Application of Fuzzy Control in PLC Temperature Control System Based on OPC Technology”, 2014 Seventh International Symposium on Computational Intelligence and Design (ISCID), , Volume: 2, , DOI: 10.1109/ ISCID.2014.260, IEEE Conference Publications, Pages: 288 – 291.

BIOGRAPHY

Ali SAYGIN was born in 1974, Sivas, Turkey. He received the BS degree in 1995, the MSc degree in 1998, and the PhD degree 2004 from Gazi University, Ankara, Turkey. He is currently an assistant associate professor at the department of Electrical and Electronics Engineering Gazi University. His research interests include, PLC, Automation, Power Electronics, DSP and DSP.

Yücel BEŞYAPRAK was born in 1982, Aksaray, Turkey. He received the BS degree in 2001 from Mersin University, Mersin, Turkey. His research interests include, PLC, Automation, Laser Pointer, Power Electronics, Driver Technology and Matlab

Investigation of Relationship between Vacuum Level and Thermal Conductivity in Vacuum Insulation Panel

Hilmi Cenk Bayrakçı

Abstract

In Vacuum Insulation Panels, the effect of vacuum level on thermal conductivity is known fact. However, the number of studies examining the relationship between the vacuum level and thermal conductivity in detail is limited.

In this study, the thermal conductivity coefficients of a uniform VIP core were investigated at 11 different levels of vacuum. Fumed silica, glass fiber and silicon carbide were used in the core production. The core was individually vacuum-packed at 11 different levels of vacuum, ranging from 10000 Pa – 0.1 Pa. Thermal conductivity measurements of VIP were carried out according to heat flow meter by Lasercomb Fox 314. As a result, the change in thermal conductivity of nano powder filled core was about 0.5 mW/mK at 100-0.1 Pa levels of vacuum.

Key Words: Vacuum Insulation Panel, Vacuum Level, Thermal Conductivity

1. INTRODUCTION

VIPs are thermal insulation materials have a core material which contains about 10-100 nm small pores coated by a thin laminated film layer (envelope) has low gas permeability. Core material was emptied by vacuum to 0.2 - 3 mbar level and it has 2 - 4 mW/mK thermal conductivity depend on core material type [1].

These materials could be used as insulation materials at refrigerators, freezers, refrigerated trucks, cold storage systems and refrigerated containers because of they have quite low thermal conductivities. Because of they are thinner than traditional materials and have much lower thermal conductivities, they were used at restricted sections and high insulation performance desired places, mostly in refrigeration sector and they have big effect on energy saving.

Heat transfer is an energy transfer because of temperature difference. In an ambience or between ambiances in every temperature difference existing situation, heat transfer is absolutely performed. Heat transfer has three types: conduction, convection and radiation. Heat convection is heat transfer performed between a solid surface and moving fluid which has contacted to this surface; both have finite temperature difference.

VIP's thermal insulation performances are directly related vacuum ability and core material properties which has a mission of support versus atmosphere pressure. Core was generally produced from materials like fumed silica, precipitated silica or open pored polyurethane (or polystyrene). These materials which form core material take role as support versus atmosphere pressure. Chemical structure of solid phase and its density, quantity of voids which forms dispersed phase are affected to the thermal insulation of porous materials.

There are so many correlations were developed to estimate thermal conduction. Most of these correlations were used thermal conduction of materials which forms the core material and volume ratios (porosity). In case of using small porous micro and nano materials as core material in VIPs, it could be reached low thermal conductivity by

vacuum. Because of the relation between gas thermal conduction of air and pore diameter, core material should be suitable for vacuum and it must fulfill expected conditions from itself after vacuum [2]. Emptied core, almost have 0.004 W/mK thermal conductivity at room temperature. U value is 0.2 W/m²K at 2 cm thickness [3].

The work done at VIPs is reducing number of gas molecules in the ambient and gas pressure by vacuum effect. In this way, there is an increasing of the mean free path of motion of gas atoms in the material pores and there is a decreasing of number of collisions. The mechanism of collision of gas molecules moving freely in unit volume was lost its effectiveness. This mechanism works better when the volume which is the gas molecules makes movements in this space was decreasing. For this reason, if the pores in inner filling material used in VIP be in the smallest possible size, heat transfer mechanism's efficiency decreases. Low pressure and small pores brings heat convection mechanism of gas to the possible lowest levels [1].

In this study, it is aimed to determine effect of vacuum level to the nano powder filled VIP thermal conductivity and optimum vacuum level. For this purpose, one type of nano powder filled VIP core was vacuumed to 11 different vacuum level, after all vacuum process thermal conductivities were measured and vacuum levels were associated with thermal conductivity values.

2. MATERIAL and METHOD

In this study, one type nano powder filled core was used. The components of core panel were fumed silica, glass fiber and silicon carbide (as opacifier). Physical and chemical properties of core filling materials were given in Table 1.

Table 1. Physical and chemical properties of core filling materials

Properties		FS	SC	GF
ρ_{sg}	(g/cm ³)	2.32	3.26	2.67
SSA	(m ² /g)	322.18	0.83	-
D ₅₀	(μ m)	0.010	9.28	-
d _{av}	(μ m)	-	-	10
SiO ₂	(%)	95.81	99.70	
Al ₂ O ₃	(%)	0.30	0.16	
Fe ₂ O ₃	(%)	0.05	0.05	
CaO	(%)	0.13	0.02	
MgO	(%)	0.10	0.00	
Na ₂ O	(%)	0.67	0.01	
K ₂ O	(%)	0.05	0.00	
TiO ₂	(%)	0.00	0.00	
SO ₃	(%)	0.12	0.01	
LOI	(%)	2.78	0.00	
FS	<i>Fumed silica</i>			
SC	<i>Silicon carbide</i>			
GF	<i>Glass fiber</i>			
ρ_{sg}	<i>Apparent density</i>			
SSA	<i>Specific surface area</i>			
D ₅₀	<i>Mean particle size</i>			
d _{av}	<i>Average diameter of fiber</i>			

thermal conductivity is 2.5 % at 1-0.01 mbar range. It could be say that this decreasing was quietly approached “0” level under 0.01 mbar.

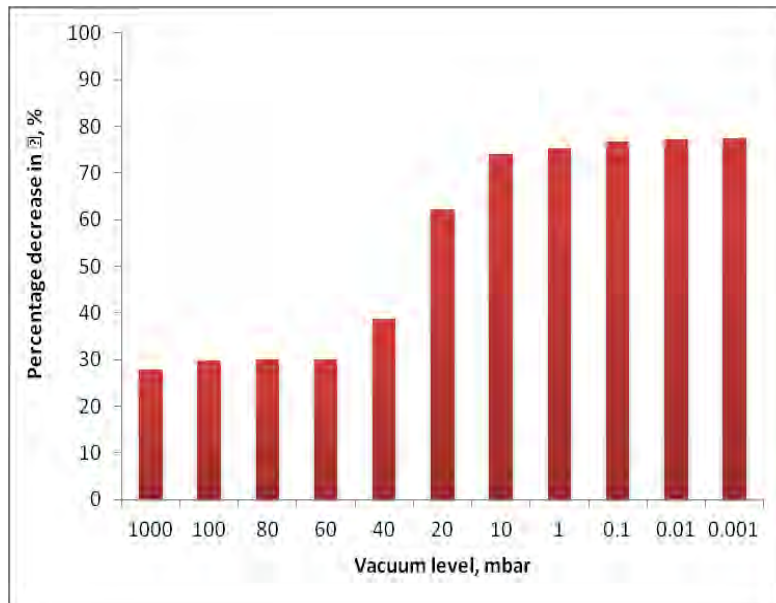


Figure 1. Variation of thermal conductivity coefficient of VIP according to vacuum level (%)

4. CONCLUSION

When the vacuum level decreases in VIPs, heat transfer by convection also decreases. Thermal conductivity of VIP decreases 28 % at 100 mbars vacuum level, 62 % at 10 mbars, 74% at 1 mbar and about 75% at 0.1 mbars. This decreasing was stayed steady 77% at 0.01 mbars level and there were no significant changes at thermal conductivity for higher vacuum levels. In this regard, the effective vacuum level is about 1 mbars at nano powder filled VIPs. It could be accepted that thermal convection as “0” at 1 Pa vacuum level.

As a result, thermal conductivity about 1mbar level at VIPs uses adequate and suitable opacifier is more related of heat transfer of solid ambient. At these vacuum levels, an effective decreasing at thermal conductivity may be possible with nano powders which have higher specific surface area and particle size.

5.ACKNOWLEDGEMENTS

This study was supported by the Scientific and Technological Research Council of Turkey (TUBITAK-Project No: 213M740).

6. REFERENCES

- [1] Simmler, H., Brunner, S., Heinemann, U., Schwab, H., Kumaran, K., Mukhopadhyaya, P., Quénard, D., Sallée, H., Noller, K., Küçükpinar- Niarchos, E., Stramm, C., Tenpierik, M. J., Cauberg, J. J. M., and Erb, M. *Vacuum Insulation Panels. Study on VIP-components and Panels for Service Life Prediction of VIP in Building Applications* (Subtask A): IEA/ECBCS Annex 39 High Performance Thermal Insulation (HiPTI), .2005.

- [2] Baetens R., Jelle B. P., Thue J. V., Tenpierik M. J., Grynning S., Uvsløkk S., Gustavsen A. *Vacuum insulation panels for building applications: A review and beyond*, Energy and Building, 42:2, 147-172, 2009.
- [3] Caps R., Heinemann. U., Ehrmanntraut M., Fricke J. *Evacuated Insulation Panels Filled with Pyrogenic Silica Powders: Properties and Application*. High Temperatures - High Pressures, Vol. 22. pp. 151-156, 2001.
- [4] DIN EN 12667:200105. *Thermal performance of building materials and products-Determination of thermal resistance by means of guarded hot plate and heat flow meter methods*.

Aerodynamic Nose Shape Optimization for Performance Maximization of Morphing Autonomous Aerial Robot

Tuğrul Oktay³⁶, Metin Uzun³⁷, Ilker Yılmaz³, Mehmet Konar⁴

Abstract

The aim of this conference article is to improve flight performance of an autonomous aerial robot by applying aerodynamic nose shape optimization both experimentally and computationally. Aerodynamic performance criteria (i.e. maximum fines) of a scaled model of our autonomous aerial robot called as Zanka-II produced in Erciyes University Faculty of Aeronautics and Astronautics Model Aircraft Laboratory is first observed in sub-sonic Wind Tunnel. Results obtained are validated using a computational fluid dynamics software (i.e. Ansys). Nose cone of fuselage is optimized in order to maximize maximum fines of our autonomous aerial robot by using Ansys. A novel scaled model using optimum data is then produced and placed in Wind Tunnel in order to validate Ansys results with experimental results. By using geometrical data of eventual aerodynamically optimized aerial robot, better autonomous flight performance is found both in simulation environment (i.e. Matlab) and real time flights.

Keywords: Aerial robots, Autonomous Performance, Aerodynamics, Nose Shape Optimization.

70. INTRODUCTION

For the last four and five decades *aerial robots* have been broadly benefited for military tasks and also in commercial applications since they have numerous advantages with respect to the traditional manned vehicles. These advantages are cheap manufacturing and operation, flexible configuration for customer request and not risking the pilot's life on hard missions.

Aerial robots have also been applied in aerial agriculture such as crop monitoring and spraying, photography for instance film and video, coast guarding such as coastline and see-lane, conservation such as pollution and land monitoring, etc. for civilian tasks.

They have also been applied for military operations. For example, they have been benefited for navy such as decoying missiles by the emission of artificial signatures and shadowing enemy fleets, army such as reconnaissance and surveillance of enemy activity and air force such as radar system jamming and destruction and airfield base security. Many other aerial robot applications is examined in detail by [1]. Lots of scientific study for aerial robot design, manufacturing and autonomous control have been recently examined such as [2], [3], [4] and [5].

In order to obtain better performance several studies are done for aerodynamic shape optimization (for instance, [6], [7]). In [7] several nose cone shapes are applied in order to minimize drag such as eelliptical nose, conical nose, bi-conical nose, spherically blunted tangent ogive nose.

This is the *first conference article* examining aerodynamic nose shape optimization for maximization of autonomous flight performance of morphing aerial vehicle during simultaneous design of a load-carrying morphing aerial robot and autopilot system. Furthermore, for this drive a stochastic optimization method

³⁶ Corresponding author: Erciyes University, Faculty of Aeronautics and Astronautics, Kayseri, Turkey, 38039 tugruloktay52@gmail.com,

³⁷ Erciyes University, Faculty of Aeronautics and Astronautics, Kayseri, Turkey, 38039 m.uzun2010@gmail.com

³ Erciyes University, Faculty of Aeronautics and Astronautics, Kayseri, Turkey, 38039 iyilmaz@erciyes.edu.tr

⁴ Erciyes University, Faculty of Aeronautics and Astronautics, Kayseri, Turkey, 38039 mkonar@erciyes.edu.tr

(i.e. SPSA, simultaneous perturbation stochastic approximation) is *first time* benefited and using it, optimal results are found safely and fast. Moreover, aerodynamic nose shape optimization progresses autonomous flight performance noticeably, therefore less overshoot, less settling time and less rise time are obtained during trajectory tracking.

71. OUR AUTONOMOUS AERIAL ROBOT

In Figure 1 (a) Solidworks drawings of morphing aerial robot, Figure 1 (b) side and upper view photos of Zanka-II (e) are given.

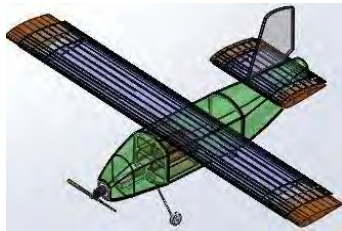


Figure 1. Aerial Robot: (a) Solidworks drawing of it



(b) A photo of the Zanka-II



(c) Another photo in which both non-morphing and morphing wings are put

Aircraft or aerial robots wings are a compromise allowing the aerial robot to fly at a range of flight conditions, nonetheless the performance at each situation is sub-optimal. Mechanisms like deployable flaps, wing tips delivering the capability of a wing surface to alter its geometry during flight has interested researchers and designers over the last years as this reduces the design compromises required. Placing mechanical elements on the wing tips and according to quantified values given by remote control extension of wing tips is delivered and thus, wing area increases. Principal components of the system are reductive micro motor, two equal number of gear teeth, M3 worm gear, bidirectional mini brushing ESC.

The system is consisted of the simple association of the elements listed before. As given in Figure 2 (a, b), micro motor is a DC motor operating between ranges 6-9 V range and creates a torque of 1.8 kg. A gear motor is mounted to the shaft of this related motor. This gear works together with a second gear mounted on a bearing (see Figure 2 (c, d)).

Inside of the gear mounted on bearing has M3 tooth in released state. Signal sent to ESC through a bistable switch defined on the remote control provides the engine right or left turn. ESC is a brushed and bidirectional circuit and according to the directly incoming signal through remote control switch works in two ways (see Figure 2 (e)). Motor, and hence mechanical systems moving according to the direction of rotation of gears lead worm screw in-or-outward (see Figure 2 (f)). This movement consequences by moving wing tips parts, produced by outer mold method, over main section so therefore to provide the alteration of the wing area.



Figure 2. Morphing mechanism: (a) and (b) DC Motor and gear motor mounted to shaft

(c) Placement of the Servo motor in the wing



(d) Electronic speed controller



(e) Montage of the expanding parts of the wing



(f) 3D View of the Over-expanding part of the wing

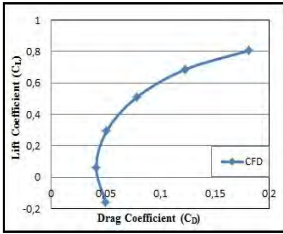
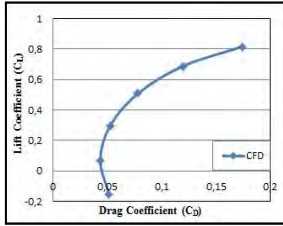
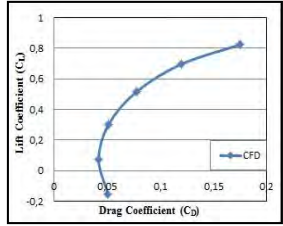
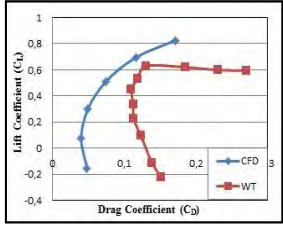
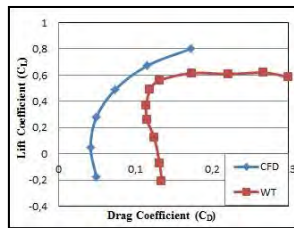
Nose Cone	CFD	$C_L - C_D$	E_{max}
Elliptical			6.33
Conical			6.22
Bi-Conical			6.36
Spherically Blunted Tangent Ogive			6.54

Table 1. Optimization

Produced
Aircraft



Result

6.35

72. AERODYNAMIC SHAPE OPTIMIZATION

In this conference article several nose shapes are investigated in order to maximize the value of maximum fines (E_{max}) such as elliptical nose, conical nose, bi-conical nose, spherically blunted tangent ogive nose. In Table 1 for this nose shapes, CFD drawings, CFD and Wind Tunnel (WT) results and E_{max} values are given. From this table it can be seen that the maximum value of E_{max} is obtained for spherically blunted tangent ogive nose shape. The maximum value for it is around 3% larger than the one for initial aerial robot. This amount seems smaller but it is very advantageous for performance characteristics such maximum range, endurance and autonomous performance. In Figure 3 wind tunnel experiments for initial and optimum geometry is presented.



Figure 3. Wind Tunnel Test: (a) Spherically Blunted Tangent Ogive Nose

(b) Initial Nosecone

73. AUTOPILOT SYSTEM AND AUTONOMOUS PERFORMANCE EVALUATION

73.1. Autopilot System

For our both simulation environment (i.e. Matlab) study and real-time flight study conventional PID based hierarchical autopilot system is preferred (see [8] and [9]). In this structure three layers PID controller to accomplish waypoint navigation is used (see Figure 4). In Figure 5 more detailed version of PID-based hierarchical autopilot system is shown. In Figure 6 an Ardupilot equipped Zanka-II aerial robot is shown.

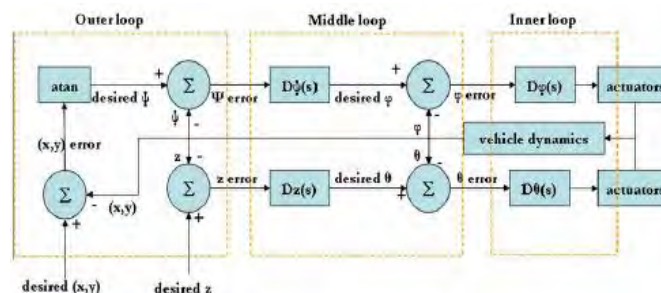


Figure 4. Hierarchical Autopilot System (taken from [9])

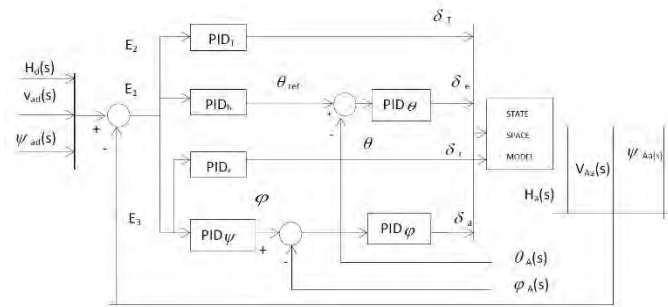


Figure 5. PID Based Autopilot Structure



Figure 6. Autopilot Equipment of ZANKA-II

73.2. Autonomous Performance Evaluation

In most general situation, PID-based hierarchical autopilot system lets height, yaw angle, and velocity trajectory tracking. This system had 6 P-I-D controllers inside of the 3 layers (outer, middle, inner). These PIDs have upper and lower constraints and let trajectory tracking. If any interested autopilot user requests to benefit from all of them, he/she needs to tune 18 parameters (i.e. 6 P parameters, 6 I parameters and 6 D parameters). Nevertheless, in this conference article for simultaneous morphing aerial robot and autopilot design strategy there are two additional structural parameters (optimum extension ratios of wing and horizontal tail). A cost function consisting of settling time, rise time and overshoot is reputable choice for high-performance trajectory tracking (see Eq. (1)).

$$J = \sum g(T_{st} - T_{st_u})^2 + g(T_{rt} - T_{rt_u})^2 + g(\%OS - \%OS_u)^2 \quad (1)$$

The simultaneous optimization problem can be described as follows:

$\min \{J\}$ where

$$J = f(x_w_{morph}, x_{ht}_{morph}, K_{P1}, K_{I1}, K_{D1}, K_{P2}, K_{I2}, K_{D2}, \dots, K_{P6}, K_{I6}, K_{D6}) \quad (2)$$

and it is function of 20 terms (2 aerial morphing parameters and 18 autopilot system design parameters). Terms of cost function is calculated in this conference article as below:

If $T_{st} \geq T_{st_u}$, T_{st} is non-defined else

$$T_{st} < T_{st_u}, T_{st} \text{ is its value} \quad (3)$$

If $T_{rt} \geq T_{rt_u}$, T_{rt} is non-defined else,

$$T_{rt} < T_{rt_u}, T_{rt} \text{ is its value} \quad (4)$$

If $\%OS \geq \%OS_u$, $\%OS$ is non-defined else

$$\%OS < \%OS_u, \%OS \text{ is its value} \quad (5)$$

The %3 improvement in maximum value of E_{max} causes around 2.1% improvement in autonomous performance. This amount may seem small. However, it is obtained with a very small modification in aerial robot geometry. In future it will be combined

with tail cone shape optimization in order to increase the amount of improvement in autonomous performance. In Figure 7 when Von Karman turbulence exists, trajectory tracking for aerial robot pitch angle is given and it is satisfactory.

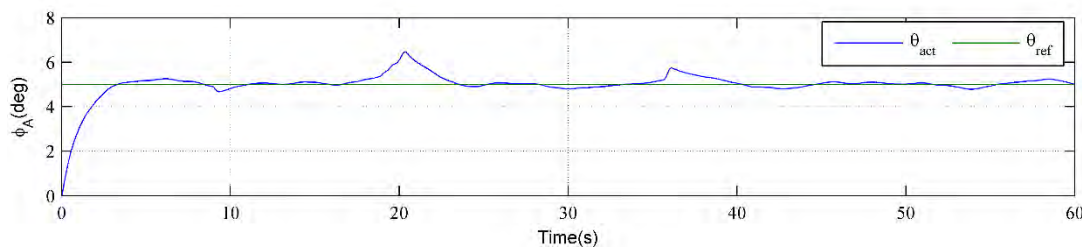


Figure 7. Trajectory Tracking for Resulting Aerial Robot

74. CONCLUSIONS

In order to improve flight performance of an autonomous aerial robot, aerodynamic nose shape optimization both experimentally and computationally was applied. Aerodynamic performance criteria (i.e. maximum fines) of a scaled model of our autonomous aerial robot called as Zanka-II produced in Erciyes University Faculty of Aeronautics and Astronautics Model Aircraft Laboratory was first observed in sub-sonic Wind Tunnel. Results obtained was validated using a computational fluid dynamics software (i.e. Ansys). Nose cone of fuselage was optimized in order to maximize maximum fines of our autonomous aerial robot by using Ansys. A novel scaled model using optimum data was then produced and placed in Wind Tunnel in order to validate Ansys results with experimental results. By using geometrical data of eventual aerodynamically optimized aerial robot, better autonomous flight performance was found both in simulation environment (i.e. Matlab) and real time flights.

A small increase (around %3) for the maximum value of fines is found via aerodynamic nose shape optimization for morphing autonomous aerial robot. A minor improvement (around %2.1) in autonomous performance is obtained.

ACKNOWLEDGEMENT

This work was supported by Research Fund of The Scientific and Technological Research Council of Turkey (TUBITAK) under Project Number: 214M282.

REFERENCES

- [136]. Austin, R., Unmanned aircraft systems, Wiley, 2010.
- [137]. Ding, Y., Liu, Y. C., and Hsiao, F. B., The application of extended Kalman filtering to autonomous formation flight of small UAV system. *Aircraft Engineering and Aerospace Technology*. 1(2), 154-186, 2013.
- [138]. Drak, A., Hejase, M., ElShorbagy, M., Wahyudie, A., & Noura, H., Autonomous Formation Flight Algorithm and Platform for Quadrotor UAVs. *International Journal of Robotics and Mechatronics*. 1(4), 124-132, 2014.
- [139]. Luca De Filippis, Giorgio Guglieri, Fulvia B. Quagliotti, A novel approach for trajectory tracking of UAVs. *Aircraft Engineering and Aerospace Technology: An International Journal*. 86 (3), 198 – 206, 2014.
- [140]. Hadi, G., Varianto, R., Trilaksono, B., and Budiyo, A., Autonomous UAV System Development for Payload Dropping Mission. *Journal of Instrumentation, Automation and Systems*. 1(2), 72-77, 2014.
- [141]. Xuetao, Z., UAV Design and Manufacture, BS Thesis, 2010.
- [142]. Lyu, Z., Kenway, G. K. W., Martins, J. R. R. A., Aerodynamic Shape Optimization Investigations of the Common Research Model Wing Benchmark. *AIAA Journal*, 2014.
- [143]. Jang, J. S., Liccardo, D., Automation of small UAVs using a low cost mems sensor and embedded computing platform, 2006.
- [144]. Chao, H., Cao, Y., and Chen, Y. Q., Autopilots for Small Fixed-Wing Unmanned Aerial Vehicles: A Survey. Paper presented at IEEE International Conference on Mechatronics and Automation, Harbin, China, 2007.

The Effect of Graphite Content on the Wear Behavior of ZA27/Al₂O₃/Graphite Hybrid Nanocomposites

Onur Güler^{1*}, Hamdullah Çuvalcı³⁸, Aykut Çanakçı¹, Müslim Çelebi¹

Abstract

ZA27 based hybrid composites with hard particles and dry lubricating particles can use for bearing applications with their good tribological properties instead of traditional bearing materials. In this study, the wear behavior of ZA27 based hybrid nanocomposites reinforced nano-graphite particles and hard nano-alumina (Al₂O₃) particles was investigated under dry sliding conditions. While the content of nano-alumina that is one of reinforced materials was selected in 4 vol. %, the contents of nano-graphite particles was determined in different volumes (%1-%2-%3 and %4). The effect of graphite content was studied on wear behavior under different sliding distance conditions. A block-on-disc sliding wear testing apparatus was used to carry out dry wear tests. The sliding distances was found to be significant parameter detecting effect of graphite content. The worn surfaces were investigated by scanning electron microscopy (SEM) and the wear mechanisms were identified. While the lowest wear loss was seen in hybrid nanocomposite with content of 4 vol. % graphite and 4 vol. % alumina, the highest wear loss was determined in ZA27. It was determined that abrasion is the dominant mechanism in all hybrid nanocomposites except for composite including 4 vol. % graphite and 4 vol. % alumina. However, the worn surface of the hybrid nanocomposite that is with content of 4 vol. % graphite and 4 vol. % alumina showed that adhesion is dominant as the wear mechanism.

Keywords: Alumina, graphite, hybrid nanocomposite, wear

75. INTRODUCTION

Zinc-aluminum (ZA) alloys are used for bearing applications and they can be used as matrix material in metal matrix composites because of their superior tribological properties. Besides, it has been known that they have lower melting point and better tribological properties than traditional bearing materials like brass, copper and bronze [1]. ZA alloys can be classified as ZA8, ZA12 and ZA27 alloys according to their aluminum content. ZA27 alloys have perfect bearing and wear resistance properties and they have the lowest density of the ZA alloys [2]. However, its mechanical properties deteriorate at temperatures up to 100 °C. This problem can be thermally solved with the hard ceramic particles reinforcement to ZA27 matrix [3].

Metal matrix composites (MMCs) have recently studied for their potential applications as engineering materials in the aerospace, automotive and power utility industries [4]. Particle reinforced ZA27 based composites with hard ceramic particles and solid lubricant graphite particles are widely used for a few applications such as pistons, engine bearings and cylinder liners [5]. Thus, these MMCs have a great number of advantages for tribological applications such as good wear resistance, light weight and low cost. Superior wear resistance of particle reinforced MMCs caused by the hard ceramic particle such as alumina that preserves the metal matrix wear-out failure and enhances mechanical properties of composite [6]. Besides, recent studies show that the particulate reinforced composites have inherent isotropic properties [7].

Recently, the reports show that nano-sized particulates reinforced composites exhibit better physical and mechanical properties in the composites. Because the unwished phases between matrix material and nano particulates are inhibited at low temperatures and nano particulates increase the hardness of composite to dispersive in the matrix uniformly [8].

The powder metallurgy method is used for producing MMCs conventionally but uniform distribution of reinforced materials is difficult with this technique. Therefore, an alternative method of MMCs production is high-energy milling before applying of hot pressing [9].

Although, the effect of nano-sized materials content on the wear behavior of ZA27 based hybrid nanocomposites and production method of these hybrid nanocomposites has been investigated in the past but that is, indeed, a little. Therefore, the aim of this

^{1*} Corresponding author: Karadeniz Technical University, Department of Metallurgical and Materials Engineering, 61040, Trabzon, Turkey. onurguler@ktu.edu.tr

¹ Karadeniz Technical University, Department of Metallurgical and Materials Engineering, 61040, Trabzon, Turkey. hcuvalci@ktu.edu.tr

¹ Karadeniz Technical University, Department of Metallurgical and Materials Engineering, 61040, Trabzon, Turkey. aykut@ktu.edu.tr

¹ Karadeniz Technical University, Department of Metallurgical and Materials Engineering, 61040, Trabzon, Turkey. muslimcelebi@ktu.edu.tr

study is to produce hybrid nanocomposites with mechanical alloying technique and to investigate effect of the nano graphite and nano Al₂O₃ ratio on tribological properties of hybrid nanocomposites of ZA27/Graphite/Al₂O₃ produced by mechanical alloying and hot pressing.

76. EXPERIMENTAL

Firstly, ZA27 matrix powder was produced from ZA27 alloy which was produced via casting by gas atomization method (İKİ-EL Metal Powder Company, Turkey). The ZA27 powder has density of 5 gr/cm³ and the chemical composition of that matrix powder (wt.) is 27.2 Al%, 2.01 Cu%, 0.02 Mg% and Zn (balance). The matrix powders that have the average size of 40.2 μm were obtained by sieving and nano-graphite and nano-alumina powders which have the average size of 100 nm were used as reinforcing materials (Grafen Chemical Industries Company, Turkey, %99.9 purity).

The hybrid nanocomposite powders which is with the ZA27 metal matrix powder and nano Al₂O₃ particulates (4 vol. %) and different content of nano graphite particulates (1, 2, 3 and 4 vol. %) were obtained by mechanical alloying method. As a reference sample, ZA27 powder was milled with nano graphite particulates content of 1 vol. % and nano-alumina particulates content of 4 vol. %, then entitled as SM1 (Table 1). 0.25 wt. % of methanol (Merck) was used as a process control agent (PCA) to minimize the agglomeration, excessive cold welding of ZA27 powders and sticking of powders on the wall of the vial. The mechanical alloying process was executed in a planetary ball-mill (Retsch PM 100) with evacuated and filled with argon gas vials to avoid oxidation during milling process. Ball milling was carried out with a rotation speed of 300 rpm and 5:1 was selected as ball-powder mass ratio for 8 h. The milling balls with a diameter of 10 mm and vials (125 ml) were made from tungsten carbide.

The produced hybrid nanocomposite powders by mechanical alloying were filled in a die in order to obtain wear test specimens. These specimens were shaped as bulk and the technical drawing of these samples was given in Figure 1. And after the specimens in the die were heated to 432 °C under vacuum and sintered at this temperature for 3 hours, they were pressed at a uniaxial pressures of 350 MPa constantly and the pressure and vacuum were not released until the die was cooled down to prevent the oxidation and formation of pores.

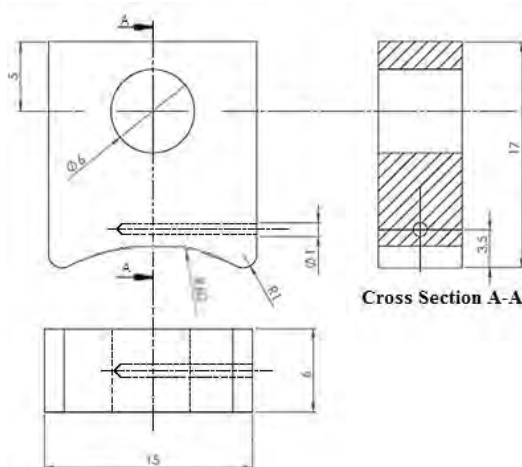


Figure 1. Technical drawing of the wear specimens which produced by hot pressing

After the samples that cutted out from the die, a hole in diameter of 6 mm was formed on each wear test samples to arrange these samples on the specimen holder in the wear test machine. Similarly, an inlet port of 1 mm in diameter was formed for temperature measurement by means of a thermocouple (Figure 1).

Hardness values of the samples was determined by the way of Brinell method using a 31.25 kg load and 15 s indentation time on the Brinell hardness machine and the hardened steel ball used in this process have diameter of 2.54 mm.

Table 1. The produced samples

Sample Number	Milling Time (h)	ZA27 (vol. %)	Al ₂ O ₃ (vol. %)	Graphite (vol.%)
SM0	0	100	0	0
SM1	8	Balance	4	1
SM2	8	Balance	4	2
SM3	8	Balance	4	3
SM4	8	Balance	4	4

Before the wear tests carried out, the surfaces roughness of the wear tests samples were controlled with a profilimeter (Mahr MarSurf PS1). The roughness test were done five times for each sample and average values were saved. The grinding processes were carried out for each sample to obtain the approximate roughness values on the surfaces of each sample. Then these surfaces were polished with alumina.

Morphologies of the powders including matrix and reinforcement materials was investigated by scanning electron microscopy (SEM). Moreover, the worn surfaces of the samples were studied in the SEM and the wear mechanisms of the samples were determined after the wear tests.

The tribological tests of the hybrid nanocomposites were performed using a computer-supported block-on-disc tribometer (Plint&Partners) which the schematic configuration is given in Figure 2 (a). The wear test samples were loaded on the steel disc during the wear tests (Figure 2 b). The counter disc was made of 4140 steel with hardness of 60 HRC and this rotational disc had diameter of 60 mm, width of 12 mm while the blocks (wear test samples) were made of the tested ZA27 and ZA27/graphite/Al₂O₃ hybrid nanocomposites. Previous to all tests, the disc and block surfaces were cleaned with acetone. All samples were weighed to an accuracy of 0.1 mg to determine the amount of wear losses before and after carrying out the wear tests. All dry sliding wear tests were done 2 times and then average of the results were noted. Wear tests were executed in dry conditions at applied load of 10 N, sliding speed was 0.3 m/s and variation of sliding distances of 565, 1130, 1695 and 2260 m.

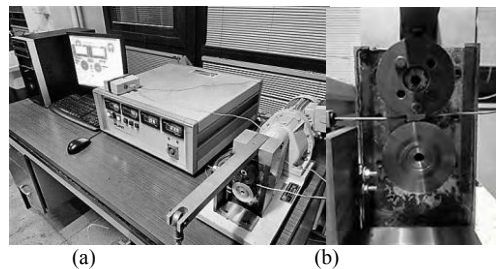


Figure 2. Image of the wear test apparatus; (a) the block-on-disc tribometer, (b) the close-up view of the disc and block

3. RESULTS

3.1. Morphology

Figure 3 shows morphologies of the ZA27 powder (a) which used as a matrix material in producing the hybrid nanocomposites, nano-graphite (b) and nano-alumina (c) powders used as reinforcement materials. As seen in figure, while morphology of as-received ZA27 powder is ligament, morphology of graphite particulates used as reinforcement material in hybrid nanocomposites is laminated and morphology of Al₂O₃ particulates which is another reinforcement material is spherical. As known, by reason of the graphite has a laminal structure, it is preferred as the solid lubricant while alumina is used to increase the mechanical properties of the materials owing to its hardness.

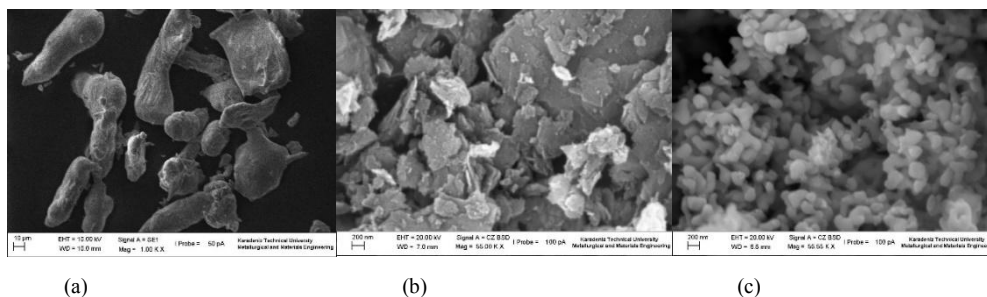


Figure 3. Morphology of as received powders (a) ZA27, (b) nano-graphite, (c) nano-alumina

3.2. Roughness values

It is shown that the roughness values of all contact surfaces were too different in Table 2. Therefore, the differences of roughness values were minimized to rubbing and polishing processes was performed to surfaces of the wear test samples, respectively. As a

result of this process, it has been understood that the differences of the roughness values of the wear test samples were minimized as given in Table 3.

Table 2. The roughness values of the samples after producing by hot pressing

Table 3. The roughness values of the samples after grinding and polishing processes

Sample	Ra(μm)
SM0	1,385
SM1	1,426
SM2	1,512
SM3	1,368
SM4	1,465

3.3. Hardness

Effect of the reinforcement content on Brinell hardness values is shown in Figure 4. According to data in this figure, the hardness is decreased with the increasing of graphite content for hybrid nanocomposites due to soft nature of graphite. It was determined that the Brinell hardness value unreinforced material (ZA27) is 125 HB and it is understood with reinforcing the hard nano-alumina particulates of the ZA27 matrix, the hardness is increased. As seen Fig. 4, ZA27 alloy has the lowest hardness value again because of the soft nature of structure and the graphite reinforcement in it provides characteristic of solid lubricating. Therefore, while nano-alumina particulates ensure improvement of the mechanical properties; the hybrid nanocomposite has good wear resistance owing to reinforcement of nano-graphite particulates.

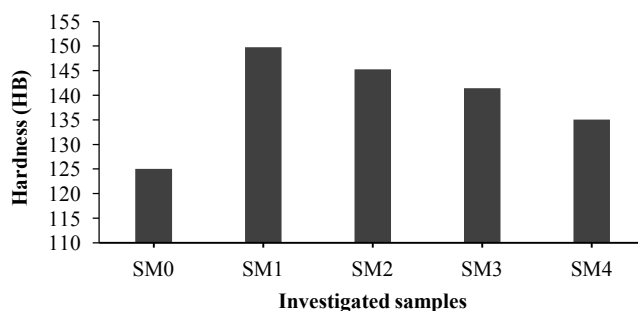


Figure 4. Hardness values of ZA27 and hybrid nanocomposites

3.4. Tribological properties

Figure 5 (a) shows the wear losses of ZA27 and hybrid nanocomposites under the load of 10 N and the sliding speed of 100 rev/min with the increase of the seen that the hybrid wear loss than ZA27 base material. approximately 2.5 times higher the end of sliding distance of 2260 resistance may be better with the the results in this work shows that exhibit the best wear resistance distance. Because, the graphite SM4 improve the wear properties of this hybrid nanocomposite with the character of solid hardness value. Moreover, in the end of sliding distance of 565 m, it is understood that SM1 hybrid nanocomposite have the best wear resistance but with the lengthening out of distance, the wear loss increase more than the other hybrid nanocomposites. As a result of this situation, it can be said that with the lengthening the distance, abrasion affects the wear loss because of hard nano-alumina content in hybrid nanocomposite.

Sample	Ra(μm)
SM0	5,343
SM1	4,872
SM2	4,028
SM3	3,196
SM4	2,935

sliding distances conditions. It is nanocomposites presented lower The wear loss of the ZA27 is than SM4 hybrid nanocomposite in m. It can be seen that the wear increase of material hardness. But, the material has the lowest hardness with the increase of sliding particulates with 4 vol. % in the

Figure 5 (b) shows effect of graphite content on wear behavior according to sliding distance under load of 10 N and sliding speed of 100 rev/min. As seen in this figure, the values of the friction coefficients increase with the lengthening of sliding distance for all samples which are tested and the optimum values of friction coefficient belong to SM4 material. It can be said that this effect

is resulted from by nano-graphite particulates which is expanded on the sliding surfaces of the sample during the test. On the other hand, the highest values of the coefficients are seen on the ZA27 base material and the value of friction coefficient which is measured from SM4 in the end of the longest distance (2260 m) is about 2 times lower than the ZA27 that is unreinforced material.

The temperature values on all the samples which tested under 10 N and 100 rev/min test conditions are shown in Figure 5 (c) and 22 °C is determined as the initial temperature. As demonstrated in the figure, the temperature increase during the wear tests in all samples with the distance lengthens out. However, all the hybrid nanocomposite materials have the lower temperatures than the ZA27 sample under the all distances conditions. Besides, as seen in graph, the temperature increases less with the nano-graphite content raise. It can be considered that the samples which relate the lower values of friction coefficient exhibit the lower values of the temperature due to the fact that the lines on the temperature graph and the lines on the friction are same character. Because, when the friction force is lower between the disc and the block samples, the temperature increase less. Shortly, the optimum values for tribological properties among all the samples tested is seen on the SM4 including 4 vol. % nano-graphite and 4 vol. % nano-alumina.

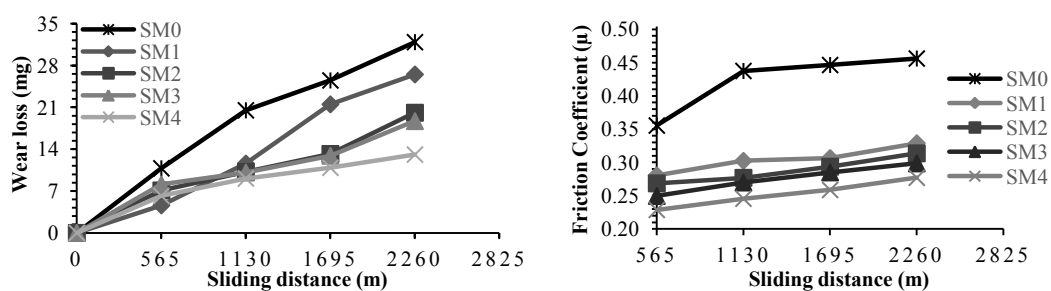
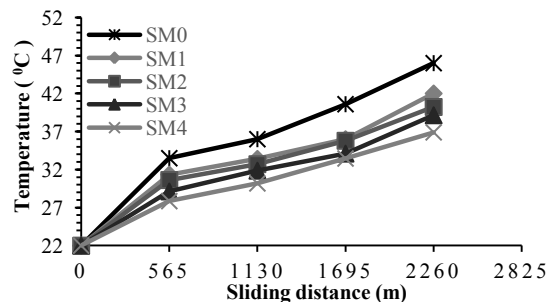


Figure 5. (a) Wear losses of ZA27 and hybrid nanocomposites (b) Friction coefficients of ZA27 and hybrid nanocomposites under 10N and 100 rev/min



(c) Temperature values of ZA27 and hybrid nanocomposites under 10 N and 100 rev/min

3.5. Wear Mechanisms

The obtained worn surfaces of ZA27 and all the hybrid nanocomposites tested under the load of 10 N, the sliding speed of 100 rev/min and the different sliding distances by a scanning electron microscopy (SEM) is exhibited in Figure 8. Firstly, it is seen that the worn surfaces of all the hybrid nanocomposites appeared smoother than the worn surface of the ZA27 base material (SM0). Figure 8 (a) shows the worn surface of the SM0 and as seen in that figure, plastic deformation with delamination and pits occurred on the surface in the end of the long distance due to the softness of SM0. Besides, the parallel narrow grooves can be seen over this surface. On the other hand, softening of the SM0 and existing of adhesive wear is seen due to the decrease of the yield strength with the increase of temperature during the test. In the event of SM1, the mechanism is changed by reinforcing 4 vol. % nano-alumina and 1 vol. % nano-graphite as seen in Figure 8 (b). The adhesive wear is transformed to the abrasive wear with ploughing grooves because of hard nano-alumina particulates at the contact region. The existed of uninterrupted and deep grooves shows that the dominant wear mechanism is abrasion. The worn surface of SM2 is shown in Figure 8 (c). It can be understood that the SM2 has the smoother worn surface, leading to the lower wear loss by comparison with the worn surface of SM1. The increase of nano-graphite content (2 vol. %) hinder the deep grooves in this material (SM2) because of lubricative effect of graphite particulates. However, the abrasive grooves and the cracks at the edge of these grooves are still seen on the worn surface. Moreover, the spalls as a result of adhesive wear are observed at the contact area. Figure 8 (d) shows the worn

surface of SM3 which has 4 vol. % nano-alumina and 3 vol. % nano-graphite. By the increase of graphite content, it is seen that the grooves which is seen on the worn surface of SM1 and SM2 narrow and they occur as shallow continuously. In addition to that, hard debris particles observed in contacting surface and these hard debris cause the abrasive wear. The worn surface of SM4 which has the highest wear resistance among the tested samples in Figure 8 (e). It can be understood that the increase of graphite content from 3 vol. % to 4 vol. % hinders the abrasion on the contact region and the wear mechanism transforms to adhesive and delamination in this figure. Furthermore, the debris particles which break loose from delamination craters can be seen on the worn surface. In spite of the hardness value of SM4 is the lowest when compared with the other tested materials, the wear resistance is the highest. Although the pits exist on the worn surface due to softness of the structure, these pits may be filled by layer of mixed matrix, nano-graphite and nano-alumina particulates with continuation of the wear tests. It can be considered that the graphite particulates provide lower friction coefficient between the disc and the block samples during the tests, while the hard ceramic particulates (Al_2O_3) protect the soft ZA27 matrix and it can be seen that the optimum values are with content of 4 vol. % alumina and 4 vol. % graphite particulates for the best wear resistance of ZA27/graphite/ Al_2O_3 hybrid nanocomposites at the long distances.

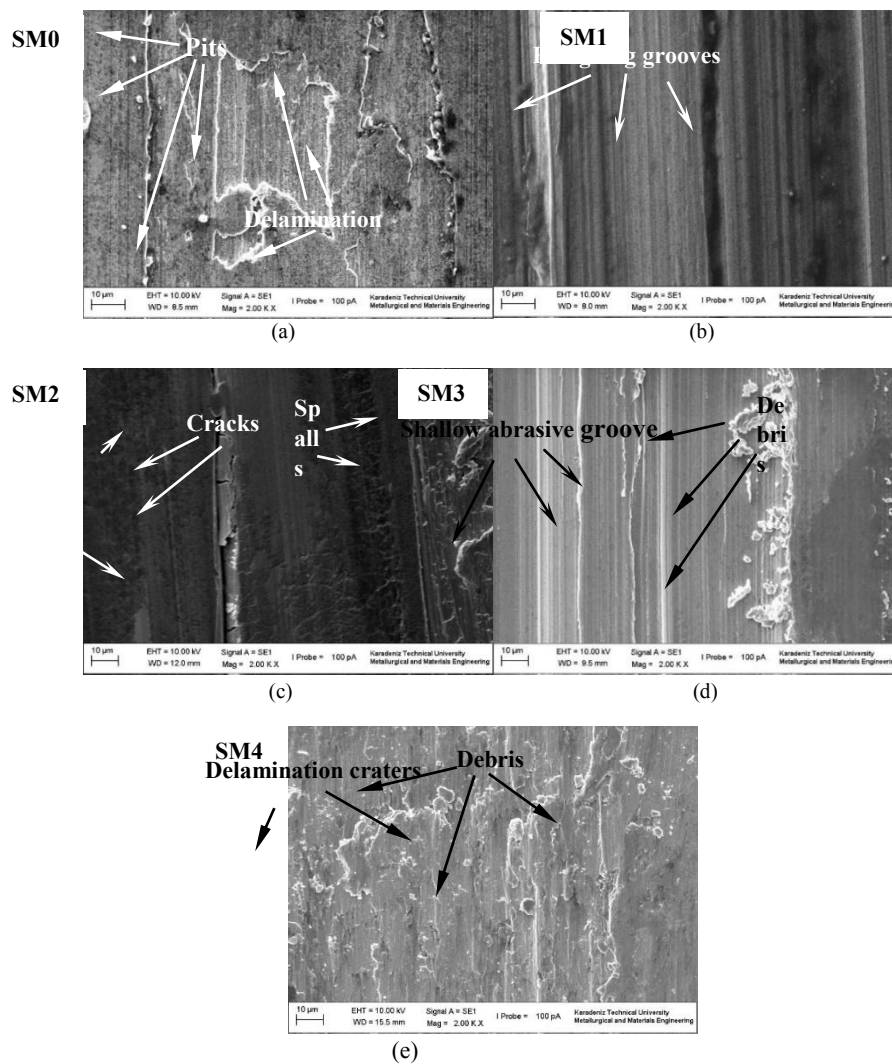


Figure 8. SEM images of worn surfaces of base material and hybrid nanocomposites under magnification of 2000 X; (a) SM0, (b) SM1, (c) SM2, (d) SM3 and (e) SM4

4. CONCLUSIONS

1. The hardness value of SM0 (ZA27) have been improved with reinforcing the nano-alumina content of 4 vol. % and nano-graphite content of 1, 2, 3, vol. % owing to high hard nano-alumina particulates but for higher nano-graphite content, it has decreased due to softness and laminated structure of graphite particulates.
2. All the hybrid nanocomposites have had the higher wear resistance than ZA27 base material at the long distances.
3. During the tests for long distances, the wear resistance of ZA27 based hybrid nanocomposites have increased with the increasing of nano-graphite particulates at the long distances and the best wear resistance belong to the based hybrid nanocomposite with 4 vol. % nano-alumina and 4 vol. % nano-graphite particulates.
3. The friction coefficient values of the tested materials have been in proportion with the wear resistance of these materials. In other words, while ZA27 (SM0) have exhibited the highest friction coefficient value during the tests, SM4 (ZA27/ 4 vol. % nano-alumina/ 4 vol. % nano-graphite) have presented the lowest value of friction coefficient at the same conditions because of lubricative character of graphite particulates.
4. The lowest values of sample temperature have been observed on the SM4 depending on friction coefficient of that sample.
5. While the nanocomposite with nano-alumina content of 4 vol. % and nano-graphite content of 4 vol. % (SM4) which has improved wear resistance have shown adhesive wear mechanism without pits or grooves, the other hybrid nanocomposites have exhibited the abrasive wear mechanism because of the hard nano-alumina particles. Therefore, it has been seen that the hybrid nanocomposites with 4 vol. % nano-alumina and 4 vol. % nano-graphite (SM4) can be great choice to get improved wear resistance for long distances because it has optimum values of contents for ZA27 base material.

ACKNOWLEDGMENT

This study was supported by ‘Scientific and Technological Research Council of Turkey’ 1001 project entitled ‘The improving of nanoparticle reinforced Zn-Al based nano-composite materials by mechanical alloying method, the investigation of their microstructure-mechanical and tribological properties’. (Project no: 213M276)

REFERANCES

- [1]. Guler O., Cuvalci H., Celebi M., Canakci A., “The Effect of Al₂O₃ Content on The Wear Behavior of ZA27/Al₂O₃/Graphite Hybrid Nanocomposites,” in *Proc. KOMPEGE’15*, p. 558-569.
- [2]. Girish B.M., Prakash K.R., Satish B.M., Jain P.K., Devi K., Need for Optimization of Graphite Particle Reinforcement in ZA27 Alloy Composites for Tribological Applications, *Material Science and Engineering A*, pp. 382-388, 2011.
- [3]. Abou El-Khair M.T., Lotfy A., Daoud A., El-Sheikh A.M., Microstructure, Thermal behavior and Mechanical Properties of Squeeze Cast SiC, ZrO₂ or C Reinforced ZA27 Composites, *Material Science and Engineering A*, pp. 2353-2362, 2010.
- [4]. Sharma S. C, Girish B. M, Kamath R, Satish B. M, Effect of SiC Particle Reinforcement on the Unlubricated Sliding Wear Behaviour of ZA27 Alloy Composites, *Wear*, pp. 33-40, 1997.
- [5]. Celebi M., Cuvalci H., Canakci A., Guler O., Karabacak A.H., Microstructural Evolution and Mechanical Properties of ZA27 Alloys Reinforced by Nano-graphite and Nano-alumina, in *Proc. KOMPEGE’15*, p. 400-407.
- [6]. Kok O., Ozdin K., Wear Resistance of Aluminum Alloy and Its Composites Reinforced by Al₂O₃ Particles, *Journal of Materials Processing Technology*, pp. 301-309, 2006.
- [7]. Deaquino-Lara R., Soltani N., Bahrami A., Gutierrez-Castaneda E., Garcia-Sanchez E., Hernandez-Rodriguez M.A.L., Tribological Characterization of Al7075-Graphite Composites Fabricated by Mechanical Alloying and Hot Extrusion, *Materials and Design*, pp. 224-231, 2014.
- [8]. Aahamed H., Senthilkumar V., Consolidation Behavior of Mechanically Alloyed Aluminum Based Nanocomposites Reinforced with Nanoscale Y₂O₃/Al₂O₃ Particles, *Materials Characterization*, pp. 1235–1249, 2011.
- [9]. Ravindran P., Manisekar K., Vinoth Kumar S., Rathika P., Investigation of Microstructure and Mechanical Properties of Aluminum Hybrid Nano-composites with the Additions of Solid Lubricant, *Materials and Design*, pp. 448-456, 2013.

BIOGRAPHY

Onur Güler received his metallurgical and materials engineer MSc degree in January, 2016 in Karadeniz Technical University (KTU) in Trabzon, Turkey. He is a PhD student at the department of Metallurgical and Materials Engineering in KTU in Trabzon, Turkey. His researches include composite materials, powder technology and mechanical alloying.

The Effect of Nano-Particle Content on the Wear Behavior of ZA27/ Al_2O_3 Nanocomposites

Onur Güler^{1*}, Hamdullah Çuvalcı³⁹, Müslim Çelebi¹, Aykut Çanakçı¹

Abstract

In this study, the effects of volume fraction of nano- Al_2O_3 on the abrasive wear properties of Al_2O_3 nano-particle reinforced ZA27 alloy metal matrix nanocomposites produced by mechanical alloying and hot pressing method have been studied. The density, porosity and hardness of nanocomposites were also examined. Wear behaviour of Al_2O_3 nano-particle reinforced ZA27 alloy metal matrix nanocomposites was investigated by a block-on-disc abrasion test apparatus under unlubricated conditions. The effects of sliding time and the content of Al_2O_3 nano-particles on the abrasive wear properties of the nanocomposites have been evaluated. The dominant wear mechanisms of nanocomposites were identified using SEM. It was found that the density decreased with increasing reinforcement volume fraction but the porosity and hardness increased with increasing nano-particle content. Moreover, The wear resistance of the all composites was found to be considerably higher than that of the ZA27 matrix alloy. The wear loss of composite increased with increasing nano-particle volume fraction after Al_2O_3 nano-particles reinforcement content of 1 vol. %. Furthermore, it was understood that the main wear mechanisms of ZA27 are adhesive and delamination while the dominant wear mechanism of Al_2O_3 /ZA27 nanocomposites is abrasive.

Keywords: Alumina, nanocomposite, ZA27, mechanical alloying, wear

77. INTRODUCTION

Metal matrix composites (MMCs) are made by dispersing ceramic reinforcements into a metal matrix. MMCs have become the desirable materials in engineering applications like aerospace, marine, automobile and turbine-compressor engineering applications due to their higher specific modulus and strength, higher thermal stability and higher wear resistance in comparison with monolithic metals or alloys [1-5]. Fabrication process, the volume fraction and particle size of the reinforcement and bonding between the matrix phase and the reinforcement phase of the composite effect these properties [6-8]. Much researcher works have been focused on the ceramic reinforced aluminium matrix composites [9]. There is also an increasing demand in using ceramic reinforced zinc matrix composites. Zinc-aluminium (ZA) alloys exhibit an exceptional combination of properties such as excellent castability, low melting point, high strength and equivalent or often superior bearing

properties as compared to standard bronze bearings. Accordingly, they have been used as alternative materials to some of aluminium casting alloys, bearing bronzes and cast iron. Amongst the family of ZA alloys used as matrix materials, ZA27 (Zn-27wt.% Al) alloy has been particularly popular during recent years. ZA27 exhibits good physical, mechanical and tribological properties, and hence it is commonly used as foundry alloy in a variety of engineering applications [10-12].

Alumina, silicon carbide, mica, zircon and graphite are used as reinforcement materials into ZA27 matrix. Among all the ceramics, alumina (Al_2O_3) is one of the frequently used ceramic reinforcement. Al_2O_3 exhibits high values of hardness, compressive strength, wear resistance, thermal and chemical stability and elastic modulus. Moreover, it does not react with the matrix at high temperatures and does not create undesired phases [13,14].

Mechanical alloying (MA) is one of the important methods in powder metallurgy because of the high flexibility, simple control of process parameters and ability to fabricate a wide spectrum of materials [15-16]. The easy control and ability to produce nanocrystalline materials makes this method effective for the powder metallurgy of nanoscale and ultra-dispersed material [17]. In this technique, powder particles are being milled using ball collisions which obtain very fine particle size and homogenous distribution. MA is known as a useful method for developing the reinforcement particle distribution not only in composites but also in nanocomposites [18,19].

^{1*} Corresponding author: Karadeniz Technical University, department of metallurgical and materials engineering, 61040, Trabzon, Turkey. onurguler@ktu.edu.tr

¹ Karadeniz Technical University, Department of Metallurgical and Materials Engineering, 61040, Trabzon, Turkey. hcuvalci@ktu.edu.tr

¹ Karadeniz Technical University, Department of Metallurgical and Materials Engineering, 61040, Trabzon, Turkey. muslimcelebi@ktu.edu.tr

¹ Karadeniz Technical University, Department of Metallurgical and Materials Engineering, 61040, Trabzon, Turkey. aykut@ktu.edu.tr

The present research work is primarily aimed to study and investigate the synthesis, characterization and mechanical properties of Al₂O₃ particle reinforced ZA27 matrix nanocomposites via MA followed by the hot pressing technique. The effects of various Al₂O₃ content (vol.%) on the mechanical properties and wear behaviour of ZA27/Al₂O₃ nanocomposite have also been investigated.

78. EXPERIMENTAL

In this study, ZA27 alloy powders (d_{50} :40.2 μ m, İKİ-EL Metal Powder Company, Izmir, Turkey) with the theoretical density of 5 g/cm³ was used as the matrix material, while Al₂O₃ particles (d_{50} :100 nm, Grafen Chemical Industries Company, Ankara, Turkey) with the density of 3.95 g/cm³ were used as the reinforcement. The chemical composition (in wt%) of the ZA27 alloy was as follows: 27.2 Al%, 2.01 Cu%, 0.02 Mg%, with the balance being Zn.

The nanocomposite powders which is with the ZA27 metal matrix powder and different content of nano-Al₂O₃ particles (1, 2, 3 and 4 vol. %) were obtained by mechanical alloying method. The mechanical alloying (MA) process was conducted in a planetary ball mill (Retsch PM 100) at the room temperature. The ZA27 and nano-Al₂O₃ powders were milled for 8 h with following parameters: ball-to-powder weight ratio: 5:1; ball diameter: 10 mm; speed: 300 rpm. The mixed powders were loaded into a steel die, cold pressed at 175 MPa and then hot-pressed for 3 h at 432^oC at pressure of 350 MPa.

Brinell hardness values (HB) were measured on the polished samples using a ball with 2.5 mm diameter at a load of 62.5 kg. Morphologies of the powders and the worn surfaces of the samples was investigated by scanning electron microscopy (SEM) and the wear mechanisms of the samples were determined after the wear tests.

Before the wear tests carried out, the surfaces roughness of the wear tests samples were controlled with a profilimeter (Mahr MarSurf PS1). The roughness test were done five times for each sample and average values were saved. The grinding processes were carried out for each sample to obtain the approximate roughness values on the surfaces of each sample. Then these surfaces were polished with alumina.

The wear tests of the nanocomposites were performed using a computer-supported block-on-disc tribometer (Plint&Partners). The wear test samples were loaded on the steel disc during the wear tests. All samples were weighed to an accuracy of 0.1 mg to determine the amount of wear losses before and after carrying out the wear tests. Wear tests were executed in dry conditions at applied load of 10 N, sliding speed was 0.3 m/s and variation of sliding distances of 565, 1130, 1695 and 2260 m.

Table 1: Some properties of the ZA27 and ZA27/Al₂O₃ nanocomposite samples

Code	Composition	Theoretical density (g.cm ⁻³)	Experimental density (g.cm ⁻³)	Porosity (%)
SM0	ZA27 (unreinforced, unmilled)	5	4,89	2,20
SM1	ZA27-1 vol.% Al ₂ O ₃	4,99	4,80	3,80
SM2	ZA27-2 vol.% Al ₂ O ₃	4,98	4,75	4,60
SM3	ZA27-3 vol.% Al ₂ O ₃	4,97	4,74	4,60
SM4	ZA27-4 vol.% Al ₂ O ₃	4,96	4,69	5,41

3. RESULTS

3.1. Density and Porosity

The theoretical and experimental densities and porosities of ZA27/Al₂O₃ nanocomposites according to the volume fractions of nano-Al₂O₃ particles are shown in Table 1. The results show that the theoretical density values of the composites decrease linearly (as expected from the rule of mixtures). Although a linear decrease can be also seen in the experimental densities, the values are lower than those of the theoretical ones. The results show that the experimental density of ZA27/Al₂O₃ nanocomposites decreased with increasing nano-Al₂O₃ particle volume fraction. This is because the densities of nano-Al₂O₃ particles is lower than that of ZA27 alloy matrix powders. The density measurements show that nanocomposites contain some porosity, and the amount of porosity in the nanocomposites increased with the increasing volume fraction of nano-Al₂O₃ particles.

3.2. Roughness values

It is shown that the roughness values of all contact surfaces were too different in Table 2. Therefore, the differences of roughness values were minimized to rubbing and polishing processes was performed to surfaces of the wear test samples, respectively.

Table 2. The roughness values of the samples after producing by hot pressing

Sample	Ra(μm)
SM0	5,245
SM1	4,678
SM2	5,102
SM3	2,978
SM4	3,985

Table 3. The roughness values of the samples after grinding and polishing processes

Sample	Ra(μm)
SM0	1,263
SM1	1,137
SM2	1,298
SM3	1,431
SM4	1,178

3.3. Hardness

The relation between the nanoparticle volume fraction and the Brinell hardness values of ZA27 (unreinforced) and ZA27/Al₂O₃ nanocomposites is plotted in Fig.5. As seen in Fig. 1, the hardness values of ZA27/Al₂O₃ nanocomposites were higher than that of ZA27 alloy matrix simple. Moreover, the hardness of the nanocomposites increased with increasing nano-Al₂O₃ particle volume fraction (Fig.5). This can be attributed to the number of particles in the nanocomposite powder mixture. The presence of hard Al₂O₃ particles enhanced the work hardening rate of the matrix resulting in an increase in hardness. The hardness of SM4 simple was 172 HB that was the highest hardness value.

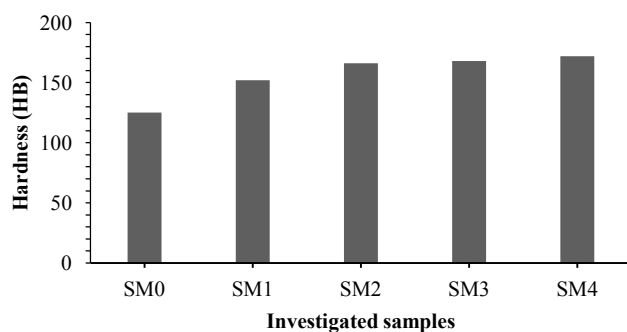


Figure 1. Hardness values of ZA27 and ZA27/Al₂O₃ nanocomposites.

3.4. Tribological properties

Fig. 2 shows the wear losses of ZA27 and nanocomposites under the load of 10 N and the sliding speed of 250 rev/min with the increase of the sliding distances conditions. It is seen that the nanocomposite samples presented lower wear loss than ZA27 base material. The wear loss of the ZA27 is almost the same with SM4 nanocomposite in the all sliding distances. The excessive increase in hardness have a negatively effect on the wear resistance of nanocomposites. The results shows that nanocomposite had the lowest hardness exhibits the best wear resistance with the increase of sliding distance. Moreover, in the end of sliding distance of 565 m, it is understood that SM1 nanocomposite have the best wear resistance but with the lengthening out of distance, the wear loss increase more than the other nanocomposites. As a result of this situation, it can be said that with the lengthening the distance, abrasion affects the wear loss because of hard nano-alumina content in nanocomposite.

Figure. 3 shows effect of nano-Al₂O₃ content on wear behavior according to sliding speed under load of 10 N and sliding distance of 565 m. From the figure it can be easily seen that the wear loss of all specimens increased at the beginning of the test. After reaching a maximum point the wear losses decreased with sliding speed. Minimum wear loss was observed SM1 simple at sliding speed of 250 rev/min.

The comparative wear loss of the tested alloys as a function of the normal load is presented in Fig. 4. One can notice that for all the test alloys, the intensity of wear increases with the increase of the normal force. However, the gradient of that increase is not the same for all the alloys. The lowest increase corresponds to the SM1. This is due to the fact that Al₂O₃ particles play an important role of the load carriers. However, it can be seen that when the particle content increased after reinforcing content of 1 vol. % Al₂O₃, the wear loss of nanocomposites are increased. This is due to the excessive increase of material hardness. The presented dependencies of the wear loss on the normal load clearly show that in the whole range of load, the wear loss of SM1 is significantly lower as compared to that of the others.

Also, from Figure. 3 and 4 it can be clearly seen that sensitivity of composites to variation of the normal load and sliding speed decreases with the increase of the Al₂O₃ reinforcing particles content. The graphs also suggest that composite specimens

exhibited almost lower wear loss than the ZA27 matrix alloy specimen in all combinations of applied loads and sliding. The difference in the wear resistance of composites with respect to the matrix alloy increased with the increase of applied load and decrease of the sliding speed.

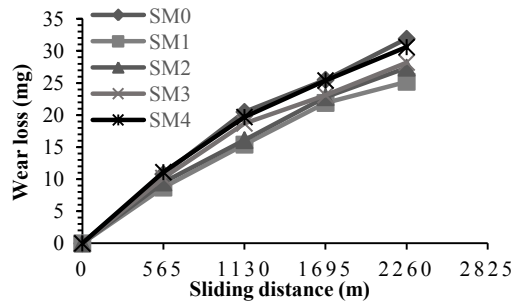


Figure 2. The effect of sliding distance on the wear loss of ZA27 and nanocomposites under 10 N and 250 rev/min

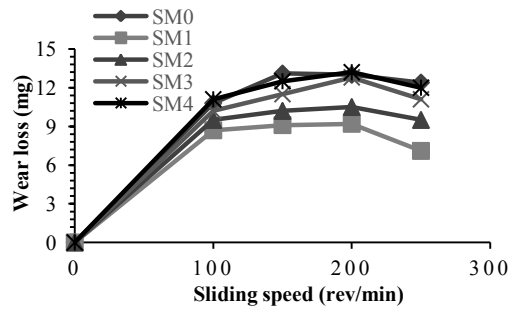


Figure 3. The effect of sliding speed on the wear loss of ZA27 and nanocomposites under 10 N and 565 m

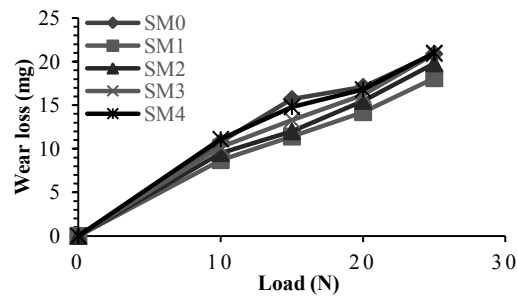
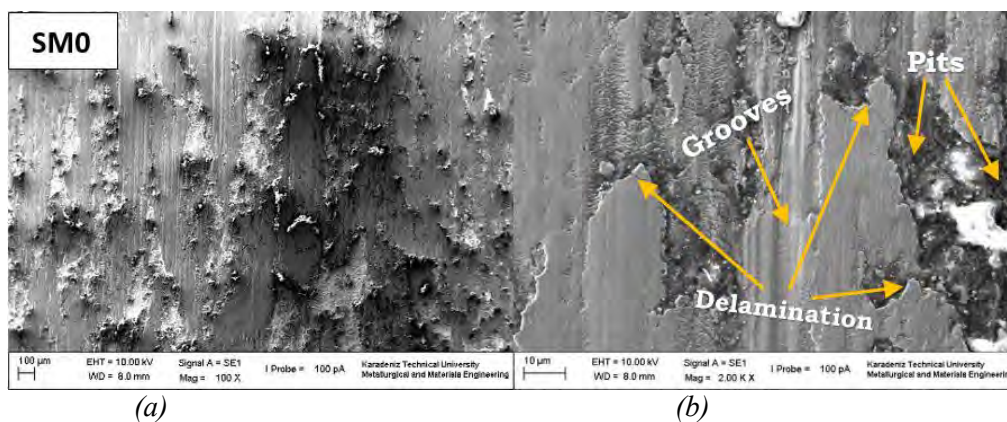


Figure 4. The effect of load on the wear loss of ZA27 and nanocomposites under 565 m and 250 rev/min

3.5. Wear Mechanisms

The worn out surfaces of ZA27 and $\text{Al}_2\text{O}_3/\text{ZA27}$ nanocomposites is shown in Fig 5. The wear surfaces obtained under the load of 10 N, the sliding distance of 565 m and the sliding speed of 250 rev/min were investigated in a scanning electron microscopy (SEM). As seen in Figure 5 (a,b), the worn surfaces of ZA27 (SM0) showed a little abrasive grooves. But the morphological patterns have dominant delamination and pits. Moreover that behavior has been stimulated the plastic deformation on the wear surface. So it has been understood that the main wear mechanism of this sample is delamination and adhesive. The worn surface of SM1 (ZA27-%1 vol. Al_2O_3) openly shows the existence of the permanent and shallow grooves caused from the abrasive behavior because of hard alumina content (Figure 5 c,d). But the worn surface of this sample looks smoother than the SM0 because delamination mechanism and plastic deformation is not effective like in SM0. Moreover, this wear surface has the smoothest surface among the worn surfaces of the all samples performed the wear tests. SM1 has had the best wear performance already because the hard alumina particulates provide the hardness value that is higher than ZA27 matrix alloy. On the other hand, Figure 5 (e,f) exhibits that the worn surface of SM2 (ZA27-%2 vol. Al_2O_3) has heavier deformation than SM1 because of sticking debris and smearing the material on the surface during the test performed under high sliding speed. The ploughing and smearing behaviors on the surface of this sample cause the high amount of the wear loss than SM1. SEM images of the wear surface of nanocomposite with content of %3 vol. alumina are shown in Figure 5 (g,h). as understood in that figure, the content of the hard alumina particulates affect the wear resistance adversely. In that the friction coefficient increases during the tests due to the hard particulates during the wear tests and therefore, the temperature also rises with the increase of the friction between the disc and the surface of sample. For this reason, the matrix alloy made from ZA27 that is a soft material damages with the increase of the temperature during the wear tests. Besides, the porosity rise with the increase of the content of alumina in the ZA27 matrix alloy. So, hard alumina particulates can not embed in the matrix alloy and can take out because of sliding the disc on the wear surface. On the other hand, when the hardness of the samples exceed the optimum values, the wear losses can be increase too due to the failure of bonding between the ZA27 matrix and reinforcement material. Subsequently, these particulates can be fracture and smear on the wear surface with the effect of the sliding disc under high temperature for the wear tests. Moreover, it can be see that the fracture particles existed on the surface due to surplus of the content of nano-alumina in the matrix material stick and smear on the wear surface during the test under high sliding speed condition. Figure 5 (i,j) shows the worn surface of the nanocomposite sample (SM4) with ZA27 matrix and %4 vol. alumina. In this figure, it is understood that the wear debris and cracked particles emerge the hard nano-alumina particulates in the matrix cause the highest value of the hardness of nanocomposite material and in the other hand, it causes the heaviest abrasive wear among the other nanocomposite materials performed the tests.



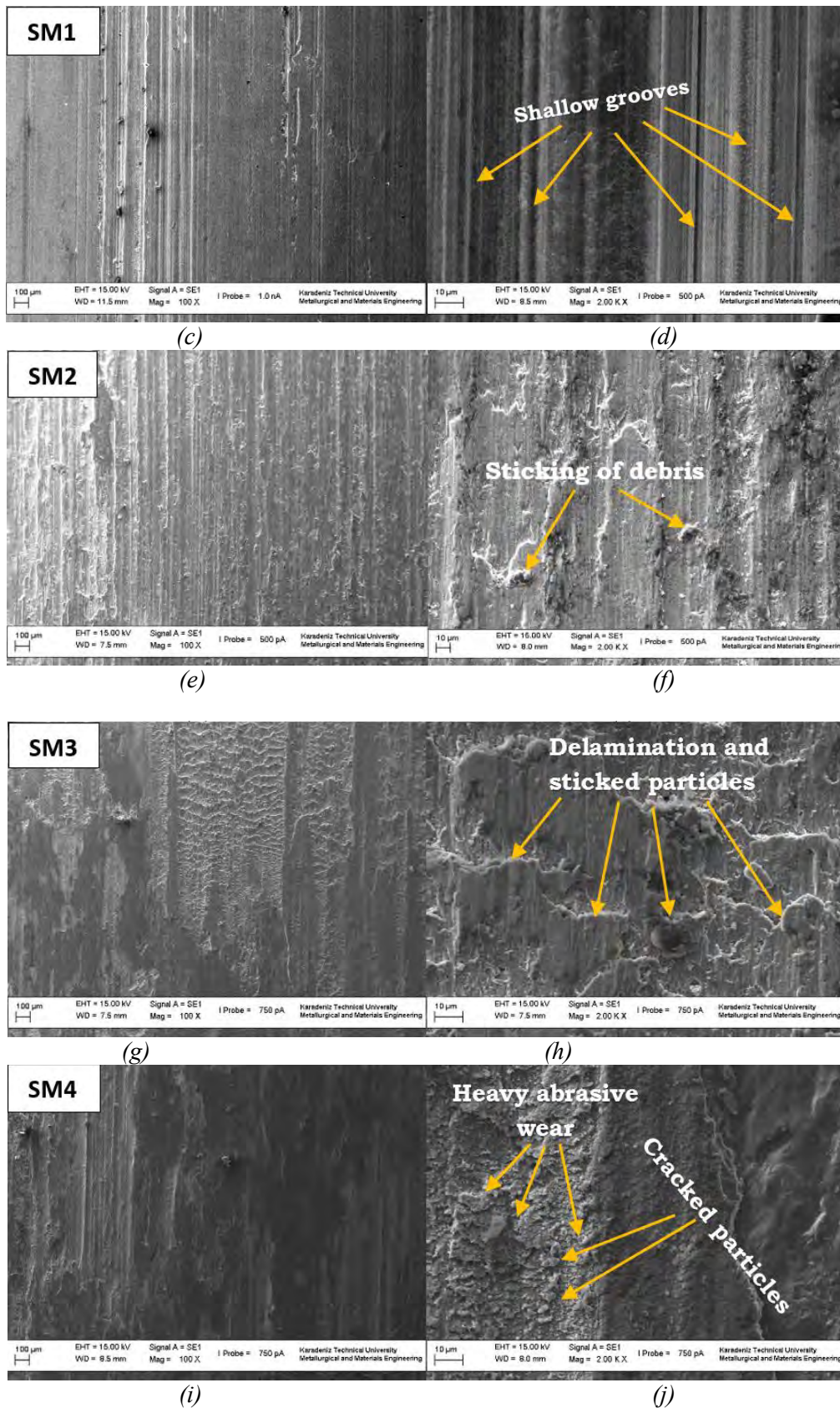


Figure 5. SEM images of worn surfaces of base material and hybrid nanocomposites under magnification of 100X and 2000X; (a,b) SM0, (c,d) SM1, (e,f) SM2, (g,h) SM3 and (i,j) SM4

4. CONCLUSIONS

1. The highest hardness value belongs to the SM4 because of its high content of hard nanoalumina particulates.
2. The mechanical alloying method can be used for the production of ZA27 based nanocomposite material
3. SM4 has the highest porosity and the lowest density values because it has the maximum content among the other nanocomposites.
4. All of the nano-composites applied the wear tests in this study show the lower wear losses than the ZA27 matrix material.
5. SM1 has the most improved wear resistance under the all wear test conditions.
6. With the reinforce of alumina content in the ZA27 matrix material, wear loss decrease but when this content of alumina is higher than %1 vol., the wear loss of nanocomposites increase because of the increase of porosity and the decrease of density in the structure.
7. The nanocomposite samples demonstrate abrasive wear due to hard alumina particulates while the matrix material exhibit delamination and adhesive wear mechanism.

ACKNOWLEDGMENT

This study has been supported by ‘Scientific and Technological Research Council of Turkey (TUBITAK)’ 1001 project numbered 213M276 titled ‘The improving of nanoparticle reinforced Zn-Al based nano-composite materials by mechanical alloying method, the investigation of their microstructure-mechanical and tribological properties’.

REFERANCES

- [1] Ibrahim, I.A., Mohamed, F.A. and Lavernia, E.J., Metal matrix composites—a review, *J. Mater. Sci.*, pp. 1137–1157, 1991.
- [2] Sinclair, I. and Gregson, P.J., Structure performance of discontinuous metal matrix composites. *Mater. Sci. Technology*, pp. 709–715, 1997.
- [3] Goni, J., Mitxelena, I. and Coletto, J., Development of low cost metal matrix composites for commercial applications, *Mater. Sci. Technol.*, pp. 743–746, 2000.
- [4] X.Z. Kai, Z.Q. Li, W.L. Zhang, G.L. Fan, L. Jiang, W.J. Lu. and D. Zhang, *Mater. Sci. Eng.*, pp. 574–579, 2011.
- [5] Y.F. Hua, L.T. Zhang, L.F. Cheng, Z.X. Li. and J.H. Du, *J. Mater. Sci.*, pp. 392–398, 2010.
- [6] E.J. Wentzel and C. Allen, Erosion–corrosion resistance of tungsten carbide hard metals with different binder compositions, *Wear*, pp. 63–69, 1995.
- [7] R. Cooper and D. McHattie, *Using Powder Metallurgy in Design: Wear, Corrosion and Fatigue Resistance*, vol. 5 Institution of Mechanical Engineers Seminar Publication, pp. 19–37, 2000.
- [8] K. Anand, H. Conrad, Microstructure effects in the erosion of cemented carbides, *Wear Mater.*, pp. 136–142, 1989.
- [9] A. Canakci, T. Varol, F. Erdemir, and S. Ozkaya, New Coating Technique for Al–B4C Composite Coatings by Mechanical Milling and Composite Coating, *Powder Metallurgy and Metal Ceramics*, pp. 11–12, 2015.
- [10] Smith, W., *Structures and Properties of Engineering Alloys*, 2nd edition, McGraw-Hill, New York, 1993.
- [11] B.K. Prasad, A.H. Yegneswaran and A.K. Patwardhan, *Journal of Materials Engineering and*, pp. 130–135, 1998.
- [12] I.G. Ritchie, Z.L. Pan and F.E. Goodwin, *Metallurgical and Materials Transactions*, pp. 617–622, 1991.
- [13] Seah, K.H.W., Shatma S.C. and Girish, B.M. Mechanical properties of cast ZA-27/graphite particulate composites, *Materials and Design*, pp. 271–275, 1995.
- [14] M. Kok, “Production and Mechanical Properties of Al₂O₃ Particle-Reinforced 2024 Aluminium Alloy Composites,” *Journal of Materials Processing Technology*, pp. 381–387, 2005.
- [15] Suryanarayana C., Mechanical alloying and milling, *Prog Mater Sci* , pp. 1–184, 2001.
- [16] Zhang D.L., Processing of advanced materials using high-energy mechanical milling. *Prog Mater Sci*, pp. 537–560, 2004.
- [17] Nakhjavani, O.B. and Ghoreishi, M., Multi-criteria optimization of laser percussion drilling process using artificial neural network model combined with genetic algorithm. *Materials and Manufacturing Processes*, pp. 11–18, 2006.
- [18] Mohammad Sharifi E, Karimzadeh F. and Enayati M.H., Fabrication of aluminum matrix hybrid nanocomposite by mechanical milling. *Int J Mod Phys B*, pp. 4825–4832, 2009.

[19] C.L. De Castro and B.S. Mitchell, Mater. Sci. Eng. A, pp. 124–128, 2005.

BIOGRAPHY

Onur Güler is a PhD student at the department of Metallurgical and Materials Engineering in Karadeniz Technical University (KTU) in Trabzon, Turkey. He received his Metallurgical and Materials Engineer MSc degree in January, 2016 in Karadeniz Technical University (KTU) in Trabzon, Turkey. His scientific study fields are composite materials, powder metallurgy and mechanical alloying.

Horizontal and Vertical Balancing For Cloud Environment

Mirsat Yeşiltepe⁴⁰

Abstract

Today the border has increased work to be done using computers, as well as developments in all areas with the expansion of the concept of non-specific cloud. Then carried out on the data files in the beginning of operations on data stored carried on through databases accessible anywhere through increased provision enables the desired jobs. In particular, cloud computing can be used in my parallel programming is provided by the concept of data to be processed in multiple environments. The two most important factors that determine the quality of the software produced for the cloud are security and other quality factors. Other factors must be in balance due to the mentioned factors as a whole. One factor that is not the case as more important. In this section, horizontal and vertical balancing concepts used in the processing of requests, load balancing, automatically balancing.

Keywords: Forwarding, auto-balancing, conditional, not-conditional, rationality, request.

79. INTRODUCTION

This paper is built on a section of the configuration and security environment that this application is a mobile application to return more than one cloud connected perhaps hundreds of thousands of people a day use, it is treated the issue of how to manage user traffic.

The first path to the server and the number of requests submitted under a certain number of clients that I am not required to stop the big servers. But the desire for a larger number of servers needed to answer the request exceeds a certain number. In this method, the demands of the increasing scope because the server must rise vertically. Buddha will cause problems. When a certain number of requests exceeded the server will now start problems it cannot be enlarged. Server no longer be able to support this. All requests will not be processed within a single machine.

The second way is to make it work by splitting the application machine as a partner. In this way, the application will not need to shut down the server to adapt the new situation of increasing demand. This is called horizontal equalization.

Horizontal balancing of service in the construction of the cloud service is a desirable situation. Thus, new installations come when they can be easily divided on other machines. The new capacity will be sufficient when the server requested the addition of new machines. Horizontal equalization is not easily being used in this case. Because it increases the costs. When will be made to optimize the allocation of new installations to other machines must be given the best land [1].

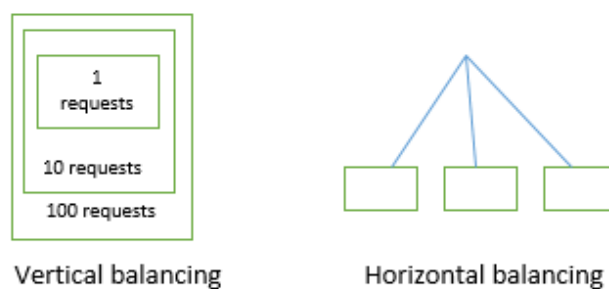


Figure 11. Vertical and horizontal balancing

In Figure 1. can be understood that distribution of the vertical balancing mechanism is not working, horizontal balancing work done at the same time has a distribution request. Vertical offset is essentially a client's request in time cannot be answered without answering the request of another client, this is the opposite horizontal balancing.

With the computing power is measured in requests per second that. This number correlates with the number of application servers. The increased number of machines in the environment is increased computing power and thus increases the number of requests processed per second. But the reality may not be directly related to the request processing per second of computing

⁴⁰ Corresponding author: Yildiz Technical University, Department of Mathematical Engineering, 34220, Esenler/İstanbul, Turkey.
m@yildiz.edu.tr

power. This application as a whole in accordance with the number relates to the handling of client requests. That fact does not depend on a single variable.

In fact, balancing and horizontal applications they want to use it are built in accordance with the appropriate architecture. But they do not want to use this machine for cost. There are machines which want to use the most optimized. But they want answers quickly on clients request their developers into a paradox. Increasing the cost side in a machine with more than one side are those who want to be quick in response. It is also a disadvantage in the event of the installation of the new machines into existing client information.

If we want to get away from an intention to practice situational disadvantages. If these situational applications will not remember anything about a client server. This occasion can be sent to any server in the client's environment demands. This allows each server to the client added the new server environment will disappear introduced the obligation [2].

Sometimes some of the important conditions must be associated with the request. Here, too, the situation of how to get a new machine, how will the client access to the information in this new machine how to move and how to transfer their problems will arise. The solution of this problem is more difficult than usual.

No-stable is desired to be archived in practice. Requests is desirable to be able to handle any request. When one wishes to build highly scalable applications must be optimized for the act of what could be a disadvantage.

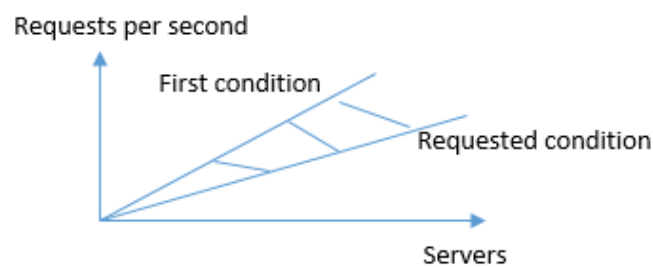


Figure 2. Computing power initial status and if desired relations

Sometimes some of the important conditions must be associated with the request. Here, too, the situation of how to get a new machine, how will the client access to the information in this new machine how to move and how to transfer their problems will arise. The solution of this problem is more difficult than usual.

As can be seen from Figure. 2. in the balance as soon as possible to request the server main objective is to reduce the time to respond. Balancing efficiency on the server is shown in the chart with shaded areas. Requests increased efficiency is further increased. Thus, a large number of mainly balancing is an important issue for the request responsive servers. Although it is difficult next time the importance of the creation of this state that allows more efficient operation of the server can be better understood.

80. NON-CONDITIONAL INSTALLING THE BALANCING AND SITUATIONAL APPLICATIONS PAGE STYLE

Usually found in applications running on multiple servers in the cloud. For example, sometimes hundreds of applications running on different servers. Transmission management of various client requests to various servers is a case to be considered. This request must be determined for each of the original server, servlet by relating way. But if there are multiple copies running on different machines, each case must be determined which machine will be forwarded to the incoming requests.

When a machine accessible externally orientation was known. But this is how it redirects requests which committed the request reaches the status of the machine and when the machine capacity are important issues. These issues are the subjects' HTTP load balancing [3].

Typically, it comes to the environment in which the request is the responsibility of load balancing for different machine how to route the request.

When the request is routed to the machine arrived. This request is forwarded to another machine when other requests. However, it must be balanced. Servlets are asked no-conditional work done in this machine. So it does not matter what it is in communication with the client machine [4].

An environment where the scanner is in communication with a particular machine are considered. Requests are sent to the machine and processed, prepared to be sent to the appropriate answer scanner. At first when it comes to the first request is sent to a set of machines in their environment. But it must first obtain approval from the head screen connection to be made before all this process. Connecting to the machinery in the transmission process has been provided with the request if success. Here,

the transmission path is often used interchangeably with transformational machine. If alternates are transmitted to other machines as they come after other requests.

All requests for load balancing in recall situations or used intelligently routing requests. It is very difficult to use any of these solutions. Individual request of the client machine instead of sending the request by grouping requests are handled in the appropriate requests to different machines that are willing specialized machine. Sometimes clients are nonetheless in relation to that client requests are sent to the machine with the machine in advance.

When a mobile cloud communication provides clients with individual machine time if the mobile device sends a request associated with a particular machine when it communicates with the same machine. Connected mobile devices are cases when information in the machine memory and recall its previously connected client machines. When connected to a mobile device associated with new know if any other machine. Sometimes it may turn again on the same machine. However, the distribution must be optimized.

If client begins to communicate with a specific machine status information from the mobile device are stored on the mobile device. The levels of the requesting client requests from mobile devices can vary. This is a condition which is considered in the planning environment.

So always be directed to the same machine made the shift to the mobile devices sometimes less intensive case study of the problem of hard work some of the other machines on some machines. But it also must be well-structured planning of the server. In this case the used state information of the application [5].

If it will be easier not-conditional orientation. Requests can be easily deployed on any machine b. But if the application situational things will be more difficult. This distribution will no longer have to work at once. Requests the client is communicating with a similar machine.

Another way that can be used is to be directed to any individual machine you want. This situation is similar to distributed session. Here two stores whose system can not connect information in the central database. Other requests are checked when a request is first connected to the system with the client before. This database is used for information control.

Its central permanent mechanism that eliminates the need to consider how the request by providing distributed over different servers. Status information is not stored in this layer. Instead stored in the lower layers.

Various loading balancing server HTTP is stateless or stateful application may be considered by reference to various criteria. If the application to edit the situational management business and the status of the individual machines stored in the memory in case it is difficult bay.

As said memory or distributed database used for distributed work on different machines. If the distributed mechanisms can be used if desired contingency.

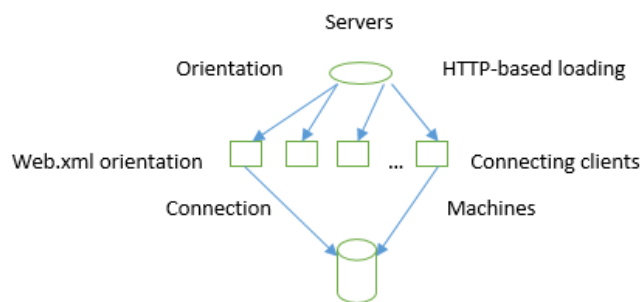


Figure 3. The load balancing and stateful applications not-conditional schema

As seen in Figure 3 it is in communication with a server and a machine. The figure is a variety of reasons clients will be known machine. Each machine is variety client is also a client types. That the servers in communication with more than one client at the same time is requested. There are some rules for communication may correctly. The load balancing in that the mechanism of HTTP mainly used for the cloud HTTP protocol is used [6]. Why cannot the lack of TCP protocol load balancing hosting infrastructure for the protocol. Lack HTTP is used as safe in terms of security and in the cloud environment.

CONCLUSION

A feature of the building is to be elastic cloud horizontal cloud balancing, reducing the cost and difficulty were to be created with automatic responses based on application requirements. If the application is carried out using load balancing horizontally by adding new machines.

How is the compensation will be taken to support the case of new units or application that runs in its own data center. That is the case of the addition of a new machine to machine it with the least possible change to ensure that the environment is sharply somehow adapt.

To create your own data center or to adapt to the new mechanism of the machine and the machine are subject to automatic stabilizers to support the new infrastructure.

Normally, you should be able to come to a certain level for the addition of new machine environment. That is, when a threshold value is exceeded is understood that developers no longer need to participate in a new machine environment

Similarly, requests to these machines when new machines need to be carried out optimally or this is the largest cost item in the new machine environment.

Adoption of new machines in the cloud is easy. Elasticity of the cloud feature is a popular feature. Because a new machine connects the cloud easily for having rules before how communicate with the environment. Changes to be made through the clouds is very artistic planning of the physical infrastructure plans. But that cost the intake of abstract machines in the cloud, it cannot fully eliminate the cost disadvantage.

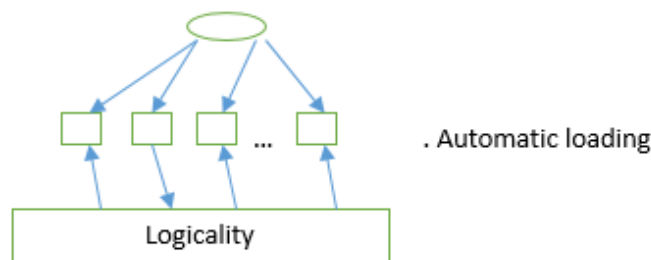


Figure 4. Fig. 1. Automatic loading mechanism

Figure 4 is obtained when examining these results. They do the balancing mechanism of communication with the server and client using a variable rate of rational criteria. The requested operation for the implementation of the stabilization can be run at the same time is not going to be determined. Examples include requests from different clients at the same time or decrease is nowhere to be processed. In fact, the only time a single request can be fulfilled [7]. The intent here is to simultaneously execute multiple jobs seem jobs are being processed simultaneously.

Another problem is to measure the load in the cloud in addition to the amount of the future moment. Well done the analysis of the added node must be able to predict the when will be added. If used in the application of existing horizontal balancing machine time to add the new machine will have to be considered when breaking the connection. Self-balancing method is used to prevent the severed this link. But the rules of the decision-making mechanism to automatically decide the best performance of works must be determined. It is easier to use in the cloud environment will be created automatically in the virtual machine balancing method [8].

Smart mechanism used only in adding machine. If it has trouble deciding on the solution to be implemented in the environment, in particular machines are able to provide the needs of the client tasks such as sorting priority. Its main purpose is to provide automatically the operation of the media.

REFERENCES

- [145]. Singing Stuo H. Singing (2012), "Horizontal vs Vertical Scaling", <http://singinghorsestudio.com/horizontal-vs-vertical-scaling/>.
- [146]. M.Kriushanth, L. Arockiam, G. Justy Mirobi (2013), "Auto Scaling in Cloud Computing: An Overview", International Journal of Advanced Research in Computer and Communication Engineering, Vol. 2.
- [147]. DeLima, Roberto, and Craig A. Lanzen. "Dynamic HTTP load balancing method and apparatus." U.S. Patent No. 7,480,705. 20 Jan. 2009.
- [148]. Openstack Cloud Software(2014), "Stateless vs. Stateful services", <http://docs.openstack.org/high-availability-guide/content/stateless-vs-stateful.html>.
- [149]. Brocade Communications Systems (2009), "Stateless Server Load Balancing".
- [150]. Del Val, David, and Anders Edgar Klemets. "Method and apparatus for communication media commands and media data using the HTTP protocol." U.S. Patent No. 6,128,653. 3 Oct. 2000.
- [151]. Bal, Henri E., M. Frans Kaashoek, and Andrew S. Tanenbaum. "Orca: A language for parallel programming of distributed systems." Software Engineering, IEEE Transactions on 18.3 (1992): 190-205.
- [152]. Luis M. Vaquero Luis Rodero-Merino Rajkumar Buyya (2011), "Dynamically Scaling Applications in the Cloud", ACM SIGCOMM Computer Communication Review.

Discrete Cosine Transform Based Automatic Gender Determination from Face Images

Betül Akkoç⁴¹, Ahmet Arslan⁴²

Abstract

Gender is one of the information that is contained in the human face. In this study, gender determination has been performed using face images. For this operation, database that consists of 100 people (50 male and 50 female) are used. Facial regions in each image are automatically determined and masked. The region within the mask is divided into blocks and discrete cosine transform is applied to each block. The feature vectors are obtained from these blocks. Support vector machine, neural networks and k-nearest neighbor algorithms are used for classification. The best success rate and the area under the ROC curve is obtained by using Support Vector Machine as 94% and 98.4%, respectively.

Keywords: Gender Determination, Image Processing, Discrete Cosine Transform.

81. INTRODUCTION

Gender is one of the information that is contained in the human face. Although people can easily determine gender from facial images, automatic determination using a computer is more difficult. Automatic gender determination is one of the important steps in such areas as human-computer interaction [1] and biometric recognition [2].

In the literature, Discrete Cosine Transform (DCT) has been used in the people recognition, gender and age determination from face images. Chadha et al. extracted local and global features from facial images using the DCT, and face recognition was performed by combining all obtained

features [3]. Pan et. al. showed that DCT-based face recognition method is much faster than PCA-based face recognition [4]. Viswakarma et al. have proposed accurate face recognition method with down scaling of DCT coefficients under varying lighting conditions [5].

Shewaye proposed automatic human gender and age group recognition system from human facial images, the best results were obtained when the DCT coefficients are used [6]. Alrashed et al. used 2-dimensional wavelet transform, gray level co-occurrence matrix and DCT in their work to identify the gender of the eye region images, and achieved the best results using DCT [7].

Kayım et al. performed Support Vector Machine (SVM) based gender recognition by using Local Binary Patterns and DCT features. Additionally, they have used random decision forests as a discriminative feature selection scheme [8]. Grassi et al. proposed 2D-DCT and Neural Network (NN) based system to recognize gender [9]. Nazir et al. performed gender detection by using DCT and k nearest neighbor (kNN) method [10]. Majid et al. proposed gender classification system based on modified-kNN classification and DCT [11].

In this study, the DCT-based automatic gender detection was conducted from facial images. Feature extraction steps and using methods in our study were mentioned in material and methods sections. Experimental results are given in Section 3 and the article is completed with conclusion section.

⁴¹ Corresponding author: Department of Computer Engineering, Selçuk University, Konya, Turkey
betulakkoc@selcuk.edu.tr

⁴² Department of Computer Engineering, Konya Food & Agriculture University, Konya, Turkey
ahmet.arslan@gidatarim.edu.tr

82. MATERIAL AND METHODS

In the first stage of the study, the face regions were determined from the images and obtained face regions were made in standard size 128x128. Masking is made to discard non-face parts (such as hair) in the image. The region within the mask was divided 8x8 blocks and DCT was applied to each block. The feature vectors were obtained from these blocks. Gender determination was performed through the obtained features and artificial intelligence methods. The applied steps are shown in Figure 1.

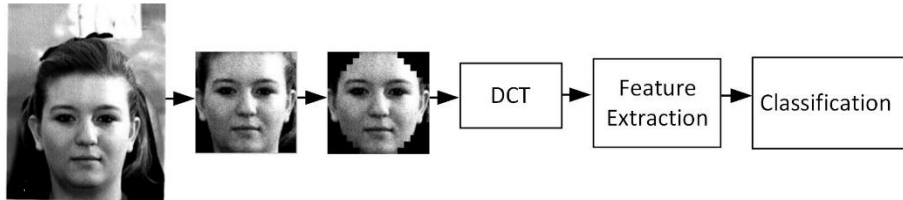


Figure 12. The Applied Steps

82.1. Feature Extraction

In the first stage of the study, the face regions automatically were determined from the images by using OpenCv Library Haar Cascade function. The obtained face regions were made in standard size 128x128. After obtaining facial region, masking process was made.

Masking

The non-face parts (such as hair) in the image were discarded. For this purpose a special mask was proposed. Fifteen 8x8 blocks were removed from each corner, because DCT was implemented into 8x8 blocks. DCT was applied to blocks remaining in the mask. This process is shown in Figure 2.

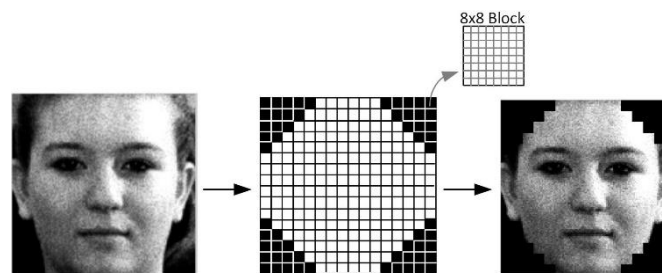


Figure 2. The Masking Process

Discrete Cosine Transform

DCT was introduced in 1974 by Ahmed et. al. [12]. DCT is one of the method often used in facial image analysis. DCT is used in applications of image compression and size reduction. The DCT has high energy compression property and it requires less computing resources [13].

DCT converts the original signal to the frequency domain by applying the cosine function. There are 2 types of DCT, one-dimensional and two-dimensional DCT. Two dimensional DCT is used in our study, because the image is a two dimensional matrix.

In this study, the image was divided into 8x8 sub-blocks before DCT applying. Thus, each block defined a certain part of the face. Thereafter, the DCT coefficients from each block were calculated. 64 DCT coefficients were in each block.

The coefficient at upper left corner is DC component and the rest of the coefficients are AC component. DC represents the low-frequency coefficients and AC represents the high frequency coefficients.

We scanned DCT coefficients by the zigzag scanning starting from the upper left corner. Consequently, coefficients were transformed into one-dimensional vector. This also gives the order of importance of the coefficients. We have chosen 5 first coefficients to generate feature vectors; these are DC, AC1, AC2, AC3 and AC4. Placements of these coefficients in the block were shown in Figure 3.

DC	AC1						
AC2	AC4						
AC3							

Figure 3. DC, AC1, AC2, AC3 and AC4 coefficients in 8x8 block

83. EXPERIMENTAL RESULTS

In this study, the Nottingham face database [14] that consists of 100 images (50 male 50 female) was used. Face region has been automatically detected and made in standard size of 128x128. The obtained face region was masked and DCT was applied to the remaining region within the mask into 8x8 sub-blocks. 5 coefficient features (DC, AC1, AC2, AC3 and AC4) were used from each block. The remaining region within mask contained 196 blocks and 5 features were taken from each block, so $196 \times 5 = 980$ features were obtained.

Orange 2.7. software [15] was used for classification. Gender determination was performed by using SVM, NN, kNN.

The performances of the methods were tested by using 10-cross fold validation. As the result of the experiments the most suitable SVM type, kernel function and complexity bound were found as v-svm, polynomial and 0.50, k value and metric were found as 5 and Manhattan for kNN, number of hidden layers for ANN was found as 16 and regularization factor was found as 0.5, respectively. The success rates of gender determination were given in Table 1.

Table 4. Gender Determination Results

Method	Success Rate
SVM	94%
ANN	89%
kNN	87%

The best success rate and the area under the ROC curve is obtained by using SVM as 94% and 98.4%, respectively. The confusion matrix obtained through SVM for female class is given in Table 2.

Table 2. The confusion matrix obtained through SVM for female class

		Prediction	
		True	False
Correct Class	True	47	3
	False	3	47

ROC curve that was drawn by using SVM in Orange software is shown in Figure 4.

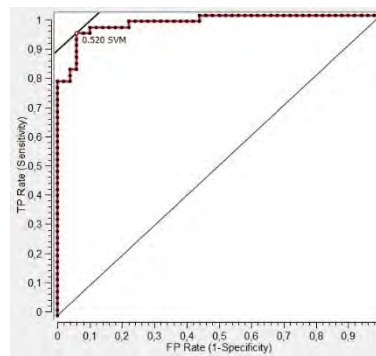


Figure 4. ROC curve that was drawn by using SVM

84. CONCLUSIONS

Human face contains gender information that is the important source for biometric recognition and human-computer interaction. In this study, we have performed the DCT-based automatic gender determination from face images. We have automatically detected the face regions in the images. It has been masked to extract the non-face parts (such as hair). DCT has been applied the remaining region within the mask. The features were obtained DCT coefficients. Then these features have classified through SVM, ANN and kNN. The best success rate and the area under the ROC curve has been obtained by using SVM as 94% and 98.4%, respectively.

ACKNOWLEDGMENT

The authors acknowledge the support of this study provided by Selçuk University Scientific Research Projects Fund for project no: 16701155. Also, the authors would like to thank TUBITAK (The Scientific and Technological Research Council of Turkey) for 2211 scholarship.

REFERENCES

- [153]. H.-C. Kim, D. Kim, Z. Ghahramani, S.Y. Bang, "Appearance-based gender classification with Gaussian processes," *Pattern Recognition Letters*, vol. 27, pp. 618-626, 2006.
- [154]. E. Makinen, R. Raisamo, "An experimental comparison of gender classification methods," *Pattern Recognition Letters*, vol. 29, pp. 1544-1556, 2008.
- [155]. A.R. Chadha, P.P. Vaidya, M.M. Roja, "Face Recognition Using Discrete Cosine Transform for Global and Local Features," in *Proc. International Conference on Recent Advancements in Electrical, Electronics and Control Engineering (IConRAEeCE)*, 2011, p. 502-505.
- [156]. Z. Pan, A.G. RustH., Bolouri, "Image redundancy reduction for neural network classification using discrete cosine transforms," in *Proc. IEEE-INNS-ENNS International Joint Conference on Neural Networks*, 2000, p. 149-154.
- [157]. V.P. Vishwakarma, S., Pandey, M.N. Gupta, "An Illumination Invariant Accurate Face Recognition with Down Scaling of DCT Coefficients," *Journal of Computing and Information Technology - CIT*, vol. 18, pp. 53-67, 2010.
- [158]. T. Shewaye, "Age Group and Gender Recognition From Human Facial Images," in *Proc. Ethiopian Society of Electrical Engineers 6th Scientific Conference on Electrical Engineering*, 2012.
- [159]. H.F. Alrashed, M.A. Berbar, "Facial Gender Recognition Using Eyes Images," *International Journal of Advanced Research in Computer and Communication Engineering*, vol. 2, 2013.
- [160]. G. Kayim, C. Sari, C.B. Akgül, "Facial feature selection for gender recognition based on random decision forests," in *Proc. IEEE 21st Signal Processing and Communications Applications Conference (SIU)*, 2013, p. 24-26
- [161]. M. Grassi, M. Faundez-Zanuy, O. Smirg, H. Mikulka, "Face Gender Recognition Using Neural Networks and DCT Image's Coefficient Selection," *Frontiers in Artificial Intelligence and Applications, In Neural Nets WIRN11 - Proceedings of the 21st Italian Workshop on Neural Nets*, 2011, p. 255-261.
- [162]. M. Nazir, M. Ishtiaq, A. Batool, M. A. Jaffar, A. M. Mirza, "Feature selection for efficient gender classification," *Proceeding of the 11th WSEAS International conference*, 2010, p. 70-75.
- [163]. A. Majid, A. Khan, and A. M. Mirza, "Gender Classification using Discrete Cosine Transformation: A Comparison of Different Classifiers," *Proceedings of 7th International IEEE Conference (INMIC 2003)*, 2003, p. 59-64.
- [164]. N. Ahmed, T. Natarajan, and K. R. Rao, "Discrete cosine transform," *IEEE Transactions on Computers*, vol. C-32, pp. 90-93, 1974.
- [165]. S. Shrestha, "Hybrid dwt-dct algorithm for image and video compression applications," Msc, Department of Electrical and Computer Engineering, University of Saskatchewan, Saskatoon, Saskatchewan, Canada, 2010.
- [166]. (2016) Nottingham Scan face database. [Online]. Available: http://pics.psych.stir.ac.uk/2D_face_sets.htm
- [167]. (2016) Orange 2.7. software. [Online]. Available: www.orange.biolab.si

Enhancing Heat Transfer from a Porous Plate with Transpiration Cooling

Mustafa Kilic⁴³, Tolga Taner⁴⁴

Abstract

The present study is focused on developing structural solid surface geometry to improve heat transfer by cooling of air with transpiration cooling. Effects of flow rate of water ($\dot{m}_{\text{water}} = 0.000083, 0.000116, 0.000166, 0.000249$ kg/s) and particle diameter of porous plate ($D_p = 40, 50, 100, 200$ μm) on local wall temperature and cooling efficiency of porous plate and the system inside a rectangular channel with air as a hot gas stream and water as a coolant were investigated experimentally. High performance polyethylene as a porous media was used not only to form a thermal barrier but also an active cooling plate by evaporating water from the surface of porous media to cool air. Temperatures were measured by T-type thermocouples. Two electric heaters were used to support enough power to the system. It was observed that increasing water flow rate did not cause a prominent decrease on surface temperature and cooling efficiency of porous plate. The higher injection rates result in further increase of the cooling effectiveness. Cooling efficiency of porous plate changed from 38 to 90 %. Increasing water flow rate as a coolant causes a prominent increase on cooling efficiency of the system. Increasing water flow rate three times causes an increase of 26.4 % on cooling efficiency of the system. Decreasing particle diameter causes a significant decrease on surface temperature. Difference of cooling efficiency of porous plate from $D_p = 40$ to $D_p = 200$ μm decreases from 12% to 2 % from inlet region to end of porous plate.

Keywords: Heat Transfer, porous plate, structured surface, transpiration cooling.

85. INTRODUCTION

Transpiration cooling is considered as an attractive cooling technique. This method has been used to protect solid surface exposed to high-heat-flux, high-temperature environments such as hypersonic vehicle combustors, liquid rocket thrusters, gas turbine blades, water oxidation technology, the first wall and blanket region in fusion reactors, the nose of aerospace vehicles during the atmospheric re-entry phase of their flight. Transpiration cooling processes involve simultaneously two different heat transfer mechanisms: conduction through a solid plus convection. In transpiration cooling process: fluid coolant is injected into porous matrix in the direction opposite to heat flux, at the same time absorbs the heat conducted into the solid matrix and transports heat flux through the convection passing pores, finally the coolant forms a thin film on the hot side surface to reduce the heat flux coming into the porous matrix and to cool the hot gas stream. The porous matrix in transpiration cooling can be some different types of porous media. Sintered stainless steel walls, metal fibers ceramics and porous plastics can be used as a porous media. The structure generally has a large number of pores with diameter ranging between 5 and 200 μm and can be made of different shaped particles as spherical, porous plate thicknesses can be change between 1 and 10 mm or more.

Interest and research in this topic may even have accelerated in recent years because of its high potential of heat transfer. Many investigators have performed experimental and numerical studies to determine the heat transfer characteristics for transpiration cooling. Jiang et al. [1] investigated turbulent flow and heat transfer in a rectangular channel without and with transpiration cooling experimentally and numerically. They used two-layer k- ϵ model to calculate the turbulent velocity and thermal characteristics of the main flow. They used sintered bronze particles as porous wall and air as coolant. The nominal particle diameter of the sintered porous wall was 0.1 mm and the porosity was 0.45. Their results showed that the transpiration cooling greatly increases the boundary layer thickness and reduces the wall skin friction and increasing coolant blowing ratio sharply reduced both the wall temperature and the convection heat transfer coefficient. Liu et al. [2] investigated the transpiration cooling mechanisms for thermal protection of a nose cone experimentally and numerically for various cooling gasses. In their study: the effects of injection rates, model geometry, inlet temperature and Reynolds number of the main stream were studied for air, nitrogen, argon, carbon dioxide and helium. Two-dimensional numerical simulation using the RNG k- ϵ turbulence model for the main stream flow and the Darcy-Brinkman- Forchheimer momentum equation and thermal equilibrium model were used to compare the general features in the experiments. Their results showed that the injection rate strongly influenced the cooling effectiveness. The increase of the main stream inlet Reynolds number dramatically reduced the cooling effectiveness. And the coolant thermos physical properties, especially specific heat, most strongly influenced the cooling effectiveness. Liu et al.[3] investigated the flow and heat transfer characteristic of transpiration cooling through sintered porous

⁴³ Corresponding author: Adana Science and Technology University, Department of Mechanical Engineering, 01180 Seyhan /Adana, Turkey. mkilic@adanabtu.edu.tr

⁴⁴ Aksaray University, Department of Motor Vehicles and Transportation Technology, 68100, City Centre/Aksaray, Turkey. tolgataner@aksaray.edu.tr

flat plates with particle diameters $dp= 40$ and $90 \mu\text{m}$ experimentally and numerically with dry air as the coolant stream. In their study their parameters were solid matrix thermal conductivity, injection rate and particle diameter. They showed that the cooling effectiveness increased with increasing injection rate, the temperature distribution on the porous bronze plate was more uniform than that on the sintered stainless steel plates and the cooling performance for the porous wall with the smaller particle diameters was better. Arai and Suidzu [4] investigated experimentally effects of the porous ceramic coating material such as permeability of cooling gas, thermal conductivity and adhesion strength. The mixture of 8 wt.% yttria-stabilized zirconium and polyester powders was employed as the coating material, in order to deposit the porous ceramic coating onto Ni-based super alloy substrate in their study. They showed that porous ceramic coating has superior permeability for cooling gas and transpiration cooling system for gas turbine could be achieved by using porous ceramic coating. He et al. [5] investigated new conversation equation for mass, momentum and energy to describe the performances of fluid flow, heat absorption and phase change in porous matrix. Their model's main differences from previous models are firstly, considering the compressibility of vapor in the momentum and energy equations, secondly, adding a term of the momentum transfer caused by liquid phase change into the momentum equation of vapor and liquid phases in two-phase region, finally in the energy equation of two-phase region, taking the variations of temperature and pressure into account. Their results showed that with an increase in heat flux and decrease in coolant mass flow rate the temperature difference over the two-phase region falls and a higher external heat flux or lower coolant mass flow rate will accelerate the phase change process and increase the area of two-phase region and vapor region. Wang et al [6] investigated the effect of different mainstream temperature, Reynolds numbers, and coolant injection ratio on transpiration cooling of the wedge shape nose cone with an equal thickness porous wall using liquid water as coolant. They obtained that the average temperature over the transpiration area falls with an increase in the coolant injection ratio, whereas the average cooling effectiveness rise and There is an optimal injection rate, at which the coolant passing through pores with liquid state when the driving force for the coolant injection is the minimum and the cooling effectiveness is high. Tsai et al. [7] investigated the transient cooling process in a sudden-expansion channel with the injection of cold air from the porous bottom wall experimentally. They identified distinct flow features under various rates of coolant injection. They categorized flow features to four cooling patterns; the recirculation pattern, the elevated recirculation pattern, the transpiration pattern and film pattern. Langener et al. [8] investigated transpiration cooling applied to flat C/C material under subsonic main-flow conditions. In their study; main-stream Mach number ranged from $Mg= 0.3-0.7$ and total temperature was 523 K. Air, argon and helium were used as coolants. They showed that thickness of sample and main stream total temperature did not affect the cooling efficiency. The coolant used and its specific capacity was the most influential parameter for the cooling efficiency. And with higher Mach number the cooling efficiency decreased. Tsai and Lee [9, 10] investigated the correlation between superheat levels and heat fluxes when used sintered powder structures as wicks. Their parameters were $45 \mu\text{m}$, $75 \mu\text{m}$, $150 \mu\text{m}$ of powder sizes and powder shapes of spherical, dendritic. Their results showed that smaller powders structures achieved higher effective thermal conductivities for both powder shapes. Spherical powder structures achieved twice the effective thermal conductivity of dendritic powder ones for each powder size. And at the same superheat level structures of smaller powder size and dendritic powder shape achieved higher heat fluxes. He et al [11] investigated performance of evaporative cooling with cellulose and Polyvinyl Chloride (PVC) corrugated media experimentally. The heat and mass transfer and pressure drop across the two media with three thicknesses (100, 200, 300 mm) were studied. Their results showed that the pressure drop range of the cellulose media is 1.5-101.7 Pa while the pressure drops of the PVC media are much lower with the range of 0.9-49.2 Pa, depending on the medium thickness, air velocity and water flow rate. The cooling efficiency of the cellulose media vary from 43% to 90% while the cooling efficiency of the PVC media are 8% to 65% depending on the medium thickness and air velocity.

Most of these previous investigations can be divided into two categories. The first group focused on analyses of the characteristics of the boundary layer, turbulent or laminar flow in transpiration conditions. The second group focused on transpiration cooling effectiveness at high pressure and temperature to simulate practical operational conditions. However, there are few studies of developing structural solid surface geometry and controlling the temperature of hot gas stream and surface to enhance heat transfer by using transpiration cooling. The objective of this study is to investigate the local wall temperature and cooling effectiveness distribution along the surface of a porous flat plate with air as a hot gas stream and water as a coolant to figure out the influence of mass flow rate of water, and particle diameters of porous plate.

86. MATERIALS AND METHODS

In This study; an experimental investigation of effects of mass flow rate of water, and particle diameters of porous plate on local wall temperature and cooling efficiency along the surface of a porous flat plate inside a rectangular channel with air as a hot gas stream and water as a coolant was done. For this purpose a porous plate was used not only to form a thermal barrier but also an active cooling system by evaporating water from the surface of porous media.

86.1. Experimental Apparatus

A schematic of the experimental facility, which consists of an air blower, flow meter for air and water, a computerized data acquisition system, a test section, a power unit, an absolute and differential manometer and a calibrator thermometer, is shown in Fig. 1. The power unit includes variac and parallel connected air heaters. The test section is composed of a polycarbonate rectangular channel and a porous plate. Details of the test section are shown in Fig.2. The channel is made of polycarbonate sheet and its geometry is shown in Fig. 2. Dimensions of test section were arranged as 220x880x10 mm (width, length, high). Hydraulic diameter of the channel is 19.1 mm. Then porous plates (high performance polyethylene) were arranged and located over water channel in test section precisely. Temperatures at the centers of porous plate were measured using calibrated T-type

thermocouples inserted through 2 mm holes inside the thickness of the porous plate. Calibrated thermocouples were located in the middle of porous plates in this arrangements (6,16,28,38,50,60,72,82 cm).

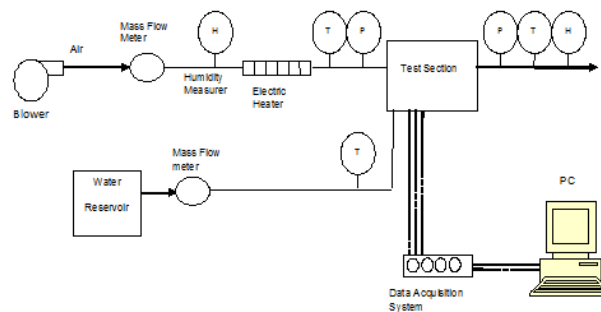


Fig. 1. Schematic of experimental apparatus

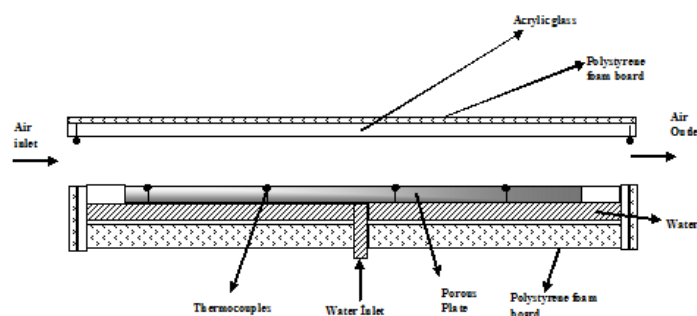


Fig. 2. Details of the test section

Conventional temperature measurements of the porous plate surface were used to evaluate cooling efficiency of the system. Two electric heaters were used to support enough power to the system to increase air temperature to the needed level. This electric heater was connected parallel and they supplied 280-620 W power to the system according to needed power. A variac was used to arrange voltage to support needed power for the system. The total power supplied was monitored using digital multimeters for the control of voltage and current. Then flow meter of air and water were added to the system. For each particle diameter (40, 50, 100, and 200 micrometer) porous plates were prepared again and tested for different parameter. Air temperatures ranged between 47°C and 77°C. Polystyrene foam board was used to insulate the top side of the channel with a thickness of 50 mm ($k = 0.032 \text{ W/(m.K)}$). The ambient temperatures in the experiments varied between 20°C to 24°C. The system was assumed to be steady state when variations of the surface temperatures and the inlet and outlet fluid temperatures of water and air were all within $\pm 0.1 \text{ }^\circ\text{C}$.

86.2. Data Reduction

The focus of the present investigation is to develop structural solid surface geometry to improve heat transfer by cooling of air with transpiration cooling. Inlet and outlet temperature of hot stream gas (air) were chosen according to the inlet and outlet temperature of cooling systems. In this application there is a porous plate in a rectangular channel, this porous plate is wetted by water of which reservoir temperature is $T_{\text{water}} = 22 \text{ }^\circ\text{C}$. Air enters into the channel with some different temperatures and velocities. For this application dry air (relative humidity of air, $x=0$) was used as a hot gas stream.

In this application; all Reynolds numbers were bigger that 3000 so it can be assume that it is a turbulent flow. Mean average film temperature in the channel is calculated as;

$$T_{avg} = \frac{T_{airin} + T_{surface}}{2} \quad (1)$$

where T_{airin} is the inlet temperature of air, $T_{surface}$ is the average surface temperature of porous plate. So It can be calculated, as explained by Mills [12], some physical properties of air by using thermodynamics tables as; ρ is the density of air, c_p specific heat of air, γ is the kinematic viscosity, Pr is the Prandtl number and Sc Schmidt number. So Stanton number with zero porosity can be calculated as;

$$St^* = 0.0296(Re)^{-0.2}(Pr)^{-2/3} \quad (2)$$

And convective heat transfer coefficient with zero-mas-transfer will be;

$$hc^* = \rho.V_{air}.Cp.St^* \quad (3)$$

where ρ is the density of air, V_{air} is air velocity, cp specific heat of air and St^* is stanton number.

So mass transfer driving force is;

$$B_m = \frac{m_{ev} - m_s}{m_s - 1} \quad (4)$$

where m_{ev} is mass fraction of water vapor at channel flow and m_s is mass fraction of water vapor at surface.

And mass transfer St number can be calculated as;

$$St^*_{mass} = 0.0296(Re)^{-0.2}(Sc)^{-2/3} \quad (5)$$

So the zero mass transfer limit conductance will be;

$$g^*_{mass} = \rho.V_{air}.St^*_{mass} \quad (6)$$

where ρ is the density of air, V_{air} is air velocity and St^*_{mass} is the mass transfer stanton number. And the mass transfer conductance is;

$$g_{mass} = g^*_{mass} \cdot \frac{\ln(1 + B_m)}{B_m} \quad (7)$$

where g^*_{mass} is the the zero mass transfer limit conductance, B_m is the mass transfer driving force. So mass flow rate of evaporated water is;

$$m_{ev} = g_{mass}.B_m \quad (8)$$

Then heat transfer blowing parameter is;

$$B_h = \frac{m_{ev}.Cp}{hc^*} \quad (9)$$

where m_{ev} is the mass flow rate of evaporated water, cp specific heat of air and hc^* is convective heat transfer coefficient with zero-mas-transfer. And convective heat transfer coefficient for surface of porous plate is;

$$h_c = h_c^* \cdot \frac{B_h}{\exp(B_h) - 1} \quad (10)$$

So energy balance equation on the surface of porous plate is;

$$m_{air} \cdot (h_{airout} - h_{airin}) = m_{water} \cdot (h_{waterin} - h_{fg} - h_{waterout}) \quad (11)$$

where \dot{m}_{air} is the mass flow rate of air, h_{airout} is the outlet enthalpy of air, h_{airin} is the inlet enthalpy of air, \dot{m}_{water} is the mass flow rate of water, $h_{waterin}$ is the inlet enthalpy of water, $h_{waterout}$ is the outlet enthalpy of water, and h_{fg} is the latent heat of water.

And convection heat transfer can be calculated as;

$$\dot{q}_{conv} = \dot{m}_{water} \cdot (h_{fg} + h_{waterout} - h_{waterin}) = h_c \cdot A \cdot (T_{air} - T_{surface}) \quad (12)$$

where \dot{m}_{water} is the mass flow rate of water, $h_{waterin}$ is the inlet enthalpy of water, $h_{waterout}$ is the outlet enthalpy of water, h_{fg} is the latent heat of water, h_c is the convective heat transfer coefficient for surface of porous plate, A is surface area of porous plate, T_{air} is the temperature of air and $T_{surface}$ is the average surface temperature of porous plate.

Conduction heat transfer from porous plate to water will be;

$$\dot{q}_{cond} = \dot{m}_{water} \cdot (h_{surface} - h_{waterin}) \quad (13)$$

where \dot{m}_{water} is the mass flow rate of water, $h_{surface}$ is the enthalpy of water at surface temperature, $h_{waterin}$ is the enthalpy of water at inlet temperature.

So cooling efficiency of the porous plate, shows protecting degree of main surface by decreasing surface temperature with using porous plate, is;

$$\eta = \frac{T_{surface} - T_{airin}}{T_{water} - T_{airin}} \quad (14)$$

And cooling efficiency of the system, shows cooling degree of air with using this system, will be;

$$\eta_{sys} = \frac{T_{airin} - T_{airout}}{T_{airin} - T_{surface}} \quad (15)$$

Moffat [13, 14] presented a general description of sources of errors in engineering measurements and discussion of the use of uncertainty in the planning of experiments. In addition to that, the uncertainty associated with the experimental data is estimated using Root-Sum-Square (RSS) method, to combine the individual uncertainty terms of the independent variables in the calculation of the heat transfer, by Caggese et al. [15] and Fechter et al. [16]. Table 3 shows uncertainty levels of measured parameters and their errors in the calculation of efficiency of porous plate, efficiency of the system and the Reynolds number. In the present experiments, the temperature measurements were accurate within ± 0.1 °C, and the velocity measurements were accurate within $\pm 2\%$. The uncertainty of Re, efficiency of porous plate, and efficiency of the system for the ranges of parameters studied under steady-state conditions is within $\pm 0.7\%$, $\pm 3.4\%$ and $\pm 6.4\%$, respectively.

Table 3. Experimental uncertainties

Parameter	Units	Value	Errors	%
V_{air}	m/s	3.35	± 0.2	± 5.9
$T_{surface}$	°C	$T_{surface} = 33$ °C	± 0.1	± 0.3
Re	-	Re = 3580	26.57	0.7

η	-	$\eta = 79.1$	2,68	3.4
η_{sys}	-	$\eta_{sys} = 48.74$	3.13	6.4

87. RESULTS AND DISCUSSION

In this section, experimental results were presented for different water flow rate as a coolant, and particle diameters of porous plate.

87.1. Effect of water flow rate

Experiments were conducted for different water flow rate for $Re=3300$ and $T_{inlet} = 77\text{ }^{\circ}C$. Water flow rates applied in experimental, are between $0,000083$ and 0.000249 kg/s. Surface temperature was measured for different water flow rates. Measured temperature was shown in Fig. 3.

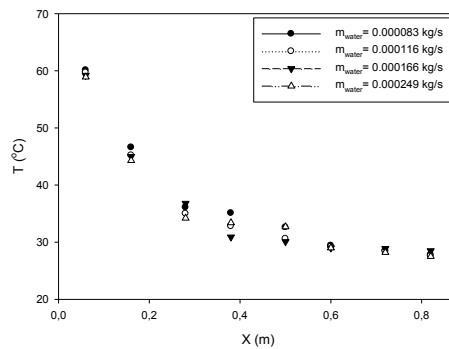


Fig. 3. Surface temperatures for different water flow rate

It was observed that increasing water flow rate did not cause a prominent decrease on surface temperature and cooling efficiency for the water flow rate of experiments. Because flow rate of water is slightly changed to determine the optimum value of water flow rate. The higher injection rates result in further increase of the cooling effectiveness. The difference of cooling efficiency decreased up to the end of the porous plate because air temperature also decreases at that region. Cooling efficiency of porous plate for different water flow rate was shown in Fig.4. It is observed that surface temperature changed from 27 to $56\text{ }^{\circ}C$ and cooling efficiency changed from 90 to 38% . If we continue to increase flow rate of water, droplets would occurred on the surface of porous plate and covered the surface. Then amount of evaporated water from the surface decreased. So effect of porous plate on heat transfer, extending surface area, also decreased. Cooling efficiency of the system for different water flow rate was shown in Fig.5.

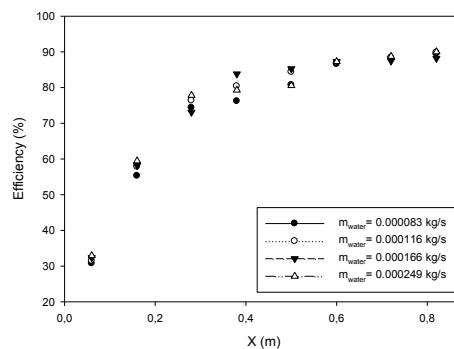


Fig. 4. Cooling efficiency of porous plate for different water flow rate

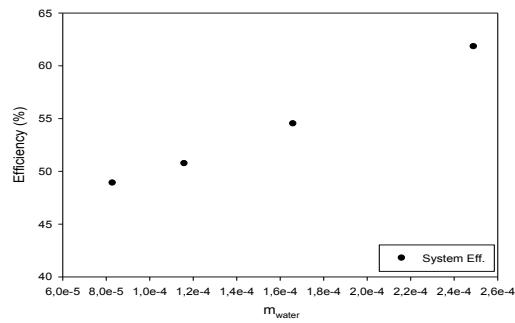


Fig. 5. Cooling efficiency of the system for different water flow rate

Increasing water flow rate as a coolant causes a prominent increase on cooling efficiency of the system. Increasing water flow rate three times causes an increase of 26.4 % on cooling efficiency of the system. Because increasing flow rate of water not only causes an increase on the quantity of evaporated water and amount of heat taken from the air but also decrease of temperature of air and surface.

87.2. Effect of Particle Diameter

In this study effect of particle diameters on heat transfer from the surface is investigated. It is known that heat transfer occurs from the cavities of particles of surface. It is thought that if particle diameter of porous plate is decreased an increase on heat transfer can be obtained. But there should be a limit for decreasing particle diameter of surface. So experiments were conducted for different particle diameter $D_p=40, 50, 100$ and $200 \mu\text{m}$ for $Re=3300$, $T_{inlet}=77 \text{ }^\circ\text{C}$ and water flow rate $m_{water}=0,000083 \text{ kg/s}$. Surface temperature was measured for different x values were shown in Fig. 6.

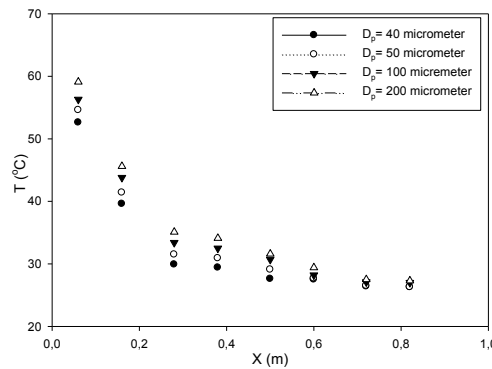


Fig. 6. Surface temperatures for different particle diameter

It can be seen that decreasing particle diameter causes a significant decrease on surface temperature. The reason of this, decreasing particle diameter causes an increase on surface area for evaporation and heat transfer. Effect of particle diameter on surface temperature can be detected easily at the inlet region of porous plate but this difference decrease slightly to the end of porous plate. Cooling efficiency of porous plate for different particle diameter was shown in Fig. 7.

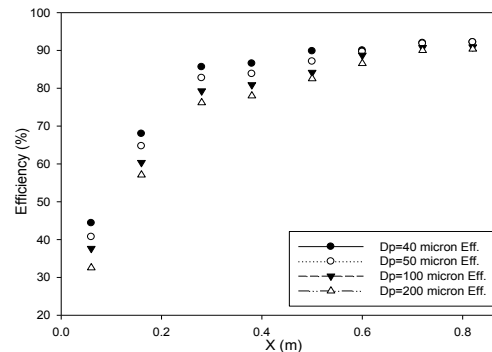


Fig. 7. Cooling efficiency of porous plate for different particle diameter

Beyond the point of $x=0,6 \text{ m}$ there is not a significant change among different particle diameter. Difference of cooling efficiency from $D_p=40$ to $D_p=200 \mu\text{m}$ decreases from 12% to 2 % from inlet region to end of porous plate.

88. CONCLUSIONS

The present study is focused on developing structural solid surface geometry to improve heat transfer by cooling of air with transpiration cooling. Effects of particle diameters and mass flow rate of water on local wall temperature and cooling effectiveness along the surface of a porous flat plate inside a rectangular channel with air as a hot gas stream and water as a coolant were investigated experimentally. Surface temperature of porous plate were measured and cooling efficiency of system were calculated for different flow rate of water ($\dot{m}_{\text{water}} = 0.000083, 0.000116, 0.000166, 0.000249$ kg/s) and particle diameter of porous plate ($D_p = 40, 50, 100, 200$ μm).

The following conclusions can be drawn from the experimental results;

Increasing water flow rate did not cause a prominent decrease on surface temperature and cooling efficiency of porous plate for the water flow rate of experiments. Because flow rate of water is slightly changed to determine the optimum value of water flow rate. The higher injection rates result in further increase of the cooling effectiveness. Surface temperature changed from 27 to 56 °C and cooling efficiency changed from 90 to 38 %. Increasing water flow rate as a coolant causes a prominent increase on cooling efficiency of the system. Increasing water flow rate three times causes an increase of 26.4 % on cooling efficiency of the system.

Decreasing particle diameter causes a significant decrease on surface temperature. The reason of this, decreasing particle diameter causes an extension on surface area for evaporation and heat transfer. Difference of cooling efficiency of porous plate from $D_p = 40$ to $D_p = 200$ μm decreases from 12% to 2 % from inlet region to end of porous plate.

Acknowledgment

The financial support of this study by the Scientific Research Council of Turkey (TUBITAK), with the program of postdoctoral scholarship (2219) and University of California Los Angeles Post Doctorate Program (UCLA/USA), is gratefully acknowledged.

References

- [168]. P.X.,Jiang, L.Yu, J.G.Sun, J.Wang, "Experimental and numerical investigation of convection heat transfer in transpiration cooling", *Applied Thermal Engineering*, vol.24, pp.1271-1289, 2004.
- [169]. Y.Q.Liu, P.X. Jiang,.S.S. Jin, J.G. Sun, "Transpiration cooling of a nose cone by various foreign gases", *Int. Journal of Heat and Mass Transfer*, vol.53 , pp.5364-5372, 2010.
- [170]. Y.Q. Liu, P.X. Jiang, Y.B. Xiong, Y.P. Wang, "Experimental and numerical investigation of transpiration for sintered porous flat plates", *Applied Thermal Engineering*, vol.50, pp.997-1007, 2013.
- [171]. M. Arai, T. Suidzu, "Porous ceramic coating for transpiration cooling of gas turbine blade", *J.Thermal Spray Technology*, vol.22, pp.690-698, 2012.
- [172]. F. He, J. Wang, L. Xu, X. Wang, "Modeling and simulation of transpiration cooling with phase change", *Applied Thermal Engineering*, vol.58, pp.173-180, 2013.
- [173]. J. Wang, L. Zhao, X. Wang, J. Ma, J. Lin, "An experimental investigation on transpiration cooling of wedge shaped nose cone with liquid coolant", *Int.J.Heat and Mass Transfer*, vol.75, pp.442-449, 2014.
- [174]. G. Tsai, Y.C. Lin, H.W. Wang, Y.F. Lin, Y.C. Su., T.J. Yang, "Cooling transient in a sudden-expansion channel with varied rates of wall transpiration", *Int.J.Heat and Mass Transfer*, vol.52, pp.5990-5999, 2009.
- [175]. T. Langener, J. Wolserdorf, M. Selzer, H. Hald, "Experimental investigations cooling applied to C/C material", *Int.J. Thermal Science*, vol.54, pp. 70-81, 2012.
- [176]. Y.Y Tsai, C.H. Lee, "Experimental study of evaporative heat transfer in sintered powder structure at low superheat levels", *Experimental Thermal and Fluid Science*, vol.52,pp.230-238, 2014.
- [177]. Y.Y Tsai, C.H. Lee, "Effect of sintered structural parameters on reducing the superheat level in heat pipe evaporators", *Int.J.Thermal Science*, vol.76, 225-234, 2014.
- [178]. S. He, Z. Guan, H Gurgenci., K. Hooman, Y. Lu, A.M. Alkhedhair, "Experimental study of film media used for evaporative pre-cooling air", *Energy Conversion and Management*, vol.87, pp.874-884, 2014.
- [179]. A.F. Mills, *Mass Transfer*, University of Los Angeles California, USA, 2001.
- [180]. R.J.Moffat, "Describing the uncertainties in experimental results", *Experimental Fluid Science*, vol. 1, pp.3-17, 1998.
- [181]. R.J.Moffat, "Using uncertainty analysis in the planning of an experiment", *ASME Journal of Fluid Engineering*, vol.107, pp.173-178, 1985.
- [182]. O.Caggese, G.Gnaegi, G.Hannema, A.Terzis, P.Ott, "Experimental and numerical investigation of a fully confined impingement round jet", *International Journal of Heat and Mass Transfer*, vol. 21, pp.156-163, 2000.
- [183]. S.Fechter, A.Terzis, P.Otto, B.Weigand, J.V.Wolfersdorf, M.Cochet, "Experimental and numerical investigation of narrow impingement cooling channels", *International Journal of Heat and Mass Transfer*, vol. 67, pp.1208-1219, 2013.

Detecting Moving Objects from Unmanned Ground Vehicles Using Hybrid Image Registration Method

Barış Gökçe⁴⁵, Güray Sonugür⁴⁶

Abstract

In this study, a global positioning system-aided model was developed to detect moving objects located on the route of unmanned ground vehicles by using computer vision systems. Before implementing a real-time application, a reference model representing a default background (no extra object) image was generated on all geographical coordinates of the determined route. 64x52 pixel blocks are used to produce the models. Each model was stored in the application database associating with its coordinate information. This model is a type of a feature matrix consist of gradient vector which are the first and second derivatives of each block. The model is much smaller than the pure image matrices. During the real time movement of the vehicle a number of snapshots are captured and modelled using the same method when the vehicle reached the specified coordinates. Then, modelled instant snapshots were aligned with the reference model of the associated coordinates by using the 2D image registration method. The location of the object was detected on the instant image frame by subtracting aligned models. In the developed approach, moving objects can be detected by the camera on the spatially moving platform using recorded models per specified coordinates. There is no need for complex and costly process to compensate for the noise generated by the moving camera. In the experimental study, the object detection accuracy in the instant background image frame of the developed system is observed between 100% and 77.5%, also It was determined that low-cost computer system can be used with 0.024 Sec processing time per frame and 5% CPU load.

Keywords: *Image processing, Unmanned ground vehicle, Moving object detection, Image registration*

89. INTRODUCTION

Nowadays, the studies focused on detecting moving or stationary objects from a real-time video sequence obtained patrol vehicle's camera [1],[2]. In particular, unmanned ground vehicles (UGV), aerial surveillance systems [3], vehicle driving assistance systems [4] and unmanned submarines [5]. Interpretation of environmental images taken by the cameras is important for a patrol UGV.

These types of patrol UGVs manage their interaction system, communication applications and their own spatial movements using the data obtained through the cameras. For this reason, object detection and recognition applications are indispensable for computer vision systems.

Today, despite the reduction of the size of the computer system, speed of data processing and storage capacities has increased a lot. In addition, data access technologies are quite advanced due to SSD (Solid State Disk) technology. Intensive database access and big data storage are considered to be a constraint formerly in moving object detection and recognition studies. But these processes are no longer a constraint now. In some studies, it has been mentioned that computational cost constraints are taken into consideration [6] -[9]. As a result of

the literature search, it is understood that it has been developed low cost approaches due to equipment limits and inherently the success of such systems is also limited. In developed approach, the models representing default backgrounds have been able to be stored in the database by using high-capacity computer systems. In this study, dimensions of composed model matrices are quite small and able to represent the entire default background. During the real-time movement of the UGV, captured instant frames are modelled the same method. In this way, the comparison is performed between small-dimensional matrixes. Thus substantial savings in time and computational cost is provided.

The first step of the object recognition process in any video sequence is correctly detection of the objects. The objects to be detected may be stationary or moving between consecutive image frames. Many approaches have been developed for stationary objects but it is required to reveal information hidden between consecutive image frames. Optical flow methods [10] gives decisive results in object detection applications with moving cameras. This method can be applied as feature based or area based [11]. However, due to computational complexity and excessive CPU load it is not suitable to use in real-time applications except specialized hardware [12]. In background estimation methods using of the algorithms used for stationary cameras is not possible for moving cameras. When using moving cameras the angular and spatial differences occur between consecutive

⁴⁵ Corresponding author: Afyon Kocatepe University, Department of Mechatronic Engineering, 03200, Afyonkarahisar, Turkey. bgokce@aku.edu.tr

⁴⁶ Afyon Kocatepe University IT Department, Afyonkarahisar, Turkey, gsonugur@aku.edu.tr

image frames. For this reason, primarily, it is necessary to compensate the differences between the two consecutive frames induced by camera movement to detect moving objects. This method is called as an image registration method [13].

After recovering image there is need for some transactions to detect and recognize objects. As a result of these transactions, the focused object will be able to be separated from the background. These transactions have to be applied each consecutive image frames. Because of the computational cost of this process it is not possible to run image registration code directly on a personal computers. For this reason in this study, 2-D image registration process has not been performed on the entire image frame, only been performed on smaller dimensional models which representing frames. As a result of the image registration process a shifting vector is calculated. Using this shifting vector instant (real-time) images are recovered and aligned to reference images. After alignment, object silhouettes are obtained by using interframe difference method [14].

90. METHOD

The unmanned vehicle passes from about the same point on horizontal axis along the programmed route. Default background images which obtained from points where the vehicle passes through on the horizontal axis at the coordinates of any K_i will be almost the same characteristics. Moving objects can be detected in the case where a model that represents the background can be created at the coordinates of determined K_i . First of all, Default background image frames are taken at the coordinates of determined K_i , along a predetermined route with the camera on the vehicle to create a default background model. This image frames called R_i as reference images. This frames are taken to be one for each of the K_i point on horizontal axis ranges as shown in Fig. 1. The reference images of R_i are averaged by dividing into blocks and obtained a single reference model which representing the default background on the current coordinates. These blocks are separated reference model can be expressed as a matrix smaller than the original image. In this way, the default background is modelled by small-dimensional matrix. This model matrix is stored in the system memory and each model is associated with its own GPS coordinate system. This models have the same background matrix properties with captured snapshots during the real-time movement of the vehicle. In this way, default background in the K_i position has taught computer running the system and image features are obtained to determine barriers and identify objects around the vehicle. In this study, the intervals switched on the horizontal axis for the vehicle are determined between 2 m and 1 m. The study consisted of two stages. In the first stage, one-time preparatory work for modelling of default background before real time application was done. In the second stage, real-time application was carried out.

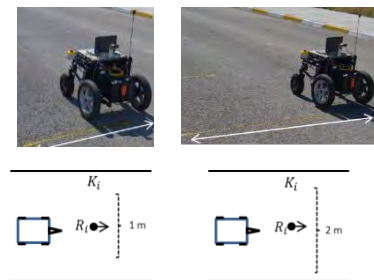


Figure 1. Horizontal course intervals

Flowchart algorithm of the system is given in Fig. 2. According to the algorithm, the vehicle starts moving by capturing snapshots on the determined route and reads the GPS location concurrently. If read location is a location associated with any reference model in the memory, the reference model for the associated location was matched quantitatively with calculated snapshot model. According to obtained results, capturing snapshots are analyzed whether the object is moving or stationary.

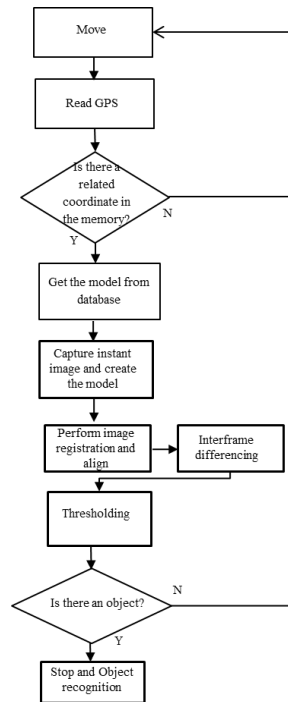


Figure 2. Flow chart of the algorithm used real time movement of the UGV

90.1. Creating Default Background Model

There are some preparations to be done for the system to work correctly before real time application. This preparation was accomplished by the following steps;

Step 1:

The default background images were captured at the coordinates of K_i on the determined route of Afyon Kocatepe University Campus. These background images called reference images. In this study, one reference image was used for each coordinate. Photographed images obtained from a point for each coordinates where the vehicle can pass in the transition intervals in shown in Figure 1.

Step 2:

In this step, the models of reference images " R_i " photographed from K_i coordinates were created. All reference images system and obtain more precise results. Examples of an image divided into sections as shown in Figure 3. B_2 is the focused section for detecting moving objects. Therefore, 4928x636 size of the images was evaluated in the section B_2 .



Figure 3. Partitioned image

Firstly, mosaic image was obtained by dividing all R_i images into blocks of 64x52 size. The mean gray level of each block was accepted as the intensity value of that block. In this way, representation of the most accurate way of the pixels around each block, elimination of small noise and reduction of the impact of local sharp changes in the tone were achieved. Thus, a single reference model R_i representing the default background was obtained at the coordinates of each K_i . This reference image matrix is the default background model of associated coordinates. Reference image taken from any K_i coordinate, mosaic image divided into blocks of the image and an example of a model matrix is given in Figure 4.

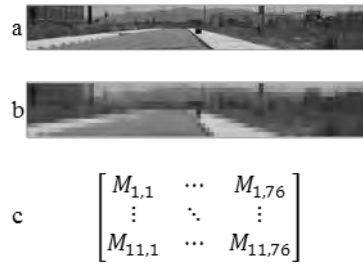


Figure 4. A sample of (a) original and (b) mosaic images and (c) model matrix of reference image

Step 3:

Common features are needed to be extracted by comparing reference and instant models to calculate shift vector. In the literature, SURF [15], Harris [16] and FAST [17] feature extraction methods are used but these methods has huge computational complexity because of detailed and complex algorithms. Instead of these methods, some features have been created by modelling gray level changes of between blocks in mosaic image.

When these two-dimensional image is expressed as $f(x,y)$ function in which x :row and y :column.

1. Change of gray level along the horizontal and vertical axes of each block, the value of the amplitude of gradient section (Equation 2) given in Equation 1,
2. The value of the angle of gradient section (Equation 3),
3. The first derivative value of each block,
4. The second derivative value of each block.

$$\text{gradyan}(f) = \nabla f = \begin{bmatrix} g_x \\ g_y \end{bmatrix} = \begin{bmatrix} \frac{\partial f}{\partial x} \\ \frac{\partial f}{\partial y} \end{bmatrix} \quad (1)$$

$$\text{mag}(\nabla f) = \sqrt{g_x^2 + g_y^2} = \sqrt{\left(\frac{\partial f}{\partial x}\right)^2 + \left(\frac{\partial f}{\partial y}\right)^2} \quad (2)$$

$$\theta(x, y) = \tan^{-1} \begin{bmatrix} g_y \\ g_x \end{bmatrix} \quad (3)$$

Thus, a feature matrix F_M was created and saved into database system for K_i coordinates of a reference model. Feature matrix consists of the vector in 1x4 size for each block.

90.2. Real time dynamic object detection

At the start of the real time movement, A model matrix has been already created for each K_i coordinate. During the real time movement the UGV gets the GPS signal for each 500 ms using GPS receiver system mounted on it. The GPS information is compared with coordinate data in the memory in a temporal loop. An instant image is captured by the UGV's camera when the both coordinate match each other. This image has to be modelled with the same method in order to be compared existing model in the memory. Therefore, the instant image is divided into 64x52 pixel blocks and each block is represented by its mean gray level value. Thus, the model which belongs to instant image F_A has been created. Then, instant and reference models are compared in order to align instant and reference image frames. This comparison is performed by calculating Euclidean distance between F_M and F_A . After calculation, most similar horizontal and vertical intensity changes between subsequent blocks of instant and reference models are obtained. Then the $U_{i,j}$ matrix has been created using the shortest distances between two models. This matrix is expressed as below.

$$U_{i,j} = \min \left(\sqrt{(F_M(i,j) - F_A(i,j))^2} \right) \quad (4)$$

In this study, the most repetitive distance value in $U_{i,j}$ is accepted as shift value between instant and reference image. Shift value is a vector which contain horizontal and vertical shift values and it has been used for aligning instant and reference images.

91. RESULTS AND DISCUSSION

Experimental results from different distances with various objects are presented in this section. In these experiments it has been used pedestrians and cars located at various distances away from K_1 ile K_{20} coordinates. The reference models have been calculated from images taken from different horizontal courses. Mobile vehicle has captured a snapshot (instant image) when it reached each coordinate mentioned above and the images are divided into 64×52 pixel block for calculating instant model matrices. Then shifting vectors have been calculated by comparing reference and instant models. Thus, reference and instant image frames have been aligned each other by using shifting vector and object silhouettes have been extracted applying interframe difference method to reference and instant models. The silhouettes were obtained as mosaic binary images.

The results of two experimental studies are shown at Figure 5. In the first column there is a pedestrian 10 m away from the camera and in the second column there is a car 30 m away from the camera. In this experiment, reference images were taken from 2 m horizontal course distance.

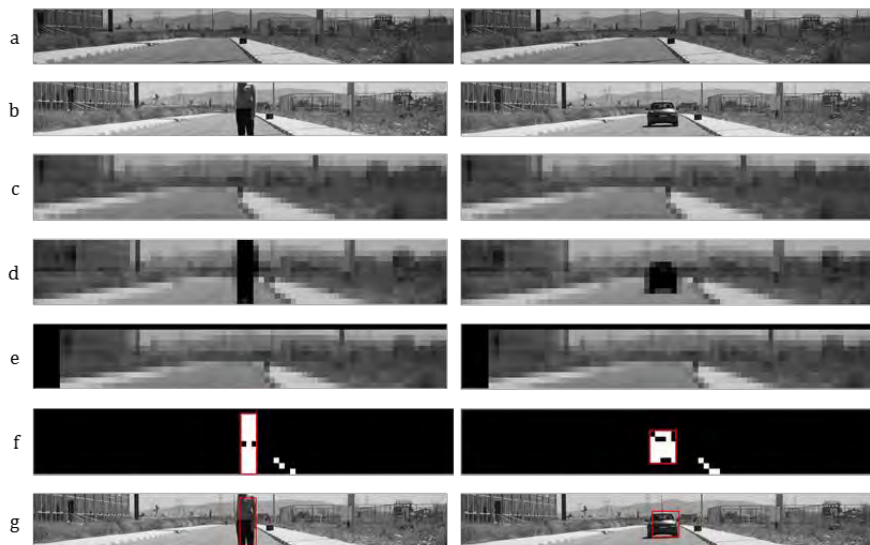


Figure 5. Various results of processes from K_1

In this figure shown that, (a) reference image, (b) captured snapshot at K_1 coordinate (instant image), (c) the reference model in the form of a mosaic image, (d) the instant model in the form of a mosaic image, (e) the reference model translated using the shifting vector, (f) the object silhouette in the form of binary mosaic image obtained by interframe difference method, (g) the object in the original image obtained by transforming silhouette boundaries from model to original image. Identification of the pixel clusters shown in Fig. 5 (f) has performed with (connected component labelling - CCL) [18] method. The cluster which has the maximum area is selected as the object. Thus, the pixel groups where the maximum change occurred between reference and instant images have been clustered and got into the rectangles. In the experimental study expressed in Figure 6, more distant pedestrians and cars have been used than the first study. In the first column there is a pedestrian 20 m away from the camera and in the second column there is a car 40 m away from the camera. In this experiment, reference images were taken from 1 m horizontal course distance.

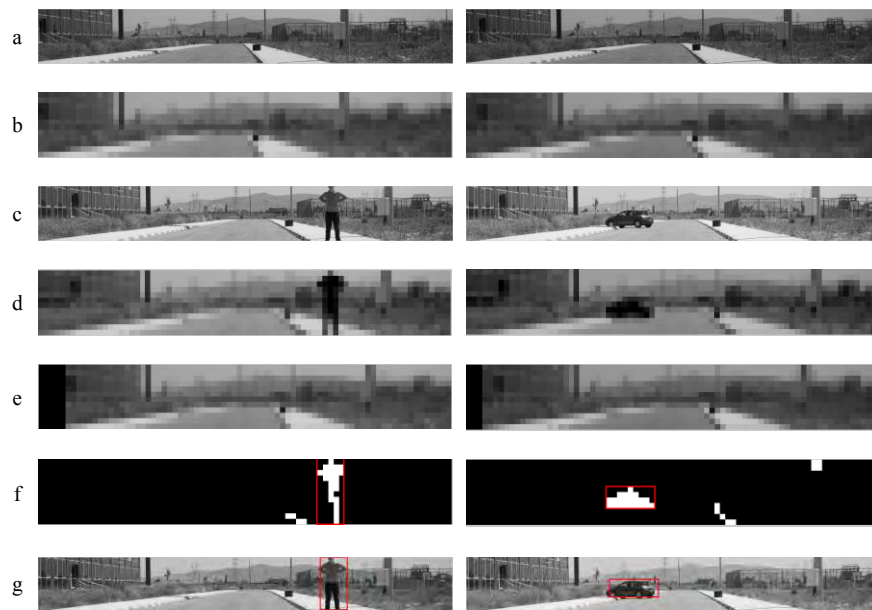


Figure 6. Various results of processes from K_3

In all the experimental studies, 10 m, 20 m and 30 m distant pedestrians and 10 m, 20 m, 30 m and 40 m distant cars were detected by using the developed approach. There has been performed 40 experiments for each distances using 1 m and 2 m horizontal courses. The results are given in Table 1 and Table 2.

Table 5. True detection rates for 1 m horizontal course

Object	Distance (m)	Success Rate (%)
Pedestrian	10	100
Pedestrian	20	90
Pedestrian	30	80
Car	10	100
Car	20	100
Car	30	87.5
Car	40	77.5

Table 2. True detection rates for 2 m horizontal course

Object	Distance (m)	Success Rate (%)
Pedestrian	10	100
Pedestrian	20	87.5
Pedestrian	30	80
Car	10	100
Car	20	100
Car	30	85
Car	40	75

In the experiments performed with both cars and pedestrians a rapid decline in the success rate is observed in the experiments between 30 m and 40 m distances. As a result of these observations, it is understood that an accurate detection cannot be made for distances longer than 30 m for pedestrians and distances longer than 40 m for cars. In addition, it has been observed that, when the horizontal course is reduced success rate has increased.

It has been also performed experimental studies about speed of computer systems. First, CPU usage has been observed. The PC with quad-core 2.8 GHz processor with 4 GB RAM has been used in the experiments. Observed performance results of PC are given in Table 3.

Table 3. Performance of different methods

Method	CPU load (%)	Processing time per frame (s)
GT[19] + IFD[14]	99	5.475
GT + Gauss[20]	99	5.91
DA	4	0.024

In the Table 3 GD abbreviation refers to the geometric transformation method, IFD abbreviation refers to inter frame difference method and DA abbreviation refers to developed approach.

92. CONCLUSIONS

In this study, GPS coordinates of geographical locations taken from regular intervals on the route of mobile vehicle have been related to reference model representing the default backgrounds taken at these coordinates and recorded to database of the computer system. The recorded information is not entire background images. It is only a small feature matrix modeling the background accurately. The feature matrices are not calculated by SURF, Harris or FAST method that are required huge computational complexity and can be expressed by high-dimensional vectors. The feature matrices consist of first derivatives, second derivatives and gradient of model components. Thus, the feature matrix represents simply the gray level changes in the model along the horizontal and vertical axis. Moving object detection difficulties arising from movement of the vehicle camera have been overcome by proposed method. In the experimental studies the success rates have been observed between %80 and %100 at distance between 10 m and 30 m for pedestrians. For cars the success rates have been observed between %100 and %75 at distance between 10 m and 40 m. In this way, the performance requirement of a computer system has been reduced for processing of high resolution images and detecting dynamic or stationary objects. The reducing of the requirement of the high performance computer system reduces the costs, thus, it provides energy saving by diminishing system sizes and weight.

93. REFERENCES

- [184]. S. Shimizu, K. Yamamoto, C. Wang, Y. Satoh, H. Tanahashi and Y. Niwa, "Moving object detection by mobile Stereo Omni-directional System (SOS) using spherical depth image," *Pattern Anal Appl.*, vol. 9(2-3), pp. 113-126, 2006.
- [185]. D.A.M. Gamez and M. Devy, "Active vision-based moving objects detection from a motion grid," in *Proc. Mobile Robots (ECMR) IEEE 2013 European Conference*, 2013, Barcelona, Spain, p. 373-378.
- [186]. Q. Yu and G. Medioni, "Map-enhanced detection and tracking from a moving platform with local and global data association," in *Proc. IEEE Workshops on Motion and Video Computing WMVC '07*, 2007, Austin, TX, USA, p.3.
- [187]. H. Kong, J. Audibert and J. Ponce, "Detecting abandoned objects with a moving camera", *Ieee T Image Process.*, vol. 19, pp. 2201–2210, 2010.
- [188]. G.L. Foresti and S. Gentili, "A vision based system for object detection in underwater images," *Int. J. Pattern Recogn.*, vol.14(02), pp.167-188, 2000.
- [189]. A. Andreopoulos and J.K. Tsotsos, "50 Years of object recognition: Directions forward," *Comput Vis Image Und.*, vol. 117, pp. 827–891, 2013
- [190]. Y. Guo, Y. Chen, F. Tang, A. Li, W. Luo and M. Liu, "Object tracking using learned feature manifolds", *Comput Vis Image Und.*, vol.118, pp.128-139, 2014
- [191]. D. Koller, Q.T. Luong and J. Malik, "Using binocular stereopsis for vision-based vehicle control," in *Proc. Proceedings of the Intelligent Vehicles' 94 Symposium*, 1994, p. 237-242.
- [192]. A. Bugeau and P. Pérez, "Detection and segmentation of moving objects in complex scenes," *Comput Vis Image Und.*, vol. 113(4), pp. 459-476, 2009.
- [193]. S. Roth and M.J. Black, "On the Spatial Statistics of Optical Flow," *Int. J. Comput. Vision.*, vol. 74(1), pp. 33-50, 2007
- [194]. H. Liu, T.H. Hong, M. Herman and R. Chellappa, *Accuracy vs. efficiency trade-offs in optical flow algorithms*, B. Buxton, R. Cipolla., Ed. Lecture Notes in Computer Science, 271–286, Cambridge, UK: Springer Berlin Heidelberg, , 1996.
- [195]. Y. Ren, C.S. Chua and Y.K. Ho, "Statistical Background Modeling for Non-stationary Camera". *Pattern Recogn. Lett.*, vol. 24, pp. 183–196, 2003.
- [196]. A.D. Sappa, F. Dornaika, D. Ger'onimo and A. L'opez, "Registration-Based Moving Object Detection From A Moving Camera," in *Proc. Workshop on Perception Planning and Navigation for Intelligent Vehicles IROS 2008*, 2008, Nice, France, p. 65-68

- [197]. M. Weng, G. Huang and X. Da, "A New Interframe Difference Algorithm for Moving Target Detection", in *Proc. Image and Signal Processing (CISP) 3rd International Congress*, 2010, Yantai, China, p. 285-289.
- [198]. H. Bay, T. Tuytelaars and L. Van Gool, *Surf: Speeded up robust features*, A. Leonardis, H. Bischof and A. Pinz, Ed. Computer Vision–ECCV 2006, Springer Berlin Heidelberg, pp. 404-417, 2006 .
- [199]. C. Harris and M. A. Stephens, "Combined corner and edge detector," in *Proc. Alvey Vision Conference*, 1988, Manchester, UK, p. 50.
- [200]. E. Rosten and T. Drummond, *Machine learning for high-speed corner detection*, A. Leonardis, H. Bischof and A. Pinz, Ed. Computer Vision–ECCV, Springer Berlin, Heidelberg ,2006, p. 430-443.
- [201]. F. Heijden, *Image Based Measurement Systems: Object Recognition and Parameter Estimation*, Chichester: Wiley, 1996.
- [202]. R.C. Gonzalez, R.E. Woods and S.L. Eddins, *Digital image processing using MATLAB*, 2nd ed., USA: Gatesmark, 2009.
- [203]. C. Stauffer and W.E.L. Grimson, "Adaptive background mixture models for real-time tracking," in *Proc. IEEE Computer Society Conference on Computer Vision and Pattern Recognition* ,1999, Fort Collins, CO, USA, p. 246-252.

Automatic Detection and Localisation of Sick Animals by Sound Technology

Arda Aydın

Abstract

In recent years, numerous applications in the framework of precision livestock farming for animal production have been reported. Precision Livestock Farming is a management system developed utilizing the latest developments in technology which can work in real time with fully automated monitoring and control systems to continuously (7/24) follow the animal production, impact on the environment and health and welfare of animals, by using different modelling techniques which can predict the realization of important events such as illness and allows the taking the necessary precautions. As an example of this system, it was shown that the cough sounds of animals analysed in real time with sound technology and reduce the use of antibiotics by providing early detection. For early detection, several studies conducted in recent years on pigs, an automatic classification algorithm was developed by examining the sounds characteristics of animals. Together with the classification of the cough sounds of animals, the location of the sick animals within the farm was also provided automatically. The first purpose of this study, is to share with interested researchers that the further technological applications and some examples in Europe to assist farmers by automatically and continuously monitoring health and welfare of animals. The second purpose of this study is to represent that how the sound technology used to continuously monitor health of the pigs which is intensively produced in Europe. The third and the most important purpose of this study is to submit of attention to scientists who interested in precision livestock farming on this system which is not used yet in Balkan countries. Additionally, it was aimed to start discussions on the advantage and disadvantage of this system whether it can be integrated to the pig, cattle, sheep and poultry breeding facilities in Balkan countries.

Keywords: Sound analysis, localisation, cough, animal welfare.

94. INTRODUCTION

In recent years, numerous applications in the framework of precision livestock farming for animal production have been reported. For example; [8] describe a cough as a natural acoustic indicator of animal welfare. Other approaches examine the relationship between vocalisation [9], drinking behaviour [5] or temperature [3] and animal welfare. It has been shown that pig vocalisation is directly related to pain and a classification of such sounds has been attempted by [6]. More recent research has focused on sound analysis from commercial piggeries in both their characteristics [2] and in creating automatic classifiers (Figure 1) ([1], [7]) while work has also been performed in the localisation of the pig sounds [7] and in combining the localisation and classification algorithms [1] by measuring the arrival of cough sounds to microphones (Figure 2, 3 and 4).

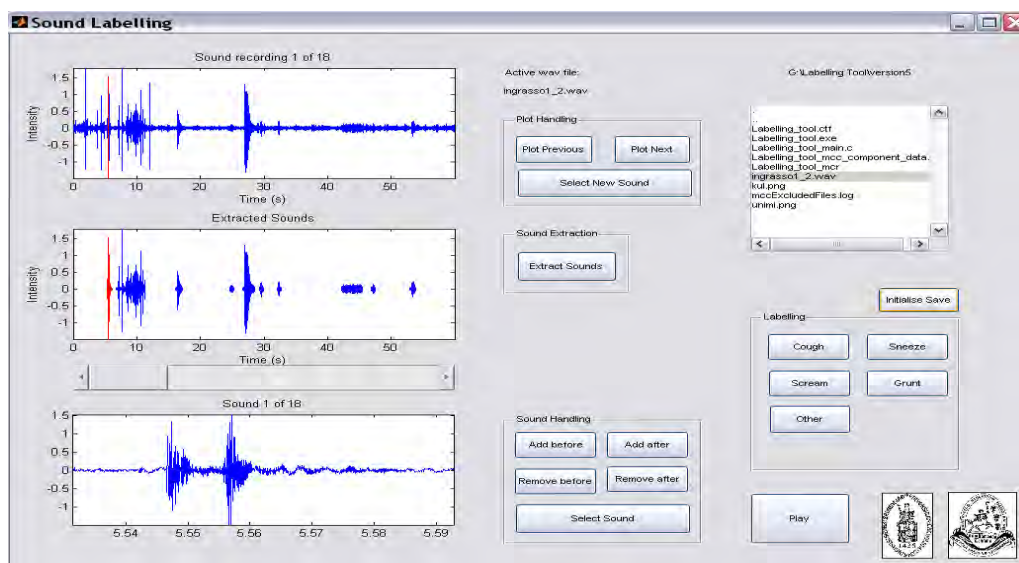


Figure 1. Labelling tool to validate the detected sounds [1].

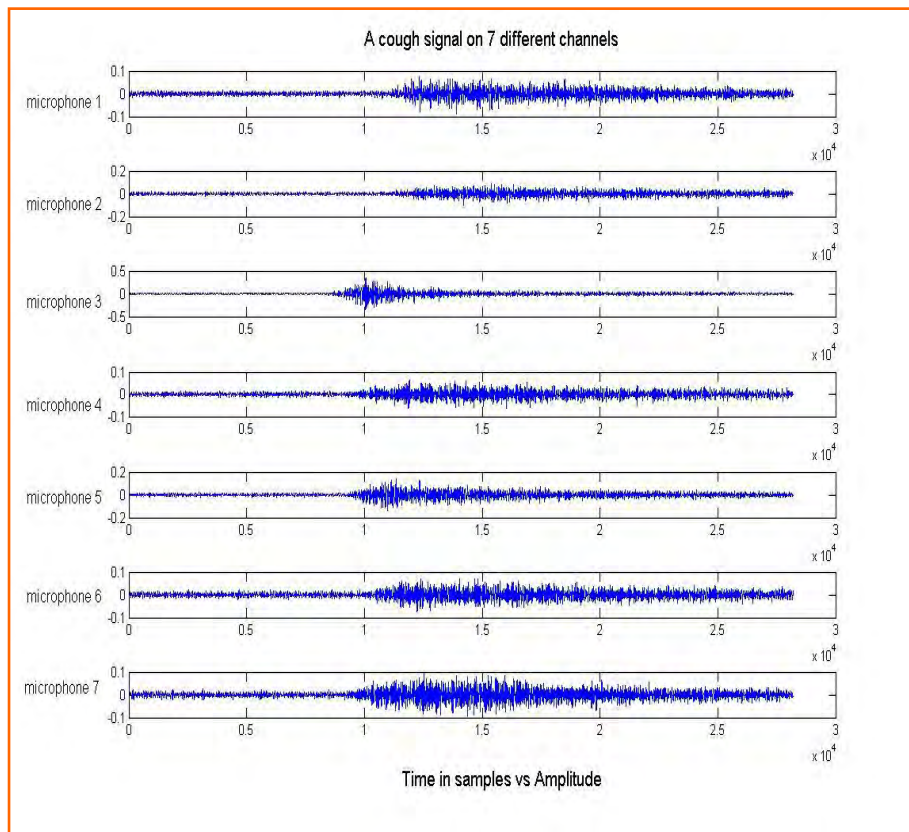


Figure 2. An example of a cough signal on 7 different channels [7].

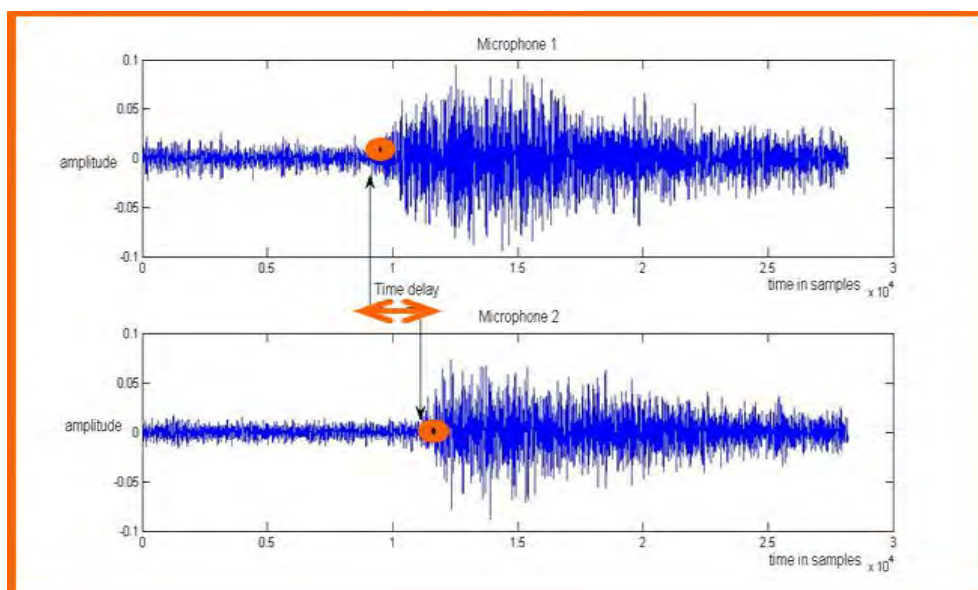


Figure 3. Time difference of arrival between microphones [7].

The first purpose of this study, is to share with interested researchers that the further technological applications and some examples in Europe to assist farmers by automatically and continuously monitoring health and welfare of animals. The second purpose of this study is to represent that how the sound technology used to continuously monitor health of the pigs which is intensively produced in Europe. The third and the most important purpose of this study is to submit of attention to scientists who interested in precision livestock farming on this system which is not used yet in Balkan countries. Additionally, it was aimed to start discussions on the advantage and disadvantage of this system whether it can be integrated to the pig, cattle, sheep and poultry breeding facilities in Balkan countries.

95. RESULTS AND DISCUSSION

In a first study, with experiments under laboratory conditions, algorithms have been developed to detect cough sounds from all other sounds. A sound-database of 5319 individual sounds including 2034 coughs was collected on 6 healthy animals containing both animal vocalisations and background-noises. This resulted in a positive cough-recognition of 92% [8]. In another study, the classification resulted in correct classification of 85.5% for the cough sounds and 86.6% correct classification of the other sounds [4]. In the second step, existing cough identification methods was extended and proposed a real-time method for identifying sick pig cough sounds. In total, 11 experiments were conducted to 3 male and 3 female healthy Belgian Landrace piglets of 9–12 weeks of age and 20–40 kg of weight. The generated data set includes individual sounds of 231 chemically induced coughs, 291 sick coughs, 149 other sounds. Preliminary results for the evaluation of the algorithm are based on individual sounds of healthy and sick animals acquired in laboratory conditions. As shown in table 1, an 85% overall correct classification ratio is achieved with 82% of the sick cough sounds being correctly identified (Şekil 5) [1].

Table 1. The results of the sound recognition algorithm [7].

Mic.	Sick cough sound (Algorithm)	Sick cough sound (Reference method)	Accuracy (%)
1	88	64	73%
2	101	76	75%
3	41	33	80%
4	40	37	93%
5	35	29	83%
6	47	38	81%
7	37	31	84%

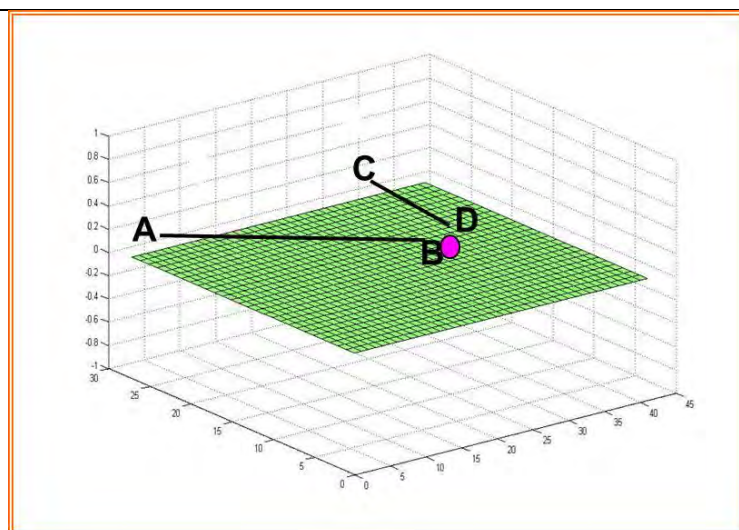


Figure 4. Sound source position [7].

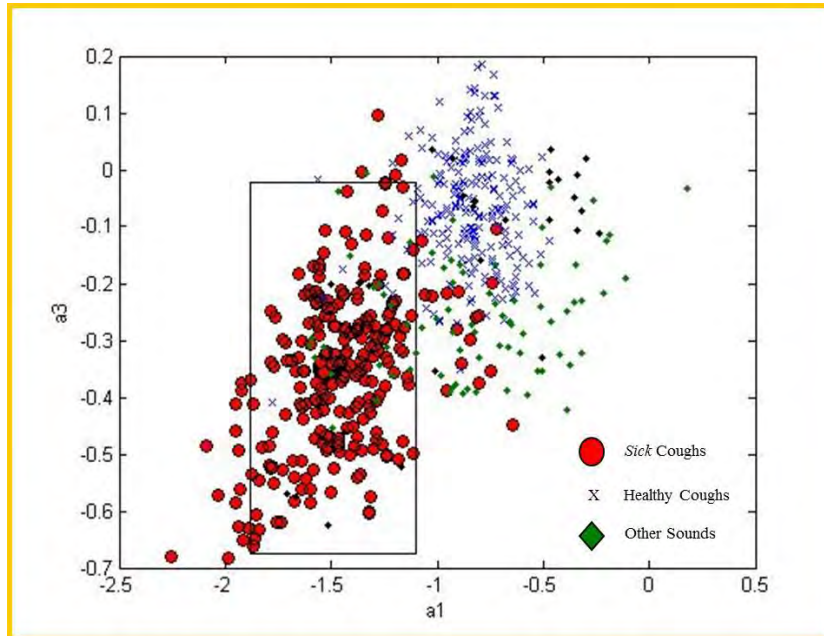


Figure 5. Sick cough sounds, healthy cough sounds and other sounds detected by the developed algorithm [7].

In the last step, the position algorithm was applied on the localization of coughing pigs in a stable in field condition. As shown in table 2, by using this method it was possible to localize cough attacks of pigs (Figure 6).

Table 2. The number of coughs and their positions in the stable [7].

X Coordinate	Y Coordinate	Number of Cough	Zone No
0,2	4,2	9	15
0,3	4,2	4	15
0,3	4,4	14	15
14	10,3	8	5
1,8	3,3	2	16
14	21	16	8

During a 3h recording trial, soundwas recorded using seven microphones in which 179 coughs were collected, originating from 19 cough attacks. After mapping the locations in the stable, some hazard zones could be identified. Although the algorithm is able to show the locations of the coughs (cough attacks), this does not mean the coughs originate from different pigs. It might be that different coughs, which were recorded in a pen, possible from a single pig. All the configurations showed good position estimation, with mean error between 1.5 and 0m, and a maximum standard deviation on the error of 0.4 m [7].The ability of detecting and localizing cough sounds and the increasing importance of animal welfare and monitoring indicate that in the future such systems will become available. Not only will the veterinarians have a quantitative indication about condition of the pigs, but also the farmer would get continuous feedback on the pigs' condition by automatic on-line monitoring.

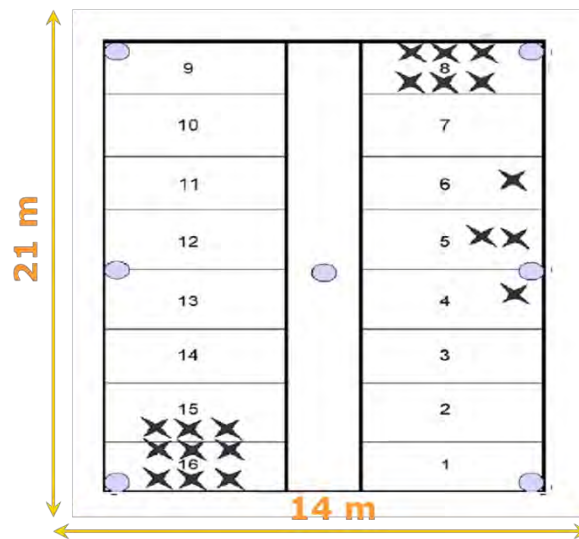


Figure 6. Overview of stable and detected cough sounds [7].

96. CONCLUSION

This methodology can be used for visualizing the spread of respiratory diseases and contribute to the reduction of the use of antibiotics by means of selective and early treatment of single pens instead of the whole compartment. The most important advantage of these types of automated sound monitoring systems is that measurements may be taken automatically and continuously during the life-span of animals with a completely non-intrusive and non-invasive way. These systems also do not include the biosecurity risk of assessors visiting different farms to score and assess the animals. These kinds of systems can be used for early detection of the health and welfare problems of animals. It is very important to detect any kind of problem at an early stage because it allows to farmers and veterinarians to take immediate management actions in time.

REFERENCES

- [204]. Exadaktylos, V., Silva, M., Aerts, J.M., Taylor, C.J., Berckmans, D., 2008. Real-time recognition of sick pig cough sounds. *Comput. Electron. Agric.* 63, 207–214.
- [205]. Ferrari, S., Silva, M., Guarino, M., Aerts, J.M., Berckmans, D., 2008. Cough sound analysis to identify respiratory infection in pigs. *Comput. Electron. Agric.* 64, 318–325.
- [206]. Geers, R., Puers, B., Goedsels, V., Wouters, P., 1997. *Electronic Identification Monitoring and Tracking of Animals*. CAB International Wallingford.
- [207]. Guarino, M., Jans, P., Costa, A., Aerts, J.M., Berckmans, D., 2008. Field test of algorithm for automatic cough detection in pig houses. *Comput. Electron. Agric.* 62, 22–28.
- [208]. Madsen, T.N., Kristensen, A.R., 2005. A model for monitoring the condition of young pigs by their dinking behavior. *Comput. Electron. Agric.* 48 (2), 138–154.
- [209]. Marx, G.; Horn, T.; Thielebein, J.; Knubel, B.; von Borell, E. 2003. Analysis of pain-related vocalization in young pigs. *Journal of Sound and Vibration*, Volume 266, Issue 3, p. 687-698.
- [210]. Silva, M., Ferrari, S., Costa, A., Aerts, J.M., Guarino, M., Berckmans, D., 2008. Cough localization for the detection of respiratory diseases in pig houses. *Comput. Electron. Agric.* 64 (2), 286–292.
- [211]. Van Hirtum, A., and D. Berckmans. 2001. The fundamental frequency of cough by autocorrelation analysis. In *Proc. EUROSPEECH: 7th European Conference on Speech Communication and Technology*, 2435–2438, Aalborg, Denmark.
- [212]. Van Hirtum, A., Berckmans, D., 2004. Objective cough-sound recognition as a Bio marker for aerial factors. *Trans. ASAE* 47 (1), 351–356.

Automatic Detection of the Lateral Body Oscillations to Assess the Lameness of Broilers

Arda Aydın⁴⁷, Anil Çay⁴⁸

Abstract

Lameness is one of the major causes of poor welfare in broilers. Previous studies have documented approximately 30% of the chickens were seriously lame. In this study, a new and non-invasive technique was developed to automatically assess the lameness of the birds. For this aim, video images of broiler chickens with five different predefined gait scores were recorded as they walked along a test corridor. Afterwards, the image processing algorithm was applied to detect the lateral body oscillations of broiler chickens. Then, the relation between lateral body oscillation and gait scores (as a measure of lameness) of broilers was investigated. The results showed a positive significant correlation between lateral body oscillations detected by the proposed algorithm and gait score level of broilers given by an expert ($P < 0.05$). Since strong correlations were found between lateral body oscillations and gait score level of broiler chickens, the results suggest that this automatic monitoring system has the potential to be used as a tool for assessing lameness of broiler chickens.

Keywords: body oscillation, broilers, gait score, lameness, image analysis.

97. INTRODUCTION

The broiler industry has grown continuously over the last 50 years. Meanwhile, public anxieties with regard to the welfare of broilers have grown too [24]. The major questions relating to broilers welfare that have been increased in the last twenty years are the increasing susceptibility to metabolic and movement problems [5]. Lameness is a general word which is used for broilers to describe a range of injuries with infective and non-infective source [29]. In some broiler farms it has been detected that around 27% of broilers showed poor movement and 3% of broilers were nearly unable to move [22]. The existence of lameness was sorely correlated with the growth rate and live weight [31]. In another research, the same conclusion was stated by [21]. Locomotion problems can be painful for broilers and decrease their mobility while increasing some problems, such as chest soiling [30]. The effects of lameness can be seen in the run ability. These can subjectively a "gait score" judged ([6], [20]-[31]).

Beside these manual scoring methods, some kind of computer based systems were used to assess the lameness of broilers. For example, kinetic data have been obtained from broilers using with a different kind of techniques, such as the pedobarograph ([14], force plate [17] and piezoelectric pressure-sensing mat [25]. Most of the current kinetic methods based on the system invented by [13]. This system which was called as pedobarograph was improved by ([7], [8], [9]). In the other studies which have been focused on kinematic analysis, broilers were recorded for the lateral body oscillations with markers attached to the hock, knee and metatarsus ([1], [19]). Nevertheless, it was concluded that there was some disadvantage of this method. For example, markers position can be changed during experiments due to skin displacement. Furthermore, the lower accuracy can take place if the broilers diverge from walking in a plane parallel to the camera [14]. In another very recent

⁴⁷ Corresponding author: Canakkale Onsekiz Mart University, Department of Agricultural Machineries and Technologies Engineering, 17020, Merkez/Canakkale, Turkey. araydin@comuz.edu.tr

⁴⁸ Canakkale Onsekiz Mart University, Department of Agricultural Machineries and Technologies Engineering, 17020, Merkez/Canakkale, Turkey. anilcay@comuz.edu.tr

study, the lateral body oscillations in turkeys were investigated by [28]. The objective of their research was to find the effects of waddle on the ground reaction powers and gait kinematics of turkeys. Their results showed that the increased body weight results in movement changes [28]. It was found by the ground reaction power and influence primary mechanics, such as the motion of body [28].

Nevertheless, these types of existing tests (manual scoring and gait kinematics) are time-consuming and the measurements cannot be performed automatically and continuously with a non-invasive and non-intrusive way. As a consequence, there is no possibility for early detection of lameness when these evaluation methods are used. Additionally, a big amount of manpower is necessary, especially to perform these type of tests on huge broiler houses with more than 50,000 chickens in a farm.

As an alternative to these evaluation methods, the raising availability of low-cost technology currently make possible to use image analysis systems for lameness assessment. 2D and 3D camera technology associated with image analysis software, allow animal locomotion to be evaluated to a specific extent ([2], [3], [4], [10]- [23]). All these automated systems have been validated against traditional manual labelling methods. Additionally, it is certainly clear from the literature that using automated monitoring systems with image processing software to analyse individual and group level behaviours of broilers is an emerging technology. The main advantage of this type of automated behaviour monitoring is that the measurements can be automatically and continuously performed throughout the lifespan of broilers with a non-invasive and non-intrusive way. These systems also do not include the biosecurity risk of assessors visiting different houses to score and to assess animals [18].

On the other hand, it was concluded by [27] that broilers have a different locomotor pattern to laying hens. Laying hens place their feet under their bodies' centre of gravity while walking. In contrast to this, broilers move their whole body over the respective supporting leg for each step [27]. This causes the body to oscillate during walking. Lamé broilers usually run with bigger lateral body oscillations than sound birds ([11] [26]- [27]).

Based on all these literal knowledge, the objective of this research was created as to develop an automatic monitoring system to assess the lameness of broilers. This is done by investigating lateral body oscillations of broilers in relation to their gait scores.

98. MATERIALS AND METHODS

98.1. Experimental Setup

The experimental setup composed of a wooden test corridor, with dimensions 2.40 m (length) x 1.00 m (width) x 0.50 m (height). A video camera, Guppy F036C, was used in the experiments with a C30811KP 8.5 mm lens (Pentax). It was fixed 3.0 m above the ground. It was positioned exactly above the centre of the testing corridor in order to cover all of the experimental setup (Figure 1). It was also connected to a computer by an IEEE 1394 fire-wire cable. Images of broilers were recorded by this camera with five frames per second. The resolution of this camera was 1024 x 768 pixels.

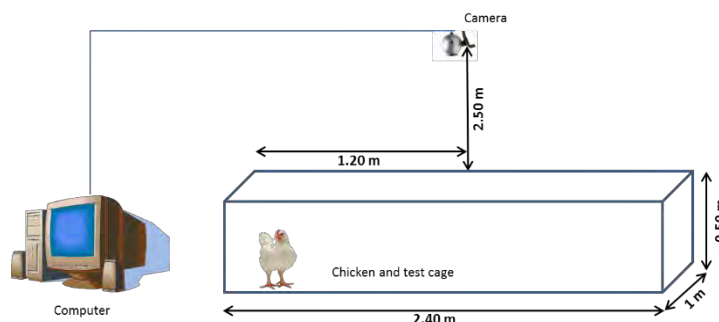


Figure 1. Experimental setup.

Five experiments were carried out with a total of 250 male broilers (Ross 308). The broilers were gait scored and selected according to their degree of lameness by expert using the method developed by [20]. GS5 broilers were not used in the experiments as these broilers cannot walk due to the severity of lameness. In each experiment, a broiler was placed at the start point in the experimental setup and video images of the experimental setup (all walking area) were recorded during five minutes while the broiler walked from the start point to the end point of the setup with a distance of 2.4 m.

98.2. Image calibration

Before the experiments, the image of camera was calibrated with the known dimensions of the experimental setup (2.4m×1m). The pixels areas in the image were transformed to units of cm² on the experimental setup. These distances was measured in the image with the pixels units, then the positions within the experimental setup was calculated as $f = 0.47\text{cm}$ per pixel using a linear factor related to image coordinates. Thus, the interval between two points, one pixel apart was 0.47cm on the experimental setup and the one pixels area was calculated as $f^2 = 0.22\text{cm}^2$ on the experimental setup.

98.3. Image analysis

The background subtraction method was used for the separation of the broilers shape. This method was chosen because the camera setup was fixed. Therefore the background remained stable over time. Separation was made by extracting the background image of the empty setup from each recorded image of the setup containing a broiler. When the difference was bigger a certain threshold, it was defined as belonging to the shape of the animal [23]. After this step, the animal shape could be characterised using some parameters, such as the shape centre and the area of the shape [23]. Furthermore, an image analysis algorithm was used to detect a chicken from a sequence of video images. The centre point, orientation, length and width of the broiler in the image were identified by fitting an elliptical shape around the bird [23].

98.4. Calculations of the lateral body oscillations

The detection procedure involved the orientation change and the back area of the chicken covered by pixels in each image. It means that the developed algorithm automatically detected all pixels covered by broiler in each frame. Then the algorithm focused to calculate the covered pixels for each step based on the orientation of the broiler. Afterwards, the pixel differences were automatically calculated by the proposed algorithm for each step of the broiler as a function of time. At the end of the each experiment, the lateral body oscillation level of the bird was cumulated by the proposed algorithm. To remove errors existing due to different size of broilers, the total amount of measured movement in each experiment was normalised by dividing the average size of the birds [2].

98.5. Statistical analysis

The statistical analysis was performed out on 50 video data sets per experiment with ten data sets belonging to each of the gait score groups. In total, 250 data sets were used to investigate the differences in the lateral body oscillations between the gait score groups. The Friedman test was used to analyse the effects of gait score on the lateral body oscillations of the broilers. The Friedman test was chosen for statistical analysis because it is a non-parametric test that compares the columns without the row effects [2]. With this method, size and dependencies did not affect the test results in the test sample. Following the Friedman Test, the Dunn test was applied to determine the statistical differences between the gait score levels of broilers. The Dunn test crosschecks the difference in the sum of ranks between two columns based on the number of groups and their size. The statistical calculations were performed using the Statistics Toolbox of Matlab (The Math Works, Massachusetts, USA).

99. RESULTS AND DISCUSSIONS

99.1. Detection of the lateral body oscillations

Five experiments were carried out with a total of 250 male broilers (Ross 308) to find a relation between the lateral body oscillations and lameness of broilers. The broilers were manually leaved to the start point of the setup. A correlation test was performed to define the coefficient of determination between the lateral body oscillations obtained by the proposed algorithm and the gait score of the birds, which resulted in $R^2 = 0.947$, ($p < 0.05$). The results of the algorithm were statistically analysed for differences between the different gait score levels. As shown in Table 3, the lateral body oscillations in GS3 and GS4 (mean +/- standard deviation) was significantly ($P < 0.05$) higher than in GS0, GS1 and GS2 (Figure 2). However, there were no significant differences between GS0, GS1 and GS2 in terms of the lateral body oscillations.

A novel monitoring system using computer vision with image processing software was developed to automatically collect information relating to the back surface area from video footage of broilers with different gait scores that had been individually placed within a test corridor. The automatically extracted lateral body oscillations were evaluated and the results of this research showed a similarity with the results of [28]. They also found that there was a big lateral oscillation during walking in domestic turkeys [28]. As also concluded by [28] this “waddle” can be ascribed to the need for animal to bring their bodies directly over the stance foot for stabilize.

Table 1. The lateral body oscillations (LBO) of broilers.

Lateral Body Oscillations (in pixels)					
Exp.	GS0	GS1	GS2	GS3	GS4
1	7702	7745	7475	9892	12141
2	7513	7865	7325	9654	12145
3	7618	7698	7421	9774	12245
4	7642	7687	7369	9712	12219
5	7598	7852	7401	9759	12315

The results of this research showed similarity also with the results of previously published studies about the lame broilers usually run with bigger lateral body oscillations than healthy broilers ([11], [12]-[26]).

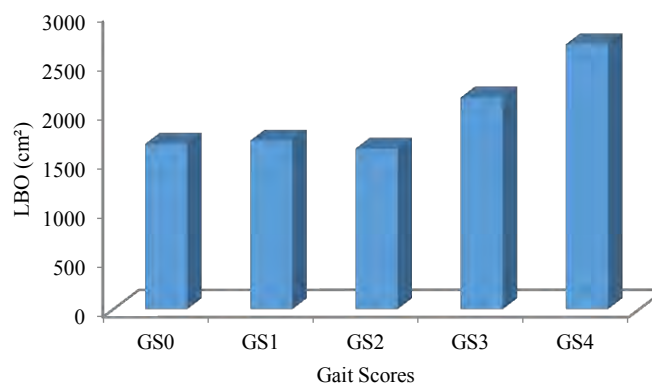


Figure 2. The lateral body oscillations (LBO) of broiler chickens with different gait scores.

When broilers were promoted by both legs the center of body was placed between the feet and body weight was shared between two legs, resulted in balance. The results of this research showed similarity also with the study of [12] about that the increased lateral movement was related with raised lameness degree. Since broiler morphology pushes their legs further apart [15], with step width increasing markedly in lameness (Farage and Elwar, 1989), they move their body laterally towards the position of each sequential supporting leg, resulting in the stereotypical side-to-side waddle ([1], [16]-[26]). The findings of this research support this since the sound broilers collectively had the least lateral body oscillation and the lame broilers had the most. However it should be stressed out that in this study, only the broiler breed Ross 308 which is the most popular breed in Europe was used in order to produce comparable data. The lateral body oscillations can be different in other breeds.

Table 2. The statistical results of the lateral body oscillations of broilers.

Gait scores	Body area (cm ²)	LBO (cm ²)
	Mean±std	Mean±std
GS0	43.07±3.21 ^a	1675.21±15.16 ^a
GS1	45.21±3.17 ^a	1709.27±18.55 ^a
GS2	44.45±4.11 ^a	1627.60±12.37 ^a
GS3	46.56±4.09 ^a	2146.80±19.41 ^b
GS4	37.10±3.41 ^b	2686.86±16.04 ^c

On the other hand, there are some advantages to use this automated monitoring systems to assess lameness and welfare of broilers. The most important advantage of these types of automated monitoring systems is that measurements may be taken automatically and continuously during the life-span of broilers with a completely non-intrusive and non-invasive way. These systems also do not include the biosecurity risk of assessors visiting different broiler houses to score and assess the broilers [18].

100. CONCLUSION

Since important correlations were determined between the lateral body oscillations and gait score level of broilers, the results of this research suggest that this image analysis system has the potential to assess the lameness of broilers. The proposed system has potential but of course needs further optimisation to improve accuracy and also needs to be validated in different field conditions, on different types of chickens. To increase the accuracy of the system, a high-resolution camera with a higher frame rate can be used in the future experiments. If validation is successful, the developed monitoring system is a promising tool for analysing some feature variables of broilers and indicating lameness.

REFERENCES

- [213]. Abourachid. A. (1991) Comparative gait analysis of two strains of turkey, Meleagris gallopavo. Br Poult. Sci. 32, 211-277.
- [214]. Aydin A, Cangar O, Eren Ozcan S, Bahr C, Berckmans D 2010. Application of a fully automatic analysis tool to assess the activity of broiler chickens with different gait scores. Computers and Electronics in Agriculture 73: 194-199.
- [215]. Aydin, A., Bahr, C., Pluk, A., Leroy, T., Berckmans, D., 2013. Automatic Identification Of Activity And Spatial Use Of Broiler Chickens With Different Gait Scores. Transactions Of The Asabe 56 (2013) 1123-1132.
- [216]. Aydin, A., Bahr, C., Berckmans, D., 2015. Automatic classification of measures of lying to assess the lameness of broilers. Animal Welfare 24, 335-343.
- [217]. Bauer M, Heissenhuber K, Damme K, Köbler M 1996 Welche roilerherkunft eignet sich? DGS Magazin 44: 22-26.
- [218]. Berg C, Sanotra GS 2003 Can a modified latency-to-lie test be used to validate gait-scoring results in commercial broiler flocks? Animal Welfare 12: 655-659.
- [219]. Betts, R. P. & Duckworth. T. (1978) A device for measuring plantar pressures under the sole of the foot. Engineering in Medicirze 7(4f, 223-228.
- [220]. Betts, R. P., Franks, C. I. & Duckworth; T. (1980a) Analysis of pressure and loads under the foot. Pti II: Quaatitation of the dynamic distribiltion. Clinical Physics and Physiological Measures I (2), 113-124.

- [221]. Betts, R. P., Duckworth, T., Austin, I. G., Crocker, S. P. & Moor & S. (1980b) Critical light reflection at a plastic/glass interface and its application to foot pressure measurements. *Journal of Mechanical Engineering and Technology* 4 (3), 136-142.
- [222]. Cangar O, Leroy T, Guarino M, Vranken E, Fallon R, Lenehan J, Meed J, Berckmans D 2008 Automatic real-time monitoring of locomotion and posture behaviour of pregnant cows prior to calving using online image analysis. *Computers and Electronics in Agriculture* 64: 53–60.
- [223]. Caplen G, Hothersall B, Murrell JC, Nicol CJ, Waterman Pearson AE 2012. Kinematic analysis quantifies gait abnormalities associated with lameness in broiler chickens and identifies evolutionary gait differences. *PLoS ONE* 7(7): e40800. doi:10.1371/journal.pone.0040800.
- [224]. Caplen, G., Colborne, G.R., Hothersall, B., Nicol, C.J., Waterman-Pearson, A.E., Weeks, C.A., Murrell, J.C. 2013. Lame broiler chickens respond to non-steroidal anti-inflammatory drugs with objective changes in gait function: A controlled clinical trial *Veterinary Journal*, 196 (3), pp. 477-482.
- [225]. Chodera, J. (1957) *FU-Czechoslovakian Academy of Sciences, Prague, Yols* 1-3.
- [226]. Corr SA, McCorquodale CC, Gentle MJ (1998) Gait analysis of poultry. *Res Vet. Sci* 6: 233–238.
- [227]. Corr S A, Gentle M J, McCorquodale CC, Bennett D 2003 The effect of morphology on walking ability in the modern broiler: a gait analysis study. *Anim. Welfare*. 12(2):159-171.
- [228]. Corr SA, McCorquodale CC, McGovern RE, Gentle MJ, Bennett D (2003) Evaluation of ground reaction forces produced by chickens walking on a force plate. *Am J Vet Res* 64(1): 76–82.
- [229]. Corr SA, McCorquodale CC, McDonald J, Gentle M, McGovern R (2007) A force plate study of avian gait. *J Biomech* 40: 2037–2043.
- [230]. Dawkins MS, Lee HJ, Waitt CD, Roberts SJ 2009 Optical flow patterns in broiler chicken flocks as automated measures of behaviour and gait. *Applied Animal Behaviour Science* 119(3-4), 203-209.
- [231]. Gatesy, S.M., Biewener, A.A. (1991). Bipedal locomotion: effects of speed, size and 795 limb posture in birds and humans. *J. Zool.* 224, 127-147.
- [232]. Kestin SC, Knowles TG, Tinch AE, Gregory NG 1992 Prevalence of leg weakness in broiler chickens and its relationship with genotype. *Vet. Rec.* 131: 190–194.
- [233]. Kestin SC, Gordon S, Su G Sorensen P 2001 Relationships in broiler chickens between lameness, live weight, growth rate and age. *Vet. Rec.* 148(7):195-197.
- [234]. Knowles TG, Kestin SC, Haslam SM, Brown SN, Green LE, Butterworth A, Pope SJ, Pfeiffer D, Nicol CJ 2008 Leg disorders in broiler chickens: prevalence, risk factors and prevention. *PLoS One*, 3: e1545.
- [235]. Leroy T, Vranken E, Van Brecht A, Struelens E, Sonck B, Berckmans D 2006 A computer vision method for on-line behavioral quantification of individually caged poultry. *Transactions of the ASABE* 49 (3): 795-802.
- [236]. McKay JC, Barton NF Koerhuis ANM, McAdam J 2000 The challenge of genetic change in the broiler chicken. Pages 1–7 in *The Challenge of Genetic Change in Animal Production*. Edinburgh, UK.
- [237]. Naas IA, Almeida Paz, ICL, Baracho MS 2010 Assessing locomotion deficiency in broiler chicken. *Scientia Agricola*, v.67, p.129-135.
- [238]. Reiter K, Bessei W (1997) Gait analysis in laying hens and broilers with and without leg disorders. *Equine Vet J Suppl* 23: 110–112.
- [239]. Reiter K. 2002. Analysis of locomotion of laying hen and broiler. *Archiv für Geflügelkunde* (2002), Vol. 66 (3), 133 - 140
- [240]. Stover, KK; Brainerd, El; Roberts, T.J., 2015. Supersize me: Extreme body mass in domestic turkeys influences locomotor mechanics. *Integrative and comparative biology* 55, E180.
- [241]. Thorp BH and Dduff SRI 1988 Effect of exercise on the vascular pattern in the bone extremities of broiler fowl. *Research Veterinary Science* 45: 72-77.
- [242]. Weeks CA, Danbury TD, Davies HC, Hunt P, Kestin SC 2000 The behaviour of broiler chickens and its modification by lameness. Department of Clinical Veterinary Science, University of Bristol, Langford, Bristol BS40 5DU, UK *Applied Animal Behaviour Science* 67: 111–125.
- [243]. Vestergaard KS and Sanotra GS 1999 Relationships between leg disorders and changes in the behaviour of broiler chickens. *Veterinary Record*, 144: 205–209.

Assessment of the Mining Accidents from the Stand Point of Occupational Health and Safety

Cem Şensöğüt^{1*}, Özer Ören²

Abstract

Mining sector is one of the ancient and the leading sectors which have taken a place in historical time course. Increase in the demand to better life standards together with the increase in the number of living people in the world has also brought the growth in the production especially in mining sector which takes an important role in the supply of raw material. Taking no precautions for the occupational health and safety is unfortunately the main reason for the disasters occurred in the working places causing many fatalities as well as the loss of goods. The main drawback for not taking the preventive necessary measures is because of not comprising the occupational health and safety culture sufficiently.

In the present study; the reasons for the occupational accidents originates in underground mines and the significant mining accidents took place in Turkey and in the world along with the measures to be taken from the view of the safety and health at work have been emphasized.

Keywords: Mining, mining disaster, occupational health and safety

101. INTRODUCTION

Human beings have consumed and still continue to consume many things to stay alive as a matter of course during their lives from an earlier time to the present day. Apart from satisfying their first priority needs, they also consume some other materials in order to compensate their basic needs of shelter, dressing up etc. for a safer and healthier life. Most of these materials are obtained from the productions of mines. Especially after the industrial revolution, almost all of the technological equipments and technology use the minerals obtained from natural sources at different rates in order to ease the life. The majority of mines were formed in deeper parts of the ground. The sector of mining is one the oldest sector arisen to present these sources to the benefit of human beings. There are numerous circumstances experienced during the mining activities such as exploiting, hauling to the surface and separating the impurities of these natural sources which cause occupational accidents by means of leaks of poisonous and suffocating gases, explosive gases or dusts, collapsing of hanging wall of mines, flooding, malfunctioning mining equipment etc. The main intention from the point of occupational health and safety should be zero work accident or pull the rate of accidents down as much as possible.

102. THE MAIN REASONS FOR WORK ACCIDENTS IN MINES

Here, occupational accidents frequently occurring mainly in underground mines and their causes are represented. Activities realized in underground working can be fundamentally outlined as follows (Figure 1):

^{1*} Corresponding author: Dumlupinar University, Department of Mining Engineering, 43100, Kütahya, Turkey. sensogut@dumlupinar.edu.tr

² Dumlupinar University, Department of Mining Engineering, 43100, Kütahya, Turkey. ozer.oren@dumlupinar.edu.tr

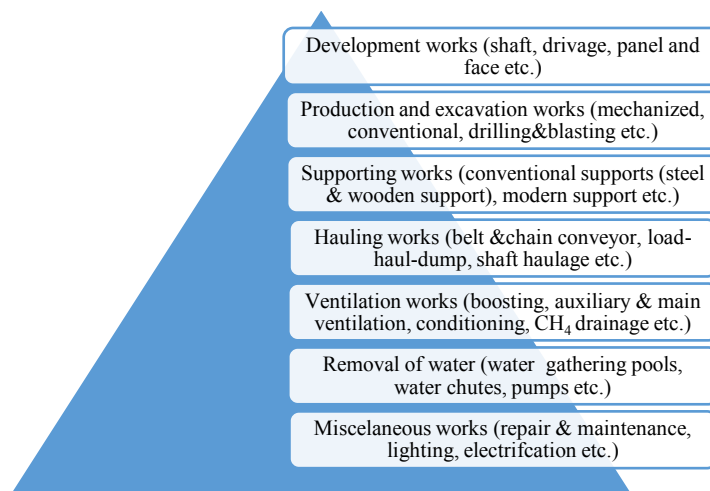


Figure 1. General works carried out in underground mines

During these activities performed in underground mines, both endogenous and exogenous fires can be composed. Additionally, when the concentration of the gases and dusts generated builds up to a certain value and reacts with a source of heat, it may cause explosions resulting in very high pressures. Workers may be trapped in a section of mine due to the fires induced after the explosions. Similarly, gases, which is not kept under control and not swept out of the mine by the ventilation system, such as methane, carbon monoxide, carbon dioxide, sulphur dioxide, oxides of nitrogen etc. may have an effect of poisoning and suffocation on the miners with respiration. Drilling and blasting works are frequently employed for both development and excavation purposes in underground mines operated with conventional production methods. It is very often for the workers to get jammed under the rock masses fallen either from roof or side walls of mines or drifts following blasting works as the records state.

Additionally, rock parts fallen from hanging wall regardless of their sizes following sudden discharge of mine props after blasting works or seismicity of ground may also be the significant reasons for mining accidents. Miners may have accidents caused by electrical shocks or jamming during the work of mechanical and electro-mechanical machineries. It is not very occasional, however the occupants of an underground mine may lose their lives as a result of drowning induced by flooding of waters either subsurface or surface sourced. Main components taking place in an occupational accident regardless from the cause are illustrated in Figure 2.

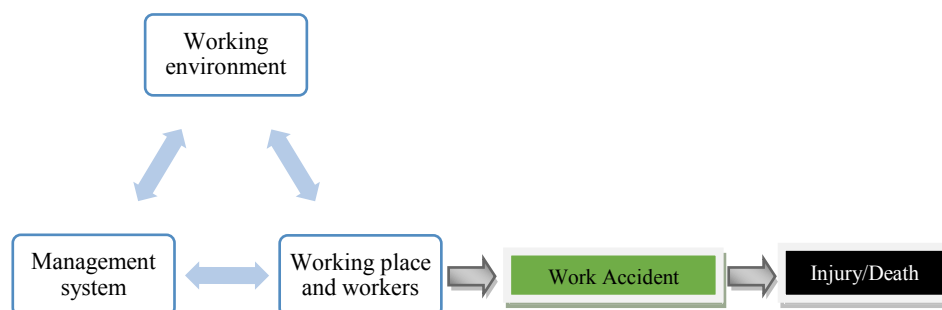


Figure 2. Main components of an occupational accident

As many of these accidents are aggravated by lack of regulation and/or enforcement, around the world, thousands of miners die or are injured each year from mining accidents.

103. THE MOST EXTRAORDINARY MINING DISASTERS IN THE WORLD

The biggest mining accidents according to the records of some countries in the world are given in Table 1.

Table 1. The most catastrophic mining accidents in the world

Mine	Date	Deaths	Cause	Explanation
Oaks Coal Field (United Kingdom)	12 September 1866	388	Methane and coal dust explosion	It was thought to be caused by the work of driving of a drift near the main seam which ignited pockets of firedamp. An initial blast may have been the main reason triggering a chain reaction of the firedamp and coal dust explosion [1].
Brunner Coal Mine (New Zealand)	26 March 1896	65	Exposure to CO ₂ & nitrogen mixture after explosion	After hearing an explosion, the men went underground for investigation were found unconscious from black damp together the rest of the miners also suffered from the noxious gases. It is biggest mining disaster in the history of New Zealand [2].
The Mount Kembla Coal Mine (Australia)	31 July 1902	96	Methane and coal dust explosion	The Royal Commission held between March and May of 1903 determined that methane and coal-dust were responsible for the explosion, and concluded that only the substitution of naked lights with safety lamps could have prevented the disaster. It is biggest mining disaster recorded in the history of Australia Continent [3].
Courrières Coal Mine (France)	10 March 1906	1099	Explosion after coal dust fire	The biggest mining disaster in French history was likely induced by the ignition of coal dust, or probably by a miner's lamp (they used open flames rather than electric lights in 1906) [4]. Today, it is still not clear what caused the explosion.
Monongah Coal Mine (USA)	6 December 1907	362	Methane and coal dust explosion	It is very doubtful whether the real causes of the explosion will ever be known. The verdict anticipated was that the explosion was caused by a blow-out shot igniting the dust [5]. It is known as the worst mining disaster in the continent of America.
Senghenydd Coal Field (Wales-UK)	14 October 1913	439	Coal dust explosion and CO poisoning	An arc from an electric bell was thought to ignite a tremendously dangerous mixture of methane gas and coal dust, known as firedamp by the miners [6].
Stag Canon No. 2 Coal Mine (USA)	22 October 1913	263	Explosion	An improper blasting of dynamite was thought to cause the explosion of coal dust [7].
Hillcrest Coal Mine (Canada)	19 June 1914	189	Exposure to CO ₂ after methane explosion	It was the worst coal mining disaster occurred in Canada. After the explosion of methane, the level of carbon dioxide was estimated to be at a rate of 50% causing the deaths of miners [8].
Mitsubishi Hojo Coal Mine (Japan)	15 December 1914	687	Methane explosion	The disaster took place in the literature as Japan's deadliest mine accident. The reason of the deaths was the explosion of methane [9].
Granite Mountain – Copper Mine (USA)	8 June 1917	163	Fire	The tragedy was caused by the fire and deadly smoke fanned through the stopes and shafts to connecting mines. The fire was the deadliest disaster in metal mining history [10].
West Virginia Hawk's Nest Tunnel (USA)	1927	476	Silicosis	The disaster happened in Gauley Bridge, West Virginia blasting away at the rock in order to build a tunnel produced the silica dust causing the death of 476 with taking no precaution against the inhalation of the dust [11].
Benxihu Coal Field-Honkeiko Coal Mine (PRC)	26 April 1942	1549	Exposure to CO after coal dust explosion	It is the most deadly accident of mining history around the world. In the record of Soviet researchers, it was revealed that after the explosion of gas and coal dust, most of the miners died from CO poisoning [12].
Braden Copper-El Teniente Mine (Chile)	19 June 1945	355	Exposure to CO after a fire	Reason for the death of the miners was carbon monoxide poisoning due to a fire broke out near the mine, trapping the workers. Along with improperly marked emergency exits, the workers were unable to escape the flames [13].
Le Bois du Cazier Coal Mine (Marcinelle-Belgium)	8 August 1956	262	Fire	It was the worst ever disaster in Belgian mining history. A fire broke out in the coalface underground and spread to all levels of the mine, trapping the miners to death. After this deadly event, a commission for safety in mines was established in September 1956 [14].
Coalbrook Coal Mine (South Africa)	21 January 1960	435	Exposure to methane after collapse	The accident was believed the worst mine disaster in South Africa and have been caused by the disintegration of some 900 underground pillars spreading over an area of 3 km ² causing a massive collapse and trapping more than half of the miners [15]. The most of the miners suffered from methane exposure.
Laobaidong Coal Field (PRC)	9 May 1960	684	Methane explosion	A methane gas explosion took the lives of 684 miners, and it was the second most tragic and disastrous mine accident in Chinese history [16].
Mitsui Miike Coal Mine (Japan)	9 November 1963	458	Coal dust explosion and CO poisoning	Coal was hauled to the surface by the four-wheeled carts in convoy of ten. After derailling of a cart on the 3rd row, rest of the carts began a free-fall run to the bottom of the mine. They ran free for about 360 metres, having a speed of approximately 120 km/h. Then all of the carts were derailed and turned over. At this point the explosion took place producing the spark that ignited the coal dust creating CO and causing a disastrous poisoning situation [17].
Dhanbad-Dhori Coal Mine (India)	27 May 1965	375	Methane and coal dust explosion	The reason of the disaster was an explosion in Dhori colliery near Dhanbad, it was a firedamp and coal dust explosion. The initial ignition was suspected to have been caused by the hurricane lantern of a person who entered underground [18].
Wankie Coal Field (Zimbabwe)	6 Nisan 1972	427	Methane explosion	A massive methane gas explosion occurred ripping through the workings with unpredictable destruction. It was the worst mining disaster in the long history of Rhodesian mining [19].
Dhanbad-Chasnala Coal Mine (India)	27 December 1975	372	Coal dust explosion	According to the records, the coal dust explosion in the mine led to a blast damaging the roof barrier with a huge water body located above it. Most of the deaths were because of the enormous flooding of water into the mine [18].
Prestavel Mine (Tesoro-Italy)	19 July 1985	268	Collapse of tailings dam	It is one of the most deadly two accidents took place in Italy, collapsing of the tailing dams of Prestavel Mine caused the death of the workers as well as the demolition of 63 buildings and 8 bridges [20].
Nambija Mine (Ecuador)	9 May	300	Landslide	Nambija mine disaster was caused by a landslide occurred in a distant mining settlement in the south-eastern part of Ecuador [21]. A definite number is

	1993			never known, as there was no record about the number of people living or working in Nambija.
Ulyanovskaya Coal Mine (Russia)	22 March 2007	107	Methane and coal dust explosion	It was known as Russia's worst mining disaster according to the records. The explosion ripped through the private coal mine in the Kemerovo region could have been caused by coal dust, but was more likely caused by miners breaking through into a pocket of methane gas trapped deep underground as officially announced [22].
A Gold Mine in Jebel Amir (Sudan)	29 April 2013	109	Collapse of mine	As a result of collapse in an unlicensed gold mine, 109 miners including 9 people of the rescue team died [23].

When the mining history of the world is analysed, it may be observed that the disasters having the most casualties and devastations generally took place in the coal mines. The most deadly mining accident occurred in Honkeiko Coal Mine (Benxihu Coal Field – China) in 1942 and 1549 miners lost their lives as seen from Table 1. The reason of the disaster in concern was the explosion caused by the mixture of methane and coal dust.

104. MINING ACCIDENTS IN TURKEY

Approximately 3800 miners have lost their lives in the accidents taken place in mines since 1941 together with the injuries over 100.000 in Turkey [24]. The causes of these accidents are mostly encountered as methane and dust explosion, fire, gas poisoning and suffocation, collapse of hanging or sidewalls of the strata. The city where these occupational accidents often occurred in Turkey is Zonguldak and its province. The worst disaster happened and recorded in mining sector of Turkey took place in Soma District of Manisa on 13th May, 2014 resulted 301 occupants in losing their lives as well as 162 injuries [25].

The list of mostly known and recorded occupational accidents occurred in Turkish underground mines is illustrated in Table 2 [26].

Table 2. Significant mining accidents appeared in underground mines in Turkey

Mine	Date	Deaths	Explanation
Armutçuk Bituminous Coal Mine (Zonguldak)	7 March 1983	103	Methane explosion
Kozlu Bituminous Coal Mine (Zonguldak)	10 April 1983	10	Methane explosion
Yeni Çeltik Coal Mine (Amasya)	14 July 1983	5	Methane explosion
Kozlu Bituminous Coal Mine (Zonguldak)	31 January 1987	8	Collapse
Amasra Bituminous Coal Mine (Zonguldak)	31 January 1990	5	Methane explosion
Yeni Çeltik Coal Mine (Amasya)	7 February 1990	68	Methane explosion
Kozlu Bituminous Coal Mine (Zonguldak)	3 March 1992	263	Methane explosion
Sorgun Coal Mine (Yozgat)	26 March 1995	37	Methane explosion
Aşkale Coal Mine (Erzurum)	8 August 2003	8	Methane explosion
Ermenek Coal Mine (Karaman)	22 November 2003	10	Methane explosion
Bayat Coal Mine (Çorum)	9 August 2004	3	Methane explosion
Küre Copper Mine (Kastamonu)	8 September 2004	19	Fire
Gediz Coal Mine (Kütahya)	21 April 2005	18	Methane explosion
Dursunbey Coal Mine (Balıkesir)	2 June 2006	17	Methane explosion
Mustafakemalpaşa Coal Mine (Bursa)	10 December 2009	19	Methane explosion
Dursunbey Coal Mine (Balıkesir)	23 February 2010	13	Methane explosion
Karadon Bituminous Coal Mine (Zonguldak)	17 May 2010	30	Methane explosion
Kozlu Bituminous Coal Mine (Zonguldak)	8 January 2013	8	Methane explosion
Eynez Coal Mine (Soma-Manisa)	13 May 2014	301	Fire
Ermenek Coal Mine (Karaman)	28 October 2014	18	Flooding

As Table 2 is analysed, if mine accident took place and resulted with 19 deaths in Küre Copper Mine is excluded, the remaining accidents occurred in coal mines with a main reason of almost methane explosion.

105. EVALUATION OF MINING ACCIDENTS IN THE LIGHT OF SAFETY AT WORK

When evaluating the mining accidents faced in Turkey and in the world together, the higher similarities amongst the reasons may be noticed. For instance, accidents sourced by methane or dust explosion may be pronounced as the accidents with more than one death and injury at the same time. The precautions which were not taken in these mines may be listed as;

- Preparation of emergency action plans,
- Taking heed of proper ventilation works,

- Appropriate continuous monitoring of gas make in the mine,
- Convenient supervision and inspection works,
- Vocational training of occupants in parallel with the improvements arising in technology,
- Encouraging the culture of occupational health and safety,
- Enforcement of legal aspects.

Working environment in terms of health and safety at work is important for preventing the occupational accidents before it had occurred by means of adopting a high level safety culture and even making this idea as the life style (Figure 3). This may only be possible by training all occupants in a working place regardless from their position for occupational health and safety. Therefore, the accidents, which may occur in spite of taking all remedies, will be minimized.

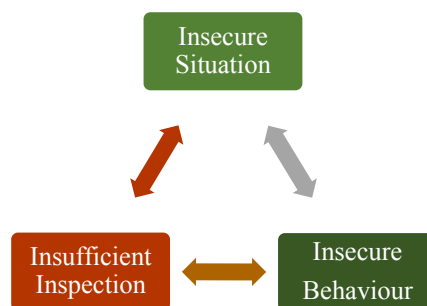


Figure 3. Risk management in occupational health and safety

In short, all estimated precautions will be taken at the working places such as mines before the accidents to happen by encouraging proactive approach instead of reactive approach.

Supervision and inspection of underground mines are highly difficult; however this task should be carried out by a sufficient number of personnel. An underground mine may be consisted of many works emphasised in Figure 1 and located very far away from surface connections. The very first and the important task, which should be realized by the mine management, are to supply the workers continuously with the fresh air. It is also specifically important to consistently monitor the mine air in order for taking necessary measures before, during and after a fire or an explosion that may occur. In case of methane existence and continuity in the mine, methane drainage works should be made. Mines should periodically be inspected by the centralized administration, sanctions should be enforced in case of a fail in occupational health and safety works or determination of deadly risks.

106. RESULTS AND SUGGESTIONS

A common mind should be composed by the occupants, the employers and the mechanism holding the legal enforcements in hand in order to minimize the level of deadly accidents to a possible degree. It is more important to put forward the necessary actions before the accidents occur not after. The workers of an underground mine may face not only with the occupational accidents but also with the occupational diseases depending on the working environment. Surveillance of working environment and improving working conditions for the occupants should have a priority in the responsibilities of the employer. In spite of taking all precautions necessitated, a remediation cannot be realized for the risky events, and then the occupants should be provided with personal protective equipments by the employers.

Remedies taken for the occupational health and safety are not only a responsibility for the right of workers to live but also a contribution in order to prevent the lost of national income occurring due to accidents and diseases as well as an aid to ensure the productivity and safety of production.

REFERENCES

- [244]. <http://www.bbc.com/news/uk-14941020>
- [245]. <http://www.TeAra.govt.nz/en/speech/7453/brunner-mine-disaster-1896>
- [246]. <http://www.mineaccidents.com.au/mine/90/mt-kembla>
- [247]. <http://seanmunger.com/2014/03/10/fire-in-the-dark-the-astonishing-story-of-the-courrieres-mine-disaster/>
- [248]. <http://www.wvculture.org/history/disasters/monongah03.html>
- [249]. <http://www.mirror.co.uk/news/real-life-stories/senghenydd-coliery-disaster-439-victims-2364024>
- [250]. <http://www.msha.gov/news-media/events/2016/02/09/stag-canon-mine-disaster-1923>
- [251]. <http://coalminersmemorial.tripod.com/hillcrestminedisaster.html>
- [252]. <http://5bbambi.weebly.com/social-studies/mining-disaster/#/>
- [253]. <http://www.butteamerica.com/gmtn.htm>
- [254]. <http://tunneltalk.com/Hawks-Nest-Tunnel-tragedy-Sept09.php>
- [255]. http://sputniknews.com/in_depth/20150901/1026441814.html
- [256]. <http://www.history.com/this-day-in-history/fire-traps-262-miners>
- [257]. <http://www.sahistory.org.za/dated-event/more-400-miners-are-killed-underground-collapse-coalbrook-mine>
- [258]. https://en.wikipedia.org/wiki/1945_El_Teniente_mining_accident
- [259]. <http://www.worldatlas.com/articles/worst-mining-disasters-in-human-history.html>
- [260]. <http://archive.unu.edu/unupress/unupbooks/uu35ie/uu35ie0f.htm#iv>. the miike coal mine explosion of 9 November 1963
- [261]. <http://www.mining-technology.com/features/feature-world-worst-coal-mining-disasters-china/>
- [262]. <https://www.newsday.co.zw/2012/06/06/2012-06-06-hwange-mine-tragedy-revisited/>
- [263]. Luino, F. & Graff, J.V.D., "The Stava Mudflow of 19 July 1985 (Northern Italy): a disaster that effective regulation might have prevented", *Natural Hazards and Earth System Sciences*, 12, 1029-1044, (2012)
- [264]. https://en.wikipedia.org/wiki/Nambija_mine_disaster
- [265]. <http://www.npr.org/templates/story/story.php?storyId=9072275>
- [266]. <http://news.yahoo.com/photos/worst-mining-disasters-1400093088-slideshow/worst-mining-disasters-photo-1400094626850.html>
- [267]. http://www.kanalb.com.tr/haber.php?HaberNo=55702#.U3VDmoF_tio
- [268]. <http://www.ndtv.com/world-news/dozens-go-on-trial-over-turkeys-worst-mining-disaster-754434>
- [269]. Report for the Occupational Accidents in Mining Sector (in Turkish), The Chamber of Mining Engineers of Turkey, June, Ankara, p152, (2010)

The Role and the Importance of Universities in Establishing the Culture of Occupational Health and Safety

*Cem Şensöğüt**

Abstract

According to the records of the International Labour Organisation (ILO), an occupant dies as a result of a work-related accidents or disease while 153 workers have an occupation-related accident every 15 seconds in the world. Under the light of these figures, 5760 workers lose their lives due to the occupational accidents or diseases every day resulting in more than 2.1 million deceases per year. Additionally, it may be pronounced that 322 million job oriented accidents take place annually with a similar evaluation [1]. The same records also illustrates that the economic burden of these accidents occurred may reach up to 4% of global gross national product each year.

In addition, improper implementation of occupational health and safety thought may bring about an economic loss up to 10-20% of the gross domestic product of a country as emphasised in the World Health Organization (WHO) registries [2].

The safety culture is a life style targeting occupational health and safety with a top priority. There is knowledge in base of safety and this knowledge transformed into a style of living forms the safety culture. In the case of not interiorizing the safety culture, work related accidents will be inevitable. Furthermore, an institution's safety culture reflects the behaviours and attitudes of its occupants towards the job based hazards. From this perspective, the safety culture espoused to the personnel and the students of a university may cause the university to work in accordance with the safety culture as well as it affects its graduates positively in their inbred behaviours at the institutions for which they are to work in the future resulting in the working life retrieving to a better level. This paper examines the safety culture together with the contribution supplied by the universities

Keywords: *Safety culture, universities, occupational health and safety*

107. INTRODUCTION

Former General Secretary of United Nations, Kofi Annan, stated that employing right occupational health and safety system at work is not only a sound economic policy but also it is a basic human right [2]. Although the right of living for human beings is the most essential right, countless occupants lose their lives at work every day in the world. According to the records of ILO, number of deaths caused by the occupational disease is over that induced by the work related accidents. In order to prevent this scary reality from happening repeatedly and stop the loss of lives at work occurring due to occupational accidents, communal awareness should be realized at first and following that safety culture should be established. Therefore, universities have a lot to do for this respect.

* Corresponding author: Dumlupinar University, Department of Mining Engineering, 43100, Kütahya, Turkey. sensogut@dumlupinar.edu.tr

108. OCCUPATIONAL HEALTH AND SAFETY CULTURE

Researches carried out on the safety culture by now, have shown that there is not any acceptable compromise on the matter as they appeared with different definitions of safety culture at work [3]. Occupational health and safety culture stated mostly and briefly as safety culture found a place in the research works and the literature after the disaster of Chernobyl in 1986 was stated under 13 different definitions according to Wiegmann et al. [4]. However, the identification made in 1993 is still approved

today by all parts [5-7]. By this description, the safety culture of an organization is a product of individual or group values, attitudes, thoughts, competencies and behaviour models.

Every one prolonging their lives in a society or culture shows a similar behaviour in any event and thinks that it is a standard and normal attitude. In other word, safety culture of an organization is related with its cooperative applications, tendency to accept or tolerate the risk, controlling way of hazards and reactions against accidents or near miss events [8, 9]. Safety culture has also become a research topic carried out from different perspectives such as psychology, engineering, sociology, anthropology and organizational theory. In taking this distinction into consideration, Guldenmund [10] tried to explain the approaches towards to the safety culture in three sections including analytic, pragmatic and academic (Table 1).

Three main parameters belonging to the positive safety culture can be seen in Figure 1 [11];

Table 1 Approaches made for safety culture [3, 10]

Main approach	Time focus	Information aimed to retrieve	Research characteristics	Assessment strategy and methods
Academic (anthropological)	Past	Qualitative information	Descriptive	Fieldwork, ethnographical-inspired methods (e.g. document analysis, observations, focus groups, interviews)
Analytical (psychological)	Present	Quantative information	Descriptive	Safety climate scales, questionnaires
Pragmatic (experienced based)	Future	Safety culture level	Normative, prescriptive	Behaviourally Anchored Rating Scales (BARS)

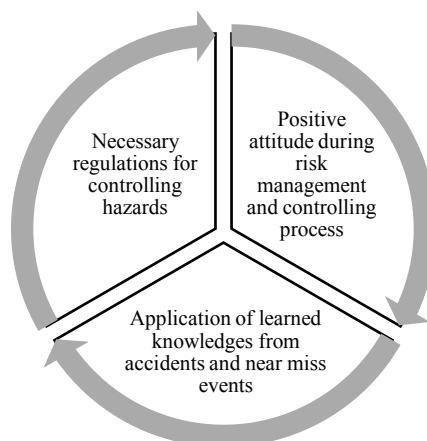


Figure 1 Basic parameters of positive safety culture

Recent working fields established due to the rapid development occurring in technology and the precautions not taken parallel with this improvement may cause facing with serious problems in terms of safety and health at work. Occupational accidents and diseases arising because of not taking these measures as serious as possible will result in significant losses in relation to both economic and social

life. Additionally, change of safety culture in these new working sites may take very long time. Therefore, the plans towards this purpose should precisely be made and thoughtfully chased after. In order to obtain a successive result in this change, the personnel of an organization from top to bottom should have a belief in it. The change expected in safety culture may be made possible by specified models of behaviour changes. However, these models may be successful for one organization while they may be not for another. The model presented in Figure 2 may be assistive in choosing a right model [12].

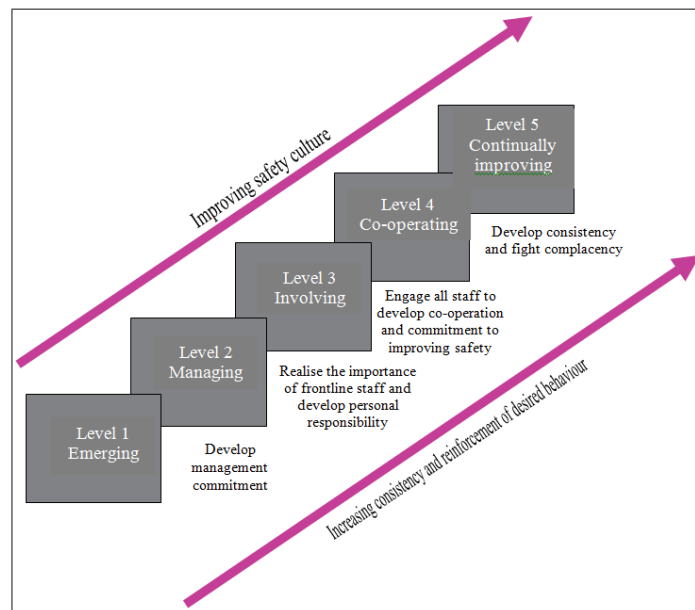


Figure 2 Formation of safety culture [12]

109. TARGETS IN THE FORMATION OF OCCUPATIONAL HEALTH AND SAFETY CULTURE

Targets foreseen to establish occupational health and safety culture can be outlined under the headings given below when taken globally:

- Composing of occupational health and safety awareness for each stage at work is a prime concern,
- Exposing the present situation in order to establish a base for the awareness formed and determination of expectations should be realized for the workers by means of questionnaires,
- Improvements to be made towards the legal aspects and their implementations should be carried out in accordance with up to date technological level ,
- Supplying the organizations with consultancy for the field of occupational health and safety at the highest level in order to educationally guide them,
- Environmental monitoring should continuously be made and improvements should be realized when necessary to increase the working productivity while decreasing accidents at work by giving the opportunity of ergonomic working conditions to the workers,
- Establishing co-operation with national and international organizations,
- Formation of an improved data base related with occupational accidents and diseases,
- Bringing in a speed for setting up an awareness of safety culture by the campaigns utilising all written and visual mediums,

- Decreasing the events of occupational accidents and diseases to a minimum level as much as possible.

110. PARTNERS IN DEVELOPMENT OF OCCUPATIONAL HEALTH AND SAFETY CULTURE

Safety is a positive value under normal conditions and also an important phenomenon for the salvation of injuries, saving of lives and increasing of productivity and products. In the course of this speech, if the safety is actively applied and seen as an important matter by senior management, workers also take the matter seriously and become a part of it [13]. A reasonable safety culture is consisted of the parameters illustrated in Figure 3. In the realization of such a safety culture, many partners should take a part for it and be decisive on three matters given below [14]:

- 1- In the verification of occupational health and safety management system for organizations,
- 2- In the desires of workers for being a part and promoting of the system, and
- 3- In the attitudes towards some apprehension to stop the attempts for safety culture.

The partners for improving and realizing the safety at work such as;

- 1- Government,
- 2- Employer,
- 3- Workers-unions,
- 4- Universities and
- 5- Occupation bodies have variety of responsibilities [15].



Figure 3 Factors promoting the safety culture

111. PLACE OF UNIVERSITIES IN SAFETY CULTURE ADOPTION

Universities taking a part amongst the partners which may provide significant supports in adopting and improving a strong safety culture as a style of life should have a role model in scientifically analyzing the events comprising hazards. Therefore, both the tenderness of academic personnel at the universities in terms of safety culture will develop and research activities towards for determining drawbacks in the formation of safety culture will be realized. By enforcing the safety culture in its organization (university-institute), works to become role model will be carried out in the highest level. Additionally in case of completing their educations, both undergraduate and graduate students will have important

tasks for establishing safety cultures in their organizations. Universities with strong safety culture will be more effective in the situations such as determination, evaluation and decreasing the influence of hazards. A scientific method to be used for the analysing of hazards is seen in Figure 4 [13]:

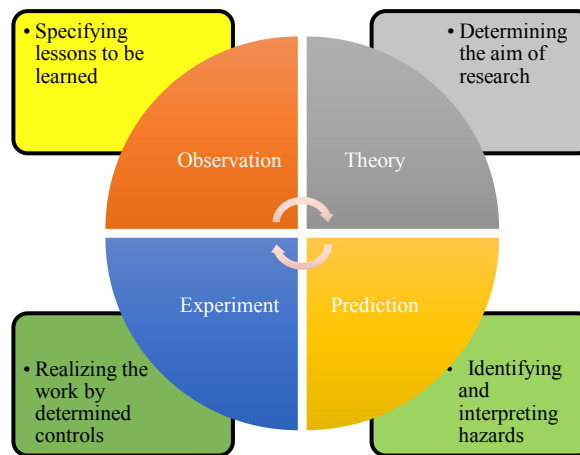


Figure 4. Integration of hazard analysis with the scientific procedure [13]

Universities have the following duties in developing of safety culture [15]:

- 1- Contribution to social policies from the point of health and safety at work,
- 2- Establishing a scientific and sound recording system,
- 3- Analysis of occupational accidents and diseases by scientific techniques,
- 4- Providing the workforce planning to work for the field of occupational health and safety with necessary training,
- 5- Contribution to continuous training of workers who aim to work for the area of health and safety at work in parallel with the improvements in technology after graduation,
- 6- Realizing the research activities related to safety culture and
- 7- Comprising of laboratories and academic environments related to the safety culture.

112. RESULTS AND SUGGESTIONS

It is obviously very important for all social sides to put forward whatever they can for developing the safety culture. However, there should be a responsible body for it. An organizational body which has the legal force and the control mechanism may realize this task. This institution should inform the social sides and guide for the application of legal aspects by carrying out the research works on the safety culture or getting them done. Another important point in establishing the safety culture is the training. Universities may have a contribution on the matter as the important partner by practising their responsibilities of research and training activities.

REFERENCES

- [270]. <http://www.ilo.org/global/topics/safety-and-health-at-work/lang--en/index.html>
- [271]. Amponsah-Tawiah, K. & Dartey-Baah, K., "Occupational Health and Safety: Key Issues and Concerns in Ghana", *Int. J. Of Business and Social Science*, 2(14), 119-126, (2011)
- [272]. EU-OSHA, "Occupational Safety and Health culture assessment-A review of main approaches and selected tools, Luxembourg, p77, (2011)
- [273]. Wiegmann, A.D., Zhang, H., Thaden, T.V., Sharma, G. & Mitchell, A., "Safety Culture: A Review", Technical Report prepared for Federal Aviation Administration Atlantic City International Airport, NJ, May, p20, (2002)

- [274]. Health & Safety Executive (HSE), "Organising for Safety –Third Report, Advisory Committee on the Safety of Nuclear Installations", (1993)
- [275]. Fleming, M., "Patient Safety Culture Measurement and Improvement: A "How to" Guide", Healthcare Quarterly Vol. 8, Special Issue, October, 14-19, (2005)
- [276]. Aytac, S., "Importance of safety culture in preventing occupational accidents (in Turkish)", Turkmetal Journal, Oct., (2011)
- [277]. Reason, J., "Achieving a safe culture theory and practice", Work and Stress, 12(3), 293-306, (1998)
- [278]. Health and Safety Executive (HSE), "A review of safety culture and safety climate literature for the development of safety culture inspection toolkit (RR 367) (2005)
- [279]. Guldenmund, F.W., "Understanding and exploring safety culture", PhD Thesis, Delft University, (2010)
- [280]. Pidgeon, N.F., "Safety culture and risk management in organisations", Journal of Cross-Cultural Psychology, 22, 129-140, (1991)
- [281]. Fleming, M., "Safety Culture Maturity Model (OTO 2000-049), HSE Books, (2001)
- [282]. ACS (American Chemical Society), Creating Safety Cultures in Academic Institutions, p57, (2012)
- [283]. Peksen, Y. & Canbaz, S., "Policy of safety and health at work and the role of social dialog in safety culture (in Turkish)", Journal of Occupational Health and Safety, No.25, 12-15, (2005)
- [284]. Pala, K., "OHS policy and safety culture (in Turkish)", Journal of Occupational Health and Safety, No.25, pp18-22, (2005)

Neuromarketing Application for the Television Commercial of a Bank

Mehmet Cabir Akkoyunlu⁴⁹¹, Erhan Ceylan¹, Coşkun Özkan¹

Abstract

Neuroscientific studies have proposed that emotions are considered on a preferential basis, not rationality, that play a significantly important part in affecting decision making, cognition, perception, and behaviour. Understanding emotions are important for the development of marketing and advertising, because consumers tend to choose products and brands according to emotions they sense from those.

Depending on these needs of knowing consumer's behaviour, in recent years neuroscience has been experiencing a quick development, while new brain imaging techniques invent, and old techniques improve to come up with better results.

In this paper it was intended to apply a well known neuroscience technique, EEG, into marketing, which is started to become commonly known as the field of Neuromarketing. The focus of the study is on how brain responds to and get affected by advertising videos. Using the electroencephalography (EEG) we will study the metrics of brain and define them to make improvements.

Keywords: Emotions, neuromarketing, consumer, behavior, EEG

1. INTRODUCTION

Marketing is a outstanding challenge in modern world. It can be thought as a resultant of philosophy, technique, tool and discipline. For years, marketing managers and experts have been trying to reach the audience with the best behaviour possible and to influence the mind of the consumers worldwide. Marketing has evolved from a global and mass marketing to a more distinctive one. As a result, in need of new possibilities of marketing to influence consumers, a new era of marketing has shown up: Neuromarketing.

Neuromarketing is a new field of marketing research. It comes from neurosciences, it's the scientific study of the nervous system, which is originally used to study the brain and find the causes of the main abnormal behaviours and diseases. This field of science crosses the biologic, chemical, psychological and mathematic fields to create an interdisciplinary science. Thanks to neurosciences, scientist are able to draw a map of the brain and understand what the role of each part is. In this paper today's famous tool to perform neuromarketing can clearly be observed and understood via neuromarketing study for a television commercial to demonstrate how EEG is used and analyzed to create a better content in the commercial.

⁴⁹ Corresponding author: Mehmet Cabir Akkoyunlu, mcabir@yildiz.edu.tr

¹Yildiz Technical University, Mechanical Engineering Faculty, Department of Industrial Engineering, Beşiktaş/İstanbul, Turkey.

2. MATERIALS AND METHODS

Paul Postma describes in his book “Anatomie van de Verleiding” three methods which can be used for pursuing neuromarketing goals[1]. According to Postma these methods complement one another. The three methods are: internal reflexes, external reflexes and input/output models [1]-[2]. Internal reflexes refer to the neuroimaging techniques such as fMRI, MEG, EEG, PET and TMS, while external reflexes refer to body language, eye tracking and facial coding. In this paper it correlates with EEG which is a neuroimaging technique [4]. The last method, the input/output method is a practical method where just simple observations are made and requires a expert point of view [5]. Since this paper includes an EEG application, other techniques such as fMRI, eye tracking, etc.. are not going to be mentioned.

2.2 Electroencephalography

The EEG is an acronym of the Electroencephalography. Hans Berger designed the first practical application of EEG in 1920. This passive technology uses sensors to collect electrical signals due to activation of brain waves. To do this, it uses a cap with electrodes that are placed on the head of each participant of the study to measure low voltage signals. When a stimulus is presented to a subject, such as a television commercial, neurons produce a small electrical current that can be amplified. This electric power has multiple frequency patterns, called brain waves, which are associated with different states of consciousness[3]. Electroencephalography (EEG) measures brain activity by placing electrodes on the scalp of the subject. The signals that are being collected are a result of voltage differences due to neural activity in the brain. Even though such voltage differences can occur spontaneously, certain particular patterns can be collected when the subject is subjected to various marketing stimuli such as advertisements[5]. It is estimated that about 80% of our brain activity is used to maintain a state of rest or baseline so it cannot be assumed that the brain waves generated are entirely produced by a stimulus. The EEG has become the best instrument to evaluate the wave brain handles cognitive information along providing subjacent information about neural mechanisms. The EEG is also a very sensitive device to measure low voltage signals so before the assessment is carried out a search of the subject's brain activity to create a baseline and reduce noise [3]. When a subject is subjected to a marketing stimulus, visual activity in the EEG occurs approximately after 300 milliseconds, depending on stimulus occurrence and intensity [5]. The main advantage is thus the high temporal resolution and should be used to follow the time course of neural activity and should not be used to detect the locations of the neural activity [2].

As outputs of EEG, 3 neurometrics are directly recorded from brain: Engagement, excitement and frustration (Table. 3.1). According to the patterns of these neurometrics, it is possible to interpret as below.

Metric	Details	Emotion Range (0-100)
Engagement	Shows mental activity regarding interest, excitement and involvement triggered by stimulus.	Boring ↓ Attractive
Excitement	Shows the enthusiasm and psychological arousal activation controlled sympathetic nervous system.	Calm ↓ Exciting
Frustration	Shows confusion, stress and aggression state caused by the obscurity and complexity of the stimulus.	Clear ↓ Frustrating

Table 1. Neurometrics recorded from EEG

With the help of EEG we can learn; instantly identify the most effective, the most engaging, and the most memorable elements regarding visual, auditory and cognitive stimulus, affects on people's engagement and excitement levels, confusing and boring components, eliminate the alternatives to find the best and most suitable option for the brand, detect the initial attitudes which later on transform into brand impact.

2.3 EEG Application

In this application of EEG technology, a TV commercial which belongs to a Turkish Bank called “Türkiye İş Bankası” is tested and analyzed by neuromarketing executioners in IPSOS Consultancy. In the commercial, one of the most famous stand-up comedian “Cem Yılmaz” plays and it lasts 104 seconds. The aim of neuromarketing application is to make the commercial more productive and recognisable by its target audiences. The name of the commercial is “Servet Bey’in Tasarruf Hikayesi” (Saving Story of Mr. Servet). In the commercial, Servet Bey (Cem Yılmaz) talks with Naci, his customer, and tries to convince him to put his first wage into saving account. To do this, Servet Bey tells a story of his own in which he spends his first wage lavishly. After that, we see how Servet Bey spent his money throughout time and bankrupted eventually. In the end Naci says he had already decided to put his money into the saving account.



Figure 1. Some scenes of the commercial

In this study, between 30-40 volunteers have been tested by EEG while they watch the commercial, and as mentioned above, three different neurometrics, engagement, excitement and frustration, were recorded. Analysis details can be seen below.

2.3.1 Engagement

The commercial’s rate of interest is above average which demonstrates it takes attention of audience. When Servet Bey takes Naci from his seat and starts to tell the story, interest increases. However, we can see a high rate of increase, when the scene of car begins. After a while it reaches it’s peak value. From the beginning of the scene where Servet Bey starts to dance in his suit, engagement value decreases. Until the soup restaurant scene, throughout 25 seconds, audience loses his attention. When the music is off and in the scene of dishes interest is increasing significantly. Although it decreases after a while, kitchen-office lap dissolve helps audience to recover his attention to the commercial. When Servet Bey finishes his last words, audience loses his attention again, and it lasts until the time off-voice starts to talk on pack shot.

Figure 2. Engagement analysis of the commercial



2.3.2 Excitement

In the first 25 seconds of the commercial, there's a downward trend level of audience excitement. When Servet Bey lifts Naci from his seat and starts to tell his story, this leads excitement to rise quickly. Decreasing excitement level, until lap dissolve and the time when music starts, starts to increase again in the scene of car. In the beginning of the scene when Servet Bey starts to dance in his blue suit, excitement tends to decrease alike interest (engagement). The audience, recovering their excitement in the scene of bumping the machine, with the effect of turning down music they can follow the conversation calmly between Servet Bey and Naci. The audience's excitement is increasing with the music in pack shot.

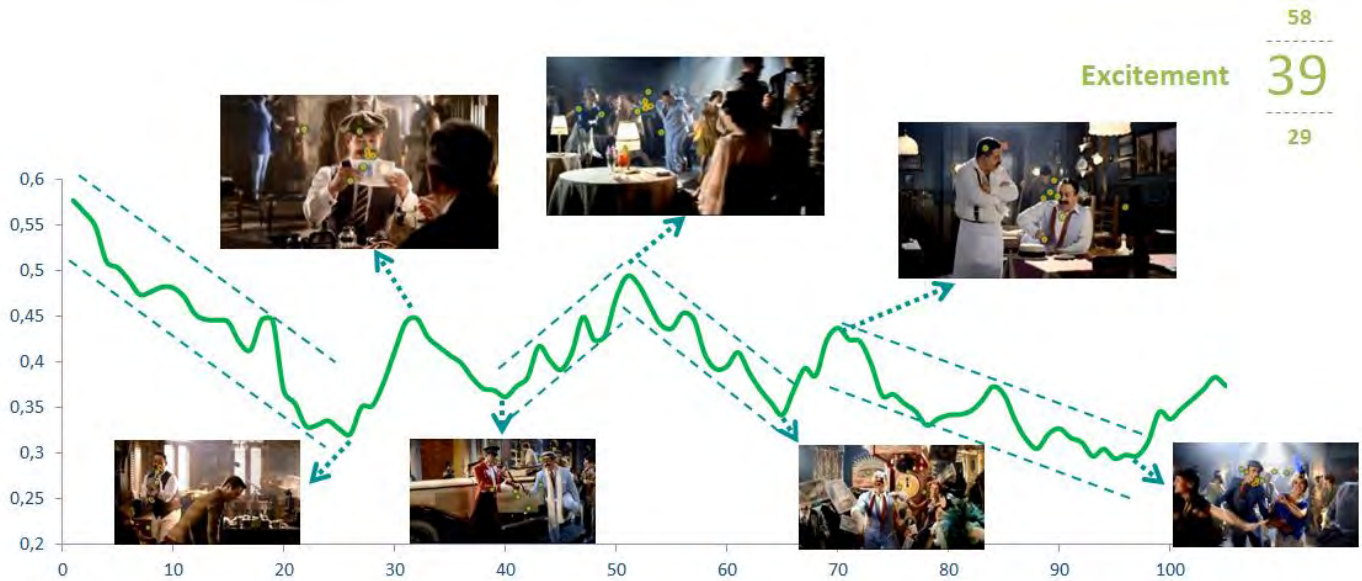


Figure 3. Excitement analysis of the commercial

2.3.3 Frustration

The commercial grabs the audience's attention very quickly. They know Servet Bey from previous commercial, therefore in the first couple minutes they understand this is the last commercial. The audience's frustration level is decreasing through 60 seconds where Servet Bey tells the story of his splendet life. When the music turns down in the scene of soup restaurant, with the concern of not knowing where topic is going, frustration level is increasing. The audience understands the main topic with the help of Servet Bey's important sentence which is "Gözünü seveyim tutumlu ol" (Please be thrifty), therefore frustration decreases again. In the Pack Shot, it is also decreasing, so it is a good sign of that the commercial is going to be recognizable.



Figure 4. Frustration analysis of the commercial

3. Results and Discussions

In the light of the tests and analyses, there are some recommendations for the bank that help them benefit.

Firstly, as a result of the study, there is a 25 seconds lap which is inefficient for the audience. These scenes can be distracted from original commercial or maybe in the future when it will be needed to cut the scenes.

In Turkey, minimum cost of one second commercial, on widely known TV channel, is approximately 240 Turkish Lira. It is a cost of to show it off Prime Time, which means it won't be reached by most of the audience. If it is wanted to show it on Prime Time this cost is going to be much more higher. By using minimum cost, it is frankly said that the bank can benefit 6000 Turkish Lira from every shown commercial. If it is just wanted to shown on 4 channel and 3 times a day, in a month the benefit will be 2160000 Turkish Lira which is immense.

Secondly, it is recommended that where excitement and interest levels are high, there can be put on the screen a logo of the bank which lead the audience to recognize the bank better.

Overall, the study helps the bank benefit in monetary and perception.

4. Conclusion

The purpose of this paper was to gain a better understanding of the concept of neuromarketing and furthermore discuss how the EEG concept is approached in the context of our commercial example.

Although test audience is less, which is 30-40 in this study, it is possible to generate better results with better pick ups of test audience. For example, if target audience is teenagers, choosing teenagers as test audience is surely the most effective way to examine study which lead to certain results of neuromarketing.

It also must be stressed that neuroimaging research with EEG is constantly evolving, both in terms of technology as well as insights into exactly what activity and processes in various areas of the brain actually sense. For example, as technology evolves we are able to measure frequency, temporal, and spatial characteristics of brain activity more accurately and in a complimentary fashion, potentially leading to new insight into what were previously well-accepted brain functions and areas of activity and as a result understanding consumer needs is going to be possible without directly contacting with consumer.

To conclude, the implementation of neuromarketing and neuroscientific techniques resulted more objective results than without these techniques, which are expected to reveal unknown internal information about human behavior, benefits can also be seen in our example on a TV commercial - since neuromarketing and neuroscience are expected to clarify the issue of human behavior, research in all directions should definitely be continued.

ACKNOWLEDGEMENTS

For the Application part of the paper, we would like to thank IPSOS Consultancy for sharing their datas.

REFERENCES

- [1] Paul Postma, (2014). "Anatomie van de Verleiding", Adfo Groep, Netherland.
- [2] Plassman, H., Ramsay, T., Milosavljevic, M., (2011). "Branding the Brain: A Critical Review and Outlook".
- [3] Sebastian, V., (2014). "Neuromarketing and Evaluation of Cognitive and Emotional Responses of Consumers to Marketing Stimuli".
- [4] Kotler, P., Postma, P., (1998). "The New Marketing Era".
- [5] Schaik, K.V., (2013). "How Neuroscience Contributes to Neuromarketing".

ISBN: 978-605-83575-0-1

2016 BOOK OF PROCEEDINGS

ICENS

International Conference on
Engineering and Natural Sciences

www.icens.eu

ICOEST

International Conference on
Environmental Science and Technology

www.icoest.eu

ICSD

International Conference on
Sustainable Development

www.icsd.eu



**EUROPE
CONGRESS**

**TURKISH
AIRLINES**



**ZENITH
GROUP**

**enJOY
Balkans**

CNRGROUP